136

Karlsruher Schriftenreihe Fahrzeugsystemtechnik

Stefan Schläfle

The Influence of Vehicle Operating Conditions on Tire–Road Particulate Matter Emissions

KIT Scientific Publishing

Stefan Schläfle

The Influence of Vehicle Operating Conditions on Tire–Road Particulate Matter Emissions

Karlsruher Schriftenreihe Fahrzeugsystemtechnik
Band 136

Herausgeber
FAST Institut für Fahrzeugsystemtechnik
Prof. Dr.-Ing. Martin Cichon
Prof. Dr. rer. nat. Frank Gauterin
Prof. Dr.-Ing. Marcus Geimer
Prof. Dr.-Ing. Frank Henning
Prof. Dr.-Ing. Luise Kärger

Das Institut für Fahrzeugsystemtechnik besteht aus den Institutsteilen Bahnsystemtechnik, Fahrzeugtechnik, Leichtbau und Mobile Arbeitsmaschinen.

Eine Übersicht aller bisher in dieser Schriftenreihe erschienenen Bände finden Sie am Ende des Buchs.

The Influence of Vehicle Operating Conditions on Tire–Road Particulate Matter Emissions

by
Stefan Schläfle

KIT Scientific Publishing

Karlsruher Institut für Technologie
Institut für Fahrzeugsystemtechnik

The Influence of Vehicle Operating Conditions
on Tire–Road Particulate Matter Emissions

Zur Erlangung des akademischen Grades eines Doktors der Ingenieurwissenschaften von der KIT-Fakultät für Maschinenbau des Karlsruher Instituts für Technologie (KIT) genehmigte Dissertation

von Stefan Schläfle, M.Sc.

Tag der mündlichen Prüfung: 6. November 2025
Hauptreferent: Prof. Dr. rer. nat. Frank Gauterin
Korreferent: Prof. Dr.-Ing. Andreas Wagner

Impressum

Scientific Publishing

Karlsruher Institut für Technologie (KIT)
KIT Scientific Publishing
Straße am Forum 2
D-76131 Karlsruhe

KIT Scientific Publishing is a registered trademark
of Karlsruhe Institute of Technology.
Reprint using the book cover is not allowed.

www.bibliothek.kit.edu/ksp.php | E-Mail: info@ksp.kit.edu | Shop: www.ksp.kit.edu

Print on Demand 2026 – Gedruckt auf FSC-zertifiziertem Papier

ISSN 1869-6058
ISBN 978-3-7315-1462-6
DOI 10.5445/KSP/1000187545

Vorwort des Herausgebers

Die Fahrzeugtechnik ist kontinuierlich Veränderungen unterworfen. Klimawandel, die Verknappung einiger für Fahrzeugbau und -betrieb benötigter Rohstoffe, globaler Wettbewerb, gesellschaftlicher Wandel und das rapide Wachstum großer Städte erfordern neue Mobilitätslösungen, die vielfach eine Neudefinition des Fahrzeugs erforderlich machen. Die Forderungen nach Steigerung der Energieeffizienz, Emissionsreduktion, erhöhter Fahr- und Arbeitssicherheit, Benutzerfreundlichkeit und angemessenen Kosten sowie die Möglichkeiten der Digitalisierung und Vernetzung finden ihre Antworten nicht aus der singulären Verbesserung einzelner technischer Elemente, sondern benötigen Systemverständnis und eine domänenübergreifende Optimierung der Lösungen.

Hierzu will die Karlsruher Schriftenreihe für Fahrzeugsystemtechnik einen Beitrag leisten. Für die Fahrzeuggattungen Pkw, Nfz, Mobile Arbeitsmaschinen und Bahnfahrzeuge werden Forschungsarbeiten vorgestellt, die Fahrzeugsystemtechnik auf vier Ebenen beleuchten: das Fahrzeug als komplexes, digitalisiertes, mechatronisches System, die Mensch-Fahrzeug-Interaktion, das Fahrzeug in Verkehr und Infrastruktur sowie das Fahrzeug in Gesellschaft und Umwelt.

Mit der stärkeren Marktdurchdringung der Elektrofahrzeuge und dem damit verbundenen Rückgang der verbrennungsmotorisch angetriebenen Fahrzeuge, wechselt im öffentlichen Bewusstsein der Blick von der Feinstaubemission der Verbrennungsmotoren zu derjenigen des Reifen-Fahrbahn-Kontakts. Bislang gibt es nur ein sehr unvollständiges Wissen darüber, was die Bildung von Feinstaub begünstigt oder sie verringert. Dies liegt u. a. auch an dem Mangel geeigneter Messverfahren.

Hier setzt die Arbeit von Herrn Schläfle an, in der er insbesondere den Einfluss der Betriebsbedingungen auf die Feinstaubemission experimentell detailliert untersucht. Darüber hinaus variiert er die Art des Reifens (Sommer-, Ganzjahres- und Winterreifen) und der Fahrbahn (Beton und Asphalt). Er schafft mit der Erweiterung eines Innentrommelprüfstands um eine Partikelabsaugung und Partikelmesstechnik eine neuartige Messmöglichkeit, die es erlaubt, Partikelemissionen im Bereich von $0.3\,\mu\mathrm{m}$ bis $10\,\mu\mathrm{m}$ hinsichtlich Anzahl, Masse und Größenverteilung in Echtzeit auf realen Fahrbahnbelägen zu bestimmen, ohne von Partikeln aus der Umgebung beeinflusst zu werden. Dabei können Antriebs-, Brems- und Seitenkräfte, Radlast, Rollgeschwindigkeit und Umgebungstemperatur realitätsnah variiert werden. Auch der Einfluss der Fahrbahngriffigkeit wird erfasst. Die quantitativ ausgewerteten Ergebnisse schaffen eine bislang nicht vorhandene Wissensbasis für die Entwicklung emissionsarmer Fahrzeuge, Fahrweisen, Reifen und Fahrbahnen.

Frank Gauterin
Karlsruhe, im November 2025

Acknowledgments

This thesis was written during my time as a research associate at the Institute of Vehicle System Technology (FAST), Division of Vehicle Technology, at the Karlsruhe Institute of Technology (KIT).

I would like to particularly thank Prof. Dr. rer. nat. Frank Gauterin for supervising the work, providing constructive suggestions, critically reviewing the manuscript, and being the first examiner in the doctoral committee. For being the second examiner in the doctoral committee and the time and effort associated with it I would like to thank Prof. Dr.-Ing. Andreas Wagner. I would also like to express my gratitude to Univ.-Prof. Dr.-Ing. Tobias Düser for chairing the doctoral committee and for the interest he has shown in my work.

Furthermore, I would like to express my deepest gratitude to Dr.-Ing. Hans-Joachim Unrau, without whom this work would not have been possible. He supported me from beginning to end with his unique ability to explain complex interrelationships in simple, understandable terms, as well as through numerous technical discussions and targeted advice. His contributions were crucial for the success of this work. Moreover, I would like to express my special thanks to Prof. Dr.-Ing. Günter Leister. He supported me in countless conversations and discussions, providing precious suggestions and his professional expertise and life experience for the content of the thesis as well as for the future course of my career. I would also like to thank Dr.-Ing. Régis Lallement and Dr.-Ing. Alexandra Killik for the professional exchange, numerous ideas, targeted support, and the excellent collaboration.

Moreover, I would like to thank Mercedes-Benz AG, especially the tire development department of Jürgen Bauer and Herbert Weidlich. By showing full

confidence in my ability to manage the project, which was the context in which most of this work was created, they directly contributed to its success.

Apart from that, I would like to thank my colleagues at the test bench, Kerstin Dietrich and Markus Diehm. They contributed to this work by giving numerous technical advice as well as by paving the way for the final results by adapting the test bench and carrying out the test series. Special thanks go to my colleague Meng Zhang representative for all other colleagues at the institute for the exceptional time I had as a research associate. One can only succeed in such a tedious venture without losing courage and joy through interchange, both professional as well as private.

I would also like to express my sincere gratitude to my parents for their active support throughout my career, which made my studies and doctoral thesis possible in the first place. Their support was invaluable, and I am infinitely grateful for it. Moreover, I would like to thank my sister: firstly, for being my guide throughout my scholastic and academic career and inspiring me to take on the challenges that come with a doctorate. Secondly, for supporting me with advice and assistance during my doctorate, especially during difficult phases.

Finally, I would like to express my special thanks to my girlfriend Catarina. Her understanding and support as well as her unwavering persistence in reminding me that even the most stressful phases of a doctorate require free time have contributed significantly to my long-term success.

Stefan Schläfle
Karlsruhe, November 2025

Abstract

The hazard to human health posed by particulate matter (PM) has been documented in countless publications. A significant proportion of PM comes from road traffic. For a long time, it was assumed that particles from internal combustion engines were mainly responsible. However, especially with the advent of electrification, it has become increasingly clear that abrasion processes also make a significant contribution to PM emissions. These include particles from friction brakes and tire–road contact. Their importance has been increasing as a result of the steady decline in exhaust emissions and will continue to do so as electrification progresses. For this reason, the upcoming Euro 7 emission standards will for the first time include limits for both emitters—on PM emission for friction brakes and on total mass loss for tire wear. Currently, there is neither a database nor a suitable measurement method to regulate tire or tire–road PM.

This work makes a significant contribution to a better understanding of tire–road particulate matter. For this purpose, an existing tire internal drum test bench was modified and extended to enable the measurement of tire–road PM in real time. A method was developed to take into account the texture of the road surface, allowing reproducible measurements on real road surfaces. This enabled the investigation of vehicle, road and environmental influences on emissions. The relationships between the vehicle influences and the emission are described by mathematical functions. The influence of the road surface and the environment is shown by means of comparisons. Driving style, characterized by longitudinal and lateral dynamics, are shown to be the most important influence of the vehicle or the driver. In addition, significant differences in emissions were found, which can be attributed to the tire type (summer, winter, all-season) and the skid resistance of the road surface. Finally, based on the correlations found between load condition

and emissions, a model was developed that uses real driving data to predict PM emissions for any route profile on public roads.

Kurzfassung

Der Einfluss der Fahrzeugbetriebsbedingungen auf die Reifen-Fahrbahn-Feinstaubemissionen

Die von Feinstaub ausgehende Gefahr für die menschliche Gesundheit ist durch unzählige Veröffentlichungen belegt. Ein wesentlicher Bestandteil des Feinstaubs stammt aus dem Straßenverkehr. Lange Zeit ging man davon aus, dass dafür maßgeblich die aus Verbrennungsmotoren stammenden Partikel verantwortlich seien. Doch insbesondere durch die Elektrifizierung zeigt sich immer deutlicher, dass auch Abriebprozesse einen wesentlichen Beitrag zum Feinstaubausstoß leisten. Dazu zählen unter anderem Partikel aus Reibbremsen und dem Reifen-Fahrbahn-Kontakt. Deren Bedeutung ist durch stetig sinkende Verbrennungsemissionen bereits gestiegen, was sich im Laufe der Elektifizierung weiter verstärken wird. Daher wird die geplante Euro 7 Emissionsnorm erstmals Grenzwerte für beide Emittenten enthalten – im Falle von Reibbremsen bezüglich der Partikelemission, im Falle des Reifens bezüglich des Massenverlusts durch Verschleiß. Zur Regulierung von Reifen- bzw. Reifen-Fahrbahn-Feinstaub fehlt aktuell sowohl die Datenbasis als auch eine geeignete Methode zur Messung.
Diese Arbeit leistet einen wesentlichen Beitrag zum besseren Verständnis von Reifen-Fahrbahn-Feinstaub. Dazu wurde ein bestehender Reifen-Innentrommelprüfstand durch Umbauten und Erweiterungen in die Lage versetzt, Feinstaub aus dem Reifen-Fahrbahn-Kontakt in Echtzeit zu messen. Es wurde eine Methode erarbeitet, die die Berücksichtigung der Fahrbahntextur erlaubt und so reproduzierbare Messungen auf realen Fahrbahnoberflächen ermöglicht. Somit konnten fahrzeug-, fahrbahn- und umgebungsseitige Einflüsse auf die Emission untersucht werden. Der Zusammenhang zwischen den Fahrzeugeinflüssen und der Emission wird durch mathematische Funktionen beschrieben. Der Einfluss

der Fahrbahn und der Umgebung wird anhand vergleichender Gegenüberstellungen aufgezeigt. Dabei zeigt sich, dass die Fahrweise, charakterisiert durch Längs- und Querdynamik, den größten vom Fahrzeug bzw. dem Fahrer ausgehenden Einfluss darstellt. Darüber hinaus wurden signifikante Emissionsunterschiede festgestellt, die auf den Reifentyp (Sommer, Winter, Allwetter) und die Griffigkeit der Fahrbahn zurückzuführen sind. Auf Basis der ermittelten Zusammenhänge zwischen Belastungszustand und Emission wurde schließlich ein Modell entwickelt, das unter Verwendung realer Fahrdaten Vorhersagen zur Feinstaubemission für beliebige Streckenprofile auf öffentlichen Straßen trifft.

Contents

Acronyms and Symbols

Acronyms

AC	Asphalt Concrete
ADAC	Allgemeiner Deutscher Automobilclub
BEV	Battery Electric Vehicle
CB	Confidence Band
CG	Center of Gravity
CI	Confidence Interval
EEA	European Environment Agency
EF	Emission Factor
ICEV	Internal Combustion Engine Vehicle
IMU	Inertial Measurement Unit
FAST	Institute of Vehicle System Technology
KIT	Karlsruhe Institute of Technology
MA	Mastic Asphalt
NEE	Non-Exhaust Emissions
PA	Porous Asphalt

PM	Particulate Matter
$PM_{2.5}$	Particulate Matter with a Diameter smaller than $2.5\,\mu m$
PM_{10}	Particulate Matter with a Diameter smaller than $10\,\mu m$
PMC	Particle Mass Concentration
PMD	Particle Mass Distribution
PNC	Particle Number Concentration
PND	Particle Number Distribution
PSD	Particle Size Distribution
RCF	Residual Cornering Force
SCRIM	Sideway Force Coefficient Routine Investigation Machine
SKM	Seitenkraftmessverfahren
SMA	Stone Mastic Asphalt
SRT	Skid Resistance Tester
TRWP	Tire and Road Wear Particles
TSP	Total Suspended Particulate Matter
TWP	Tire Wear Particles
WHO	World Health Organization

Constants

π	Pi: $3.14159\ldots$

Latin Symbols and Variables

A	Area
b	Width
c	Stiffness
$\tilde{c}$	Slip stiffness
d	Diameter
E	Energy
$\bar{E}$	Energy per unit area
F	Force
g	Standard gravity
h	Height
k	Correction factor
$\bar{k}$	Environmental parameter
l	Length
P	Power
p	Pressure
R	Radius
S	Slip distance
s	Slip ratio
T	Temperature
V	Volume

$\dot{V}$	Volume flow
v	Velocity

Greek Symbols and Variables

α	Slip angle
β	Material parameter
γ	Camber angle
Θ	Angle of misalignment
λ	Wavelength
μ	Friction coefficient
φ	Angular coordinate

General Deep Indexes

a	Ambience
ad	Adhesion
b	Braking
CG	Center of Gravity
d	Driving
e	Extraction
f	Friction
fa	Front axle
g	Glass

i	Inflation
l	Left
m	Mass
n	Number
p	Particle
r	Right
ra	Rear axle
s	Sample
sl	Sliding
t	Tire
tr	Tire–Road
w	Wheels
x	Longitudinal direction
y	Lateral direction
z	Vertical direction

1 Introduction

1.1 Motivation

Air pollution is considered to be the greatest environmental threat to human health by both the World Health Organization (WHO) and the European Environment Agency (EEA) [35, 149]. A major component of air pollution is particulate matter (PM). Long-term exposure in particular, but also short-term exposure, can lead to serious respiratory problems [128]. As a result of ever stricter emission standards, PM emissions have already decreased significantly in the last 30 years [130]. For road traffic, however, this reduction is mainly due to cleaner combustion processes and increasingly sophisticated filtration systems [92].
In contrast, there has been no decrease in non-exhaust emissions (NEE) over the same period [117]. NEE include particles from braking and tire–road contact, which are mainly caused by abrasion processes, but also particles deposited on the road that are resuspended by vehicles driving over them [8]. In order to reduce their contribution to total PM emissions, the European Union has for the first time included NEE in the new EURO 7 emission standards to be applied from 2026 [34]. Although the limit value for tires contained therein will only address overall tire wear and not PM emissions, it can be assumed that this regulation is only the prelude to ever more stringent limits that will also address PM emissions in the long term.
Such a limit value is all the more likely as numerous studies point to the risk of increasing PM emissions from tire–road contact due to electrification [92, 125]. Both the increased mass and torque of battery electric vehicles (BEVs) and the use of regenerative braking systems (reduction of PM from friction brakes) will contribute to an increasing interest in tire–road PM emissions [92]. Until now,

however, there has been a lack of both a reliable database and a reproducible method for determining a limit value. In this context, the question arises as to how exactly the vehicle, the tire, and the road surface as well as environmental conditions influence tire–road PM emissions. In addition to the level of emissions, this question also relates to the particle size distribution (PSD), as the hazard potential of particles also depends on their size [128].
This question can be divided into sub-questions, which will be answered in the context of this thesis:

- Which are the main parameters to influence the emission of tire–road particulate matter?
- Can a mathematical relationship be derived between the individual parameters and the emission?
- Does the PM size distribution change in addition to the total emission when the influencing parameters are changed?
- If so, what is the influence of each parameter?

Finally, the answers to these questions will be used to derive recommendations for mitigating tire–road PM emissions.

1.2 State of the Art

1.2.1 Particulate Matter in General

Particulate matter refers to particles in the air that do not settle to the ground immediately, but remain in the atmosphere for a certain period of time [128]. The duration in the air and the settling velocity depend on the density and size of the particle [51]. Particles can be solid or liquid, or a combination of both [134]. Individual particles are usually invisible to the naked eye because of their size.

Only their totality becomes visible under certain weather conditions as haze or smog [128, 134].

Sources and Generation

Both natural and anthropogenic sources contribute to PM pollution [128]. Natural sources include volcanoes, forest and bush fires, and erosion of soil. However, pollen, spores, bacteria and viruses also make a natural contribution to total pollution [91, 128]. The most important anthropogenic sources of PM are industrial processes, power plants, waste incineration and heating plants as well as agriculture and traffic [130].
PM can be divided into primary and secondary particulate matter depending on its origin. Particles that originate directly from the source and are emitted as solids, such as tire and road wear particles (TRWP), are referred to as primary PM [128]. However, particles can also be formed from gaseous precursors such as sulfur dioxide, nitrogen dioxide, ammonia, and hydrocarbons. PM formed in this way is referred to as secondary PM [58, 134].
The highest concentrations of PM are usually found in urban areas, where emissions from residential heating and traffic are added to the background concentration. However, significant proportions of the background concentration may originate from outside the urban area. The actual PM is only formed during transport from the gaseous precursors [128]. Nevertheless, high levels of PM are particularly problematic in urban areas because of the high number of people affected.

Implications

Once the particles are inhaled, several harmful effects can occur [135]. PM is therefore considered to be the greatest environmental risk to human health [23, 80, 88]. A particular problem with PM exposure is that there is no concentration threshold below which adverse effects are not expected [148]. In addition, not only long-term exposure is harmful, but even short-term elevated concentrations can

cause complaints [128, 148]. Evaluations by the German Federal Environmental Agency (Umweltbundesamt) have shown that elevated PM concentrations for only a few hours or days lead to an increase in hospital admissions for respiratory problems [128]. Reduced lung function, irritation of the respiratory system as well as associated coughing and asthma are observed [134].
The hazard potential of inhaled particles primarily depends on how deeply they penetrate the respiratory system and how long they remain there. The size of the particles is critical, as the depth of penetration increases with decreasing particle size. Coarse particles are more likely to be deposited in the upper airways, while the smaller ones can penetrate into the alveolar tissue [128]. The smallest ones enter the bloodstream where they can cause inflammatory reactions, cardiac arrhythmias and enhance the probability of thrombosis [80]. Once in the bloodstream, the particles spread throughout the body. Studies on the neurological effects of PM indicate that long-term exposure can impair memory performance and facilitate the development of dementia [152]. The hazard potential is not only due to the particles themselves, but also due to the harmful effects of heavy metals or carcinogenic polycyclic aromatic hydrocarbons which accumulate on their surface. This allows other pollutants to enter the body on the particles. Due to their large surface-to-volume ratio, fine particles are particularly contaminated and therefore pose an even higher health risk [128].

Legal Regulations

To reduce emissions and protect citizens from the dangers of PM and other pollutants in the air, many countries began limiting pollutant emissions in the late 1990s. The EU laid the foundation for air pollution control in its member countries with Directive 99/30/EC, which entered into force on January 1, 2005. In addition to PM limit values, it also set limit values for sulphur dioxide, nitrogen dioxide and oxides of nitrogen, and lead in ambient air. However, these limit values do not refer to emissions but to the permissible immission, i.e., the particle concentration in the ambient air [121]. Germany implemented the requirements contained in the "Verordnung über Immissionswerte für Schadstoffe in der Luft"

into national law [128] in 2002 [17]. The limit values for PM only concerned the PM_{10} size fraction (see section 2.6). Since then, a mean value of $50\,\mu g\,PM_{10}/m^3$ may not be exceeded on more than 35 days per calendar year and an annual mean value of $40\,\mu g\,PM_{10}/m^3$ must be complied with [121]. In addition, since January 1, 2015, there has been an upper limit for the finer fraction $PM_{2.5}$, according to which an annual mean value of $25\,\mu g\,PM_{2.5}/m^3$ must not be exceeded [123]. Since the directives entered into force, immission levels in Germany have been declining continuously, resulting in mean values of about $13\,\mu g\,PM_{10}/m^3$ and about $8\,\mu g\,PM_{2.5}/m^3$ in 2023. None of the almost 400 monitoring stations of the German Federal Environmental Agency [131] exceeded the limit value of 35 days.

The decline in immissions is partly due to a sharp drop in emissions from the transportation sector [124]. This reduction was mainly due to a decrease in exhaust emissions achieved through increasingly stringent emission standards [92, 124]. Over the same period, the so-called non-exhaust emissions have stagnated or even increased [92]. These include particles from friction brakes and the tire–road contact, which are largely due to abrasion, but also particles from the environment that had already been deposited on the road and were resuspended by following vehicles [8]. Both developments have contributed to a steady increase in the relative share of NEE in total PM emissions from the transportation sector. Already in 2016, PM from abrasion processes (not from internal combustion engines) contributed more than 73 % to PM_{10} and about 60 % to $PM_{2.5}$ emissions from all road transport in the UK [2, 40]. Taking into account the resuspension of previously deposited particles, even higher proportions of 90 % for PM_{10} and 85 % for $PM_{2.5}$ were found [125]. Regardless of the exact values, it is undisputed that NEE have replaced exhaust emissions as the dominant source of PM in road traffic. As electrification progresses and older vehicles are decommissioned or taken out of service, this trend will continue in the future [40, 125, 137].

In addition, electrification and the associated regenerative braking will reduce the importance of PM emissions from the braking system [10, 40, 92, 136]. Scenarios dealing with the resulting mitigation in emissions indicate potential savings of 26 % [10], 50 % [138] and 66 % [52] to even 100 % [125]. The result depends largely on the extent to which braking operations can be managed with the help

of the regenerative braking system [10]. However, given that electric vehicles still need to have a friction brake for safety reasons (e.g., for emergency braking or braking down to standstill) [49, 92], it is currently unrealistic to completely eliminate the brake as a source of PM. This is one of the reasons why the Euro 7 emission standards will regulate brake emissions in addition to exhaust emissions for the first time. For both BEVs and internal combustion engine vehicles (ICEVs), there will be a limit value for PM emissions per kilometer (on a standard cycle) [122].
Accordingly, brake emissions will be reduced regardless of the future level of electrification. Both the regulation of brake emissions and the decline due to regenerative braking in electric vehicles will contribute to this reduction and thus lead to a further increase in the relative share of PM emissions from the tire–road contact. If the resuspension of deposited particles is not taken into account, the tire–road contact is expected to become the dominant source of PM in road traffic. Some studies conclude that not only the relative fraction but also the absolute amount emitted from tire–road contact will increase [10, 92, 125]. This is due to both the typically higher unladen mass of battery electric vehicles and the higher torque that can be demanded even when stationary (starting torque) [40, 125].
Increasing PM emissions from tire–road contact are problematic in that there is no regulation and it is unlikely that there will be one in the near future. Although the Euro 7 emission standards will include tire–road contact, the current draft is limited to the total mass loss due to tire wear [34]. A limit for PM emissions from tire–road contact is not included. Such a regulation is almost impossible to implement at this stage, as there is neither a reliable database for setting a limit, nor a standardized measurement method that could be used to determine this data on a global basis.

1.2.2 Measuring Tire–Road Particulate Matter

Previous approaches to measure tire–road PM emissions can be divided into three categories [125].
For ambient [16, 24] or tunnel [75, 79] measurements, PM is collected by air

filtration at two locations in traffic over a longer period of time. The traffic continues to flow unaffected by this. In ambient measurements, collection takes place in the immediate vicinity of a road and the difference between the measured value and the background concentration at the second location (as far away as possible from the emission) is calculated. For tunnel measurements, PM is measured at both ends of the tunnel. If there are separate, unconnected tubes for the two directions of travel, i.e., if the tubes are only used in one direction and are ventilated in the direction of travel, the background concentration can be measured at the entrance of a tube. The concentration at the tube exit is correspondingly higher, since it includes the emissions of the entire distance between the entrance and exit [79]. Emission factors (EFs) for single vehicles can be calculated by first inferring the particle concentration of the filtered air from the collected amount of PM and subsequently concluding the required emission to reach this particle concentration. The total emission can be divided by the number of vehicles passed. The EFs are calculated by chemical analysis and the resulting division into a combustion and an abrasion fraction [125]. Precise statements about the influence of individual driving conditions, vehicle characteristics or tire types are not possible with this method.

In mobile measurements [22, 74, 81, 82, 115], a vehicle or a trailer is equipped with measurement systems. The vehicle is driven in different load conditions while the emitted particles are measured in or behind the wheel arch. The background concentration is measured at an additional location in the front of the vehicle, which minimizes, but does not completely eliminate fluctuations in the background concentration. Changing wind directions and flow conditions affect the reproducibility. Another challenge is the influence of changing road surfaces. For high reproducibility, the road surface would have to be known at every point along the route and be constant between multiple measurements. Furthermore, because only a portion of the air flow through the wheel arch is analyzed, rather than the entire flow, no reliable statements can be made about the total emission or the resulting EF. The limited space available in the wheelhouse makes it difficult, if not impossible, to extract the full volume flow required.

On test benches, one [1, 37, 61, 74, 98] or several [46, 47, 73] tires are tested under defined load conditions on a drum or circular surface. Test benches provide

the advantage of high reproducibility regarding the environmental conditions. In addition, they offer the possibility of stationary driving conditions, which allows reliable statements to be made about emissions at the respective load condition. Some test benches allow only a limited number of parameter variations (e.g., driving speed), while others allow the nearly realistic variation of all movements and forces occurring in real-world driving. While the use of real road surfaces is problematic on external drum test benches due to centrifugal forces, internal drum test benches have no limitations in this regard. In addition, the test bench environment offers the advantage of extracting all the air flowing around the tire–road contact. This allows conclusions to be drawn about overall emissions. Due to the well-designed enclosure and the use of real road surfaces, internal drum test benches are particularly suitable for reproducibly measuring PM emissions from tire–road contact. PM measurements on an internal drum test bench have already been described in [37, 48, 110, 111, 112, 113, 114].
Both the different measurement methods and other differences, such as different road surfaces and environmental conditions, lead to a large number of differing statements about the individual influencing parameters. The following section provides an overview of the available results from literature.

1.2.3 Influences on Tire–Road Particulate Matter

Numerous references agree that tire forces parallel to the road surface are the or at least one of the major influencing parameters on the emission of tire–road PM [37, 42, 50]. In agreement with this, Feißel et al. attribute the formation and emission of particles to the presence of slip [36]. Accordingly, it is undisputed that high forces or the resulting slippage in tire–road contact lead to a significant increase in PM emissions [11, 12]. As test results at a sufficiently high number of operation conditions and support points are missing, most authors limit themselves to qualitative statements. The few statements regarding the quantitative relationship between force or slip ratio and PM emission vary widely. In the test bench experiments of Park et al. [98], a slip angle of $4°$ led to a 2 to 3 times higher PM emission than free rolling. Kwak et al. [74] even give factors of 30 to

40 for heavy deceleration in their test bench experiments. However, since their study focused on the number of particles, it is unclear whether these values also apply to the particle mass. Nevertheless, the results of Foitzik et al. are in the same order of magnitude [37]. The authors note that driving and braking forces of the same magnitude resulted in different emissions on their sandpaper-covered internal drum. It was shown that the relationship between force and emission in the particle size range from $5.6\,\mathrm{nm}$ to $560\,\mathrm{nm}$ is best described by a second-order function for driving force and a fourth-order function for braking force. A quadratic or exponential relationship with the emission was found for the slip angle. This result is confirmed by Tonegawa et al. [126], who performed driving tests and plotted the emission over the lateral acceleration. The fact that the level of emission does not only depend on the force but also its direction is also evident from the driving tests of Feißel et al. [36]. The authors state that lateral force generally has a greater influence on emissions than longitudinal force. In view of these statements, it seems reasonable to differentiate the emissions according to the force direction. On the other hand, a sufficiently large number of support points must be examined to determine the mathematical correlation.

The influence of vehicle mass and the associated wheel load on PM emissions is of particular interest in light of the increasing electrification of the vehicle fleet. Since BEVs are typically several hundred kilograms heavier than comparable ICEVs due to the weight of the battery, this could result in significant additional emissions from tire–road contact [125]. Numerous publications have shown that a higher wheel load leads to higher emissions [1, 20, 61, 93]. They report positive linear correlations between wheel load and PM emissions for their test bench measurements [1, 61]. However, both results are from tests in which no longitudinal or lateral force was applied. This is problematic in that the heavier BEVs tend to have powerful drives which provide equal or even increased longitudinal dynamics compared to ICEVs. This raises the question of how the combination of higher wheel load and higher driving forces (to maintain longitudinal dynamics) affects tire–road PM emissions.

Much less information is available on the effect of tire inflation pressure on tire–road PM emissions. Many publications list it as an influencing parameter, but usually only with the statement that an optimal tire inflation pressure can reduce

the PM emission [40, 83]. Furthermore, some references state that higher tire inflation pressure has a positive effect on tire wear [77, 119, 144]. However, it remains to be clarified whether this correlation also applies to the emission of PM. Doubts about that are justified as PM emissions from tire–road contact do not only include tire material but also fragments from the road surface. Hence, it is quite possible that higher inflation pressure reduces PM emissions from the tire, but increases those from the road surface due to the higher contact pressure. Therefore, the exact effect of tire inflation pressure on PM emissions is still unclear.

The relationship with driving speed is also not clear. Many authors state that PM emissions increase with increasing speed [12, 20, 46, 72]. However, the statements are often not sufficiently illuminated or discussed. For example, it is not always clarified how large the increase in emissions was relative to the increase in speed. Therefore, it is not clear whether a positive correlation with the emission or the emission factor (emission per distance traveled) is meant. Only if the increase in emissions is greater than the increase in driving speed is there indeed a positive relationship with both emission and emission factor. If the increases in speed and emission are similar, it can be concluded that the emission factor is independent of driving speed. The test bench experiments by Foitzik et al. showed that this statement is true for nanoparticles. The authors did not compare the particle concentrations (per time), but the emission factors (per distance) derived from them [37]. Feißel et al. and Tonegawa et al. came to the same conclusion with their test bench measurements and driving tests [36, 126]. The authors explicitly state that although there was an increase in the emission factor (per distance), this was due to the fact that the air resistance of the vehicle increases with increasing speed [36]. Thus, the cause of the higher emission factor was the higher driving power required to overcome the air resistance, not the increased driving speed itself. Furthermore, it is important to compare the total emissions from tires and road surface, as neglecting one of the two components would lead to significant differences.

In addition to the driver and the vehicle, the tires, the road, and the environmental conditions have an influence on the emission of tire–road PM [42]. However, most the literature on the influence of tires refer to the difference between friction tires

and studded tires, which cause substantially higher emissions [46, 54, 72, 73]. This is due to the metal studs which wear the road much more than conventional tires. However, it can also be assumed that the resulting tire–road dust is a completely different mixture of that caused by friction tires. The only study including a comparison between summer and winter tires concludes that winter tires cause two to ten times more emissions than summer tires [145]. This result is plausible considering that the wear of winter tires is also significantly higher [83]. However, the exact ratio presumably depends on the chosen tires and numerous environmental and road conditions.

In terms of environmental parameters, temperature is probably the most important factor. However, there is little information about its exact influence. Yan et al. state that in their experiments on a miniature tire abrasion test bench, there was a continuous decrease in PM emissions with increasing ambient temperature [151]. Chang et al. reached the opposite conclusion in their outer drum experiments. The authors show both an increase in total emissions with higher ambient temperature and a higher proportion of coarse particles [21]. That shows that great attention must be paid to the measured particle size range, especially with the influence of temperature. This is due to the fact that the material properties of the tire rubber change as the temperature changes. On the one hand, this can lead to the formation of larger particles, as observed by Chang et al. On the other hand, an additional formation mechanism can take place, which produces mainly extremely fine particles (nanoparticles) by evaporation if the material is overheated [19]. Therefore, statements can only be made for a particular range of the entire particle size spectrum.

In addition to temperature, air humidity significantly influences PM emissions from tire–road contact [50, 71]. Higher humidity leads to lower emissions [6, 20]. On the one hand, humid or wet conditions generally lead to less tire wear than dry conditions [21]. On the other hand, the water has a binding effect on the particles. This means that deposited particles are not resuspended, and newly formed particles are bound to the tires or the road surface [71]. However, the exact manner in which humidity affects the formation of new particles is still unclear [92].

On the road side, the material used plays a critical role. The studies by Wilkinson et al. showed that different asphalt and concrete road surfaces have an influence

on PM emissions which is dependent of the tire type. However, the higher (mass-based) emissions were recorded on concrete for both summer and winter tires [145]. This is also the conclusion of Alexandrova et al. [3] and Allen et al. [4] in their ambient measurements. The authors indicate a $40\,\%$ to $100\,\%$ higher emission for concrete than for asphalt surfaces. As their results are based on ambient measurements, it is not possible to make a statement about the tire types included. In addition to the pavement material, the surface texture could have a significant effect. However, no results could be found on that in the literature.
All influences described so far were related to the magnitude of the emitted particle mass or number. However, from a medical point of view (see section 1.2.1), it is important to know the size of the emitted particles and how their size changes due to various influences. Since the particle size, as well as the height of the emission, is dependent of numerous factors, it is not possible to provide a generally valid size distribution. Many authors report a bimodal distribution for the number of particles, i.e., two peaks within the PM_{10} fraction [1, 65, 82]. However, the exact location of the peaks differs from study to study due to different tires, environmental conditions, and test methods. Nevertheless, there is agreement between the studies on the change in particles under load. Accordingly, higher load leads to an increase in particle size in the micrometer range. The higher load can either be caused by tire forces parallel to the road surface [61, 98, 115] or by additional wheel load [61]. In the case of tire forces parallel to the road surface, i.e., acceleration, deceleration, or cornering, some authors observed a strong increase of ultrafine particles [74, 98]. Apart from that, only one statement on the influence of temperature on the size distribution could be found in the literature. According to Chang et al., a lower temperature leads to a higher number of fine particles, while high temperature leads to larger particles and thus to higher total abrasion [21]. The authors of the same study [21] investigated how humidity affects the size distribution of tire wear particles between $10\,\mu\mathrm{m}$ and $400\,\mu\mathrm{m}$. Through their experiments, they concluded that fewer coarse particles are generated when the relative air humidity is increased, while the road surface is still dry, resulting in a decrease in the mean particle size. Consistent with this trend, they also observed that on wet road surfaces predominantly small particles were generated. No information is yet available on the influence of the other

parameters discussed above.
In addition to the individual influences on the level of emissions, it is particularly interesting for regulatory purposes to know what emissions a vehicle produces per distance traveled. This value is usually called the emission factor (EF) and is expressed in $\mathrm{mg/vkm}$ (milligrams per vehicle kilometer) [8]. This clearly defines that it is the EF of an entire vehicle, whereas the unit $\mathrm{mg/km}$ is sometimes used in the literature to refer to the EF of a single tire. Naturally, such a value is subject to large fluctuations, as it is significantly influenced by the factors described above, especially driving style, vehicle, road surface, and last but not least, the measurement method. Accordingly, a wide range of EFs can be found. Table 1.1 provides an overview of the range of commonly quoted emission factors for passenger car vehicles.

Table 1.1: Compilation of emission factors from the literature.

Measurement Method	EF in $\mathrm{mg/vkm}$	Reference
Indoor laboratory	2.0–5.0	Williams & Cadle (1978) [146]
Outdoor sampling	5.0–7.2	Rauterberg-Wulff (1998) [105]
Indoor laboratory	9.0–11.0	Kupiainen et al. (2005) [73]
Outdoor sampling	2.2	Sjödin et al. (2010) [116]
Outdoor sampling	2.4–7.0	Panko et al. (2013) [96]

Regardless of the measurement method, all reference values shown were obtained over an extended period of time. As there is no information on the exact load conditions, the differences cannot be attributed to specific factors. Overall, however, no trends depending on the measurement method or the year of investigation can be observed. It is therefore assumed that the values given for passenger cars are still valid.

1.3 Objective and Structure of this Work

This overview underlines the variety of influencing parameters on the emission of tire–road PM. However, only for few parameters under certain conditions is the relationship to the emission, i.e., the mathematical correlation between the influencing parameter and the emission known. This quantification is to be investigated in the context of this work for the parameters of the vehicle or the driving style. These include tire forces parallel to the road surface caused by acceleration, deceleration, up-hill driving, and cornering, as well as wheel load, tire inflation pressure and driving speed. In addition, different tire and road types, as well as the influence of ambient temperature have been investigated to provide a comprehensive picture of PM emissions in a wide range of driving situations.
The existing tire internal drum test bench at the Institute of Vehicle System Technology (FAST) at the Karlsruhe Institute of Technology (KIT) was used for the experiments. For this purpose, it had to be extended with PM measurement technology. In addition, precautions had to be taken to enable reproducible and unambiguous measurement of tire–road PM on the test bench. The knowledge required for this, the exact procedure for setting up the test bench and performing the tests, as well as the results obtained are elucidated in seven chapters.
The first chapter deals with the general background of particulate matter and places tire–road PM in this context. An overview is given of the sources, implications, and legal regulations. This is followed by a presentation of measurement methods for tire–road PM and finally a compilation of previous results on relevant parameters from literature.
The second chapter provides the technical knowledge to understand the test setup and results. The basics of tires and road surfaces are discussed, as well as the friction mechanisms occurring between the two partners. The correlations and formulas needed to understand the forces involved are presented, followed by a discussion of the wear mechanisms. Finally, the resulting particulate matter and the methods available to measure it are discussed.
The third chapter presents the tire internal drum test bench and the modifications and extensions made to it as part of this work. The modifications required for PM

measurements are discussed, as well as the dimensioning of the measurement and ancillary components. All extensions can be assigned to either the extraction, the measurement, or the sampling system.
The fourth chapter deals with the entire experimental investigation of the work. Both the performance of the test series to investigate the relationships between influencing parameters and PM emissions and the subsequent particle analyses are discussed. In addition, the data analysis procedure and the assumptions and simplifications necessary to derive the subsequent results are presented. Finally, the results are comprehensively discussed and reviewed.
The results on the influence on PM emissions can be found in the fifth chapter. Where a sufficient number of support points were available, the mathematical relationships between the influencing parameter and the emission factor were approximated using regression functions. If the number of support points was not sufficient to create qualified regression functions, the influences were compared using exemplary results. Regardless of the number of support or measurement points, the identified phenomena were then examined and discussed. Based on the results, hypotheses were formulated, some of which could still be confirmed within this work. These results include both the influences on the emission level and the associated particle size distributions.
The sixth chapter describes the development of a prediction model for PM emissions during real-world driving based on the results obtained at the test bench. For this purpose, real driving data on longitudinal and lateral acceleration has been recorded by the Mercedes-Benz AG in infinitesimal time steps. Then, an emission factor derived from the previously obtained results was assigned to each of these time steps, which ultimately led to the total emission for the distance traveled. The resulting emission factors are compared with reference values from literature.
The seventh chapter summarizes the whole work and reviews the most important findings. Finally, possible optimizations are discussed and the subsequent need for new research is outlined.
The appendix contains formulas and further diagrams that are not included in the main text for reasons of clarity and readability. However, reference is made to these diagrams and formulas where it is helpful for understanding.

2 Theory

2.1 Tires

The tire is the single most important component in terms of its influence on a vehicle's performance. It transmits all the forces between the vehicle and the road, while other components such as the wheel suspension only support it. In addition to this main task, the tire also fulfills comfort (mechanical and acoustic) and driving safety requirements [127]. In recent years, these classic requirements have been increasingly extended to include those of economy (mileage, fuel consumption) and environmental protection (wear behavior) [89].
In order to meet all the requirements, modern (radial) passenger car tires consist of a variety of different components and materials. The most important components are the steel tire beads, which ensure a firm fit on the rim; the textile substructure, or carcass as reinforcement structure, which is made of materials such as rayon, nylon, or polyester; the rubberized steel cord belt inserts, which improve driving stability, rolling resistance, and mileage; the nylon bandage, which improves high-speed suitability; and the tread, which transmits forces to or from the road surface. In addition to rubber as the main ingredient the tread also contains various fillers, such as carbon black, silica, and chalk to achieve the essential tire properties. Besides that, there are plasticizers, vulcanising agents, antioxidants, and numerous other additives that are individual to each tire manufacturer and model [89]. However, since it is impossible to develop a tire that meets all requirements simultaneously as well as completely, tires have been divided according to their intended use and optimized specifically for the respective application.
The requirements for each type of tire differ accordingly. While summer tires focus on high-speed performance, all-season tires focus on comfort, and winter tires

focus on traction in winter conditions [89]. To achieve the different characteristics, different tread compounds are used for the three types of tires. In this context, the most important parameter on which the tire types differ is the glass transition temperature T_g. It describes the temperature range in which the rubber properties change from hard and brittle ($T < T_g$) to soft and flexible ($T > T_g$) [41]. The glass transition temperature of winter tires is significantly lower than that of summer tires. This means that the viscoelastic properties and associated grip with the road surface are maintained even at temperatures below freezing. Special tread patterns can further improve traction on icy or snow-covered roads [89]. However, the lower glass transition temperature of winter tires also means that the tread is significantly softer than that of summer tires at higher temperatures [76]. Therefore, if winter tires are driven in high ambient temperatures, wear increases significantly [89]. In addition to the tread compound, numerous factors influence a tire's abrasion behavior, the most important of which are listed below. On the tire side, the factors are the tire construction, size, inflation pressure, and tread pattern, as well as the resulting ground pressure distribution. The influence of the road is essentially determined by its material and surface texture. The vehicle and, therefore, the driver and their driving style also play a key role. In this context, the most important parameters are vehicle mass, axle suspension, driving speed, and acceleration, braking, and cornering behavior. The main environmental influences are temperature, humidity, and the degree of soiling [97].
The mechanisms between the tire and road surface that lead to tire abrasion are explained in detail in section 2.5.

2.2 Road Surfaces and their Characterization

In the context of this work, mainly vehicle-related influences on the emission of tire–road PM are investigated. However, it is crucial to keep in mind that in addition to the tire, the road surface as a friction partner, characterized by the material used and its surface texture, is directly involved in the particle formation process. For this reason, the fundamental differences between diverse types of

road surfaces are presented below, along with the terms used to characterize them. First, the materials used to construct the pavement are described. Since the tire solely comes into contact with the road surface, only surface layers are described. These can vary greatly in terms of the material used and its composition.

Asphalt pavements consist of a mix, which can have different grain sizes, and bitumen as a binder. The most common types are asphalt concrete (AC), stone mastic asphalt (SMA), mastic asphalt (MA), and porous asphalt (PA) [9]. Contrary to its name, asphalt concrete does not contain a hydraulic binder. Rather, the name is derived from the fact that asphalt concrete has a screening line similar to concrete, resulting in a low void content. Stone mastic asphalt is a type of asphalt mix with a disproportionate amount of coarse mineral aggregate and a lot of filler, which creates a self-supporting aggregate structure with high load-bearing capacity [84]. Unlike the previous two, mastic asphalt is not compacted by rolling, but can be poured and then smoothed using viscosity-modifying additives (for temperature-reduced paving) [9, 59]. Porous asphalt has a much higher void content and is used mainly for absorbing tire noise and draining surface water [9].

In contrast to asphalt pavements, hydraulic binders are used for concrete pavements [84]. They consist of rigid binding elements, show little plastic deformation and have a negligible relaxation capacity. Therefore, concrete surfaces are usually divided into plates separated by joints made of filler [9]. Due to their higher load-bearing capacity and high durability compared to asphalt pavements, concrete pavements are mainly used on busy and heavily-used traffic sections [106].

In addition to the material used, road surfaces also differ in their surface texture. The texture is divided into four size ranges according to their wavelength λ [109], which are shown in Figure 2.1. Unevenness with wavelengths above the range shown ($\lambda > 50\,\mathrm{m}$) is referred to as the longitudinal profile of the road [84].

The texture intensity in the two largest wavelength ranges should be as low as possible for high driving safety and comfort [27]. The macrotexture, on the other hand, is desirable for high drainage capacity and is achieved by a suitable mix and binder ratio or surface finishing techniques [109]. In addition to the drainage capacity, the macrotexture also influences the tire–road noise and is largely responsible for the appearance of the surface [27, 53].

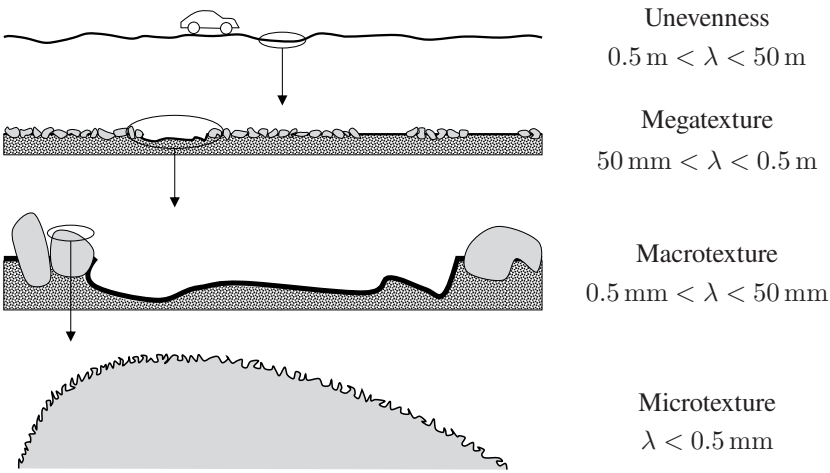

Figure 2.1: Wavelength spectra of road surface textures [Adapted from 109].

However, the most important texture wavelength range for tire abrasion [109] and thus for the investigations carried out in this work is the microtexture [27]. The individual peaks cannot be seen with the naked eye, but their shape and number determine whether a surface feels rough or smooth [27]. The microtexture is largely responsible for the frictional properties of the surface [84] and thus, together with the macrotexture, defines the skid resistance of the road surface [53]. There are two methods to determine the skid resistance. In the SCRIM method (Sideway Force Coefficient Routine Investigation Machine), a defined tire loaded with a specific wheel load is rolling on a wet road surface at a slip angle of $20°$ to the direction of travel. The lateral force generated is used to determine the grip of the road surface [33]. The SKM (Seitenkraftmessverfahren) method used in Germany corresponds to the SCRIM method described with only minor deviations. Since driving with a slip angle of $20°$ is an extremely high load, it is associated with wear (tire and road surface). Due to the repeated rolling-over of the same road sections on the test bench and the resulting changes in the road surface, this method is not suitable for determining skid resistance in this work.

The second method combines the outflow meter with the SRT (Skid Resistance Tester) pendulum. The macrotexture is characterized by means of the outflow meter. It allows to measure the outflow time of water from a stationary cylinder through the openings remaining between the cylinder and the road surface [33]. Accordingly, a short outflow time means a high macrotexture, while a long outflow time means a low one [26]. The SRT pendulum is used to determine the microtexture [33]. Since the microtexture is mainly responsible for the abrasiveness of the road surface and thus for the tire wear, only the SRT pendulum is used in this work. The equipment and the procedure for such a measurement is described thoroughly in section 3.2.2.2.

2.3 Friction Mechanisms

The following five laws apply to the classical friction theory. The coefficient of friction is [69]

- dependent on the material.
- independent of the contact surface.
- independent of the vertical load.
- independent of the sliding speed.
- higher in the adhesive state than in the sliding state.

For elastomeric friction, these laws only apply to a limited extent or not at all [85]. The relationships that apply here are more complex, which means that only the first law retains its full validity [69]. Of the four possible mechanisms for force transmission, adhesion, hysteresis, cohesion and viscous friction, the last two mentioned play a proportionately subordinate role for elastomeric materials under normal driving conditions [69, 89, 127]. The greatest contribution to rubber friction is made by adhesion and hysteresis friction [85, 89].

Molecular forces of attraction, known as van der Waals bonds, occur in the contact area between the tire and the road surface. Breaking these bonds causes the molecular chains to vibrate. The energy dissipation during the damping of these vibrations ultimately results in the adhesive contribution to rubber friction through adhesion. This can be seen in the form of shear stresses on the rubber surface (see Figure 2.2) [69]. The adhesion component is particularly pronounced when a large contact area is created, i.e., on perfectly smooth and dry surfaces [85]. For an undulating (regarding the macrotexture), well-lubricated surface, however, it is negligible [70, 85].

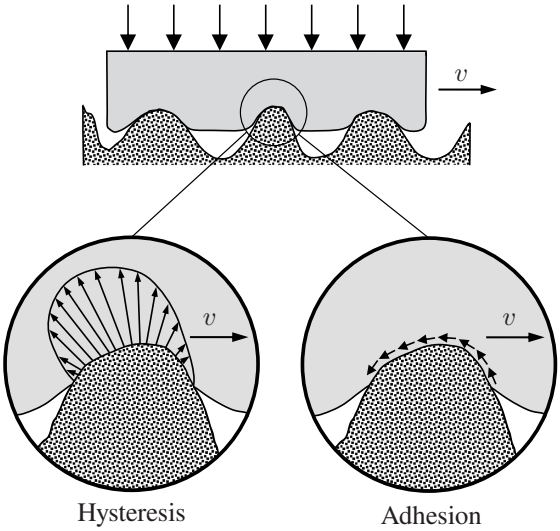

Figure 2.2: Elastomeric friction components [Adapted from 69].

When sliding over a rough surface, the tire rubber is periodically deformed [69]. Both the amplitude and the frequency of the deformation depend on the texture of the road surface [85]. As the unevenness penetrates the elastic rubber material during the sliding process, the rubber is compressed when running onto the unevenness and relaxed with hysteresis losses when running off. The asymmetrical

pressure distribution means a pressure difference, which ultimately manifests itself as a force against the direction of travel [127]. The effects on the tire tread material in the form of compressive stresses are shown in Figure 2.2. The deformation of tire rubber results in damping losses due to the viscoelastic properties of the material. This in turn creates a force against the direction of motion. Since deformation can only occur on uneven surfaces, hysteresis friction is negligible on a clean, dry glass surface. On a wavy or otherwise irregular, well-lubricated surface, friction is caused almost entirely by hysteresis [85].
Although the influence of cohesive friction on the total frictional force is proportionately small it is briefly explained at this point, as it is directly linked to tire abrasion, which is essential to this work: Cohesive forces arise during rubber wear when molecular bonds within the material are broken and particles are torn out [62, 69]. A frequently used description is the surface energy required to create a new surface. Its share of the total frictional force varies depending on the road surface roughness but remains below $2\,\%$, even on rough surfaces [69].

2.4 Tire–Road Contact Forces

Unlike in the case of a rigid cylinder, the contact between a tire and the road is not a line. Due to the elasticity of the tire, there is a flat contact area called the tire contact patch [15]. The majority of forces acting on the vehicle are transmitted to the road surface via this area [15]. The size of the footprint A_{tr} can be roughly calculated according to Equation 2.1, where F_z is the wheel load, p_i the tire inflation pressure, and k a correction factor for tire stiffness [127].

$$A_{tr} = \frac{k \cdot F_z}{p_i} \quad with \quad k \approx 0.85 \; to \; 0.9 \tag{2.1}$$

This results in the contact pressure p_z between the tire and the road surface shown in Equation 2.2, which is a major parameter for the transmittable tire force. The lower the contact pressure, the higher the achievable adhesion coefficient [89].

$$p_z = \frac{F_z}{A_{tr}} \tag{2.2}$$

In this simplicity, Equation 2.2 only applies to tires without any tread pattern (slick tires) on an ideally flat surface. Due to the tread pattern on the one hand and the roughness of the road surface on the other, the actual contact area is much smaller. Depending on the share of grooves in the tire tread and the road surface roughness, the actual contact pressure is several orders of magnitude higher [86]. As soon as the tire starts to rotate, slip occurs in the contact area. The processes involved are best explained using Willumeit's brush model [147]. In this model, the tire belt is considered as a circumferentially rigid and closed belt. The tire tread is attached to the belt and is modeled by elastic bending elements (tread bar elements, see bottom half of Figure 2.3). As long as no longitudinal force is applied, the belt rotates at the same speed as the center point of the wheel moves translationally (in a straight line). In the theoretical case of a circumferentially absolutely inelastic tire (including belt as well as tread bar elements), this would result in a slip-free driving condition, as the wheel would move in a purely rolling motion. In reality, however, local slip occurs even in the free-rolling condition (without the presence of driving or braking forces). Due to the flattening of the tire, the rubber material in the tread undergoes a continuously changing deformation between leading and trailing edge.

Immediately when entering the contact patch (leading edge), the tips of the tread bar elements adhere to the road surface. Meanwhile, their upper part continues to move with the belt, resulting in deformation in the opposite direction of travel and thus in positive shear stress in the front area of the contact patch. In order to be able to follow the belt, the tread bar elements straighten up in the further course of the contact patch [87, 89]. Around the longitudinal center of the contact patch, the direction of deformation reverses, resulting in negative shear stress in the rear area (towards the trailing edge, see Figure A.1). The areas enclosed by the curve of shear stress for the free-rolling condition are the same size (integral over the entire contact length equals zero). This condition is given by the free-rolling wheel (no longitudinal force). The adhesion limit is not reached by the so-called basic shear stress distribution. The slip occurring in the free-rolling condition

therefore basically consists of deformation slip, i.e., an interlocking of the tire tread with the road surface [89].

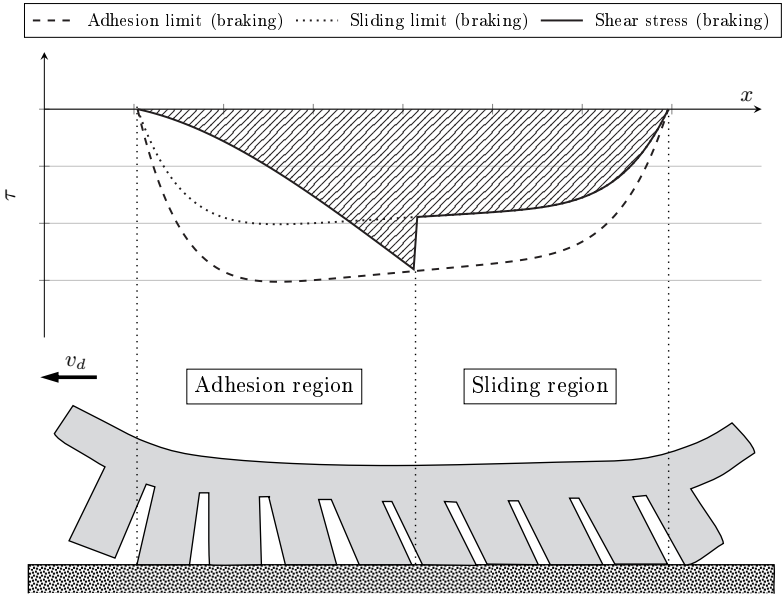

Figure 2.3: Relationship between the deformation of tread bar elements and the shear stress in the tire–road contact for a braking condition. The tire tread begins where the tread bar elements make contact with the road surface and ends where the contact ends. The area under the curve (hatching) is a measure of the force transmitted [Adapted from 86, 90]. The adhesion limit as well as the sliding limit have been plotted according to [120]. For more information on how the shear stress curve is generated, see Figure A.1.

If the rolling wheel is subjected to longitudinal force (driving or braking) in addition to the wheel load, the slip ratio increases further. In this case, the circumferential speed of the belt differs from the translational speed at the center of gravity of the wheel. The tread bar elements link the belt and the road surface. They are rigidly attached to the belt and adhere to the road surface. Due to the speed difference between belt and road, they eventually undergo a deformation that increases with the distance traveled in the contact patch. The deflection of

tread bar elements creates shear stress at their tips [15]. The curve progression of this shear stress is shown in Figure 2.3 for a tire under braking force. If the shear stress reaches the adhesion limit (maximum shear stress to be transmitted by adhesion), which is determined by the static friction coefficient μ_{ad} and the local contact pressure p_z, the tread bar elements cannot deform any further and start sliding [89]. In this state, the tread bar elements can only transmit sliding friction forces [15]. Accordingly, the local shear stress corresponds to the sliding limit (maximum shear stress to be transmitted by sliding), which is determined by the sliding coefficient μ_{sl} and the local contact pressure. This state is maintained until the tread bar elements reach the end of the contact patch [15].
The behavior of tread bar elements when transmitting lateral forces can be described in a similar way. In this case, the slip angle α is used as the reference value, i.e., the angle between the main tire plane and the velocity of the center of gravity of the tire during cornering [15]. The slip angle is always associated with lateral slip s_α, where the relationship between slip angle and lateral slip is given by Equation 2.3 [89].

$$s_\alpha = \tan(\alpha) \tag{2.3}$$

The brush model can also be used to explain the processes occurring with lateral slip. The deformation slip occurring in the longitudinal direction as the tire flattens does not occur in the lateral direction. However, as in the case of longitudinal force, tread bar elements entering the tire–road contact initially adhere. Due to the slip angle, they are increasingly deflected in a lateral direction as they pass through the tire contact patch. The elastic deflection causes shear stress in the tire material. The shear stress results in deformation slip, which ultimately generates the lateral force. If the shear stress reaches the adhesion limit prior to the end of the contact patch, the tread bar elements start sliding. Thus, only sliding friction forces are transmitted in this area of the contact patch (sliding slip). The relationship between the sliding velocity of tread bar elements in the lateral direction $v_{sl,y}$ and driving speed v_d is given by Equation 2.4 [89].

$$v_{sl,y} = s_\alpha \cdot v_d \tag{2.4}$$

This speed can be described as the average slip speed with proportions of deformation (adhesion region) and sliding slip (sliding region). The mechanisms of force transmission described above and the associated relative speed between tire and road surface inevitably lead to wear in both the longitudinal and lateral direction. The mechanisms involved are explained in detail in the following section.

2.5 Mechanisms of Tire Wear

Tire wear is caused by both physical and chemical processes. Since chemical wear is not considered in this work, only physical wear will be discussed. This is usually the result of high shear stress in combination with (sliding) slip in the tire–road contact and is thus referred to as abrasive wear. The shear stress causes cracks to form and propagate, which ultimately results in the release of particles [90]. The following is an overview of the basics of crack formation and propagation. More detailed information on both processes can be found in [99, 101, 108].
When a tire or portions of the tire tread slip on a rough and hard surface such as an asphalt or concrete road, the actual contact is made up of many small and uneven contact areas [108]. The nominal contact area, which is about the size of a postcard per tire [76], is thus reduced to about one square centimeter [108]. As a result, the tire undergoes high-frequency deformations associated with extremely high local loads (see Figure 2.2), leading to hysteresis friction. The associated damping losses in the rubber material increase the tire temperature and lead to a long-term deterioration of the rubber properties. Supported by stress and high temperature, cracks eventually form (see Figure 2.4a). Cracking is facilitated by material defects such as pores, particle inclusions, impurities, and surface defects. When a rubber surface with existing cracks slides over a rough substrate, tensile stresses are generated on the exit side of the rubber–substrate contact (see Figure 2.4b). This can cause new cracks to form and existing cracks to propagate within a thin layer of rubber. A complete crack will eventually lead to delamination of rubber material. The size of the particles depends on the roughness of the surface and is usually in the range of a few microns [100].

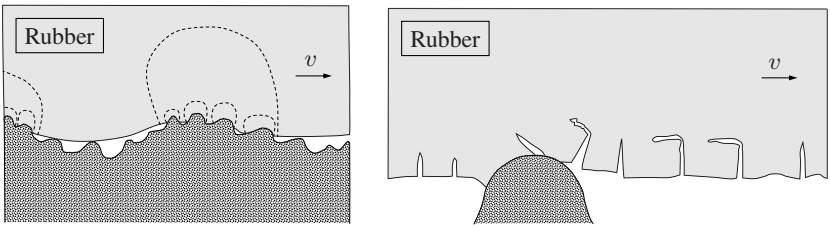

(a) Crack formation

(b) Crack propagation

Figure 2.4: Mechanisms of tire wear in contact with the road surface [Adapted from 100].

To calculate tire wear, a direct dependence on the frictional energy is assumed in common literature. The frictional energy per unit area $\bar{E}_f$ is calculated assuming an average slip distance $\vec{S}$ in tire–road contact, with a given contact length l, shear stress $\vec{\tau}$ or its components in the longitudinal direction τ_x and in the lateral direction τ_y, and slip distances S_x and S_y according to Equation 2.5 [90].

$$\bar{E}_f = \int_0^l \vec{\tau} \cdot d\vec{S} = \int_0^l (\tau_x dS_x + \tau_y dS_y). \tag{2.5}$$

A transformation of the integration variable $d\vec{S}$ in the first term, as shown in Equation 2.6, eventually leads to a clearer representation.

$$\begin{aligned} \bar{E}_f &= \int_0^l \vec{\tau} \cdot d\vec{S} = \int_0^l \vec{\tau} \cdot d(\vec{v}_{sl} \cdot t) = \int_0^l \vec{\tau} \cdot \vec{v}_{sl}\, dt = \int_0^l \vec{\tau} \cdot \vec{v}_{sl}\, dx \frac{dt}{dx} \\ &= \int_0^l \vec{\tau} \cdot \vec{v}_{sl}\, dx \cdot \frac{1}{v_d} = \int_0^l \vec{\tau} \cdot \frac{\vec{v}_{sl}}{v_d}\, dx = \int_0^l \vec{\tau} \cdot \vec{s}\, dx\ , \end{aligned} \tag{2.6}$$

where $\vec{s}$ is the slip ratio. This shows that, according to this theory, even with high shear stress, wear only occurs when slip is present. Solving the integral and

multiplying by the total contact area gives the absolute frictional energy E_f in Equation 2.7a. Alternatively, if the absolute force is directly considered instead of the shear stress, the integration also leads to Equation 2.7a. From this, the absolute frictional power P_f in Equation 2.7b with the sliding velocities in the longitudinal direction $v_{sl,x}$ and in the lateral direction $v_{sl,y}$ can be derived.

$$E_f = F_x \cdot S_x + F_y \cdot S_y \tag{2.7a}$$

$$P_f = F_x \cdot v_{sl,x} + F_y \cdot v_{sl,y} \tag{2.7b}$$

Further transformation of Equation 2.6 leads to an alternative representation of the frictional energy per unit area $\bar{E}_f$ that depends only on the applied forces, the longitudinal slip stiffness $\tilde{c}_x$, the lateral slip stiffness $\tilde{c}_y$, and the contact width b of the tire [90]. The so-called Schallamach wear formula is shown in Equation 2.8.

$$\bar{E}_f = \frac{1}{b}\left(\frac{{F_x}^2}{\tilde{c}_x} + \frac{{F_y}^2}{\tilde{c}_y}\right) \tag{2.8}$$

The two slip stiffnesses contained therein are explicitly not the longitudinal stiffness c_x and lateral stiffness c_y of the tire. Instead, they are calculated using the slip ratio in the respective load direction according to Equations 2.9 and 2.10.

$$\tilde{c}_x = \frac{F_x}{s_x} \tag{2.9}$$

$$\tilde{c}_y = \frac{F_y}{s_\alpha} \tag{2.10}$$

From Equation 2.8, the tire wear characterized by the wear volume V_t can finally be calculated according to Equation 2.11.

$$V_t = \bar{k}^{\beta_1} \bar{E}_f^{\beta_2}, \tag{2.11}$$

where $\bar{k}$ is the wear volume per unit of frictional energy, i.e., a wearability parameter, and a function of several environmental conditions such as road surface roughness, temperature, and humidity. β_1 and β_2 are material parameters, but do

not only depend on the material, but also on the road surface roughness and the temperature. They are determined experimentally and are in the range of 1.
Tire abrasion produces both coarse tire wear particles, which sometimes accumulate on the roadside, as well as fine particles, which are emitted in large numbers. Because they are formed in the contact area between the tire and the road surface, they are usually composed of fragments of tire and road material. The fine particles, known as tire–road PM, can travel long distances before settling due to air movement [8]. The technical basics of particulate matter and its measurement are explained in the following two sections.

2.6 Particulate Matter / Fine Dust

Particulate matter (PM) is usually defined as all particles in ambient air that are less than $10\,\mu m$ in diameter [18]. Thus, PM forms a sub-fraction of total suspended particulate matter (TSP) [129] and is also referred to as PM_{10} due to its upper diameter limit [18]. However, this definition is a simplification of the original published by the U.S. Environmental Protection Agency (EPA) in 1987 [30]. Therein, a weighting function was defined to include particles between $1\,\mu m$ and $20\,\mu m$ only to a certain extent. Particles with a diameter below $1\,\mu m$ are fully taken into account, those larger than $20\,\mu m$ are not. Between these two values, the fraction to be taken into account increases continuously, so that particles with a diameter of exactly $10\,\mu m$ are taken into account with a weighting factor of $50\,\%$ [32]. The weighting function should be used in an attempt to represent the sedimentation behavior in the human respiratory system as accurately as possible. However, since this is a complex definition which is difficult to apply in practice, the simplified definition is usually applied to determine PM_{10} values. This does not show significant differences in results compared to the complex definition and is therefore also specified in standards such as DIN EN ISO 16890-1 [30].
Because particles are microscopic structures, often non-spherical in shape, it is impossible to determine an unambiguous diameter. Therefore, different equivalent diameters exist for different applications and specific methods are used for

their determination. The most common equivalent diameter is the aerodynamic diameter. It is defined as the geometric diameter of a spherical reference particle with a density of $1\,\mathrm{g/cm^3}$ that has the same settling velocity in still air as the particle under consideration [139]. It is used in particular for conventions relating to the respirable, thoracic and alveolar fractions [25]. The measurement can be performed with low-pressure impactors [141] or time-of-flight spectrometers [142]. If measurements require high temporal resolution, both measurement methods are associated with high costs.

An equivalent diameter particularly suited to real-time applications is the scattered light equivalent diameter. It describes the geometric diameter of a homogeneous, spherical reference particle made of a reference substance that produces the same scattered light intensity as the observed particle under a given illumination. It is measured with optical aerosol spectrometers (see section 2.7.2) [139]. Since the amount of scattered light intensity depends not only on the particle size, but also on the refractive index of the material and the particle shape, both variables should be known to ensure high measurement accuracy. The orientation of the particle in the measurement volume also affects the level of scattered light intensity [140]. Since this cannot be controlled, the resulting uncertainty must be minimized by illuminating the measurement volume as skillfully as possible.

In addition to the equivalent diameter, particles are often described by an aspect ratio. However, since aspect ratio is not a definite term, there are many definitions for different fields [118]. In particle technology, the aspect ratio is usually defined as the ratio between the longest edge of a particle and its diameter or its shortest edge [150]. This definition is also used in the context of this work.

2.7 Measuring Particulate Matter

2.7.1 Isokinetics

When determining particle concentrations from flowing aerosols, it is essential that the sample is representative. The sample must accurately reflect both the particle concentration and the particle size distribution of the aerosol to be analyzed. To ensure this condition, the sample must be taken isokinetically from the flowing aerosol. For that, it is irrelevant whether the aerosol to be analyzed is flowing in an extraction line or in a free environment in the form of wind.
Sampling is isokinetic if the inlet axis of the sampling probe is parallel to the streamlines of the surrounding aerosol. Second, the flow velocity at the inlet of the sampling probe must be identical to that of the flowing aerosol at the level of the probe inlet. Compliance with both conditions is synonymous with the avoidance of bends or distortions in the streamlines prior to sampling [51]. Correspondingly, the sampling probe itself should be thin-walled and have the smallest possible opening angle [55] so that the streamlines remain unaffected.
If at least one of these conditions is not met, the sampling is anisokinetic, which inevitably leads to a distortion of the size distribution or a falsification of the particle concentration. The deviation between the measured and the actual aerosol properties is caused by the inertia of the moving particles. Therefore, depending on the orientation or velocity deviation from the isokinetic specification, the number of particles in a given size range will be over- or underestimated [51]. The correct setting for isokinetic sampling and several incorrect settings that lead to anisokinetic sampling are shown in Figure 2.5.
Figure 2.5a shows isokinetic sampling. The streamlines lead straight into the sampling probe. The velocities of the ambient and the sampled aerosol at the sampling plane are identical. Both the particle concentration and the size distribution of the sampled aerosol match those of the aerosol to be characterized [143].
Figure 2.5b shows anisokinetic sampling, where the sampling probe shows a misalignment angle Θ in the flow and therefore the parallelism condition is not met. This results in a deflection of the streamlines which not all particles can follow.

Large particles, which cannot follow the streamlines due to their high inertia, will deviate from the streamlines and will not be detected. This results in an underestimation of the particle concentration and a shift in size distribution towards smaller particles [51].

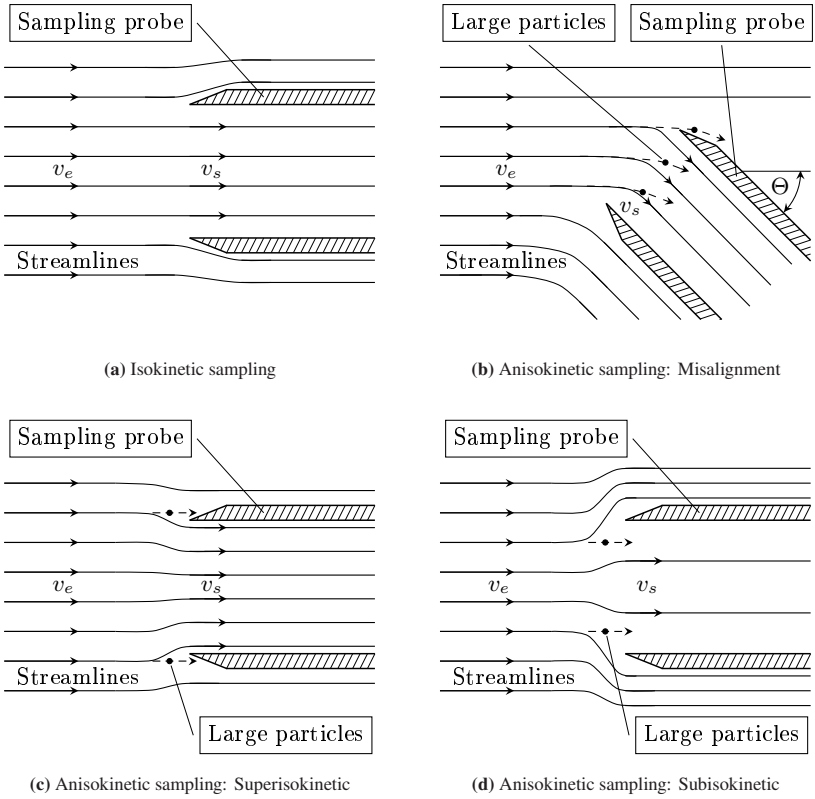

(a) Isokinetic sampling

(b) Anisokinetic sampling: Misalignment

(c) Anisokinetic sampling: Superisokinetic

(d) Anisokinetic sampling: Subisokinetic

Figure 2.5: Isokinetic sampling and anisokinetic sampling due to different incorrect settings [Adapted from 51].

Figure 2.5c shows the case of anisokinetic sampling, in which the condition of parallelism is fulfilled, but the velocity in the sampling probe is higher than that of the surrounding aerosol. Therefore, it is called superisokinetic sampling. The

streamlines run into the sampling probe in a funnel shape. Here too, large particles cannot follow the streamlines due to their inertia and are therefore not taken into account in the subsequent measurement. The particle concentration is again underestimated and the size distribution is distorted towards small particles [143]. Figure 2.5d shows the opposite case, where the flow velocity within the sampling probe is lower than that of the surrounding aerosol. The streamlines avoid the sampling probe, whereby the small particles, which are very mobile due to their low inertia, follow the streamlines. The large particles, on the other hand, flow into the sampling probe, resulting in a distortion of size distribution towards large particles and an overestimation of the particle concentration [143].
If sampling is not isokinetic, the actual particle concentration cannot be determined. If the degree of misalignment as well as the deviation of the sampling rate are known, the measurement error can be calculated for individual particle sizes. However, since the particle size distribution is distorted, it is not possible to reconstruct the actual concentration [51].

2.7.2 Optical Measurement Technology

Optical aerosol spectrometers use the intensity of scattered light to count and classify particles [140]. The aerosol flow to be characterized, in which the particles are located, is passed through a measurement volume illuminated by a light source [7]. Each particle passing through the measuring volume generates a scattered light pulse which is registered photoelectrically. The number of scattered light pulses is used to determine the number of particles and the height of the scattered light pulses is used to determine the particle size. However, the height of the scattered light pulse is not exclusively dependent on the particle size (see section 2.6), so knowledge of the particles to be measured is required to achieve a high correlation between the scattered light equivalent diameter and the actual geometric diameter of the particles. Since the relationship between scattered light intensity and scattered light equivalent diameter is complex, an experimental calibration curve with a suitable aerosol standard must be recorded for each instrument [140].

To obtain information on the particle number concentration in addition to the pure particle number and size, the volume flow through the measurement volume must be known precisely [140]. Information on particle mass concentration requires knowledge of the density of the particle material. If two or more particles are present in the measurement volume at the same time, the scattered light pulses cannot be distinguished, resulting in a so-called coincidence error. The particles are then evaluated as a single large particle. To minimize the coincidence error, the smallest possible measuring volume is recommended [7]. Therefore, the size of the measurement volume determines the particle concentration range to be measured. However, if the measurement volume is small, low particle concentrations cannot be measured accurately.
The lower limit of the detected particle size is determined by the scattered light background in the measuring chamber and is typically between $0.07\,\mu\mathrm{m}$ and $0.5\,\mu\mathrm{m}$. The upper limit which is typically in the range of $25\,\mu\mathrm{m}$ is not determined by the measuring principle itself, but by losses during particle sampling and transport due to sedimentation in the sampling probe [140].
In addition to optical instruments, there are other methods for PM measurement based on either gravimetric (cascade impactor) or aerodynamic (aerodynamic particle sizer) measurements. However, since these could not be considered due to the requirements of the measurement task, the limitations of the respective method, or the available budget, they are not described in detail here. The reasons that led to the selection of the optical measurement method are elucidated in section 3.2.2.1.

3 Test Facility

All tests described in this work were carried out at the tire internal drum test bench at the Institute of Vehicle System Technology (FAST) of the Karlsruhe Institute of Technology (KIT). The test bench as well as all extensions and conversions required for particle measurement are elucidated in the following sections.

3.1 Internal Drum Test Bench

The tire internal drum test bench at FAST/KIT (see Figure 3.1) consists of two subsystems: the drum with an inner diameter of $3.8\,\mathrm{m}$ and the sled, on which the tire as well as all systems to measure forces and torques in the tire–road contact are mounted. The tire runs at the lowest point of the vertically arranged drum. The two subsystems are driven separately using a 310-kW-engine each; the drum is driven electrically while all movements as well as the propulsion of the wheel work hydraulically. The separate drive allows for the investigation of realistic as well as stationary operation modes. If no other force but the wheel load is applied, tire and drum roll at the same speed. As they are driven separately, slip conditions in the longitudinal direction, i.e., drive and brake slip causing longitudinal forces can be set stationarily and reproducibly. In addition to driving and braking forces, the hydraulics can also be used to perform rotations around the wheel‘s vertical and longitudinal axis. Rotation around the vertical axis causes a slip angle and thus lateral forces representing cornering. Rotation around the longitudinal axis leads to camber. The test bench can be equipped with several surfaces, including sandpaper as well as realistic road surfaces such as asphalt and concrete, allowing for an accurate replication of the tire–road contact on public roads. During the

tests for this study a widespread asphalt mixture AC 11 D S has been used. This is asphalt concrete in which the maximum grain size is $11\,\mathrm{mm}$ and the aggregate and bitumen are mixed in a mass ratio of $95\,\%$ to $5\,\%$.

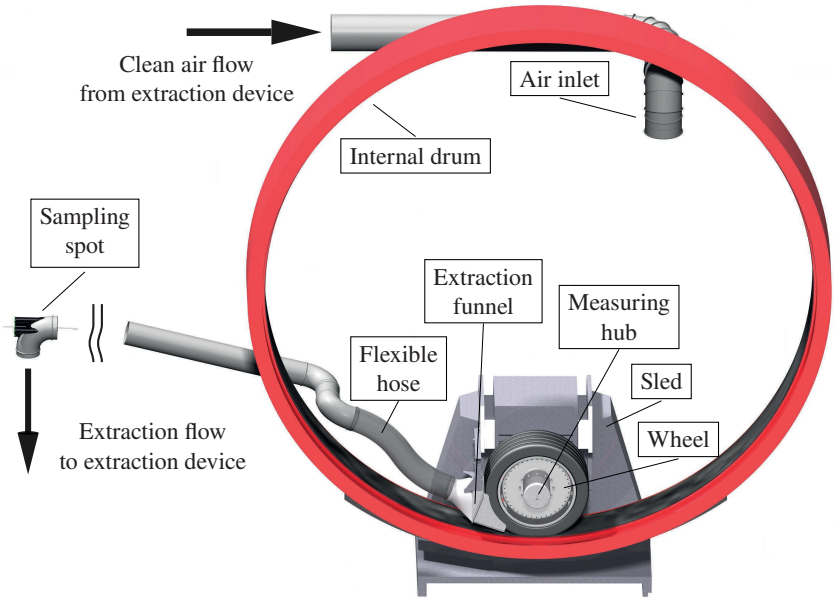

Figure 3.1: Tire internal drum test bench at FAST/KIT [112]. The rear wall of the drum is hidden in order to show all test bench components in one view. The surrounding walls and support structures of the test bench are also not shown.

The entire test bench is surrounded by an enclosed chamber, which allows the minimization of fluctuations of background concentration. Due to the hydraulic and electric drive of the two subsystems, there are no other PM sources apart from the tire–road contact within the test bench. Furthermore, different ambient conditions can be set inside the enclosed chamber: certain water film heights can be applied on the road surface as well as snow and ice. The temperature can be adjusted in a large range below and above freezing level. An overview of the parameters and the respective size ranges is given in Table 3.1.

Table 3.1: Overview of the parameters of the internal drum test bench with associated values/ranges.

Parameter	Symbol	Value	Unit
Drum diameter	d_{Drum}	3800	mm
Roadway width	$b_{Roadway}$	290	mm
Drive power	P	$2 * 310$	kW
Max. wheel load	$F_{z,max}$	15	kN
Max. driving speed	$v_{d,max}$	Asphalt/Concrete: 150	km/h
		Sandpaper: 200	km/h
Slip angle	α	-20 to 20	°
Camber angle	γ	-10 to 20	°
Ambient temperature	T_a	-20 to 30	℃

3.2 Enabling Particulate Matter Measurements

The internal drum test bench was extended as part of this work to enable the measurement of PM from the tire–road contact in real time.
The first and most important requirement is defined by the goal of determining the particulate matter from tire–road contact in its entirety. Accordingly, all components and interfaces contained in the system must be designed to generate the lowest possible particulate losses. Furthermore, the measurement should take place in real time so that an emission can be clearly assigned to each driving condition. This requirement arises in particular from the fact that some of the driving conditions to be investigated can only be maintained for short duration. Without real-time measurements, it would therefore not be possible to mathematically correlate the load condition with the associated emission. In addition, to enable downstream gravimetric and chemical analyses, the emitted particulate matter is to be captured and collected. The resulting requirements for the individual subsystems, as well as their specifications, are described in the following sections.

3.2.1 Extraction System

3.2.1.1 Extraction Funnel

For precise measurements, the PM emitted should be measured as close to the point of its release as possible. However, since measurement directly in the tire–road contact is technically not feasible, the whole air flow around the tire is extracted directly behind the tire. The resulting extraction flow carries the particles first to the sampling spot and after to the extraction and filter device.
An extraction funnel (see Figure 3.2) has been designed to surround the rear part of the tire on an angle of approximately $70°$ leaving only a thin slot of about $10\,\mathrm{mm}$. It can be adapted to different tire dimensions, ensuring that the suction slot between the funnel and the tire is small for a wide range of tire dimensions, thus keeping particle losses low. Several adjustment mechanisms integrated into the design of the funnel serve this purpose. For tires of different widths, the sidewalls laterally enclosing the tire are displacably attached to the funnel, thus allowing for the investigation of tire widths between $185\,\mathrm{mm}$ and $285\,\mathrm{mm}$. In addition, there is the possibility of displacement in radial and tangential tire direction, whereby the height of the funnel above the road surface as well as its distance to the tire can be adjusted independent of each other. This allows the investigation of tires with diameters from $550\,\mathrm{mm}$ to $740\,\mathrm{mm}$. Common tire dimensions between 185/45 R15 and 285/40 R20 can thus be investigated.
The funnel mounting consists of a frame made of square tube, which is attached to the sidewall of the test bench sled. If slip angle is applied, this movement is achieved by rotation of the sled around the vertical axis of the wheel. Because of the way it is mounted, the funnel follows the wheel and maintains its constant relative position. Camber angles, deflection movements, and changes of the wheel load are induced by internal mechanisms of the test bench sled and thus do not affect the position of the funnel. This ensures that the distance set to the road surface remains constant during all driving maneuvers and that no collisions with aggregate protruding over the road surface can occur.

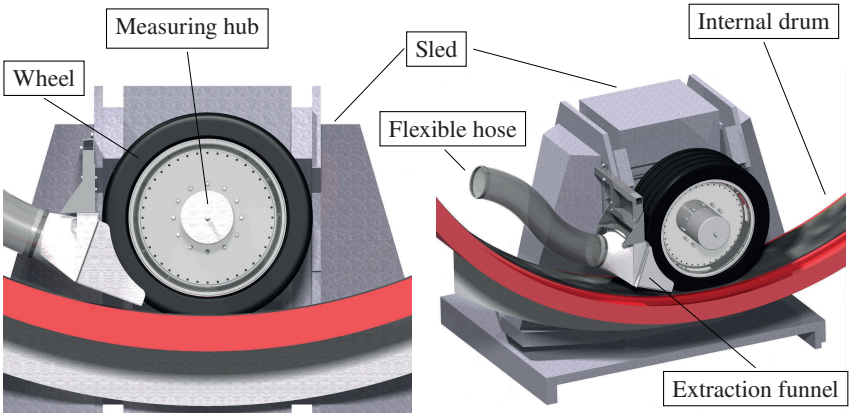

(a) Side view in mounted condition

(b) 3D view in mounted condition

Figure 3.2: Different views of the extraction funnel.

In order to minimize not only possible extraction losses but also losses due to deposition as a result of electrostatic charge, the entire funnel is made of conductive stainless steel and grounded via the test bench sled. For stability reasons, especially to counteract vibrations, the funnel mounting as well as the funnel itself are of very rigid design.

3.2.1.2 Extraction Hood

In addition to the extraction funnel, a specially designed extraction hood (see Figure 3.3) was used, which enclosed the tire and thus almost completely shielded it from the flow prevailing in the internal drum. The necessity of the extraction hood resulted from the maximum volume flow of the extraction device. In combination with the extraction funnel, a maximum flow velocity of the air of $120\,\mathrm{km/h}$ could be achieved in the slit between the tire and the funnel (see section 3.2.1.4). For reliable extraction of the particles, this extraction velocity should be significantly higher than the flow velocity in the drum. Therefore, the investigation of high driving speeds required the usage of the extraction hood.

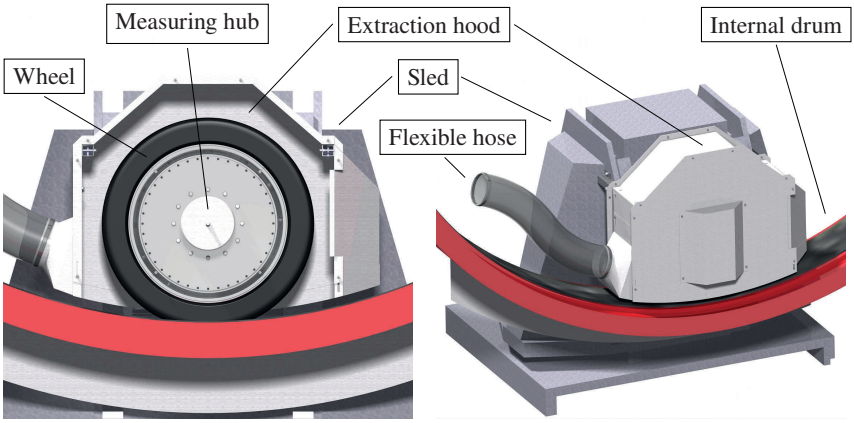

(a) Side view in mounted condition **(b)** 3D view in mounted condition

Figure 3.3: Different views of the extraction hood. For better visibility of the wheel and the slit between the hood and the road surface, the right sidewall (in driving direction) of the hood is hidden in (a). The fully-assembled hood as well as the direct connection to the extraction system is shown in (b) [114].

As the funnel, the entire hood is made of stainless steel, which serves to minimize particle losses. At the rear end, it opens into a funnel that is connected to the extraction system. At the lower edge, it has sheets that can be moved in the vertical direction, allowing the distance to the road surface to be kept small at all times when investigating tires of different sizes. Also like the funnel, the hood is mounted on the test bench sled so that it moves together with the wheel when investigating slip angles. It is decoupled from vertical movements such as deflection and rebound. The relative position of the integrated funnel to the wheel, and the flow conditions within the hood, thus remain constant.

However, shielding the wheel from the flow prevailing in the drum is accompanied by higher temperatures inside the hood, especially when the tire is heavily loaded. As higher tire temperature can lead to a change in particle formation and detachment, the hood was only used for test series in which driving speeds higher than $100\,\mathrm{km/h}$ were included. In this case, longer downtimes had to be planned for cooling the tire. In contrast, for test series with only lower driving speeds the speed of the extraction flow with the funnel was sufficient.

3.2.1.3 Flexible Tube and Spiral Ducts

There are three main requirements for the connection between the extraction funnel and the extraction device. First, it must allow all driving maneuvers, in particular slip angles. Second, both the particles contained in the volume flow and the volume flow itself should pass from the extraction funnel to the extraction device with as little loss as possible—low pressure loss as well as low particle loss. Third, the connection should allow the sampling apparatus to be accommodated at a suitable location so that a partial flow can be analyzed.

In order to be able to investigate the effect of lateral force on PM emissions, the connecting part directly behind the wheel must be designed to be flexible. Therefore, a flexible hose with a diameter of $160\,\mathrm{mm}$ was used, allowing the wheel to swivel at slip angles. To minimize particle losses due to electrostatic charge, the hose is made of permanently antistatic polyurethane. The copper spiral embedded in its wall is grounded on both ends via the test bench.

Rigid spiral ducts could be used for the rest of the connection. In order to minimize losses as well—pressure as well as particle losses—the inner diameter of the pipe was selected as large as permitted by the installation space. A large diameter is advantageous from the perspective of isokinetics, since at a given extraction volume flow, the flow velocity is determined by the pipe diameter. It must therefore be selected in a way that, together with the sampling diameter, it results in isokinetic sampling (see section 3.2.3.2). The smallest isokinetic nozzle matching the aerosol spectrometer has an inlet diameter of $\varnothing\ 2\,\mathrm{mm}$, giving the lower limit of the pipe diameter as $\varnothing\ 141\,\mathrm{mm}$ (assuming an extraction volume flow of $1600\,\mathrm{m^3\,h^{-1}}$, see section 3.2.1.5). At the same time, the design space has limited the size of the pipe diameter upward. Changes in cross-section to meet multiple requirements should be avoided due to additional losses associated with it. Since the extraction device (see section 3.2.1.4) has an intake fitting with diameter $\varnothing\ 160\,\mathrm{mm}$, resulting in a flow velocity that can be reconciled with the isokinetic nozzles of the aerosol spectrometer and the installation space, the diameter of the entire connection was chosen to be $160\,\mathrm{mm}$.

To extract a partial flow for measurement with as little losses as possible, a modified 90°-bend was installed in the pipeline, at which a partial flow can be sampled

without further bending and therefore without additional losses. The structure and function of the sampling apparatus are explained in detail in section 3.2.3.1.

3.2.1.4 Extraction Device

The extraction device generates a volume flow that absorbs the particles emitted in the tire–road contact. The volume flow is $2000\,\mathrm{m^3\,h^{-1}}$ and has been designed to give an extraction speed of $120\,\mathrm{km/h}$ in the suction slot between the tire and the extraction funnel, taking into account the adjusted secondary air flow (see section 3.2.1.5). As long as the driving speed and thus the flow speed in the drum are below this value, reliable extraction of the particles can be assumed. Using the resulting extraction volume flow, an average residence time of $13\,\mathrm{s}$ can be calculated for the air inside the drum. This means that all of the air in the test bench drum is replaced approximately every $13\,\mathrm{s}$.
On its way from the extraction funnel to the extraction device (see Figure 3.1), the volume flow passes the sampling spot, where a small partial flow is extracted (see section 3.2.3). The remaining volume flow reaches the extraction device, where a three-stage filter unit removes the particles. Coarse contaminants are separated with the aid of an impact separator and end up in a dust collection box. Finer particles reach the cartridge filters and are separated from the air flow there. Due to the regular automatic cleaning of these cartridge filters using the Jet Pulse process, these particles also end up in the dust collection box. The finest particles that could pass through the cartridge filters are collected with the help of a fine dust filter (HEPA-14, filter efficiency of $99.995\,\%$ according to DIN EN 1822-1 [31]). Since the fine dust filter is a depth filter, the particles separated in it are not available for subsequent analyses. Once the air flow has passed all three filter stages, it leaves the extraction device without any significant number of particles and can be considered clean air.

3.2.1.5 Generation of Overpressure with Clean Air

As described in section 3.1, the internal drum test bench is surrounded by an enclosed chamber. However, constructively it is neither feasible to hermetically seal the chamber from the surrounding test bench hall, nor the internal drum from the enclosed chamber. Therefore, an alternative possibility was needed to avoid contamination by airborne particles in the ambient air.
A reliable and easy-to-implement option is to generate an overpressure. This ensures that there is only a directed air flow from the test bench drum to the outside, thus preventing ambient air containing particles from entering the drum. To implement this, a secondary air flow from the test bench hall was set up in addition to the extraction volume flow from the drum. The extraction and secondary air flow are fused downstream of the sampling site, filtered by the extraction device and subsequently directed back into the test bench drum as clean air. By drawing in the secondary airflow after the sampling site, contamination of the (real-time) particle measurement is prevented. The different sizes of the extraction flow and the clean air flow create an overpressure, which results in two pressure drops: one between the test bench drum and the enclosed chamber and another one between the chamber and the test bench hall. The level of overpressure is determined by the ratio between the extraction and secondary air flow. This is set using a flow regulator at the secondary air inlet. Using this, volume flows from $125\,\mathrm{m^3\,h^{-1}}$ to $500\,\mathrm{m^3\,h^{-1}}$ can be set. While the total volume flow of the extraction system remains constant, this results in different ratios between extraction flow and clean air flow (identical with the total volume flow). For all tests performed in this work, a ratio of extraction flow to clean air flow of $1600\,\mathrm{m^3\,h^{-1}}$ to $2000\,\mathrm{m^3\,h^{-1}}$ or 4 to 5 was used.

3.2.2 Measurement System

3.2.2.1 Optical Aerosol Spectrometer System

In order to select the most suitable measurement technology, a specification sheet was drawn up, summarizing the requirements to be met. These specific requirements were used to select both the measurement method which the measurement technology is based on as well as the exact measuring device. The requirements set are listed below:

- Enabling the measurement of total particulate matter emitted in the tire–road contact, especially the PM_{10} mass fraction.
- Sufficiently wide particle concentration range to measure low emissions as accurately as possible, as well as high ones, when driving severe load conditions.
- Measurement of particle mass as well as particle number concentration in order to generate particle size distributions.
- Measurement of all quantities in real time for clear linking of emission and load condition.
- Maximum possible measurement volume flow to enable isokinetic sampling while maintaining high representativeness.

Since all requirements were to be met with one measuring instrument, only optical measurement technology could be considered. The selected aerosol spectrometer system (PALAS Promo 2000, Karlsruhe, Germany) enables the measurement of the particle number concentration as well as the particle size for the entire particle size range.
Different size ranges from $0.3\,\mu m$ to $100\,\mu m$ can be set, of which the lowest one ($0.3\,\mu m$ to $17\,\mu m$) covers the whole size range required. Both density and refractive index of the measured particles can be selected freely, so that the mass of the particles and thus the particle mass concentration can be calculated. For

all measurements in this work, a refractive index of 1.59 was assumed, which is given by the calibration with latex particles [95]. For the density, a value of $2.299\,\mathrm{g/cm^3}$ was assumed, which had been obtained from particle analyses (see section 4.3.1). In addition, the aspect ratio was set to 1, which corresponds to spherical particles. The assumption of spherical particles was confirmed by microscopy of the particles (see section 4.3.3). With the lower detection limit at $0.3\,\mu\mathrm{m}$, particles smaller than that cannot be registered or measured. However, because of their extremely low mass, they make only a negligible contribution to the total particle mass emitted.

Figure 3.4: Optical aerosol spectrometer system PALAS Promo 2000 with aerosol sensor welas 2500 [94].

In order to measure a wide variety of particle concentrations the PALAS Promo can be equipped with different aerosol sensors. To meet the requirement for a sufficiently wide particle concentration range, the expected upper and lower concentration limit had to be established. Results obtained from preliminary tests indicated that the number-based particle emission in the size range from $0.3\,\mu\mathrm{m}$ to $10\,\mu\mathrm{m}$ would be below $500\,\#/\mathrm{cm^3}$, taking into account the dilution generated by extracting the large volume flow. Therefore, to achieve the highest measurement accuracy even at low emissions, the aerosol sensor with the largest measurement volume (PALAS welas 2500, Karlsruhe, Germany) was selected. This allows the system to detect particle concentrations up to $4000\,\#/\mathrm{cm^3}$ without coincidence error and achieves the highest measurement accuracy at low concentrations.

Particle size distributions can be derived for each time step from the measured particle number and particle size data. These size distributions can be based on particle number (particle number distribution) or particle mass (particle mass distribution) and are divided into 32 size channels per decade (range of tenfold increase or decrease in particle diameter) by default. The two types of distribution can be useful for evaluating changes in different size ranges. Thus, any changes or shifts in particle size can be registered and interpreted as a function of the load condition present in each case. In addition, statements can be made about the influence of the load condition on the hazard potential of the particles generated in the process, since this also depends on the particle diameter (see section 1.2.1). In order to unambiguously link the emission with the underlying load condition, it was important that measurements could be carried out at a sufficient measurement rate, in best case in real time. This is the only way to ensure that the emission can be accurately assigned to the causative effect even in the case of load conditions which can only be held for a short time due to their intensity. The aerosol spectrometer measures all quantities with a measuring rate of $1\,\mathrm{Hz}$ and is thus real-time capable in the sense of this measuring task.

For the most precise indication possible of how many particles are emitted in tire–road contact, the measuring device should analyze a measurement volume flow as large as possible. In this way, inaccuracies resulting from extrapolation to the total extraction flow and thus for the total emission from the tire–road contact can be minimized. The aerosol spectrometer operates with a constant volume flow of $5\,\mathrm{L/min}$, which enables isokinetic sampling by using different isokinetic nozzles depending on the extraction flow specified by the extraction system. For more information on isokinetic sampling, see section 3.2.3.2.

The selected aerosol spectrometer system is especially suitable due to the possibility to move the sensor independently from the control unit. Thus, in the case of the internal drum test bench, the sensor can be placed directly at the sampling spot, which minimizes transport losses. Meanwhile, the control unit, connected to the sensor via fiber optics and a suction hose, can be operated in the control room of the tire internal drum test bench.

3.2.2.2 Skid Resistance Measurements

To characterize the pavement surface condition during the test series, an SRT (Skid Resistance Tester) or British pendulum was used. This is a standardized measuring device for determination of the skid resistance of conventional road surfaces. Therefore, the SRT value is a measure of the skid resistance, in particular of the micro-roughness or microtexture of the surface [38]. The instrument consists of a tripod, to the upper end of which a pendulum arm is fastened so that it can swing. At the lower end of the pendulum arm a standardized rubber sliding body is attached. To measure the skid resistance, the pendulum arm is deflected into a defined horizontal position and released. In contact with the road, the rubber sliding body slides over the surface while being pressed against by a spring with a constant force. Due to the sliding process, the pendulum arm is decelerated and reaches a lower maximum deflection on the opposite side, which is displayed by a drag pointer. The lower the achieved deflection, the higher the determined SRT value and the higher the skid resistance. A representation of the SRT pendulum is shown in Figure 3.5.

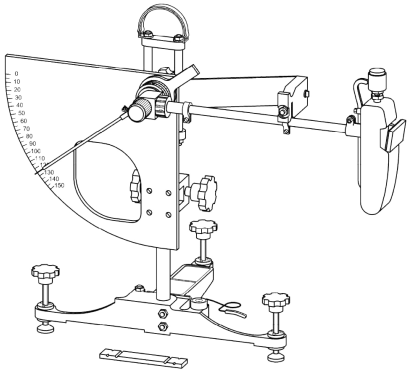

Figure 3.5: SRT (Skid Resistance Tester) pendulum [Adapted from 28].

For more information on the structure of the SRT pendulum and the standardized procedure for determination of skid resistance, see [28] or [38].

3.2.3 Sampling System

As described above, a representative partial flow should be taken from the extraction flow to be analyzed in the aerosol spectrometer. All requirements, their constructive implementation and the design of the sampling system are described in the following.

3.2.3.1 Sampling Apparatus

The following requirements were placed on the sampling system at the beginning:

- The sampled partial flow must be representative of the entire extraction flow in terms of particle concentrations.
- In addition to sampling, it should be possible to insert a pitot static tube anemometer to measure the flow velocity, and both should be possible at several points distributed across the cross-section in order to evaluate the homogeneity of the flow.
- There should be as little particle loss as possible within the sampling probe.
- It should be possible to change the isokinetic nozzle without disassembling the extraction pipe.

To meet these requirements, a multi-part sampling apparatus (see Figure 3.6) was designed and manufactured using a 3D printer. The base body of the sampling apparatus (black) is shaped to fit the outside of a $90°$-pipe bend (gray) without gaps. Any remaining voids have been sealed by adhesive that bonds the device to the pipe bend. The surface contains openings that allow insertion of the sampling probe or the pitot static tube anemometer. In the same places as the sampling apparatus, the pipe bend has openings. Parallel to the direction of flow, all openings are surrounded by a guide channel into which different plugs (green) can be inserted from the outside. Plugs with boreholes are used to take in the sampling probe or the anemometer, while all unused openings are closed. The sampling

apparatus attached to the pipe bend is shown in Figure 3.6. Four openings are closed with plugs, while the sampling probe is installed in the center one. The specific considerations that led to this type of sampling are explained below.

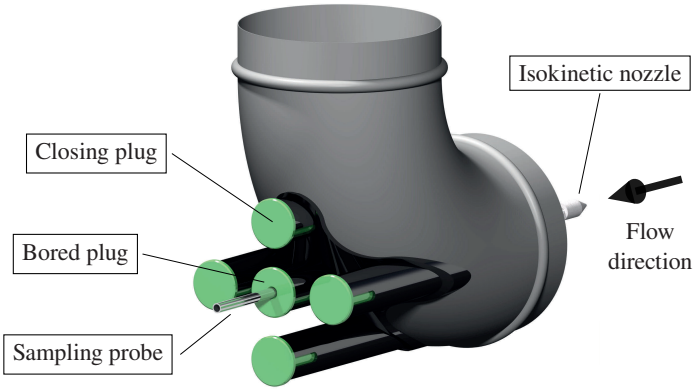

Figure 3.6: 3D view of the outside of the sampling apparatus. The green plugs can be replaced with pierced ones as needed to take samples at the desired position in the cross-section or to monitor the flow velocity.

The extraction of a representative partial flow requires homogeneous mixing of the extraction flow on the one hand and isokinetic sampling on the other (see section 2.7.1). Whether there is homogeneous mixing in the extraction pipe can be estimated by calculating the Reynolds number. Below a Reynolds number of 2300, laminar flow can be assumed, so that almost no mixing takes place. Above this value, as the Reynolds number increases, there is more turbulence, which leads to better mixing of the flow [51]. Based on the extraction flow and the pipe diameter, a Reynolds number of more than 200 000 was calculated, so that homogeneous mixing can be assumed. Isokinetic sampling is ensured with the aid of interchangeable isokinetic nozzles. This means that the required isokinetic nozzle must be matched to the respective flow velocitiy (known by measurements with the anemometer). The theoretical background of isokinetic sampling is elucidated in section 2.7.1 and the exact procedure to reach it in section 3.2.3.2. To enable both with the same plugs, sampling and measurement of the flow

velocity, the same diameter was selected for the sampling probe as for the pitot static tube anemometer. Both tubes can be inserted into the extraction flow through the boreholes provided for this purpose in the measuring plugs. To check the homogeneity of the flow, the five openings distributed crosswise over the cross-section can be used.
After sampling, the aerosol should reach the particle measurement instrument with the lowest particle loss possible. A straight-line sampling probe made of stainless steel (see Figure 3.7) is particularly suitable for this purpose, as it avoids additional losses due to sedimentation in bends or electrostatic charge. To enable straight-line sampling, however, sampling must take place at a bend in the extraction flow, since this is the only way to achieve isoaxial sampling (see section 2.7.1) without subsequent bending of the sampling probe.
To allow changing and installation of the sampling probe and anemometer during operation, the diameter of the openings is larger than the outer diameter of the isokinetic nozzles. This allows the isokinetic nozzles to be mounted on the sampling probe, passed through the plug, and only then inserted into the extraction pipe together with the respective plug.

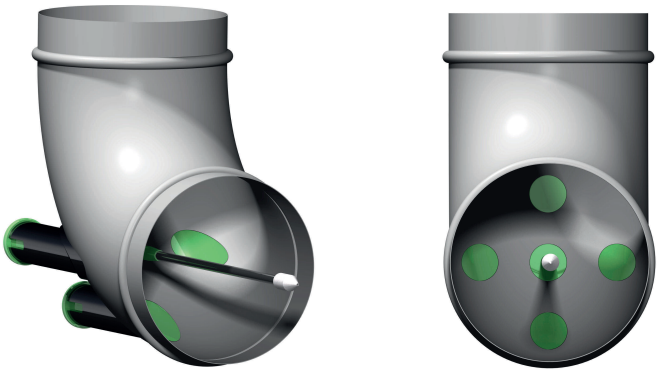

(a) 3D view of the inside **(b)** Front view

Figure 3.7: 3D view of the inside of the sampling apparatus.

All plugs are longer than the guide channels by exactly the thickness of the sheet metal of the pipe bend to create a smooth surface on the inside of the pipe bend. This helps to avoid sedimentation and turbulence in the flow. To ensure the correct alignment of the plugs without holes or those with holes when measuring the particle concentration, all plugs have an anti-rotation lock. This allows them to be mounted in only one position. Figure 3.7 shows two views of a CAD representation of the sampling apparatus in assembled state.

3.2.3.2 Isokinetic Sampling

As explained in section 3.2.1.4, the extraction flow is $1600\,\mathrm{m^3\,h^{-1}}$. An airflow of this magnitude cannot be analyzed in real time with respect to the particles contained. For this reason, it is necessary to sample a smaller partial flow, which can then be analyzed by a particle measurement device. However, when sampling from a flow, care must be taken to ensure that sampling is done isokinetically. For this purpose, the sampling probe must be inserted isoaxially into the flow. This condition is ensured by the sampling apparatus described above. Furthermore, it requires velocity equality—velocity of the sampling flow v_s equals velocity of the extraction flow v_e—at the sampling spot (see Equation 3.1).

$$v_s = v_e \tag{3.1}$$

The inlet diameter of the sampling nozzle d_s resulting from this can be calculated from the velocity of the extraction flow $\dot{V}_e$ measured by the pitot static tube anemometer, the sampling flow $\dot{V}_s$ created by the aerosol spectrometer and the diameter of the extraction pipe d_e. For this purpose, the respective cross-sectional areas are calculated using Equations 3.2 and 3.3.

$$A_s = \frac{\pi}{4} d_s^2 \tag{3.2}$$

$$A_e = \frac{\pi}{4} d_e^2 \tag{3.3}$$

Given the cross-sectional areas, it is possible to calculate the flow velocities using Equations 3.4 and 3.5.

$$v_s = \frac{\dot{V}_s}{A_s} = \frac{4\dot{V}_s}{\pi d_s^2} \tag{3.4}$$

$$v_e = \frac{\dot{V}_e}{A_e} = \frac{4\dot{V}_e}{\pi d_e^2} \tag{3.5}$$

By equating the formulas from Equations 3.4 and 3.5, the inlet diameter of the sampling nozzle required for isokinetic sampling results to

$$d_s = d_e \sqrt{\frac{\dot{V}_s}{\dot{V}_e}}. \tag{3.6}$$

By inserting the given or measured values, an inlet diameter of $\varnothing\ 2.7\,\mathrm{mm}$ results for the sampling nozzle of the aerosol spectrometer. This sampling nozzle is made of aluminum and equipped with a sealing ring. The isokinetic nozzle (light gray in Figure 3.7) can be pushed onto the sampling probe (metallic in Figure 3.7), and the sealing ring provides a tight seal.
In addition, to create conditions that are as consistent and thus as reproducible as possible, the sampling plane within the extraction pipe was determined based on ISO 9096:2017 [55] so that the extraction pipe has no bends on five hydraulic diameters in front of and two hydraulic diameters behind the sampling plane.

4 Experimental Investigation

This chapter deals with the description of the test series carried out, their design and underlying structure, as well as with the procedure for analyzing the measurement data to derive the results. Furthermore, the analyses of the collected particles are described as well as the results derived from these analyses.
All results are based on the test setup presented in chapter 3. For better understanding, the coordinate system used on the test bench is shown in Figure 4.1. Forces acting on the tire are positive if they point in the same direction as the axes shown here. According to the standard, a positive lateral force is caused by a negative slip angle [29]. This means that a positive slip angle in the measurements corresponds to driving a right-hand bend, while a negative slip angle corresponds to driving a left-hand bend.

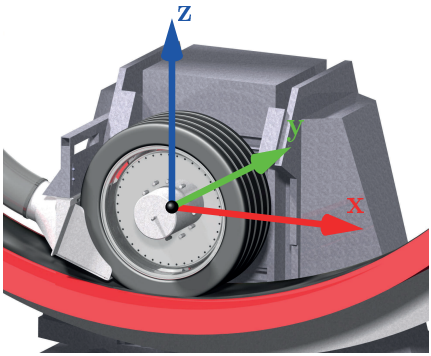

Figure 4.1: Coordinate system at the internal drum test bench which the measurements are based on. In this illustration, the rotational direction of the drum is clockwise.

4.1 Test Series Conducted

As part of a comprehensive literature review, parameters were identified, some of which have an influence on the emission of tire–road PM with certainty and some of which have only a possible influence. These include parameters of the vehicle, the tire, the road, and the environment. To experimentally determine these influences, several test series were carried out in which a single or several parameters were varied in order to be able to quantify the respective influence. Tires from premium manufacturers were used for all tests, and different tire types were examined. Table 4.1 provides an overview of the test series and the parameters varied or kept constant in each case.

In the first test series, the effect of the two main influencing parameters—longitudinal and lateral force—was investigated in detail, while all remaining parameters were kept constant. The exact combinations of longitudinal and lateral force tested are shown in Figure 4.2. As can be seen from this, not all conceivable combinations of the forces given in Table 4.1 were investigated. This is because for average drivers, high longitudinal force rarely occurs in combination with high lateral force. The focus was on the load range used by average drivers, which included maximum values (pure longitudinal or pure lateral force) corresponding to adhesion utilizations less than or equal to 0.62 (see Figure 4.2b). For combined forces—longitudinal force and lateral force at the same time—the maximum values were on the diagonal between the respective maxima of pure forces. Applied to an entire vehicle loaded in this manner at all four wheels, the maximum forces correspond to accelerations of $6\,\mathrm{m/s^2}$ or $0.62\,\mathrm{g}$ in the longitudinal or lateral direction, respectively. In all subsequent test series, only pure longitudinal and pure lateral force was applied, but no combined forces. The application of longitudinal and lateral force was rather used to assess the influence of other parameters which were varied during the respective test series.

Special cases are the second and fourth test series, in which the influence of wheel load and driving speed were examined. To investigate the wheel load, it was varied, while the emission was measured under the application of longitudinal force. However, in order to determine the influence of wheel load, the

longitudinal forces had to be selected in a way that comparable driving conditions were obtained for different wheel loads and the influence of the longitudinal force did not distort that of the wheel load. Thus, comparability was ensured using consistent adhesion utilization values, as a constant adhesion utilization leads to consistent acceleration with different vehicles. Accordingly, four longitudinal forces (positive and negative, respectively) were calculated for each of the four investigated wheel loads, corresponding to identical adhesion utilization values (see Table 4.1). To investigate the influence of driving speed, four speeds were selected and the tire was loaded by pure lateral forces at these speeds.

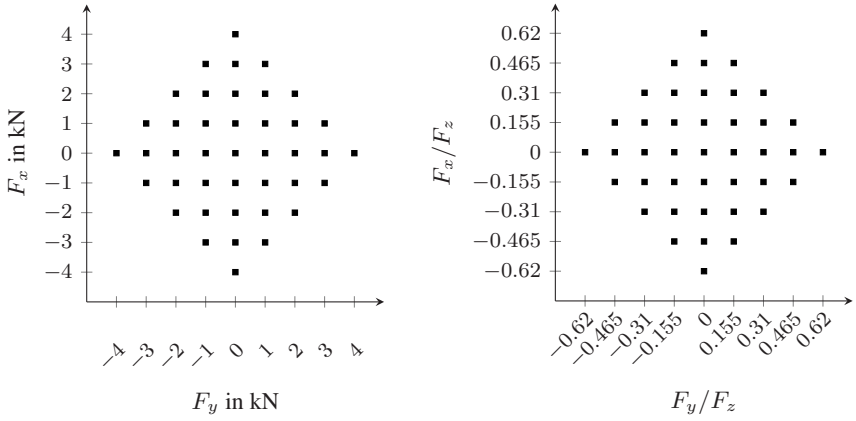

(a) Based on forces [Adapted from 112]

(b) Based on adhesion utilizations

Figure 4.2: Investigated load matrix of tire forces parallel to the road surface consisting of different proportions of longitudinal and lateral force in two different representations. For a wheel load of 6.5 kN, the force values (a) correspond to those of the adhesion utilization (b).

A full-factorial test setup (additionally investigating the combinations of wheel load and lateral force as well as of speed and longitudinal force) would have been preferable for completeness, but could not be performed due to limited project resources. Therefore, the combinations were chosen for practicality in order to learn more about the emissions under acceleration and deceleration at different wheel loads and under lateral force at different driving speeds.

Table 4.1: Overview of the test series performed and the parameters tested. The superscript numbers indicate which longitudinal forces were tested at which wheel load. All tests were conducted with a constant camber angle of 0° and tires of the dimension 255/40 R20.

No.	F_x *in kN*	F_y *in kN*	F_z *in kN*	v_d *in km/h*	*Tire type*	p_i *in bar*	*Pavement*	T_a *in °C*
1	0; ±1; ±2; ±3; ±4 [a]		6.5	80	Summer	2.6	Asphalt	25
2	(1): 0; ±0.5; ±1.0; ±1.5; ±2.0 (2): 0; ±0.75; ±1.5; ±2.25; ±3.0 (3): 0; ±1.0; ±2.0; ±3.0; ±4.0 (4): 0; ±1.25; ±2.5; ±3.75; ±5.0	—	3.25(1) 4.875(2) 6.5(3) 8.125(4)	80	Summer	2.6	Asphalt	25
3	0; ±2; ±4		6.5	80	Summer	2.0 2.6 3.2	Asphalt	25
4	—	0; ±1; ±2; ±3; ±4	6.5	30 50 80 120	Summer	2.6	Asphalt	25
5	0 ; ±2; ±4		6.5	80	Summer Winter All-season	2.6	Asphalt	5; 25
6	0; ±2; ±4		6.5	80	Summer Winter All-season	2.6	Concrete	25

[a] The investigated combinations are shown in Figure 4.2.

4.2 Structure and Performance of the Measurements

The basic procedure for the tests has already been published in [111] and has therefore been adopted analogously. All tires investigated were subjected to a defined run-in procedure before the start of the measurements. On the one hand, this ensured that the outermost layer of the tires, which can contain production residues as well as markings and inscriptions, was removed. Furthermore, since new tires usually show increased wear at the beginning, which only gradually decreases to a constant level, this also ensured that the emission values determined were as reproducible and realistic as possible.

In order to further increase the reproducibility and thus the significance of the emission values, the load conditions were applied numerous times. Preliminary tests had shown that the emission decreased with increasing test duration without any deliberate changes being made to the test setup or parameters. It turned out that the decreasing skid resistance of the road surface was responsible for this phenomenon. A decrease in skid resistance also occurs on public roads, but is slowed down and in some cases even reversed by the effect of various environmental influences. At the test bench, however, precipitation in conjunction with temperatures below freezing point does not occur, or at least not regularly, so that no natural erosion takes place. Furthermore, the reduction in skid resistance is accelerated by the fact that the tire continuously passes over the same road segments, while the average forces transmitted are significantly higher than those occurring in real-world driving. Since this unintended influence could not be prevented, it had to be included in the design of experiments.

For this purpose, the test runs consisting of individual different load conditions were grouped into test blocks, with one test block being run with one basic setting (wheel load, driving speed, tire inflation pressure, etc.) or one tire type at a time. An overview of the general structure of all test series is shown in Figure 4.3. Several (n depending on the test series) test blocks formed a test passage, at the beginning of which the road surface was regenerated. Regeneration was performed by driving with a studded tire under low slip angle. This method had

turned out to be the most efficient and the most sustainable in terms of durability in preliminary tests. Within one test series, several (m depending on the test series) test passages were performed, with the sequence of the test blocks within the test passages being varied in such a manner that each basic setting or tire was performed exactly once in each position. This eliminates the influence of the order of the set parameters on the measured emission. In addition, in order to be able to exclude the influence of skid resistance on the emission during the test runs, the sequence of the individual load conditions was varied within the test runs. The resulting experimental design was subject to deliberate randomization, with each load condition and basic setting tested at each point in a test passage.

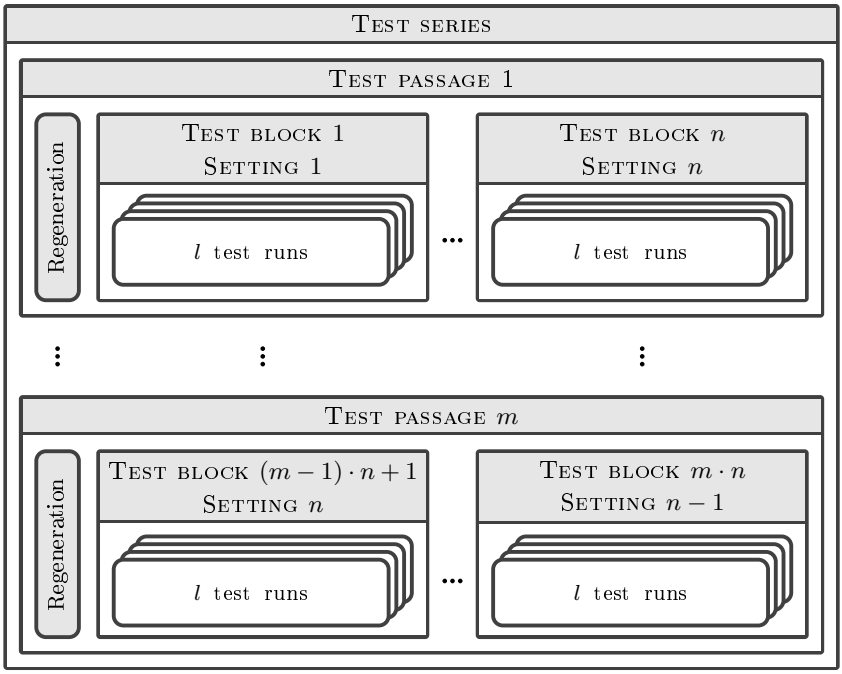

Figure 4.3: Overview of the general structure of all test series performed [Adapted from 114].

The skid resistance of the road was determined directly after regeneration, i.e., at the beginning of each test passage, between the individual test blocks, and at the end of each test passage. The measurement was performed with an SRT pendulum according to EN 13036-4:2011 [28] (see section 3.2.2.2).
To ensure that the results were as comparable and reproducible as possible, each test series was carried out according to a defined procedure. Even before the actual tests began, the air conditioning system was switched on to make sure that the tire and all surrounding components had reached the desired temperature once the measurements began. For all test series with constant tire inflation pressure, it was adjusted at this point of time. The tire was then run in a settled but free-rolling condition at a speed of $50\,\mathrm{km/h}$ until it reached a surface temperature of $28\,^{\circ}\mathrm{C}$. To produce the most realistic tire–road contact possible, $10\,\mathrm{g}$ of a self-made sand mixture comprising quartz, corundum, and calcium carbonate were sprinkled in front of the tire before the start of each test run. The mixture of these three components was modeled on the composition of sands found in the environment [56]. The sand mixture formed the third-body material and prevented the tire from generating an unrealistic surface. Preliminary tests had shown that the complete absence of contaminants, deposits, or third-body material on the road surface leads to a changing tire surface. This phenomenon and the selection of a suitable third body have been described by Haugen et al. [48]. If no third-body material is used, a sticky layer forms on the tire, which prevents realistic tire–road wear particles from being emitted. The few particles emitted are significantly larger compared to real-world particles and are therefore not representative. The regular addition of sand prevents the formation of this sticky layer. The decisive factor, so that subsequent measurements are not affected, is that the diameter of the smallest grains contained in the third-body material is above the size distribution to be measured for particulate matter. Test sands with known size distribution were therefore mixed to create a sand mixture representative for real-world driving. More details about the used sand mixture are given in Appendix A.1.
After five minutes in which the sand acted in the tire–road contact area, the extraction system was switched on, removed most of the added sand and filtered the air inside the internal drum test bench. Once the particle number concentration (PNC) had dropped to a value below $10\,\#/\mathrm{cm}^3$, the actual test run was started.

Depending on the test series, the test blocks consisted of different numbers (l depending on the test series) of test runs (see Figure 4.3). One test run, in turn, consisted of individual load conditions composed of longitudinal and lateral forces, as shown for an exemplary test run in Figure 4.4.

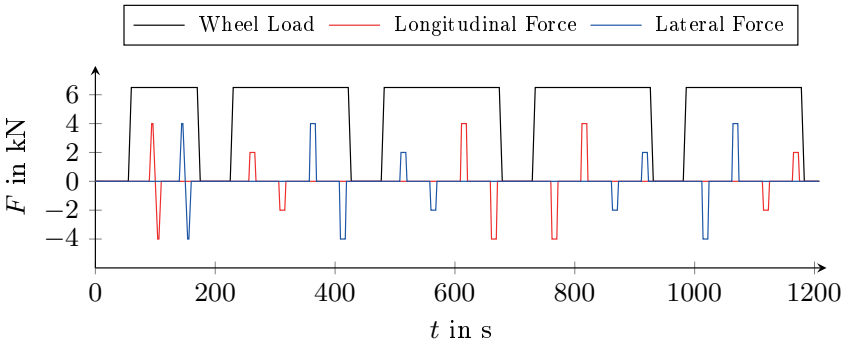

Figure 4.4: Exemplary test run comprising four initial load conditions to stir up remaining sand and 16 single measuring points, 8 for longitudinal and lateral force, respectively [Adapted from 111].

At the beginning of each test run, the driving speed was first changed to the desired value. After, the maximum longitudinal and lateral force was applied in order to remove any sand residues remaining on the road surface despite the demonstrably low background concentration. These four initial load conditions were not included in the evaluation, which ensured that the sand added before was not considered as tire–road PM. The subsequent load conditions were approached using a ramp function, held stationary for eight seconds, and then ramped back down. By keeping the load conditions stationarily, a better assignment between emission and load condition could finally be achieved. Between two load conditions there was always a phase in which the tire either rolled freely or was even lifted off to prevent overheating. To prevent the tire profile from adapting to the load, alternating loads always followed one another. Accordingly, a load with positive longitudinal or lateral force was always followed by a negative one and vice versa.

4.3 Analysis of Particles

Understanding the particle composition is necessary in order to make statements about the contribution of the tire and the road (asphalt surface) to the collected particles. In this way, it can be clearly determined which percentage contribution the two friction partners make to the particles generated.
A major part of the following sections describing the measurements and calculations used to determine the composition of collected tire–road particles was taken from a previous publication [112] and is presented here in slightly modified form.

4.3.1 Density Analysis

The dust collection box of the extraction system was emptied after each test series. When different tire models were used within one test series, a separate dust collection box was used for the test runs of each tire type so that the collected particles were eventually available separately for each tire type. For the analysis described below, the particles from the summer tire which all detailed vehicle parameter investigations are based on were used.
It is likely that small amounts of ambient particles were among the particles in the dust collection box as the secondary air flow from the environment has been fused with the extraction flow without pre-filtering. However, their number and quantity is negligible compared to the PM emitted in the tire–road contact.
All collected samples appeared to be mixtures of different materials and particle sizes (up to about $5\,\mathrm{mm}$). A significant proportion were dark, confirming the assumption that tire material was at least a significant contributor. However, a second component was lighter in color and obviously did not originate from the tire, but must have derived from either the road surface or the sand added. Density analyses of the collected material and the potential components were performed to analyze the particle composition in more detail.
The mass of the sample was first determined using a precision balance. The sample was then segregated into individual size fractions using a cascade of sieves and weighed again. The finest fraction that could be obtained with this method had an

upper diameter of $40\,\mu m$. To gain information on an even finer fraction, part of the subsample of particles below $40\,\mu m$ was subjected to a further process step. An air jet sieve machine was used to remove particles smaller than $20\,\mu m$ from the subsample. Thus, these particles were no further available for analysis. This resulted in two size fractions: one containing particles smaller than $40\,\mu m$ and the second one containing particles between $20\,\mu m$ and $40\,\mu m$.
The mass and the density of both size fractions were determined. The density was measured using a helium pycnometer, with several samples of each fraction measured. Using the densities ρ and mass fractions M as well as Equations 4.1 and 4.2, the density of the size fraction smaller than $20\,\mu m$ was calculated.
The densities and mass fractions determined for the size fractions, as well as the calculated density of the finest fraction, are shown in Table 4.2.

$$\rho_{Total} = \rho_{Fine} \cdot M_{Fine} + \rho_{Coarse} \cdot M_{Coarse} \tag{4.1}$$

$$M_{Fine} + M_{Coarse} = 1 \tag{4.2}$$

Table 4.2: Measured and calculated mass fractions and densities of different size fractions of TRWP for a summer tire driven on an asphalt road surface. The underlined value was calculated according to Equations 4.1 and 4.2, based on the measurement of the others [Adapted from 112].

Size fraction	Size range	Mass fraction M in %	Density ρ in g/cm^3
Total	$d_p < 40\,\mu m$	100.00	2.225
Coarse	$20\,\mu m < d_p < 40\,\mu m$	89.01	2.216
Fine	$d_p < 20\,\mu m$	10.99	<u>2.299</u>

Although the size fraction smaller than $20\,\mu m$ does not exactly correspond to the size range of particulate matter as defined in section 2.6, it can be assumed that the density of particles in these size ranges does not differ significantly as the particles included are generated by the same formation mechanism. However, the actual density of particles in the size range below $20\,\mu m$ is likely to be slightly

different from the density determined and given in Table 4.2. This is because the calculation is based on the mass fractions of the sample taken exclusively from the dust collection box. However, a proportion of PM is not separated in the dust collection box, but in the downstream fine dust filter (HEPA filter, see section 3.2.1). In Table 4.2, it can be seen that fine particles have a slightly higher density than coarse ones. In addition, it can be assumed that the particles separated in the HEPA filter tend to be even smaller than those in the dust collection box. Therefore, the actual density of the fine fraction presumably slightly differs from that specified in Table 4.2.
Nevertheless, the density given seems plausible for two reasons. On the one hand, it is between the densities of tire and road material, which were also determined with the helium pycnometer (see Table 4.3). On the other hand, this value is in the same range as usually given for TRWP in the literature. In [60] and [64] densities up to $2.2\,\mathrm{g/cm^3}$ are given, so the values determined here are only slightly higher. It should be noted, however, that both values mentioned there (in [60] and [64]) refer to coarser size fractions, so density differences are quite possible. For the fine fraction, numerous studies [46, 54, 116] assume an even higher density of $2.8\,\mathrm{g/cm^3}$. However, in all three studies, this density was primarily chosen since a significant proportion of PM originated from the aggregate of the road surface. Only in [1] is a plausible density used to represent the proportion of road and tire material in PM, according to the authors. The density of $2.53\,\mathrm{g/cm^3}$ assumed there is also slightly higher than the density determined here, so it must be assumed that either the composition of the PM collected or the source materials themselves were different. In summary, the density determined is within a plausible range for tire–road PM, so all emission factors have been calculated using a particle density of $2.299\,\mathrm{g/cm^3}$ (see chapter 5).

4.3.2 Particle Composition

Using the density previously determined, the composition of the PM collected could be calculated. The third-body material, which had been added prior to the tests, was not taken into account since it was assumed that the major share of the

sand had already left the drum at the beginning of the recording. It was further assumed that aggregate and bitumen were worn according to their occurrence in the road which is 95 % and 5 % by mass, respectively. This assumption was supported by the observation that the macrotexture, and thus the appearance of the road surface, did not change during the performance of the test series. Excessive wear of bitumen would have resulted in stone chipping. On the other hand, if the aggregate had been excessively abraded, the overall surface would have turned smoother. Therefore, a density of the road material was calculated assuming that 95 % by mass of the abraded road material was aggregate and 5 % by mass was bitumen. Using the resulting density and Equations 4.3 and 4.4, the mass fractions of tire and road material in the collected particles was calculated. The resulting mass fractions are listed in Table 4.3.

$$\rho_{PM} = \rho_{Tire} \cdot M_{Tire} + \rho_{Road} \cdot M_{Road} \tag{4.3}$$

$$M_{Tire} + M_{Road} = 1 \tag{4.4}$$

Table 4.3: Densities, mass fractions and volume fractions of the constituents of tire–road particulate matter (d_p < 20 µm). The two constituents shown in gray are sub-fractions of the road material [112].

Material	Density ρ in $\mathrm{g/cm^3}$	Mass fraction M in %	Volume fraction V in %
Tire tread	1.206	18.2	32.0
Road material	2.543	81.8	68.0
Aggregate	2.622	77.7	60.0
Bitumen	1.035	4.1	8.0
PM (TRWP)	2.299	100.0	100.0

Accordingly, about a fifth of the particle mass originates from the tire, while the road surface contributes four fifths of the mass. First, the proportion of the tire appears to be low and the one of the road to be high. For a long time, it was exclusively stated in the literature that TRWP consisted of approximately

equal parts of tire and road material. According to this view, the core of the particles consists of tire material, while only the surface is encrusted with minerals [8]. In recent years, however, this view has been increasingly questioned. Both Mattsson et al. [83] and Wilkinson et al. [145] have shown that minerals can also be found inside the particles. Recent studies conclude that minerals can make up a fraction of 61 % [65] to 79 % [64] by mass. Several effects could account for the relatively high proportion of road material in more recent studies. Just as the results in this study, the results in the two references were obtained from test bench measurements performed on real road surfaces. All collected particles were included in the analysis, including those consisting exclusively of road surface material. This is in contrast to previous results, which were mostly obtained from ambient measurements. Since the attribution to tire–road wear particles is usually made via the substances contained in the tire tread, only those particles that contained tire material were considered as TRWP [65, 96, 104, 132]. Pure road wear was therefore not taken into account in these studies, so lower contributions from road material are plausible. However, the results obtained here are even slightly higher than the range given in the literature, which there are several possible reasons for.

First, the calculation assumes that the density of tire material remains unchanged during the abrasion process. However, it is possible that the material changes due to the extreme force and temperature influence to the extent that the density within the particles is higher than that in the tire tread. Second, the composition of PM is likely to change with skid resistance. A road surface with higher skid resistance (many microscopic peaks) could result in a significantly higher proportion of road material due to the removal of tiny peaks and the settling of tire material in the interstitial vales. However, most road surfaces do not have this high number of microscopic peaks as they are subject to constant abrasion. On the internal drum test bench, the peaks are caused by the regular regeneration process. Since emissions are particularly high on rough roads, the contribution of the road could affect the results of the entire test series. Third, despite all precautions, it is likely that residues of the added sand remain on the road surface, are ground up by the tire, and get separated in the dust collection box. All three effects increase the mass fraction of mineral material in the particles obtained by the calculation.

Ultimately, the exact composition of particles presumably depends on the road surface used and the tires driven on it, so results from different studies are not directly comparable.
However, to check the plausibility of the results in this work, they can be validated visually. For this purpose, images of the collected particles were taken with a scanning electron microscope (SEM) (see section 4.3.3). For better comparability between the calculated proportions of tire and road material and the SEM images, it is helpful to convert mass fractions into volume fractions. Their values are also included in Table 4.3. Because of its lower density, the value of the tire is now higher. Looking at the images (see Figure 4.5, detailed descriptions of and distinction between the particles in section 4.3.3), this percentage still appears to be low, but it must be considered that tire material is not visually distinguishable from bitumen from the road surface. Therefore, it is more appropriate to assume a joint proportion of tire material and bitumen, which accounts for $40\,\%$ of the volume, and a proportion of mineral aggregate of $60\,\%$ (see Table 4.3). This ratio seems to be realistic in view of the images, since the aggregate material is present both in pure form as well as in the encrustations, and presumably also inside the tire–road wear particles (see also [104, 83]).

4.3.3 Scanning Electron Microscopy (SEM)

Figure 4.5 contains SEM images of TRWP in different size ranges and magnifications. Figure 4.5a and 4.5b show a rather large section with predominantly coarse particles, mainly in the size range of about $20\,\mu\mathrm{m}$ to $60\,\mu\mathrm{m}$. It can be seen that the particles differ in their structure. On the one hand, there are sharp-edged particles with a homogeneous and smooth surface structure whose aspect ratio varies greatly. These particles are probably minerals. On the other hand, there are heterogeneous particles with an irregular surface structure. They show the typical characteristics of tire–road wear particles: mostly elongated with encrustations of smaller mineral particles on their surface.

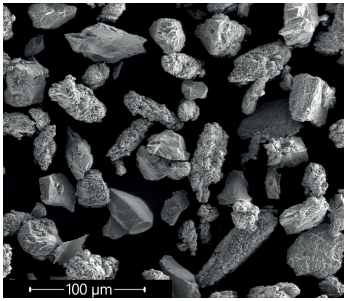

(a) [Adapted from 112]

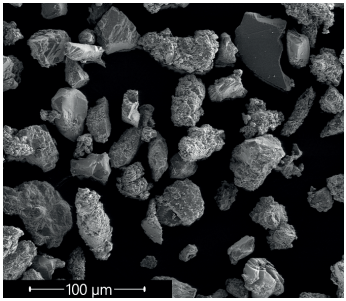

(b)

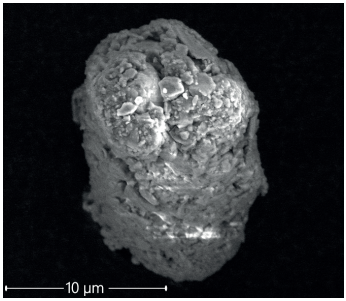

(c)

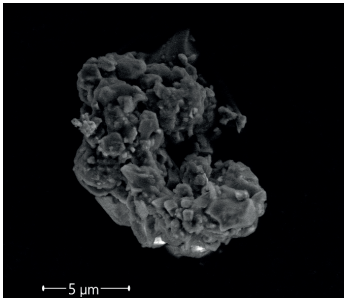

(d)

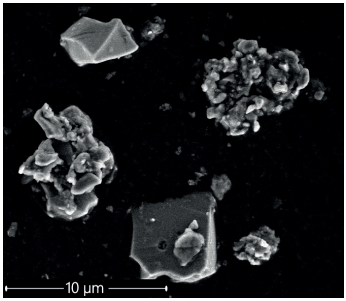

(e) [Adapted from 112]

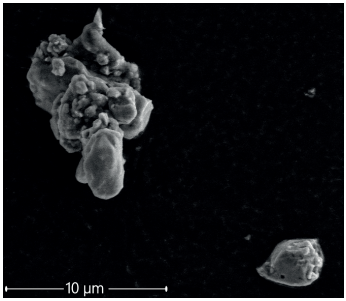

(f)

Figure 4.5: SEM images of particles of different size fractions and composition collected in the dust collection box of the extraction device during the test runs. (a) and (b) show an overview of different particles in the size range from $10\,\mu\mathrm{m}$ to $100\,\mu\mathrm{m}$. These include both pure road particles as well as tire–road wear particles. (c) and (d) each show a smaller tire–road wear particle of about $10\,\mu\mathrm{m}$ with mineral encrustations on the surface. (e) and (f) show even smaller particles around $5\,\mu\mathrm{m}$, some of which are purely mineral and some of which are composed of tire and road material.

Figure 4.5c to 4.5f show even smaller particles at higher magnification. Their size is around or even below $10\,\mu\mathrm{m}$, so they are in the size range of particulate matter. The two particles shown in Figure 4.5c and 4.5d have a surface similar to the one described above for TRWP. They are also uneven and bind smaller fragments in their surface. However, they differ in shape from the larger particles. While the majority of these were elongated, the fine particles are rather spherical with an aspect ratio that is probably in the range of 1.
The same is true for the even smaller particles shown in Figure 4.5e and 4.5f. They also tend to be spherical, or at least have no preferred direction of expansion. The spherical shape was detected in all images for particles of the fine fraction, so it is assumed that fine TRWP are indeed different in shape from those of the coarse fraction. The resulting value of 1 for the aspect ratio was stored in the aerosol spectrometer so that it was used for the calculation of particle mass concentrations. The two images also show that in addition to the typical TRWP, mineral particles are also present in the fine fraction. In view of this, the composition of the tire–road dust calculated in section 4.3.2 seems all the more plausible.

4.4 Analysis of Measurement Data

4.4.1 Data Analysis Procedure

The procedure for data analysis has been described in detail in [111]. Therefore, the following description is essentially taken from that publication.
Both particle number concentration (PNC) C_n and particle mass concentration (PMC) C_m were recorded during all test runs. In Figure 4.6 the raw data obtained for one exemplary test run are shown together with the applied forces. At the beginning, both PNC and PMC were at a low level. After, both signals increased slowly at first and then abruptly. The gradual increase in this test run, as in all the others, was due to the increase in driving speed from $50\,\mathrm{km/h}$ to $80\,\mathrm{km/h}$ with the wheel off the ground, i.e., without tire–road contact. This stirred up the fragments of the sand mixture left on the road. The abrupt rise at $55\,\mathrm{s}$ is

attributable to the settling of the wheel and the application of wheel load. The two subsequent double peaks (90 s and 160 s) are caused by the maximum forces applied to remove residues still remaining on the road. The peaks of particle concentrations for these four initial load conditions were significantly higher than all subsequent peaks in all test runs. This was an indication that fragments of the added sand had indeed remained on the road surface and had been stirred up in the process. Accordingly, the initial peaks were excluded from the evaluation. Thus, the direct influence of the sand addition on the measurements could be prevented by the choice of coarse third-body material (for detailed information on the grain size distribution see Appendix A.1). However, it could not be avoided that the sand was ground up in the tire–road contact and finally registered as smaller fragments by the aerosol spectrometer. However, it is clear from the emission curves that they always increase when a load in the form of longitudinal or lateral force is applied. Furthermore, it can be seen that the magnitude of the emission appears to depend on the magnitude of the load, suggesting a correlation between the two quantities. The investigation of the exact correlation—i.e., the mathematical relationship—between the emissions and the underlying load conditions is described in detail in the following paragraphs.

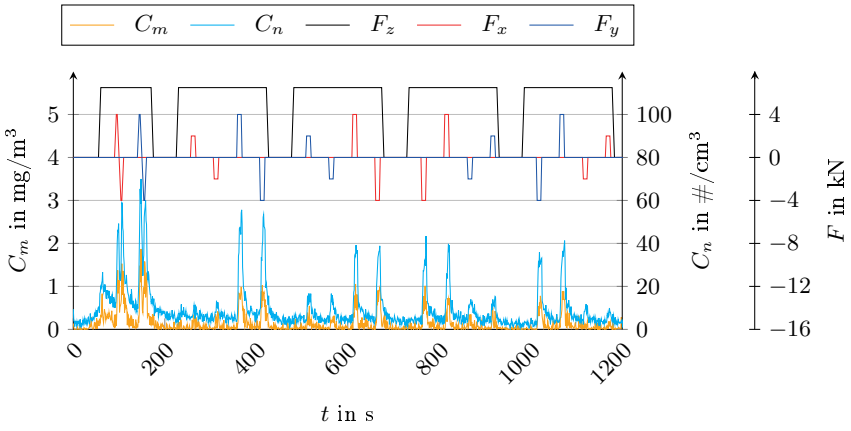

Figure 4.6: Exemplary test run with the particle mass concentration and particle number concentration recorded during the test run [Adapted from 111].

In addition to the peaks caused by tire forces, the signal contains noise. However, since this is significantly lower than the peaks caused by loading, it is only of minor relevance. In order to increase the comparability of the individual emission peaks, mean values were calculated from the emission signals present during the load conditions. In doing so, it had to be taken into account that the release of the particles still occurred when the causative loading had already ended and that the particles needed approximately one second to cover the distance between their point of release and the sampling site. Therefore, a time period was determined that served to average the emissions during all load conditions and was long enough to include the emissions of interest completely. The advantage of averaging is that the different curve progression of the emission over time (not the different level of emission) for different load conditions is eliminated. Besides that, it also levels out the noise described above.
Furthermore, it had to be taken into account that not all emissions measured by the aerosol spectrometer could be attributed to the underlying load condition. As previously described, the test runs were started when the particle number concentration had fallen below a certain limit value with the drum rotating but the wheel lifted off the ground. However, this also means that despite HEPA filtration, a certain residual concentration was present throughout the tests and was included in the measured raw data. In order to determine the net emission, i.e., the emission that is caused by the respective load condition, the so-called background concentration had to be subtracted. The challenge was that the background concentration could not be measured before each load condition, as this would have multiplied the measurement time. Therefore, it was only measured when the wheel was lifted off for cooling anyway (see Figure 4.4: 225 s, 475 s, 725 s, and 975 s). The following decline in concentrations was described with the help of mathematical functions for the standard drop of the PNC or PMC. This standard drop had been previously determined empirically by evaluating the decline of concentrations after a given load. The background concentrations obtained in this manner for any given time during the load conditions were subtracted from the measured raw data. The mean values of PMC as well as PNC for each load condition were then calculated as previously described and are shown in Figure 4.7 for the experimental run presented above.

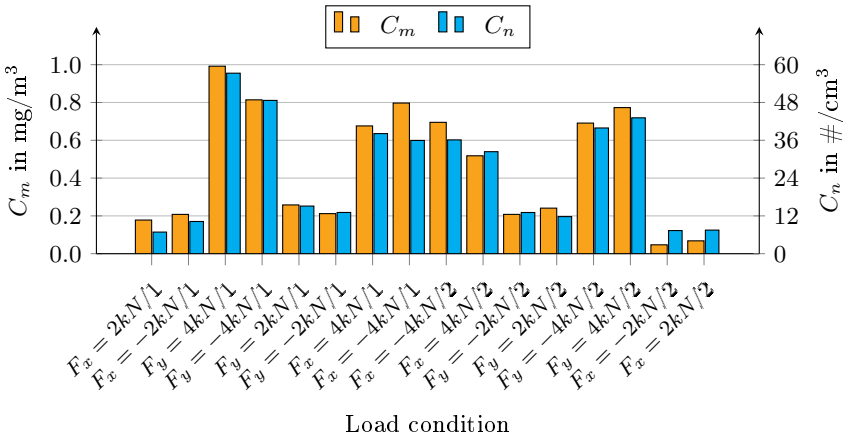

Figure 4.7: Calculated average particle mass concentration and particle number concentration for different load conditions in an exemplary test run (same test run as shown in Figure 4.6) [Adapted from 111]. The second digit indicates the repetition within the test run.

It is again clear that higher loads lead to higher emissions. This applies to both PMC and PNC, both of which appear to develop similarly.

To take into account the influence of the skid resistance of the road surface on the emission, its value had to be known at each point of time. Therefore, a curve progression was derived from the SRT values measured during the test runs (see Figure 4.8) using regression. Since very similar curves were obtained for different runs, all curves of a test series were combined into a single curve progression that served as standard SRT curve for the entire test series. One exemplary standard SRT curve is shown in Figure 4.8. The highest skid resistance occurs right at the beginning, i.e., immediately after the regeneration process of the road surface. The subsequent passes lead to a drop in skid resistance, which is initially strong and weakens as the test duration progresses.

Knowing the SRT value during the test runs, the underlying skid resistance could be assigned to each load condition. For this purpose, the calculated SRT curve was subdivided into the number of load conditions applied during one run (for detailed description of the method see [111]). The subdivision took into account that the load conditions had different intensities and thus also wore the pavement

differently. Hence, assumptions were made for the different test series to be able to describe the decrease in skid resistance as accurately as possible:

- The decrease in skid resistance is proportional to the applied force in the longitudinal and lateral direction.
- The decrease in skid resistance is proportional to the applied wheel load.
- The decrease in skid resistance is proportional to the driving speed.

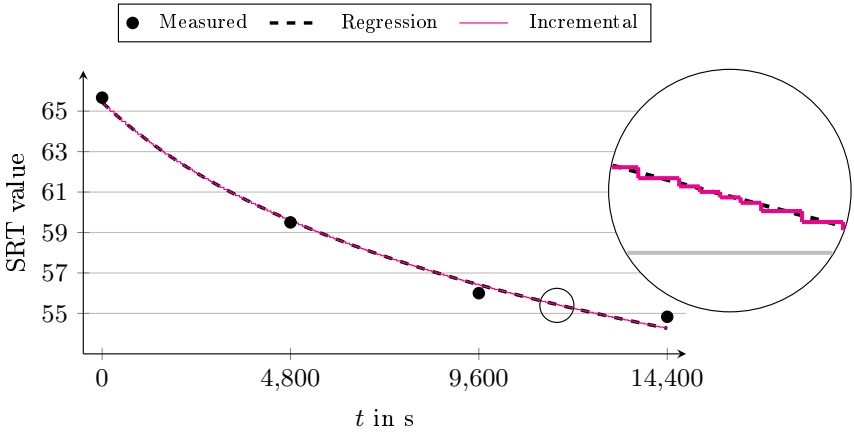

Figure 4.8: Measured SRT values and determined standard SRT curve for an entire passage [Adapted from 111].

Based on these assumptions, an incremental curve progression for the skid resistance was calculated for each test run, which is shown in Figure 4.8 as well. For better visibility of the increments, a section of the curve is shown in augmentation. In accordance with the incremental curve progression, it was assumed that the skid resistance changed abruptly between two load conditions, and remained constant in the meantime. If the emission values for same loads are plotted against the SRT value, the dependence of the emission on skid resistance becomes visible. The correlations for loading with different lateral forces are shown in Figure 4.9. Due to the rapid decrease of skid resistance at high SRT values, the distance

between two adjacent points is larger here than for low SRT values. To analyze the mathematical dependence, points of equal loading were approximated with exponential regression functions, which are also shown in Figure 4.9. This results in coefficients of determination R^2 between 0.85 and 0.91 for the curves for loading with lateral force, indicating high correlation. However, for other load conditions such as longitudinal force or the free-rolling condition, the coefficients of determination were slightly lower. This is probably due to the higher fluctuation in force when controlling longitudinal force compared to controlling lateral force at the internal drum test bench and due to the relatively larger influence of the noise from the background concentration when the emission is low.

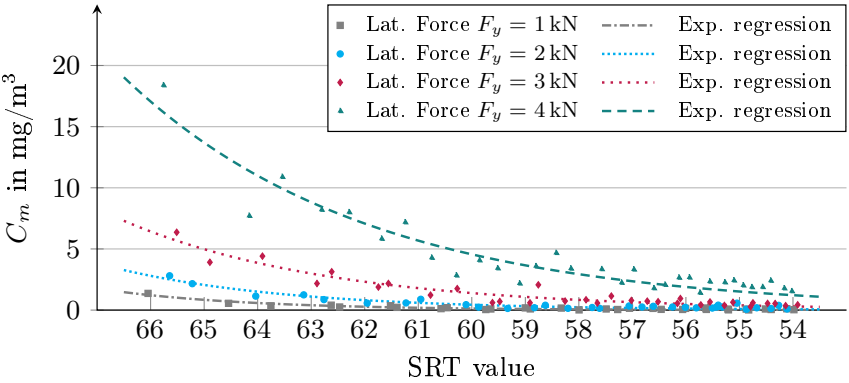

Figure 4.9: Emissions at different but constant load conditions over SRT value for a summer tire and regression functions derived from this.

The skid resistance, or the SRT value characterizing it, exerts a significant influence on the level of emission. This is true for all shown curves, but is most evident for the highest load of $4\,\mathrm{kN}$ with a factor of about 20 between the PMC at an SRT value of 55 and that at an SRT value of 65. The increase in emission is so strong for large SRT values that even the exponential regression curve significantly underestimates the values. It can therefore be assumed that the initially high emissions are mainly caused by the fact that tiny peaks formed during the regeneration process of the road surface are immediately abraded and emitted as

particulate matter. Once these fine structures have been removed, the decline of skid resistance slows down, resulting in a drop of emissions.
The particle concentrations discussed so far—PMC and PNC—are test-bench specific measurements. They are highly dependent on the level of the extraction flow. In order to be able to compare the values with the results from other test benches and with emissions for real-world driving, the measured values must be converted into emission factors. Conversion from PMC to a mass-based emission factor EF_m is done using Equation 4.5 with knowledge of the extraction flow $\dot{V}_e$ and the driving speed v_d. For all subsequent evaluations, the number of wheels n_w is set to four to represent a standard passenger car. It is assumed that all four wheels are subjected to the same load condition. The calculated emission factors thus reflect the emissions of a hypothetical four-wheeled vehicle for exactly one specific load condition.

$$EF_m = C_m \cdot \frac{\dot{V}_e \cdot n_w}{v_d} \tag{4.5}$$

This means that the curve progression of the emission factor over the SRT value is known for different but constant load conditions. To determine the dependence of the emission factor on the level of a specific load, an SRT value is selected and the emission factors determined by regression are plotted against the respective load type. This results in the diagrams shown in section 5.1.1 to 5.1.8. For all emission values presented in there an SRT value of 60 has been chosen. According to [57], this corresponds to the acceptance value recommended by the German Road and Transportation Research Association (Forschungsgesellschaft für Straßen- und Verkehrswesen, FGSV) for new roads [39].

4.4.2 Limitations in Data Analysis

Assumptions and simplifications have been made in the evaluation of the measured data and in the determination of the mathematical relationships between load conditions and PM emissions. In order to make the results more transparent, these assumptions and simplifications are explained and critically reviewed below.

Due to their operating principle, optical aerosol spectrometers cannot measure particle mass directly. It must be calculated from the scattered light pulse of the respective particle and the equivalent diameter derived from it (see section 2.7.2 and 3.2.2.1). This requires knowledge of the refractive index of the particle material. In this work, a refractive index of 1.59 was assumed for all calculations corresponding to latex particles which are used for calibration. This value probably does not correspond precisely to the actual refractive index of TRWP. However, an exact value is neither known nor easy to determine, as it can vary depending on the composition and size of the particle. The density and the aspect ratio of the particles, which are also required for the calculation, have been determined by subsequent analyses (see section 4.3).

To limit the effort for data allocation and management, all correlation analyses between load condition and PM emission are based on test bench target data. Preliminary tests had shown that the control of tire forces (vertical, longitudinal, and lateral) and the control of driving speed work precisely. The resulting high level of agreement between target and actual data can be seen in Figure 4.10. Especially for longitudinal (Figure 4.10b) and lateral force (Figure 4.10c) as well as for driving speed (Figure 4.10c) there are only small deviations between the two data series. Only the wheel load (Figure 4.10a) shows persistent, sometimes larger fluctuations. These are mainly caused by unevenness of the road surface and irregularities of the tire, and can therefore not be eliminated. This means that even if the tire forces parallel to the road surface were perfectly controlled, there would be constant changes in the frictional state of the tire–road contact (adhesion utilization), which in turn would be accompanied by a change in the current emission. Therefore, during one loaded phase, many different adhesion utilizations would occur. Since the relationship between adhesion utilization and emission is unknown, it is not possible to calculate or derive a reasonable surrogate value such as the mean value. This means that there would be no unique value for correlation analysis. Furthermore, no correlation can be made for each individual time step. Due to the small but time-varying delay between the emission and its detection by the aerosol spectrometer, the correlation must always be determined with the emission over the entire loaded period (see section 4.4.1). Accordingly, the correlation between load condition and PM emission could only be determined

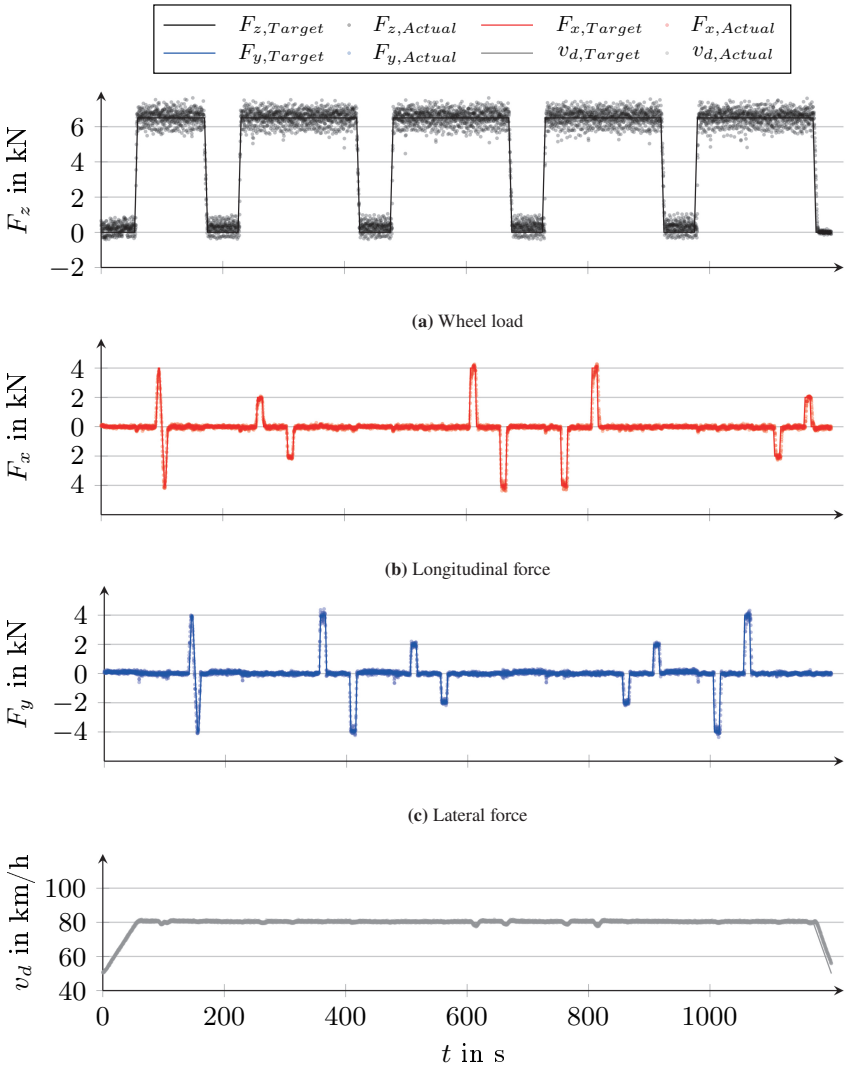

(a) Wheel load

(b) Longitudinal force

(c) Lateral force

(d) Driving speed

Figure 4.10: Comparison between target and actual data for test bench control.

by means of an iterative calculation model. Since this would require an enormous computational effort and would lead to only minimal improvements due to the already precise controlling, the target data were used instead of the actual data.
In Figure 4.9 the correlation between different lateral forces and the associated PM emission was shown as a function of the SRT value. Such correlations have been established for all influencing parameters from which the later results are derived. This is based on the assumption that skid resistance and the associated SRT value, in addition to the parameter under investigation, are the decisive influencing variables on the level of PM emissions. This assumption is plausible based on the high coefficients of determination for the summer tire. However, lower coefficients of determination were found for the all-season tire and especially for the winter tire. The correlation for both tire types is shown as an example in Figure 4.11 for one load condition each.
In the case of the winter tire (Figure 4.11a), it can be seen that the particle mass concentration has a recurring curve progression over the SRT value. Starting from the highest particle mass concentration at an SRT value of about 65, the particle mass concentration first decreases sharply and then more slowly. The following cycles start again with a higher value in the range of SRT values of 59 and 56 and subsequently flatten out. Each of these cycles (8 data points each) corresponds to exactly one test block (see Figure 4.3). During each test block, the emission decreases stronger than approximated by the regression function with repeated, identical load. At the beginning of a new cycle, the emission is initially higher before decreasing again. This emission behavior suggests that, in addition to skid resistance and load, there is another parameter for winter tires that significantly influences PM emissions. This parameter could be tire temperature. This is supported by the fact that tire temperature increases significantly under load and that repeated loading results in lower PM emissions for the winter tire (see Figure 5.15). At the beginning of each new cycle, the tire temperature is well below the temperature occurring under load, resulting in a recurring increase in emissions. Since only particles in the range smaller than $10\,\mu\mathrm{m}$ are taken into account, it is possible that at higher temperatures, due to softer tire material, larger particles are emitted which are not detected by the aerosol spectrometer. Increasing particle sizes at higher temperatures have been described in [21]. The

fact that this effect occurs only with winter tires and to a lesser extent with all-season tires, but not with summer tires, confirms this assumption, since winter tires have by far the softest rubber compound and thus the lowest glass transition temperature. Another reason for the high emission at the beginning of each cycle could be a self-forming layer on the tire surface that is susceptible to abrasion. This could also explain why the emission is high at the beginning of each new cycle (after a break of several days) and gradually decreases. However, this possibility cannot be proven either and needs to be further investigated in future experiments, together with the influence of tire temperature.

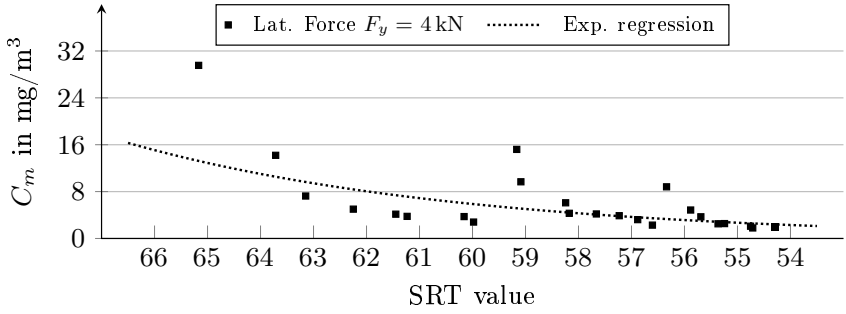

(a) Winter tire [Adapted from 111]

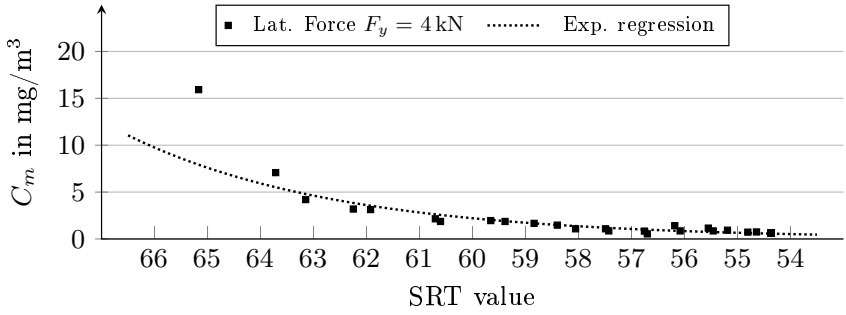

(b) All-season tire

Figure 4.11: Correlation between SRT value and PM emission at constant load condition for a winter and an all-season tire.

The same effect, but to a much lesser extent, can be seen for the all-season tire (Figure 4.11b). Again, the emissions initially decrease stronger than the regression function, and an increase in emissions can be seen at an SRT value of 56 (beginning of the third cycle).
The resulting lower coefficients of determination for the correlation between SRT value and PM emission for consistent load only affect the results in subsection 5.1.5, 5.1.6, and 5.1.7. All other results are based on driving with the summer tire only and are therefore not affected by this imprecision.

5 Influences on the PM Emission

As explained in section 4.4.1, the calculated emission factors were plotted over different types of load to determine the dependence of emission on the respective parameter or to compare the emissions of different tires with respect to this parameter. For mass-based emission factors, it is important to consider the upper particle size of $10\,\mu m$. Particles larger than this value are not included since, according to the definition (see section 2.6), they are not classified as particulate matter. As the focus of this work is on PM emissions in the PM_{10} category and the usual metrics are mass based, no number-based emission factors are given. Precise statements on this would require measurement instruments which also take into account the size range of nanoparticles. Due to their extremely small mass, these particles play a negligible role for the mass-based EFs discussed here. Many of the results shown in the following sections have been presented by the author of this work in scientific publications during the project. Therefore, both the content discussed as well as some illustrations shown are either taken from the respective publication or based on results presented there. The results in section 5.1.1.1 to 5.1.1.3 on the influence of longitudinal, lateral, and combined forces are taken from [112]. The results in section 5.1.2 to 5.1.4 on the influence of wheel load, tire inflation pressure, and driving speed have been presented in [114]. The results shown in section 5.1.5 and 5.1.6 on the influence of tire type and ambient temperature are adopted from [111]. The results on the influence on the particle size distribution (see section 5.2) are taken from the publication on the respective influencing parameter.

To describe the reproducibility of the measurements, the 95% confidence intervals (CIs) are shown for all diagrams on the level of emission. Diagrams with one or more regression functions, additionally contain the 95% confidence bands (CBs).

After the results are presented, they are interpreted and discussed. Where possible, they are compared with existing statements in the literature. However, due to a lack of information (see section 1.2.3), that is only possible for some of them.

5.1 Influences on the Level of PM Emission

5.1.1 Forces Parallel to the Road Surface

In studying the influence of tire forces parallel to the road surface, a distinction was made with respect to force direction. Longitudinal forces caused by driving and braking (see section 5.1.1.1) as well as lateral forces caused by cornering (see section 5.1.1.2) were investigated. Subsequently, forces in both directions were combined (see section 5.1.1.3). For pure longitudinal and lateral force as well as for combined forces with equal shares of both the mathematical correlations between applied force and PM emission were determined. An overview of the investigated tire forces parallel to the road surface and where to find the respective results is given in Figure 5.1.

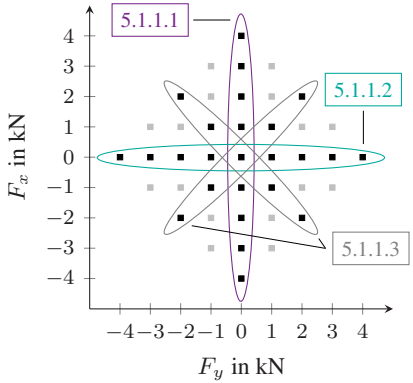

Figure 5.1: Investigated tire forces parallel to the road surface to determine the PM prediction model [Adapted from 112] with references to the respective sections.

The physical processes which lead to the emission curves obtained are discussed in section 5.1.1.4.

5.1.1.1 Longitudinal Force

The result of the procedure described in section 4.4.1 for the emission factor of a summer tire as a function of longitudinal force is shown in Figure 5.2. The graph includes braking forces ($F_x < 0$) as well as driving forces ($F_x > 0$). The support points symbolize the emission values obtained from the regression functions (see section 4.4.1) for an SRT value of 60. The support points were approximated by regression functions, resulting in the curve progression of the emission factor over the longitudinal force. Fourth-order functions gave the highest coefficients of determination and were therefore chosen to be most appropriate for approximating this relationship. The approximation for positive and negative longitudinal force was performed separately. The value in the free-rolling condition ($F_x = 0$) was specified in the form of a constraint, so that a continuously differentiable curve was obtained.

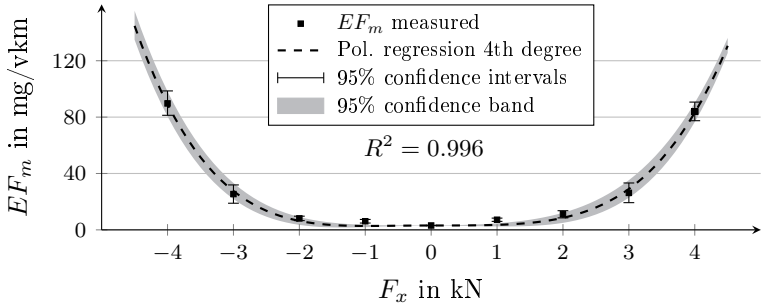

Figure 5.2: Emission factors in the size range between $0.3\,\mu\mathrm{m}$ and $10\,\mu\mathrm{m}$ over longitudinal force and regression function for a summer tire at a wheel load of $6.5\,\mathrm{kN}$, a driving speed of $80\,\mathrm{km/h}$, an inflation pressure of $2.6\,\mathrm{bar}$, an ambient temperature of $25\,^{\circ}\mathrm{C}$, and an SRT value of 60 [Adapted from 112].

The regression functions show that the emission increases only slightly at low forces. As the force continues to increase, the emission increases progressively, resulting in emission factors around $85\,\mathrm{mg/vkm}$ for the maximum longitudinal forces considered. The initial small increase in emissions can be explained by deformation slip which prevails at low longitudinal forces. When passing through the tire–road contact, the tread blocks are deformed in the longitudinal direction. However, due to the low force, they do not reach the adhesion limit, so they return to their original position when leaving the contact area without sliding beforehand. As the force continues to increase, the tread blocks are deformed more strongly within the tire–road contact and reach the adhesion limit. This results in sliding slip, causing the tread blocks to slide over the road surface for the remaining distance to the end of the contact patch, which significantly increases emissions. A more detailed description of the relationship between emission and sliding slip can be found in section 5.1.1.4.

Furthermore, it can be seen that braking results in higher emission factors than driving. This effect is due to different shear stress distributions between driving and braking. Due to the basic shear stress distribution (in the free-rolling condition), the adhesion limit is already reached at lower forces during braking than during driving (see Appendix A.3). As explained above, reaching the adhesion limit earlier results in a higher percentage of sliding slip and ultimately in higher emissions.

The results shown are highly consistent, both qualitatively and quantitatively, with trends known from the literature. The increases due to high deceleration are in the same range as in Kwak et al. [74]. As in Foitzik et al. [37], where a quadratic relationship was found between driving force and emissions and a fourth-order relationship between braking force and emissions (see section 1.2.3), emissions here are also higher during braking than during driving. However, in contrast to their results, a fourth-order regression function also shows the highest coefficient of determination for driving forces here. Such detailed differences are probably caused by different road surfaces and tires. However, it is undisputed that longitudinal force has a significant influence on tire–road PM emissions, which underscores the importance of an anticipatory acceleration and braking behavior.

5.1.1.2 Lateral Force

The influence of lateral force on PM emissions is illustrated in Figure 5.3. The support points shown represent the emissions obtained with a summer tire and an SRT value of 60. The curve progressions of the emission factor were approximated using regression functions. The passage of the emission factor at a lateral force $F_y = 0$ was specified as an additional constraint. As with the longitudinal force, fourth-order functions gave the highest coefficients of determination.

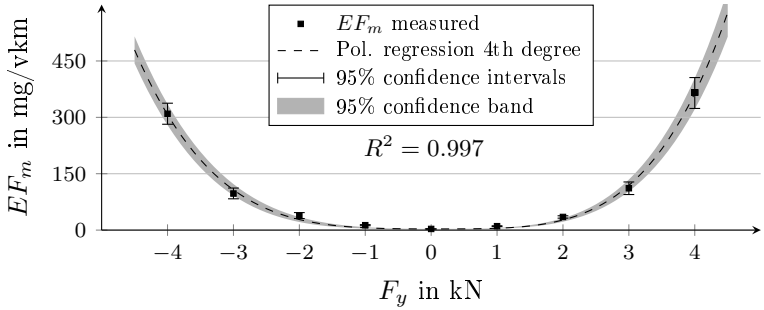

Figure 5.3: Emission factors in the size range between 0.3 µm and 10 µm over lateral force and regression function for a summer tire at a wheel load of 6.5 kN, a driving speed of 80 km/h, an inflation pressure of 2.6 bar, an ambient temperature of 25 °C, and an SRT value of 60.

This results in low increases of the emission factor for moderate forces which increase as the force increases further. Again, this effect is due to the increasing proportion of sliding slip compared to deformation slip (see section 5.1.1.4). However, it is noticeable that lateral forces result in significantly higher emissions than equivalent longitudinal forces. Over the entire force range, the emission factor is almost four times higher for lateral force than for longitudinal force for the summer tire tested. Two reasons are presumably responsible for this difference.
The first reason is due to the processes involved in forming the slip angle and the resulting lateral slip. When steering a wheel, the slip angle is formed between the main plane of the tire and the direction of travel of the wheel contact point. When the tread bar elements run into the contact area between the tire and the road

(leading edge), at first, there is essentially adhesion and the tire surface undergoes lateral deformation. The slip angle results from the deformation of the tire belt and the tire tread, with additional lateral slipping occurring in the rear part of the contact area. As the tread bar elements approach the trailing edge, the surface pressure decreases while their lateral deformation continues to increase. Eventually, the shear stress parallel to the road surface becomes too high for the remaining surface pressure to maintain adhesion conditions. The tread bar elements slide back to their original position while the belt also moves back in the direction of the tire main plane, with the sliding distance consisting of the formerly present lateral deflection of the tire belt and the tread bar elements. A schematic representation of the processes can be found in Figure A.2. The lateral slip required to apply a lateral force is ultimately significantly higher than the longitudinal slip required to apply an equivalent longitudinal force. Accordingly, the higher emission at lateral force is primarily due to the slip ratio required to achieve that lateral force. If the emissions were not compared for equivalent longitudinal and lateral forces but rather for equivalent slip ratios, it is likely that the emissions would be more similar.

The second reason is the tread geometry of summer tires, which differs in longitudinal and lateral direction. The tread pattern of the summer tire is divided in lateral direction by wide (circumferential) grooves, while in the longitudinal direction there are only few or no (transversal) grooves to divide the profile but only narrow sipes (see Figure A.4). The almost continuous longitudinal ribs result in very little deformation and edge wear when subjected to longitudinal force. By contrast, if lateral force is applied, the ribs are deformed transversely to their direction of expansion, resulting in greater deformation and more edge wear. Considering the entire tread pattern, including the center and shoulder rows, results in an overall longitudinal and lateral tread stiffness. Since the difference in emission factors under longitudinal and lateral force is particularly pronounced for the summer tire, it is assumed that the difference between the stiffness in the longitudinal and lateral directions is also particularly large. However, it is also evident to a lesser extent for the all-season and the winter tire (see section 5.1.5). Furthermore, positive lateral force results in higher emission factors than negative lateral force. This asymmetry was present in all detailed investigations of the

influencing parameters, which this summer tire was used for. For the summer tire, the effect can be attributed to the equally asymmetrical curve progression of frictional power (see section 5.1.1.4). However, for most other cases, positive lateral force also resulted in higher emissions than equivalent negative lateral force. Therefore, the asymmetry was further investigated with non-directional (inside/outside) tires, driving the tires in both rotational directions (reverse-mounted tire on the rim) and applying positive and negative lateral force. It was found that the mean values of the emissions in both rotational directions were higher for positive lateral force than for negative lateral force.

There are two possible explanations for this difference: one caused by the tire and another one by the test bench. The contribution of the tire to the asymmetrical emission curve could be caused by the tire structure. Radial tires always contain a two-plied belt of steel cords which cross at a certain angle [89, 127]. For the lateral force of the tire, it is decisive which ply of the belt is the outer one. The so-called ply-steer effect influences the residual cornering force (RCF), which describes the lateral force occurring when driving straight ahead without any slip angle. The force caused by the ply-steer effect usually points to the right in driving direction. To apply lateral force to the left (positive according to Figure 4.1), the RCF must first be equalized. Therefore, a larger slip angle is required than to apply a force of the same magnitude to the right (negative). Larger slip angle means higher proportion of sliding slip, which presumably leads to higher PM emissions. This effect remains unaffected by turning the tire on the rim. Therefore, the explanation is supported by the results of the previously described investigation of the rolling direction's effect on emissions.

However, the investigation of the influence of rolling direction did not only show that positive lateral force leads to higher emissions than negative lateral force, but also that the emissions for positive lateral force and different rolling direction differ from each other, as do those for negative lateral force. One possible reason for that is the conicity effect, which also influences the RCF. Unlike the ply-steer effect, the influence of the conicity effect is reversed when the rolling direction is changed (by turning the tire on the rim), which leads to a change in the RCF and thus explains a difference in emissions.

Another possible reason is the influence of the test bench design. Positive lateral force corresponds to a left-hand bend in the internal drum test bench (see chapter 4). This means that the airflow caused by the rotation of the drum hits the right outer side of the wheel. If particles are emitted on the right side of the tire–road contact, they will be driven into the extraction funnel, and the airflow will contribute to a higher extraction efficiency. The high flow velocity on the right side of the drum is due to the fact that the right side is the rotating part of the drum (see section 3.1). On the other hand, if the wheel is steered to the right, corresponding to negative lateral force, the airflow should hit the outer left side of the wheel. The difference, however, is that the airflow on the non-rotating left side of the test bench is significantly slower. If particles are emitted on the left side of the tire–road contact, they will partially bypass the extraction funnel.
The observed differences in emissions are presumably the result of a combination of all the described effects. Since none of them could be confirmed conclusively, only the mean values of emissions with positive and negative lateral force were used for the determination of the prediction model (see section 6.2).
As with longitudinal force, the results regarding the influence of lateral force are consistent with the literature. Although the increases determined here are significantly higher than those reported by Park et al. [98], it must be taken into account that their tests were performed on sandpaper, which means that there was no realistic tire–road contact. Foitzik et al. [37] considered both a quadratic and an exponential relationship to be possible, so that the fourth-order relationship found here fits well. Furthermore, the statement of Feißel et al. that lateral force has a stronger influence on the emission than longitudinal force [36] is confirmed. In analogy to the longitudinal force or longitudinal dynamics, low lateral dynamics or low cornering speeds are therefore a possibility to reduce PM emissions.

5.1.1.3 Combined Force (Parallel to the Road Surface)

To get an impression of how the emission evolves when the tire is loaded with longitudinal and lateral force, conditions were tested which consisted of forces in both directions. The resulting force F_{res} was calculated according to Equation 5.1

from the two components longitudinal force F_x and lateral force F_y. Figure 5.4 shows the influence of combined forces on the emission factor. Since the effect of unequal emission at positive and negative lateral force (see section 5.1.1.2) was also present here, only one curve progression is shown, which represents mean values of both combinations in negative and positive longitudinal direction, respectively. Even though the resulting force cannot take negative values according to Equation 5.1, the combined forces with a negative longitudinal component are plotted in the negative range for better visualization.

$$F_{res} = \sqrt{{F_x}^2 + {F_y}^2} \tag{5.1}$$

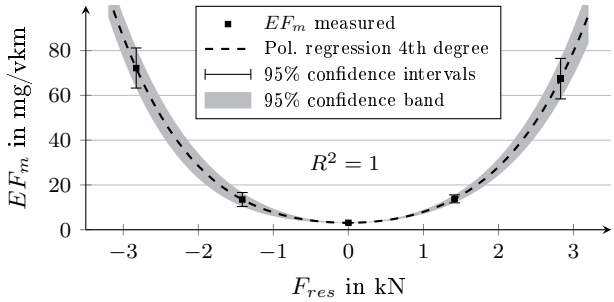

Figure 5.4: Emission factors in the size range between $0.3\,\mu\mathrm{m}$ and $10\,\mu\mathrm{m}$ over combined force and regression function for a summer tire at a wheel load of $6.5\,\mathrm{kN}$, a driving speed of $80\,\mathrm{km/h}$, an inflation pressure of $2.6\,\mathrm{bar}$, an ambient temperature of $25\,^\circ\mathrm{C}$, and an SRT value of 60 [Adapted from 112].

Since fewer load conditions were measured on the diagonals (equal shares of longitudinal and lateral force, see Figure 4.2) than with pure longitudinal and pure lateral force, the graph in Figure 5.4 contains only three support points for positive and negative resulting force, respectively. Nevertheless, fourth-order functions were chosen for regression as it was assumed that combined forces have the same effect on the emission as the two underlying forces. Again, the passage through the emission value for a free-rolling tire without lateral force was enforced. Combining the small number of support points with a fourth-order regression function results in a coefficient of determination of 1.

The statements made for longitudinal and lateral force also apply here: For moderate forces, there is only a slight increase in emission, although it is higher than for pure longitudinal and lateral force due to the lower number of support points. The emission increases progressively as the force increases. For the highest force, this results in emission factors of about $70\,\mathrm{mg/vkm}$. Note that the highest resulting force applied was lower than for pure longitudinal and lateral force, which is reflected in the changed abscissa compared to the previous graphs.

5.1.1.4 Correlation with Sliding Slip

Further investigations were carried out to explain the previously described relationships between tire forces parallel to the road surface and PM emissions. Using the same tire model as before, a lateral-force-slip-angle curve was recorded as depicted in Figure 5.5 for the range of slip angles between $-10°$ and $10°$.

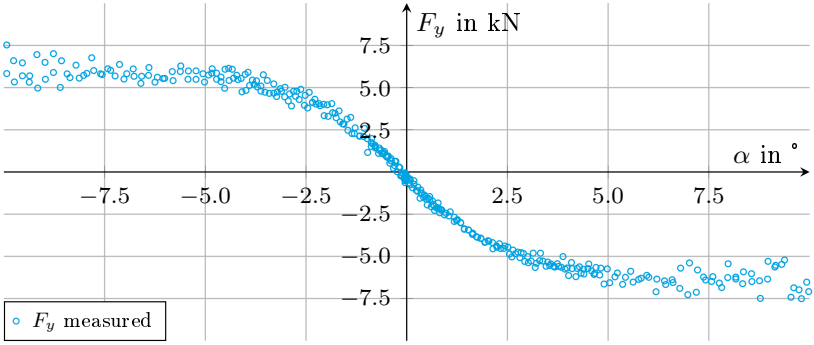

Figure 5.5: Measured correlation between lateral force and slip angle of a summer tire at a wheel load of $6.5\,\mathrm{kN}$, a driving speed of $80\,\mathrm{km/h}$, an inflation pressure of $2.6\,\mathrm{bar}$, and an ambient temperature of $25\,°\mathrm{C}$.

The curve progression was approximated in a smaller range using a fifth-order regression function (see Figure 5.6). Note that the axes from Figure 5.5 to Figure 5.6 have been swapped, meaning that the regression function obtained describes the

slip angle as a function of the lateral force. Moreover, the diagram shows a tangent to the regression function at $\alpha = 0°$, thus showing the gradient in the linear range of the slip-angle-lateral-force curve. Hence, the tangent corresponds to the slip angle associated with pure deformation of tread bar elements and the sidewall of the tire (deformation slip, see section 2.4).

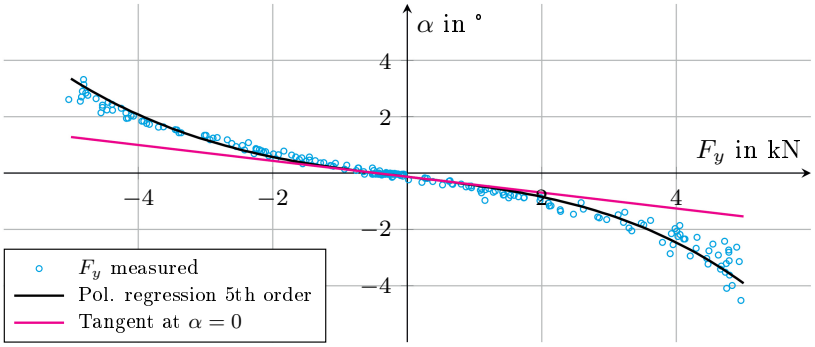

Figure 5.6: Inverted correlation between lateral force and slip angle of a summer tire at a wheel load of 6.5 kN, a driving speed of 80 km/h, an inflation pressure of 2.6 bar, and an ambient temperature of 25 °C with polynomial regression in the range between −5 kN and 5 kN and tangent to the regression curve at a slip angle of 0°.

Consequently, the difference between the regression function and the tangent corresponds to the proportion of slip angle associated with sliding of the tread bar elements (sliding slip, see section 2.4). The function of the difference shows a parabolic shape over lateral force. It can be used to calculate the friction power generated by sliding slip. For this purpose, the sliding speed of tread bar elements is first calculated from the proportion of slip angle due to sliding and the driving speed according to Equation 2.4. After, the frictional power is calculated from the sliding speed and the lateral force acting on the tire according to Equation 2.7b. This is plotted in Figure 5.7 together with the PM emission over lateral force.
The curve progressions of emission factor and frictional power are almost identical, which means that PM emission is indeed correlated with the frictional power generated by the sliding of tread bar elements. Furthermore, the frictional power has an asymmetric curve progression as well, thus explaining the asymmetric

emissions of the summer tire described in section 5.1.1.2. Whether the asymmetry of the emission curves of the other tire types is also completely attributable to the friction power or whether the test bench flow contributes to this could not be fully clarified.

The same investigation was to be made for the relationship between PM emission and frictional power due to sliding tread bar elements in the longitudinal direction. However, due to the high wheel load of 6.5 kN, it was not possible to apply a sufficiently high longitudinal force at the internal drum test bench in order to record a complete longitudinal-force-slip curve.

The relationship found here between tire forces parallel to the road surface and PM emission is described by a fourth-order function and thus differs in the exponent from Schallamach's wear formula (see section 2.5). However, this formula (Equation 2.8) refers to the complete tire wear, while the correlations found here only consider particles smaller than 10 µm. Furthermore, according to the author (Schallamach), his formula only applies to low slip ratios, which were clearly exceeded in the tests performed in this work. The differences are therefore quite possible, so that the findings in this work do not contradict Schallmach's wear formula.

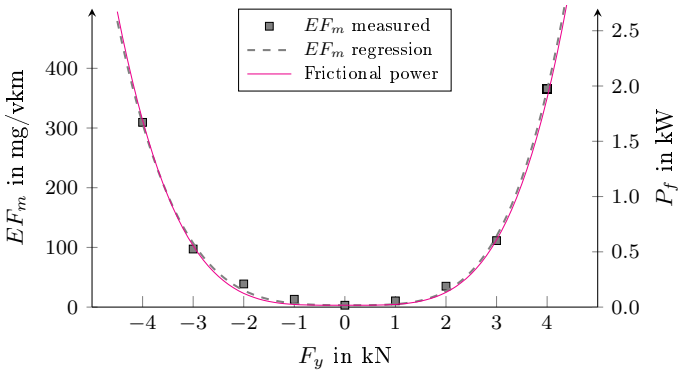

Figure 5.7: Correlation between friction power due to sliding slip and emission factor for a summer tire at a wheel load of 6.5 kN, a driving speed of 80 km/h, an inflation pressure of 2.6 bar, and an ambient temperature of 25 °C.

5.1.2 Wheel Load

The influence of wheel load on tire–road PM emissions plays an important role in the current electrification process. (Battery) Electric vehicles have significantly higher unladen masses than comparable vehicles with internal combustion engines. Due to the design of the electric motor, this is accompanied by a higher drive torque, which is already available when the vehicle is starting off. The higher torque allows for higher driving forces, which according to the relationships shown in section 5.1.1.1 lead to higher PM emissions. Furthermore, to maintain or even improve vehicle dynamics, more powerful engines are installed, resulting in even higher tire–road contact forces.
In order to quantify the influence of wheel load on the emission of tire–road PM under these aspects, the applied longitudinal forces were varied in proportion to the wheel load (see section 4.1). This means that the emission factors obtained are to be understood as emissions of a whole vehicle that is driven with consistent longitudinal dynamics (same longitudinal acceleration, consistent adhesion utilization) but with additional wheel load. The results are shown in Figure 5.8— Figure 5.8a shows the emission factors for braking forces (negative adhesion utilization), while Figure 5.8b shows those for driving forces (positive adhesion utilization).
Symbols of same color represent emission factors with same adhesion utilization at different wheel loads. The regression functions reveal a linear relationship between wheel load and emission factor, regardless of the sign of the adhesion utilization. The adhesion utilization only affects the gradient of the resulting straight line. Additionally, a comparison of the graphs for driving and braking shows again that braking forces result in higher emissions than equivalent driving forces. The responsible effect was explained in section 5.1.1.1.
The linear increase in emission factors as the wheel load increases can be explained by the resulting frictional energy. When the wheel load is increased, the tire is deflected stronger, resulting in a more pronounced flattening. This means that the contact area between tire and road increases approximately linearly with wheel load, provided that the tire inflation pressure is kept constant. The increase occurs mainly in the longitudinal direction of the tire [107]. The increased

wheel load is thus distributed over an area that has increased to approximately the same extent, so that the contact pressure remains almost constant. The level and characteristics of the shear stress that ultimately occurs in relation to the size of the contact area is therefore also almost consistent. The ratio of deformation slip to sliding slip therefore remains unchanged. Thus, the emission increases proportionally to the contact area between tire and road surface as long as the tire inflation pressure is not changed.

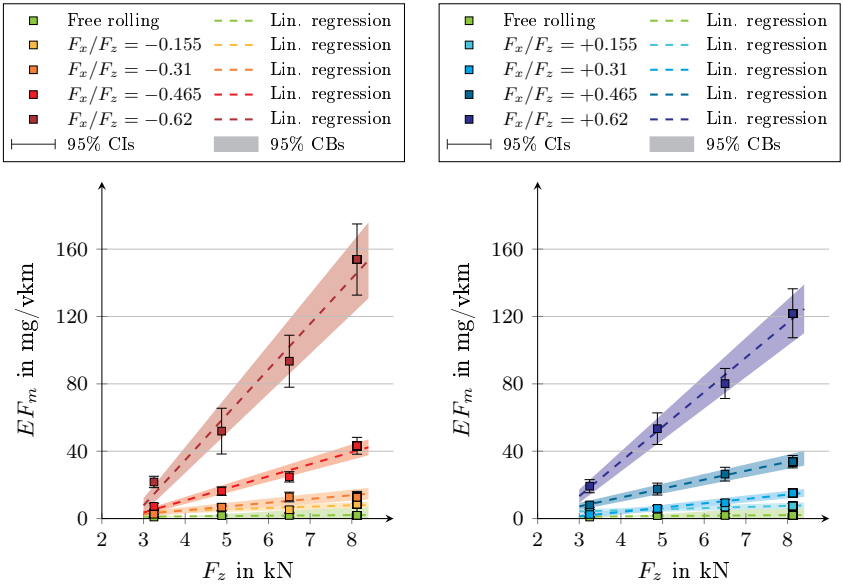

(a) Braking condition

(b) Driving condition

Figure 5.8: Influence of wheel load on the emission factor at different adhesion utilizations in the longitudinal direction F_x/F_z for a summer tire at a driving speed of 80 km/h, an inflation pressure of 2.6 bar, an ambient temperature of 25 °C, and an SRT value of 60: (a) Braking condition and (b) Driving condition [Adapted from 114].

This means an enormous emission potential for fleet electrification. Assuming consistent longitudinal dynamics (adhesion utilization), an increase in vehicle mass results in a significant increase in emission factors. If the electric motors

used have torques that allow them to even exceed the longitudinal dynamics of comparable combustion vehicles, this can result in an additional increase.
The correlations obtained, as well as numerous results in the literature, demonstrate the enormous influence of wheel load on PM emissions. Consistent with the literature, positive linear correlations between wheel load and emissions are obtained here. This statement is independent of adhesion utilization. However, the gradient of the straight line describing the relationship between wheel load and PM emissions increases with adhesion utilization. This means that the influence of wheel load increases as the adhesion utilization is increased. Therefore, both an anticipatory driving style as well as lighter vehicles can help reduce PM emissions from tire–road contact.

5.1.3 Inflation Pressure

The results on the influence of tire inflation pressure on PM emissions are shown in Figure 5.9. The emission factor is plotted in normalized form for better comparability between different types of load. Normalization has been done with reference to the emission factor at $2.6\,\mathrm{bar}$ in the respective load condition. Figure 5.9b and Figure 5.9c show the influence of inflation pressure under longitudinal force, the influence under lateral forces can be seen in Figure 5.9e and Figure 5.9f. Figure 5.9a and Figure 5.9d are identical and are only shown twice for better comparability of the gradient when loaded in different directions.
The support points show the emission factors obtained from the measurements and subsequent calculations. Regression functions show a positive linear relationship between tire inflation pressure and PM emissions, with linearity independent of load condition. As with the change in wheel load, this increase can be attributed to changes in and on the tire tread. However, unlike wheel load, inflation pressure has an inversely proportional effect on the contact area. Accordingly, higher inflation pressure results in an inversely proportional smaller (basically shorter) tire contact area. However, the same tire forces parallel to the road surface must be transmitted over the smaller contact area, resulting in higher shear stress.

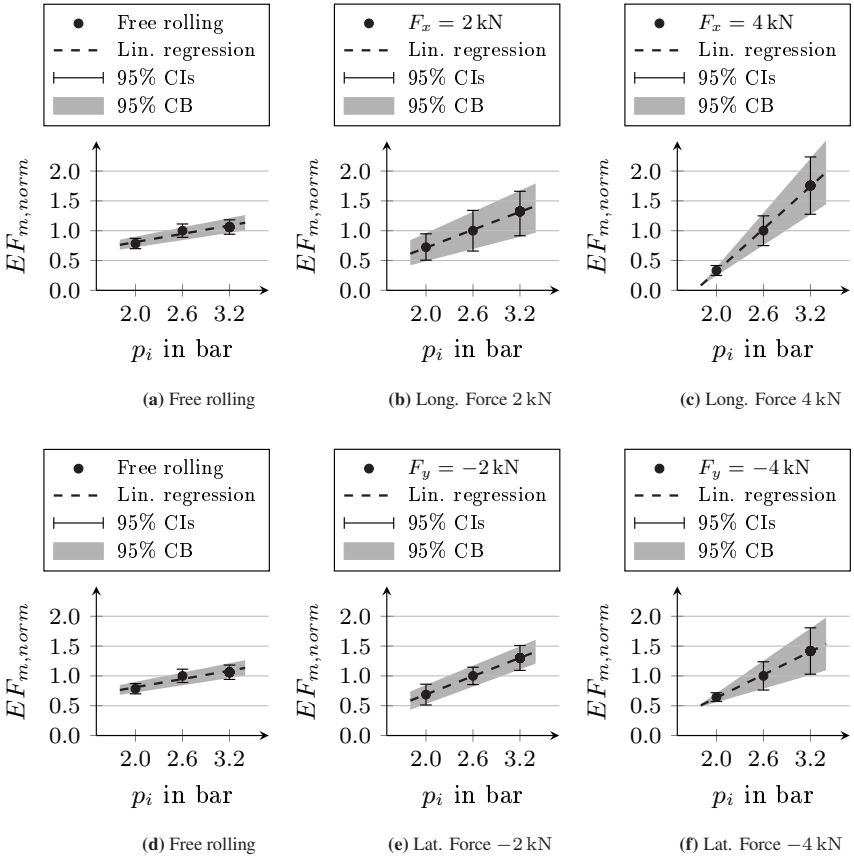

(a) Free rolling **(b)** Long. Force 2 kN **(c)** Long. Force 4 kN

(d) Free rolling **(e)** Lat. Force −2 kN **(f)** Lat. Force −4 kN

Figure 5.9: Influence of tire inflation pressure on the emission at different load conditions for a summer tire at a wheel load of 6.5 kN, a driving speed of 80 km/h, an ambient temperature of 25 °C, and an SRT value of 60 [Adapted from 114].

Despite the overall shorter contact area, this results in longer sliding distances for the individual tread bar elements, which can be explained by the higher slip required. A superlinear dependence of PM emissions on tire inflation pressure would actually be expected due to the combination of the two effects. However, there is apparently another compensating effect, so linear increases in emissions occur with increasing tire inflation pressure. The gradient depends strongly on

the tire force and its direction.
While the gradient (influence of inflation pressure on the emission factor) is small in the free-rolling condition (Figure 5.9a), it increases significantly with increasing longitudinal force (Figure 5.9b and 5.9c). This is probably due to the fact that the ratio between the longitudinal force due to sliding slip and the longitudinal force due to deformation slip increases with increasing longitudinal force and tire inflation pressure. In detail, two effects are involved. On the one hand, at constant wheel load, higher tire inflation pressure results in a smaller tire contact patch. This in turn reduces the longitudinal force, assuming the slip ratio remains constant. In addition, the maximum shear stress decreases with increasing inflation pressure and constant slip ratio. Both result in a flatter curve for the relationship between longitudinal force and slip ratio [43]. Therefore, a higher slip ratio is required to achieve the same longitudinal force at higher tire inflation pressure. The difference in slip ratio for different inflation pressures is amplified by the degressive nature of the (total) longitudinal force (see Figure A.3).
On the other hand, the ratio between the longitudinal force caused by sliding slip and that caused by deformation slip also changes with slip ratio. At low slip ratios, the force is mainly caused by deformation slip, while the proportion of sliding slip is very small. It only increases gradually with increasing slip ratio [153]. The combination of both effects leads to a continuously increasing ratio between the amount of sliding slip and deformation slip (see Figure A.3) as longitudinal force and tire inflation pressure increase. The increase in slip ratio ultimately causes higher emissions. Therefore, the influence of inflation pressure increases as the longitudinal force increases.
In contrast, the influence of inflation pressure on PM emission is smaller when lateral force is applied (Figure 5.9e and 5.9f). Due to the smaller contact area at higher inflation pressures, the stiffness of the tread decreases in the same manner as in longitudinal direction. An opposite effect occurs because the tire carcass and belt become stiffer in lateral direction and therefore deform less with increasing inflation pressure. Because of the reduced belt deformation, the absolute displacement of the tread relative to the wheel center plane increases less than for equivalent force in longitudinal direction. As the two effects overlap, they partially compensate each other and the lateral stiffness decreases only slightly with

increasing inflation pressure. The smaller change in lateral stiffness compared to longitudinal stiffness results in a smaller difference in lateral slip between the total force curves at different tire inflation pressures. The diagrams show that the effect described for longitudinal force is also present here, but to a lesser extent, so that the gradient of the emission factor increases only slightly with increasing inflation pressure.

At first glance, it seems implausible that PM emissions increase with increasing tire inflation pressure. It seems more logical that higher inflation pressure leads to lower vertical deformations, thus to lower rolling resistance and lower (basic) shear stresses, and ultimately to less tire wear. This relationship is known at least for tire wear (see section 1.2.3). However, it is important to note that the particles measured here do not consist exclusively of tire material. A significant proportion of particles comes from the road (see section 4.3.2). In addition, as tire inflation pressure increases, the frictional processes between tire and road surface take place in a smaller contact area and are therefore more intense. Together with the processes described in section 5.1.1.4, this explains the results presented here.

Since both increasing tire inflation pressure and increasing wheel load lead to higher surface pressure (or since both decreasing tire inflation pressure and decreasing wheel load lead to lower surface pressure)—albeit to a very different extent—a comparison should be made between the effect of both influencing parameters on PM emissions. For example, if wheel load (see Figure 5.8) is increased by $25\,\%$ from $4\,\mathrm{kN}$ ($408\,\mathrm{kg}$) to $5\,\mathrm{kN}$ ($510\,\mathrm{kg}$), there will be an increase in emissions depending on the load condition. In the free-rolling condition, it is $14\,\%$ and grows with increasing adhesion utilization, which leads to an increase of $69\,\%$ (mean value of positive and negative longitudinal force) at an adhesion utilization of 0.62. To achieve a comparable growth in emissions by changing tire inflation pressure, an increase of $23\,\%$ from $2.6\,\mathrm{bar}$ to $3.2\,\mathrm{bar}$ would be required for both free rolling and maximum longitudinal force (mean value of positive and negative longitudinal force). This means that not only do both wheel load and tire inflation pressure influence surface pressure, but that their effects on PM emissions are of a similar order of magnitude. This is surprising, as it is not the case for the effect on surface pressure itself. While the surface pressure changes

almost proportionally to tire inflation pressure, the influence of wheel load on surface pressure is smaller as the size of the contact area also changes.

5.1.4 Driving Speed

When comparing emissions at different driving speeds, it is especially important to consider emission factors (per distance) rather than particle concentrations or raw emissions (per time). This is as particle concentrations measured at the internal drum test bench were significantly higher at high driving speeds than at low speeds. However, when considering distance traveled rather than time, the proportions changed so that a more differentiated picture emerges for the dependence of the emission factor on driving speed.

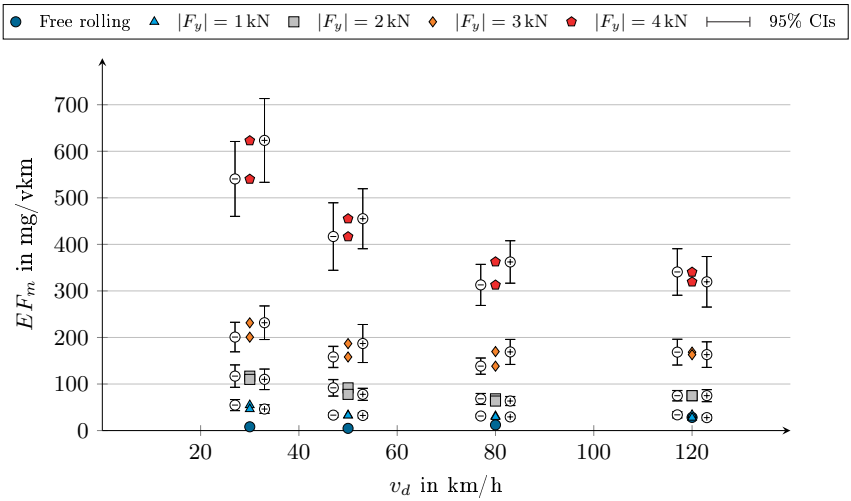

Figure 5.10: Influence of driving speed on the emission at different lateral forces for a summer tire at a wheel load of 6.5 kN, an inflation pressure of 2.6 bar, an ambient temperature of 25 °C, and an SRT value of 60.

The results of the test series on the influence of driving speed are shown in Figure 5.10. Same symbols indicate emission factors recorded at same lateral force

and at different driving speeds. In the free-rolling condition, the emission factor increases slightly with driving speed. However, a contrasting picture emerges for all load conditions with lateral force. For all lateral forces, the highest emission factor is present at the lowest driving speed. With increasing speed, it decreases and reaches a minimum at $80\,\mathrm{km/h}$. The emission factors for 120 km/h are slightly higher again.

The resulting curve progressions of the emission factor over driving speed cannot be explained conclusively. This would require further detailed testing combined with a model-based approach to clarify the processes responsible for tire–road PM emissions and to accurately analyze their dependence on driving speed. Since this means that no clear trend can be determined at this point, the use of regression functions is omitted. Nonetheless, possible approaches to explain the processes are discussed in the following.

As measurements were performed several times with same results, it is possible that there is a real tire phenomenon causing the ambiguity. However, it is also conceivable that it is due to interferences from the test bench environment. After preliminary tests had shown that a decreasing extraction efficiency was to be expected at high driving speeds ($v_d > 100\,\mathrm{km/h}$) (see section 3.2.1.2), a specially designed extraction hood (see section 3.2.1.2) was used for the test series on the influence of driving speed instead of the extraction funnel. Although this resulted in a significant improvement, it cannot be proven that afterwards the extraction efficiency was completely unaffected by driving speed. It is possible that the higher flow velocity in the drum at high driving speeds still caused particles to pass under the extraction hood and not to be captured. However, this cannot explain the large decrease in emission factor between $30\,\mathrm{km/h}$ and $50\,\mathrm{km/h}$. Therefore, it is quite possible that the curves of emission factor and the occurring minimum are actually caused by a speed-dependent effect of the tire.

The tire rolling faster means that there is less time for the rubber to penetrate microscopic depressions in the road surface. This presumably reduces the damage to the tire material caused by shear forces. On the other hand, higher driving speed with constant force parallel to the road surface leads to higher sliding speed, which should increase the emission. Apparently, however, the first effect is larger at low driving speeds, which is reversed at higher speeds.

The increase in emissions between $80\,\mathrm{km/h}$ and $120\,\mathrm{km/h}$ could also be due to increasing centrifugal forces. This causes the tire to become stiffer, though reducing the flattening, so that the resulting effect is similar to that of an increase in tire inflation pressure. Here too (see section 5.1.3), higher emissions were observed, which was attributed to longer sliding distances and higher shear stress.

5.1.5 Tire Type

The parameters described in the previous sections are primarily influenced by the vehicle and the driver. In addition, there are other influences over which the driver has only limited control. One such influence is the choice of tires. Although the drivers can choose tires for their vehicle, the choice is limited in that the tire type must be adapted to environmental conditions. Accordingly, there is a choice between summer, all-season and winter tires.

In order to investigate the extent to which these tire types differ in terms of emission behavior, a test series was carried out with one tire of each type. All three tires had the same dimension and the same load index. In contrast to previous test series, the aim was no longer to quantify the influence of a particular parameter on PM emissions, but rather to compare the emissions of the tire types under same load conditions.

To make this comparison, the tires were subjected to various longitudinal and lateral forces while maintaining constant wheel load, tire inflation pressure, and driving speed. To account for the fact that summer tires are used at higher ambient temperatures than winter tires and to make the comparison as realistic as possible, the tires were tested at different ambient temperatures: $25\,^{\circ}\mathrm{C}$ for summer tires and $5\,^{\circ}\mathrm{C}$ for winter tires meaning that both tires were tested under their usual ambient conditions. Since all-season tires are used in both high and low ambient temperatures, they were tested at both temperatures. The emission factors for the all-season tire shown in Figure 5.11 are therefore mean values of emission factors at both temperatures.

Winter tires produce the highest emissions, summer tires the lowest ones, and the emissions of all-season tires are in between. This is true for both the free-rolling

condition and the conditions in which the tires were subjected to longitudinal forces. As with summer tires, all-season and winter tires show only a slight increase in emissions at moderate forces, which increases with increasing forces. It can therefore be assumed that the fourth-order approach for the relationship between force and PM emissions found for summer tires also applies to all-season and winter tires. However, further studies are needed to make a definitive statement on this. As with summer tires, braking forces always result in slightly higher emissions than driving forces for the other two tire types, so this effect is likely to be tire-independent (for explanation see section 5.1.1.1 and Figure A.1 in Appendix A.3). For the highest braking forces, this results in emission factors above $350\,\mathrm{mg/vkm}$ for the all-season tire and above $600\,\mathrm{mg/vkm}$ for the winter tire. Emissions at maximum load are therefore about a factor of 3.6 and 6 higher than for the summer tire at equivalent load, respectively.

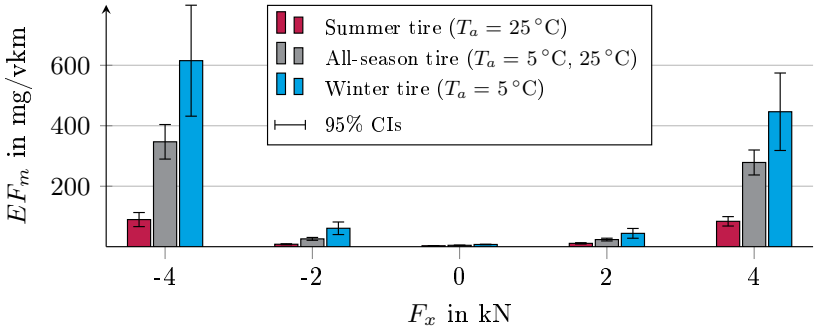

Figure 5.11: Influence of longitudinal force on the emission factors of a summer, an all-season, and a winter tire at their usual ambient temperatures, a wheel load of 6.5 kN, a driving speed of 80 km/h, an inflation pressure of 2.6 bar, and an SRT value of 60 [Adapted from 111].

The qualitative statements regarding the influence of longitudinal force apply in the same way to the influence of lateral force shown in Figure 5.12. Again, the winter tire produces the highest emissions, followed by the all-season tire and finally the summer tire. However, the overall emission level is higher, resulting in

maximum emission factors of over 500 mg/vkm for the all-season tire and over 1000 mg/vkm for the winter tire.

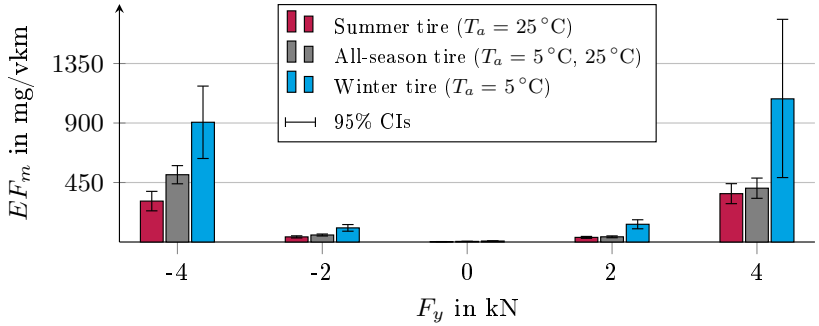

Figure 5.12: Influence of lateral force on the emission factors of a summer, an all-season, and a winter tire at their usual ambient temperatures, a wheel load of 6.5 kN, a driving speed of 80 km/h, an inflation pressure of 2.6 bar, and an SRT value of 60 [Adapted from 111].

However, the emission behavior of all-season and winter tires differs from that of summer tires in two ways. On the one hand, negative lateral forces result in higher emissions for all-season tires. This suggests that the test bench effect leading to asymmetric emissions under lateral force (see section 5.1.1.2) is relatively small, as it can be clearly outweighed by the influence of the tire. On the other hand, the comparison of Figure 5.11 and Figure 5.12 shows that the emissions of the different tire types evolve differently depending on force direction. While the summer tire under the influence of longitudinal force leads to emission factors which are lower by a factor of 3.6 or 6 than those of the all-season or winter tire, under the influence of lateral force this factor is only 1.4 and 2.9 for the all-season and winter tire, respectively. The influence of force direction on the emissions of the all-season and winter tire is smaller than for the summer tire and the magnitude of the force is more important for the emission. Accordingly, there is only a factor of 1.5 between the emissions at maximum load in lateral and longitudinal direction for the all-season tire and 1.9 for the winter tire. With the summer tire, on the other hand, force direction has a significant influence, so

that there is a factor of 3.9 between the emissions under the maximum load in different directions (see section 5.1.1.2).
Possible reasons for the direction-dependent emission behavior of the summer tire were discussed in section 5.1.1.2. The fact that the difference is much less pronounced for the all-season and the winter tire is probably due to the geometry of the tread profile. Unlike summer tires, these two tire types have larger and deeper (transversal) grooves in lateral direction (see Appendix A.4). This creates individual tread blocks which are further subdivided by fine sipes. The tread blocks can therefore tilt or deform independently of each other and of the force direction. The overall tread stiffness also introduced in section 5.1.1.2 probably differs significantly less for these two tire types in the longitudinal and lateral directions. Forces in both longitudinal and lateral directions therefore result in greater deformation and higher edge wear.
The ratios between summer and winter tire emissions obtained from the tests are in the same range as found in the literature. While factors between 2 and 10 were given for emission values there, here this range is between 2 and 6. For a comparison of the results with the emissions of the all-season tire no reference values could be found. However, it seems plausible that its emission values are between those of the summer and the winter tire.

5.1.6 Ambient Temperature

In order to evaluate the influence of ambient temperature on the emission behavior of the three tire types, the summer and winter tire were also tested at temperatures that are unusual for them. The resulting comparisons of emissions for all tire types at ambient temperatures of 5 °C and 25 °C are shown in Figure 5.13 to 5.15.
In the case of the summer tire (see Figure 5.13), higher ambient temperature leads to higher emissions for both high longitudinal and high lateral forces. Note that the difference in emissions between low and high ambient temperature is higher for longitudinal force than for lateral force. Therefore, the ratio between the emissions at maximum lateral force and those at maximum longitudinal force increases from 3.9 to 5 when lowering the ambient temperature. At moderate forces, however,

the ratio is reversed so that the emission is higher at low temperature. There is currently no explanation for this trend reversal, so further test series are needed for clarification.

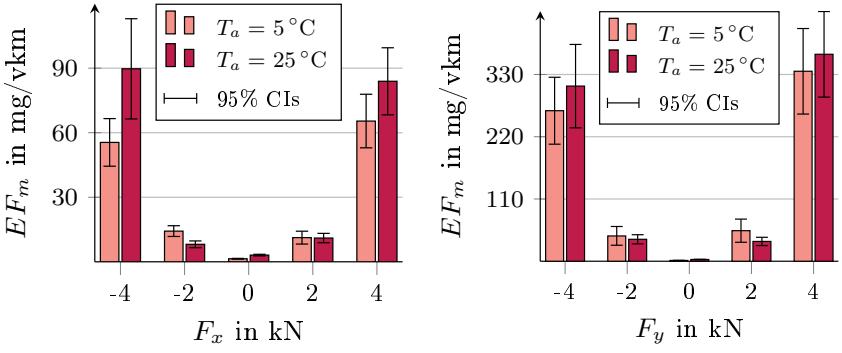

(a) Longitudinal force

(b) Lateral force

Figure 5.13: Influence of ambient temperature on the emission factors of a summer tire due to longitudinal force and lateral force, a wheel load of 6.5 kN, a driving speed of 80 km/h, an inflation pressure of 2.6 bar and an SRT value of 60.

The all-season tire (see Figure 5.14) shows a completely opposite influence of ambient temperature. While the emission at low temperature and maximum force is higher than the one at high temperature, higher temperature leads to higher emission at moderate forces. The factor between the emission at maximum lateral force and that at maximum longitudinal force only changes from 1.5 (at 25 °C) to 1.4 (at 5 °C), which is considered negligible.

The behavior of the winter tire is similar (see Figure 5.15). In most cases, the higher ambient temperature results in lower emissions. However, there are three exceptions: for moderate negative longitudinal force as well as for moderate and high positive longitudinal force, the emissions are slightly higher at 25 °C. However, the differences are so small that they are covered by the confidence intervals. Further on, it is noticeable that the influence of ambient temperature seems to be significantly greater for lateral force than for longitudinal force. The ratio between emissions at maximum lateral force and maximum longitudinal

force of 1.9 at 5 °C thus decreases to 1.3 at 25 °C. As for the summer tire, there is currently no explanation for this trend, so the tire-specific temperature influence on PM emission needs to be further investigated in future tests.

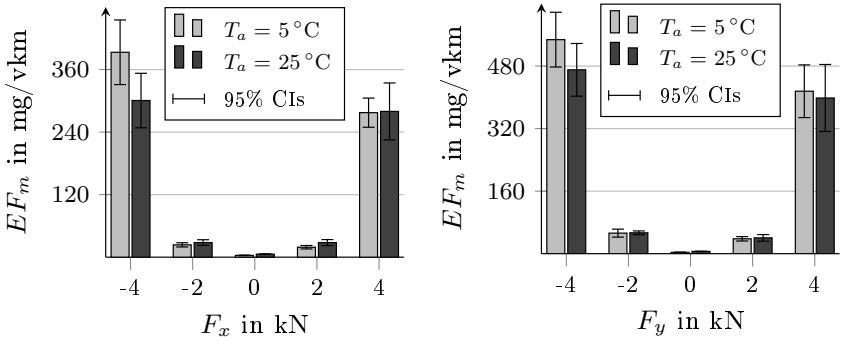

(a) Longitudinal force

(b) Lateral force

Figure 5.14: Influence of the ambient temperature on the emission factors of an all-season tire due to longitudinal force and lateral force, a wheel load of 6.5 kN, a driving speed of 80 km/h, an inflation pressure of 2.6 bar, and an SRT value of 60.

The different evolution of emissions with ambient temperature is probably due to the different tire compounds. The summer tire is made of the hardest compound, whose stiffness changes only slightly over the investigated temperature range. This is due to the fact that the low temperature of 5 °C is only slightly outside the usual temperature range for the summer tire. Nevertheless, the material becomes more brittle at low temperatures, which could lead to the tire emitting finer particles (see section 5.2.6), whose contribution to PM emissions is low.
Both winter and all-season tire are made from compounds that are significantly softer than the one of the summer tire, especially at low ambient temperature. In addition, the ambient temperature of 25 °C is well outside the range recommended for winter tires by the General German Automobile Club (Allgemeiner Deutscher Automobilclub, ADAC) [5]. The resulting even softer tread tends to emit less fine particles (see Figure 5.13), but rather favors the formation of large particles which are outside the size range detected by the aerosol spectrometer. For this

reason, the effect is not reflected in the size distributions shown in section 5.2.6. However, the hypothesis is supported by the evaluation of the total mass loss of tire material. This shows that for all three tire types the wear is greater at high temperatures than at low temperatures. The difference between the mass loss at different ambient temperatures is particularly pronounced for the winter tire. For the all-season tire it is smaller and negligibly small for the summer tire.

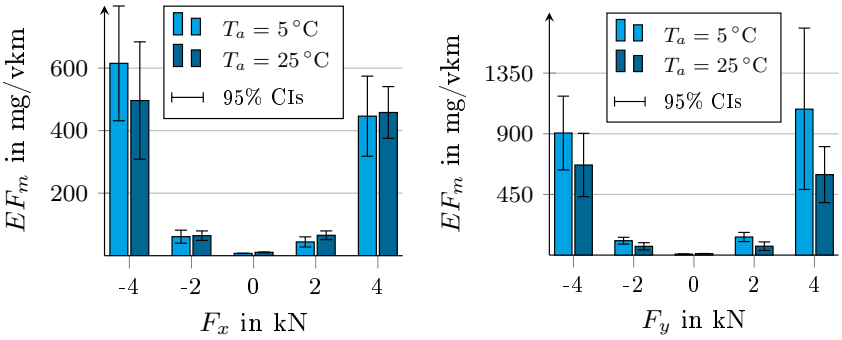

(a) Longitudinal force

(b) Lateral force

Figure 5.15: Influence of the ambient temperature on the emission factors of a winter tire due to longitudinal force and lateral force, a wheel load of 6.5 kN, a driving speed of 80 km/h, an inflation pressure of 2.6 bar, and an SRT value of 60.

The results presented for the influence of ambient temperature on PM emission are consistent with the literature. Yan et al. [151] do not specify whether their custom rubber compound is a summer or winter tire compound. Chang et al. [21] do not indicate the type of tires used in their tests. Therefore, it can only be assumed that the rubber compound used by Yan et al. was a winter tire compound, while Chang et al. used summer tires. In this way, the different trends can be reconciled with each other and with the results obtained here.

5.1.7 Pavement Material

In order to determine the influence of pavement material, an analogous test series to the one in section 5.1.5 (influence of tire type) was performed on a concrete surface. Since the focus was exclusively on the influence of pavement material, all tests were performed at an ambient temperature of 25 °C. The results for the three different tire types are shown in Figure 5.16 to 5.18.

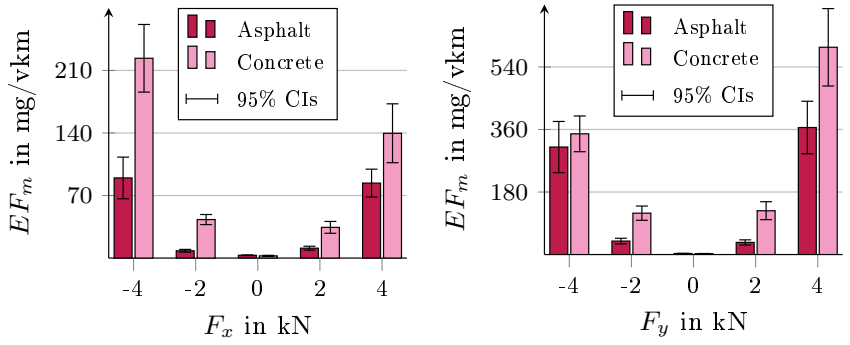

(a) Longitudinal force

(b) Lateral force

Figure 5.16: Influence of pavement material on the emission factor of a summer tire due to longitudinal force and lateral force, a wheel load of 6.5 kN, a driving speed of 80 km/h, an inflation pressure of 2.6 bar, an ambient temperature of 25 °C, and an SRT value of 60.

Figure 5.16 shows the comparison of emissions on different road surfaces for the summer tire under the influence of longitudinal and lateral force. For consistent SRT values the concrete surface results in higher emissions than the asphalt surface for all load conditions. For longitudinal forces, there are factors between 1.6 and 5.5 between the emission on asphalt and the one on concrete. It is worth noting that the higher factors occur at moderate forces, which means that concrete leads to a greater initial increase in emission with force, which then increases less than on asphalt. This is also true for lateral forces. Another similarity between the two diagrams is the asymmetry between emissions caused by driving and braking or between positive and negative lateral force. This inequality remains the same or

even increases compared to the emission on asphalt. The exact difference depends on the load condition.

When comparing the two diagrams (Figure 5.16a and 5.16b), it is also noticeable that the emission increases significantly stronger under longitudinal force than under lateral force when changing from asphalt to concrete. Thus, the ratio between the mean emissions under maximum lateral and longitudinal forces on concrete is 2.7, while on asphalt it was 3.9.

An analogous comparison is shown in Figure 5.17 for the all-season tire. As with the summer tire, the concrete surface results in higher emissions than the asphalt surface for all load conditions, so that the emission factor for longitudinal forces is up to 3.5 times higher than for asphalt. For lateral forces, there is even a maximum factor of 6.1. Also for all-season tires, the emission starts increasing stronger for moderate forces than on asphalt, but then continues to increase to a lesser extent. Again, the basic characteristic of asymmetric emission is maintained. However, in contrast to summer tires, the ratio between the emission at maximum longitudinal force and the emission at maximum lateral force hardly changes.

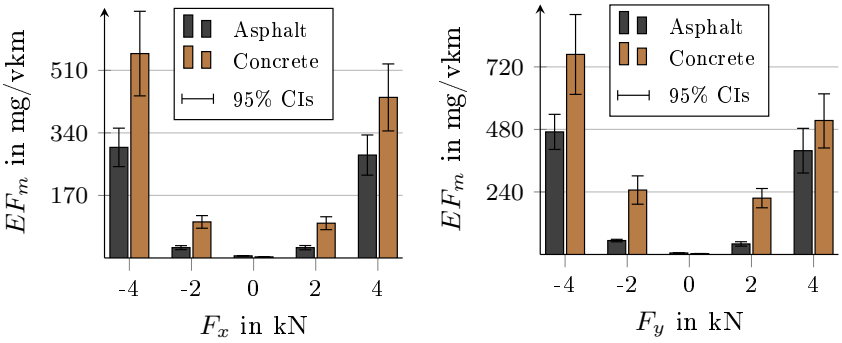

(a) Longitudinal force

(b) Lateral force

Figure 5.17: Influence of pavement material on the emission factors of an all-season tire due to longitudinal force and lateral force, a wheel load of 6.5 kN, a driving speed of 80 km/h, an inflation pressure of 2.6 bar, an ambient temperature of 25 °C, and an SRT value of 60.

The comparison of winter tire emissions is shown in Figure 5.18. This shows a more differentiated picture than for summer tires and all-season tires. While the concrete surface causes higher emissions at moderate forces, it results in lower emissions at high forces. This is true for both longitudinal and lateral forces. The ratio between emissions caused by lateral and longitudinal forces remains almost constant. The reason for the opposite trend for the winter tire at high forces could not be determined in this work and must be investigated in future studies, as must the reason for the overall higher emission level on concrete.

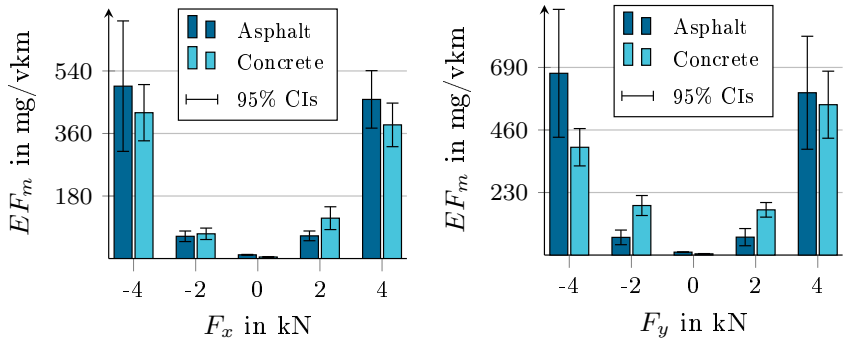

(a) Longitudinal force

(b) Lateral force

Figure 5.18: Influence of pavement material on the emission factors of a winter tire due to longitudinal force and lateral force, a wheel load of 6.5 kN, a driving speed of 80 km/h, an inflation pressure of 2.6 bar, an ambient temperature of 25 °C, and an SRT value of 60.

The results for emission levels on asphalt and concrete show a high degree of agreement with the literature [3, 4, 145]. All tire types show higher emissions on concrete than on asphalt at low loads. Only for winter tires is this relationship reversed at high loads. The quantitative differences between emissions on concrete and asphalt pavements tend to be slightly higher than those reported by Alexandrova et al. [3]. However, as no information on the driving conditions of the vehicles is available for the measurements performed in their study, there is no contradiction.

5.1.8 Skid Resistance

The influence of skid resistance on PM emissions has already been implicitly discussed in section 4.4.1 by plotting the emission for different load conditions over the SRT value (see Figure 4.9). Based on this, regression functions have been parameterized which allow for the determination of emission at different SRT values. However, since it has been shown that skid resistance is one of the most important parameters, and since all previous influences were only shown for an SRT value of 60, the influence of skid resistance will be elucidated explicitly and in detail at this point. Analogous to previous parameters, emission factors for selected load conditions are compared for the SRT values 55, 60 and 65. The two additional SRT values correspond to the highest and lowest grip values measured during the tests. The emission factors of a summer tire under the influence of longitudinal force are shown in Figure 5.19 for different SRT values.

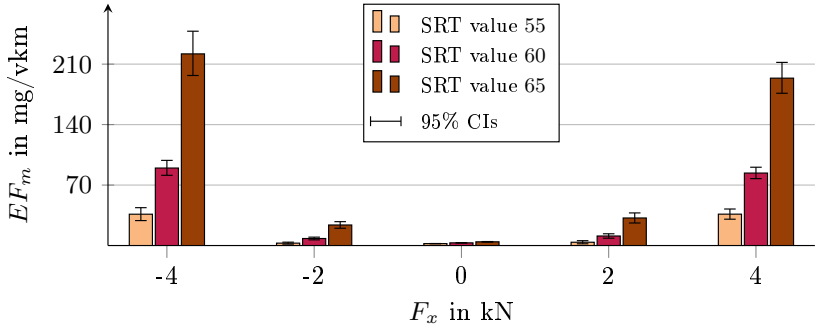

Figure 5.19: Influence of longitudinal force on the emission factor of a summer tire for different SRT values at a wheel load of 6.5 kN, a driving speed of 80 km/h, an inflation pressure of 2.6 bar, and an ambient temperature of 25 °C.

The emission increases significantly with the SRT value, regardless of the load condition. There are factors between 2 and 6 between the emission factors for same load conditions but SRT values differing by 5 points. The factor is high for moderate forces and decreases for higher forces, indicating a decreasing influence of skid resistance on PM emissions with increasing force.

A similar influence can be seen in the case of lateral force (see Figure 5.20). Again, emission factors for same load conditions and 5 points higher SRT value differ by factors between 2 and 6. Thus, at the maximum SRT value and load, the emission factor for the tested summer tire is over $1000\,\mathrm{mg/vkm}$. However, it should be noted that no statement can be made about the composition of the emitted particulate matter as a function of the SRT value. It is therefore possible that at high SRT values, innumerable tiny peaks on the road surface are initially abraded, resulting in a high contribution of road material to PM emissions. As the test progresses, this contribution is likely to decrease, while the relative contribution of the tire increases, although its absolute contribution decreases.

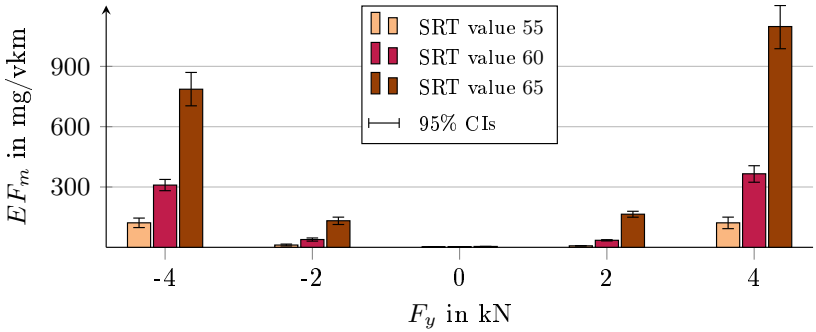

Figure 5.20: Influence of lateral force on the emission factor of a summer tire for different SRT values at a wheel load of $6.5\,\mathrm{kN}$, a driving speed of $80\,\mathrm{km/h}$, an inflation pressure of $2.6\,\mathrm{bar}$, and an ambient temperature of $25\,^{\circ}\mathrm{C}$.

The fact that a road surface with higher skid resistance or roughness increases tire wear has been confirmed in [14, 78, 103]. However, there is little quantitative information on the influence of skid resistance. Lowne [78] mentions a factor of 3 between tire wear on rough and smooth or polished road surfaces [78]. However, there are no reference values for the quantitative influence of skid resistance on PM emissions.

5.2 Influences on the Particle Size Distribution

After discussing the influences on emission levels, henceforth, particle size distributions (PSDs) will be evaluated to determine the influence of all parameters on particle size. The evaluations will be made using particle number distributions (PNDs). These have the advantage that each particle receives the same weighting, whereas particle mass distributions (PMDs) are always dominated by large particles due to their relatively higher mass. In the latter ones, changes in the range of small particles are therefore often not well visible.
For better comparability of particle number distributions during different load conditions, all curves are normalized. This means that PNDs can be compared even if the total emission is at different levels during the different load conditions. Even small changes in the distribution, such as a minor horizontal shift of a peak, become visible since all size distributions are of the same order of magnitude. Normalization was performed with respect to the total number concentration C_n present during each load condition. The corresponding non-normalized particle size distributions can be found in Appendix A.6. Furthermore, the plotted particle concentrations were divided by the respective logarithmic interval width $log(d_p)$. This prevents the width of an interval from influencing its height [51]. An exemplary PND for a summer tire in free-rolling condition is shown in Figure 5.21.
In this case, there is a peak between $0.3\,\mu m$ and $0.4\,\mu m$. However, since the peak is just above the lower detection limit of $0.3\,\mu m$, it is not possible to determine with certainty whether this is a true peak or just a rising edge. In the latter case, the actual peak would be below the lower detection limit and therefore outside the size range investigated in this work. The fact that the concentration decreases in the two lowest intervals is not a valid counterargument, as this could be caused by the fact that the counting efficiency of the aerosol spectrometer decreases in the close proximity of the lower detection limit [95]. Therefore, the only clear conclusion is that there is a peak below $0.4\,\mu m$. Between $1\,\mu m$ and $2\,\mu m$ there is an indication of a second, much flatter peak. Higher than that, the distribution decreases continuously towards larger particles, so that there is hardly any emission in the particle size range of $10\,\mu m$.

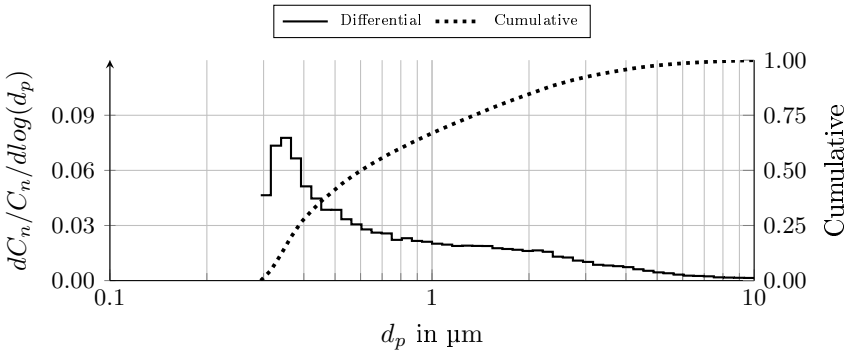

Figure 5.21: Particle size distribution of a freely-rolling summer tire at a wheel load of $6.5\,\mathrm{kN}$, a driving speed of $80\,\mathrm{km/h}$, an inflation pressure of $2.6\,\mathrm{bar}$, and an ambient temperature of $25\,^{\circ}\mathrm{C}$ in the size range between $0.3\,\mu\mathrm{m}$ and $10\,\mu\mathrm{m}$.

The cumulative distribution, on the other hand, can be used to make direct quantitative statements about the distribution. It can be used to directly read the proportion of particles below or over a certain diameter. In the present case, for example, the median particle size ($50\,\%$ of the cumulative distribution) is about $0.6\,\mu\mathrm{m}$. In general, a steeply rising cumulative curve indicates a small median particle diameter, while a flat cumulative curve indicates a large median particle diameter (in the size range of $0.3\,\mu\mathrm{m}$ to $10\,\mu\mathrm{m}$).
In the following sections, the influence of different vehicle parameters, ambient temperature, tire and road types on the particle size distribution will be discussed.

5.2.1 Forces Parallel to the Road Surface

As with total emission, tire forces parallel to the road surface have a significant influence on the particle size distribution (see Figure 5.22). The influence of longitudinal force is shown in Figure 5.22a, the one of lateral force in Figure 5.22b. Both diagrams show differential and cumulative distributions for the free-rolling condition and for four different forces in each force direction.

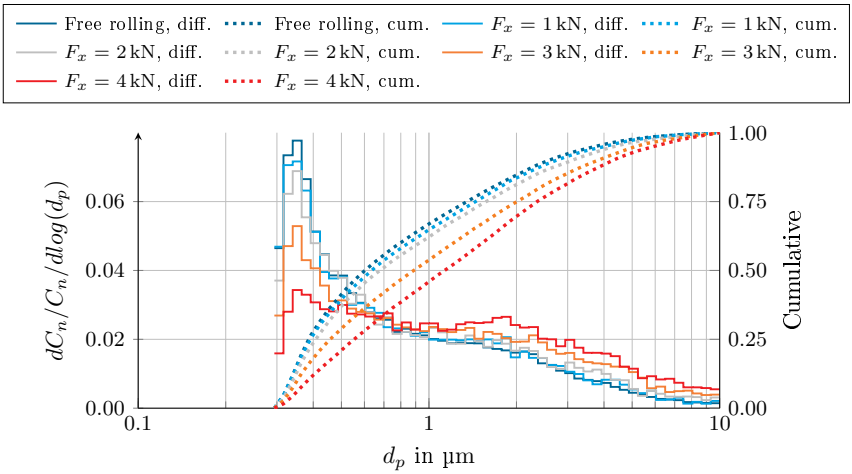

(a) Longitudinal force [Adapted from 112]

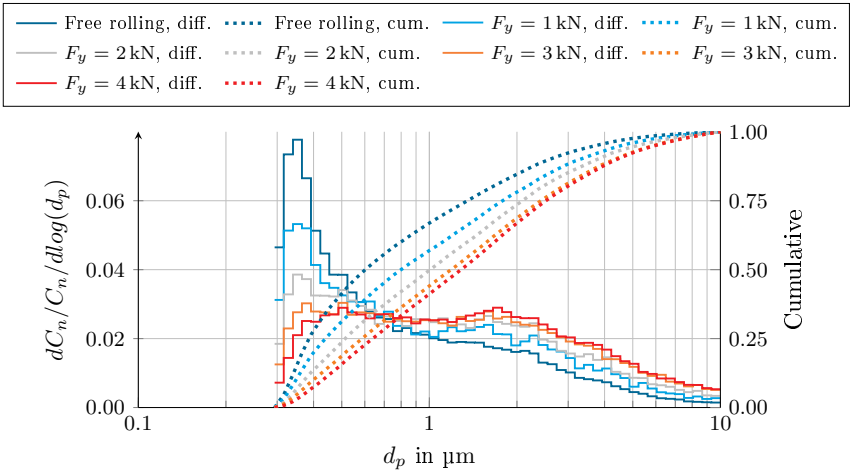

(b) Lateral force

Figure 5.22: Influence of tire forces parallel to the road surface on the particle size distribution at a wheel load of 6.5 kN, a driving speed of 80 km/h, an inflation pressure of 2.6 bar, and an ambient temperature of 25 °C in normalized representation.

The distribution of the free-rolling condition is identical to the one in Figure 5.21. Based on this, increasing longitudinal force (see Figure 5.22a) seems to reduce the first peak between $0.3\,\mu m$ and $0.4\,\mu m$, while increasing the second peak in the size range between $1\,\mu m$ and $2\,\mu m$. However, the reduction of the first peak is only an apparent effect of the normalized plot. In fact, the particle number concentration increases both in the range of small particles as well as in the range of coarse particles. As the increase in the range of coarse particles is significantly larger (in percentage terms, see Figure A.12a), this results in an apparent decrease in the first peak due to normalization. The fact that particle size increases with longitudinal force can also be seen in the cumulative distribution which becomes gradually flatter from the free-rolling condition to the load condition with a longitudinal force of $4\,kN$. Thus, the median particle size ($50\,\%$ of the cumulative distribution) of about $0.6\,\mu m$ in the free-rolling condition increases to just over $1\,\mu m$ at maximum longitudinal force.

The same trend is apparent for lateral force (see Figure 5.22b). Again, the number of particles increases in all size ranges and especially in the range of coarse particles. The median particle size increases with increasing load, resulting in a median particle diameter of about $1.3\,\mu m$ at maximum lateral force. Additionally, compared to the influence of longitudinal force, it is noticeable that lateral forces of the same magnitude lead to a lower peak in the size range of small particles. This difference is probably due to the direction-dependent properties of the tire tread profile discussed in section 5.1.1.2. Presumably, there are several reasons why the median particle diameter increases with increasing force. First, the shear stress in the tire–road contact increases, which facilitates crack formation and propagation within the tire material. Second, the tire force parallel to the road surface increases the slip ratio and thus the surface temperature. Higher slip ratio means longer sliding paths, while higher temperature makes the tire material softer. Both effects favor the formation of coarse particles. In addition, there is another effect of increased slip ratio that can lead to coarser particles. Particles which become detached in the front area of the tire–road contact are rolled over by following tread bar elements. This can result in conglomerations of small particles which are ultimately emitted as coarse particles. However, whether this effect also affects the size distribution in the range of fine particles or only in the

range of large particles needs to be investigated in future tests.
This result is consistent with information from the literature (see section 1.2.3) in which higher load leads to an increase in the median particle size. Whether this is accompanied by an increase in the number of nanoparticles cannot be answered due to the lower detection limit of the aerosol spectrometer at $0.3\,\mu m$.

5.2.2 Wheel Load

The influence of wheel load on particle number distribution is shown in Figure 5.23. In the free-rolling condition (see Figure 5.23a) similar distributions as described above are shown. For all wheel loads, there is a peak just above the lower detection limit of $0.3\,\mu m$, which decreases as wheel load is increased. However, at low wheel loads, the second peak does not appear to be present and only becomes visible as the wheel load gets higher. This shows the same trend as the application of longitudinal and lateral force, namely an increasing particle size with increasing wheel load (and constant adhesion utilization). The increasing particle size can also be seen by the fact that the distribution at high wheel loads extends to coarser particles, while at low wheel loads it ends before. This is also apparent in the cumulative curve, which shifts to the right as the wheel load is enhanced. While the median particle size at a wheel load of $3.25\,kN$ is about $0.4\,\mu m$, it is about $0.5\,\mu m$ at a wheel load of $8.125\,kN$.
The same trend emerges at an adhesion utilization of 0.62 (see Figure 5.23b). However, the second peak is present at all wheel loads and becomes more pronounced as the wheel load is increased. The distributions extend to the upper limit of the size range and the proportion of particles in this range grows with increasing wheel load. Overall, this results in flatter cumulative curves than in the free-rolling condition for all wheel loads. At a wheel load of $3.25\,kN$, the median particle diameter is about $0.5\,\mu m$. As the wheel load increases, the cumulative curve shifts to the right, resulting in a median particle diameter of about $1\,\mu m$ at a wheel load of $8.125\,kN$.

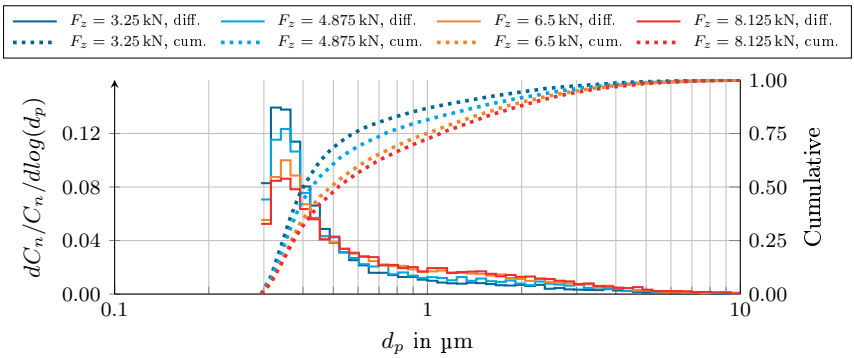

(a) Free rolling

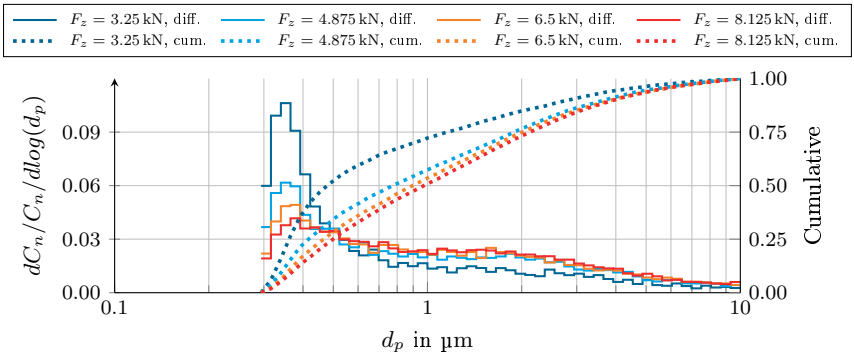

(b) Adhesion utilization 0.62

Figure 5.23: Influence of wheel load on the particle size distribution at a driving speed of 80 km/h, an inflation pressure of 2.6 bar, and an ambient temperature of 25 °C in normalized representation [Adapted from 114].

The enhancement in particle size with increasing wheel load is presumably due to the same reasons as with forces parallel to the road surface. As the wheel load increases, tire deflection increases, resulting in a tire–road contact area that is approximately proportional to the wheel load. The increase in area is mainly due to an increase in the longitudinal direction [107]. The fact that the contact area increases approximately in proportion to wheel load means that the shear stress in the contact remains nearly unchanged for consistent adhesion utilization. This

also means that the ratio of deformation slip to sliding slip remains approximately constant. However, a longer tire–road contact patch could lead to longer slip distances, i.e., a greater distance between the point in the contact patch where the tread elements begin to slide and the end of the tire–road contact. Longer sliding distance additionally results in higher temperatures. Both effects contribute to an increase in total emissions and particle size. In addition, the rolling-over by subsequent tread bar elements could contribute to the formation of larger particles with increasing wheel load (and constant adhesion utilization).
The results are in good agreement with data from the literature. Kim et al. [61] describe an increase of particle size with wheel load. However, due to their test bench setup, they were only able to investigate the trend in the free-rolling condition. From the experiments conducted here, it is now apparent that the trend also applies to higher adhesion utilization, and is even more pronounced there.
Given the current trend toward fleet electrification, this result is considered positive. Higher wheel load at consistent longitudinal dynamics leads to higher total emissions but also to higher median particle size. While this means that PM emissions from tire–road contact are likely to increase with the number of battery electric vehicles, at least each additional particle generated does not pose a greater health risk (as would have been the case with a decrease in size, see section 1.2.1).

5.2.3 Inflation Pressure

The influence of tire inflation pressure on the particle number distribution is shown in Figure 5.24 for three different load conditions. In the free-rolling condition (see Figure 5.24a), distributions with the same characteristics as already explained for tire forces parallel to the road surface and wheel load can be seen. However, the tire inflation pressure seems to have a smaller influence, so that the distributions change less with increasing tire inflation pressure. Nevertheless, the trend is the same as for wheel load. The peak just above $0.3\,\mu\mathrm{m}$ decreases with increasing inflation pressure, while the second peak in the range between $1\,\mu\mathrm{m}$ and $2\,\mu\mathrm{m}$ gets more pronounced. This results in a slightly increasing median particle size from about $0.43\,\mu\mathrm{m}$ at an inflation pressure of $2.0\,\mathrm{bar}$ to $0.5\,\mu\mathrm{m}$ at $3.2\,\mathrm{bar}$.

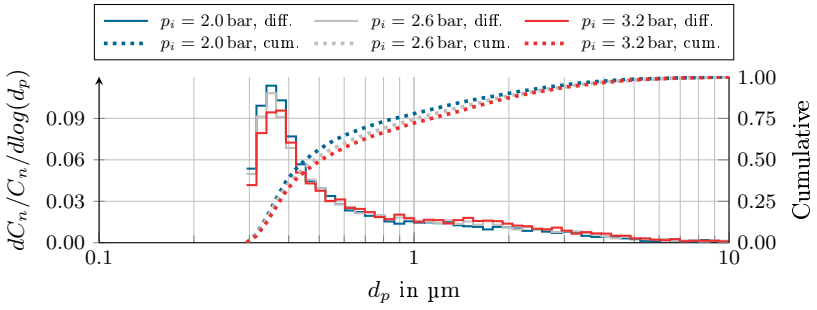

(a) Free rolling

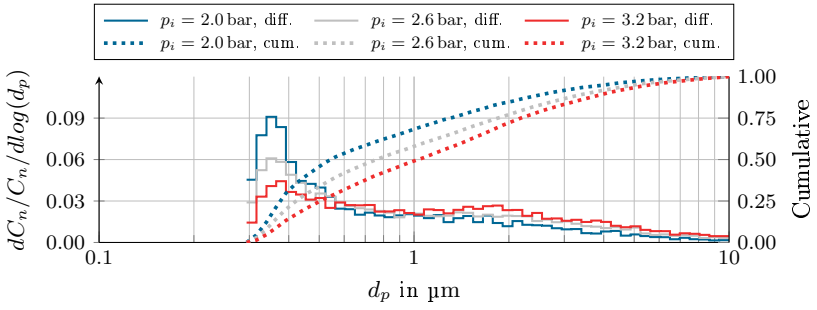

(b) Longitudinal force 4 kN

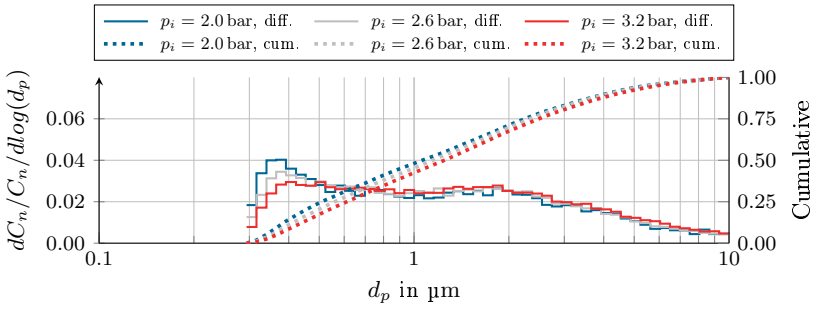

(c) Lateral force 4 kN

Figure 5.24: Influence of tire inflation pressure on the particle size distribution at a wheel load of 6.5 kN, a driving speed of 80 km/h, and an ambient temperature of 25 °C in normalized representation [Adapted from 114].

In the load condition of $4\,\mathrm{kN}$ longitudinal force (see Figure 5.24b), the influence of tire inflation pressure is greater. The height of both peaks changes significantly so that the peaks are almost balanced at a tire inflation pressure of $3.2\,\mathrm{bar}$. Besides that, two other effects are visible. First, the second peak appears to shift towards larger particle diameters with increasing inflation pressure. Second, the fraction of particles just below the upper detection limit increases. Overall, the median particle diameter increases from about $0.53\,\mu\mathrm{m}$ at $2.0\,\mathrm{bar}$ to about $1\,\mu\mathrm{m}$ at $3.2\,\mathrm{bar}$.

The same trend, although to a much lesser extent, is present under the influence of lateral force (see Figure 5.24c). This is probably due to the two opposing effects on tire stiffness discussed in section 5.1.1.2. The reason for the overall flatter size distributions under lateral force was discussed in section 5.2.1. As with the total emissions, the influence of tire inflation pressure is much less pronounced under lateral force than under longitudinal force. The median particle diameter changes only from about $1\,\mu\mathrm{m}$ to $1.2\,\mu\mathrm{m}$.

The increasing median particle diameter with increasing inflation pressure can presumably be explained by the effects on the tire–road contact. As the inflation pressure is increased, the contact area between tire and road surface shrinks, mainly longitudinally [107]. The smaller contact area results in higher surface pressure and higher shear stress. The higher shear stress could result in increased crack propagation in the tire material and the formation of larger particles.

However, since only the basic shear stress distribution is applied in the free-rolling condition, the influence of tire inflation pressure is small. When tire forces parallel to the road surface are applied, the shear stress increases as does the deformation of the tread bar elements. Compared to low inflation pressure, this eventually results in a higher slip ratio (see Figure A.3), which could also increase the formation of large particles or at least favor the general emission of particles.

Under the influence of longitudinal force, the influence of inflation pressure is particularly pronounced. This is due to the large change in tire stiffness in this direction. In the case of lateral force, the changes in size distribution are much smaller, as in the case of total emission. This is also due to the smaller change in tire stiffness in lateral direction compared to longitudinal direction (for detailed explanation see section 5.1.3.

The greater influence of lateral force on the size distribution compared to longitudinal force (Figure 5.24c compared to Figure 5.24b) is probably related to the design of the tire tread. The summer tire studied has almost continuous ribs in longitudinal direction, interrupted only by narrow sipes. This results in lower deformation and almost no edge wear. In lateral direction, the tread is divided by wide grooves. When lateral force is applied, this results in greater deformation with more edge wear. Both favors the formation of large particles. This effect was explained in more detail in section 5.1.1.2.

5.2.4 Driving Speed

The particle size distributions for the influence of driving speed are shown in Figure 5.25. Figure 5.25a shows the influence in the free-rolling condition, Figure 5.25b the one loaded with $4\,\mathrm{kN}$ lateral force. When freely rolling, the first peak increases from $30\,\mathrm{km/h}$ to $80\,\mathrm{km/h}$ while the second peak flattens. In the non-normalized plot (see Figure A.15a) it can be seen that this change is mainly due to a higher number of fine particles. However, the particle size distribution at $120\,\mathrm{km/h}$ shows an opposite trend, so that the first peak is much lower and the second peak is of the same order as the one at $30\,\mathrm{km/h}$. However, since this trend reversal can only be observed in the free-rolling condition, it is presumably not due to a real tire phenomenon. It is more likely that the turbulence caused by high driving speeds swirls up coarse particles that were already deposited in the test bench environment. Because of the low emission in this load condition, even the smallest numbers can cause a significant distortion of the size distribution. This hypothesis is supported by the fact that at high driving speeds, the number of large particles increases significantly in addition to the number of small particles. At lower speeds, however, the number of coarse particles hardly changes. Since driving speed has only a limited influence on the slip ratio, it is unlikely that the additional emission of coarse particles is due to an emission phenomenon of the tire.

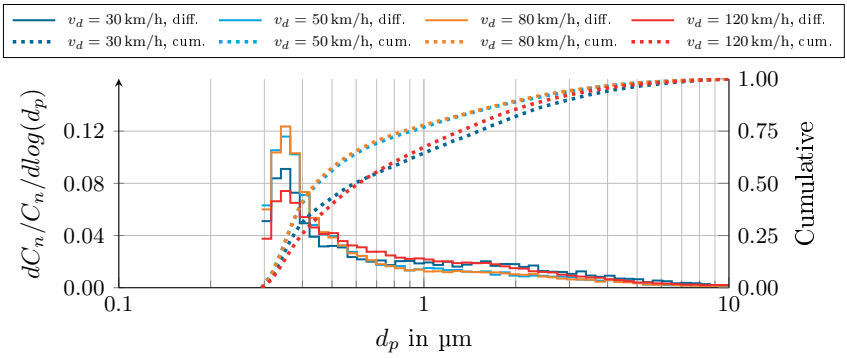

(a) Free rolling

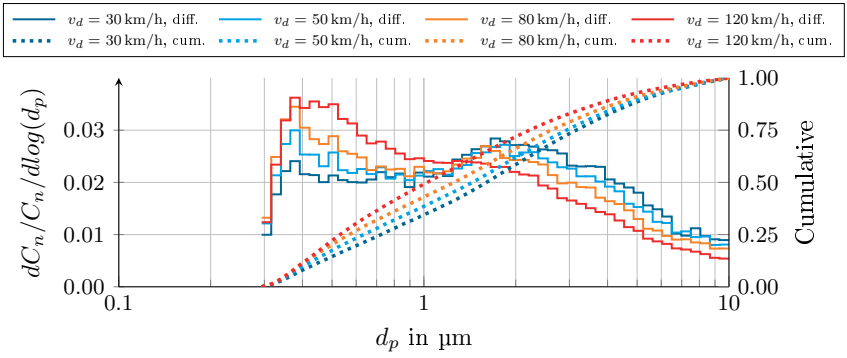

(b) Lateral force 4 kN

Figure 5.25: Influence of driving speed on the particle size distribution at a wheel load of 6.5 kN, an inflation pressure of 2.6 bar, and an ambient temperature of 25 °C in normalized representation [Adapted from 114].

However, under the influence of lateral force (see Figure 5.25b), a clear trend emerges. At low driving speed, the peak in the size range of 2 µm clearly exceeds the peak just above 0.3 µm. This observation leads to the conclusion that the formation of coarse particles is facilitated by slow processes in the tire–road contact. As driving speed is increased and lateral force is kept constant, the peak in the size range of fine particles rises while the peak in the coarse particle

range flattens and shifts slightly towards smaller diameters. However, the non-normalized particle size distribution (see Figure A.15b) reveals that there is an increase in particle number over the entire size range. Nevertheless, since the increase is much bigger in the fine particle range, the normalized plot shows the trend of the decreasing second peak. Overall, there is a clear decrease in the median particle size with increasing driving speed, which is particularly evident in the cumulative distribution. While the median particle diameter at a driving speed of $30\,\mathrm{km/h}$ is about $1.5\,\mu\mathrm{m}$, the value drops to about $1\,\mu\mathrm{m}$ at $120\,\mathrm{km/h}$. The decrease in particle size with increasing driving speed is probably due to the faster processes in the tire–road contact. On the one hand, driving speed influences the resulting forces via the viscoelastic properties of the tire material. This means that a lower slip ratio is required to achieve a given force at high speeds than at low speeds. On the other hand, a change in driving speed at constant slip ratio means a proportional change in the differential speed between tire and road surface. Since the second effect is larger, the total differential speed between tire and road surface is likely to be greater at higher speeds. This results in a higher sliding speed of the individual tread bar elements. The higher sliding speed could cause the abrasion processes to change, producing many small particles instead of few large ones. This theory can be used to reconcile the increase in emission (per time) over driving speed found in section 5.1.4 with the decrease in median particle size found here. However, the theory could neither be confirmed nor refuted in the course of this work.

5.2.5 Tire Type

Especially for different types of tires, the question arises whether their emissions differ not only in the total amount but also in the size distribution of the emitted particles. To answer this question, the particle size distributions of the summer, winter and all-season tire are plotted in Figure 5.26 for a lateral force of $4\,\mathrm{kN}$. There are no clear differences between the particle size distributions of the three tire types. Since the situation is identical for the free-rolling condition and the longitudinal force of $4\,\mathrm{kN}$, the corresponding plots are not shown here. However,

for the sake of completeness, they can be found in Appendix A.5. In addition, the non-normalized size distributions included in Appendix A.6 show that the number of particles is always highest for winter tires. There, it also becomes apparent that the summer tire is significantly more resistant to longitudinal forces than to lateral forces in terms of the number of particles emitted. In general, however, there are no different distributions or clear trends between the tire types for any of the load conditions. It can therefore be assumed that the tire types differ mainly in terms of total emissions, while the particle size distributions are almost identical.

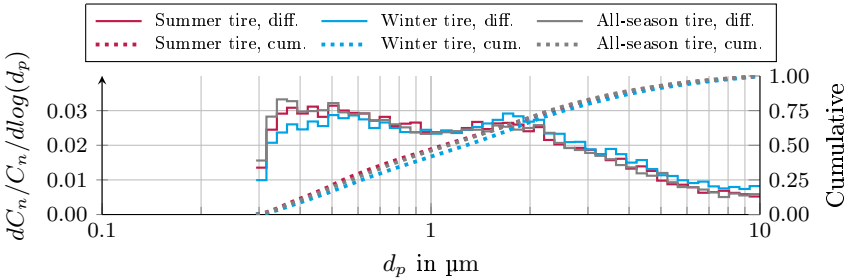

Figure 5.26: Influence of tire type on the particle size distribution at the usual ambient temperature of each tire for the load condition of 4 kN lateral force, a wheel load of 6.5 kN, a driving speed of 80 km/h, and an inflation pressure of 2.6 bar in normalized representation.

5.2.6 Ambient Temperature

The influence of ambient temperature on the particle size distribution is shown in Figure 5.27 using the example of the summer tire. Under the influence of longitudinal force (see Figure 5.27a) lower ambient temperature leads to a slightly higher first peak and a slightly lower second peak. However, the non-normalized plot (see Figure A.17a) reveals that the particle emission does not change in the range of fine particles and that there is only a particle decrease in the range of coarse particles when the ambient temperature is decreasing. This results in the shift towards smaller particles in the normalized plot. This is also visible in the cumulative plot.

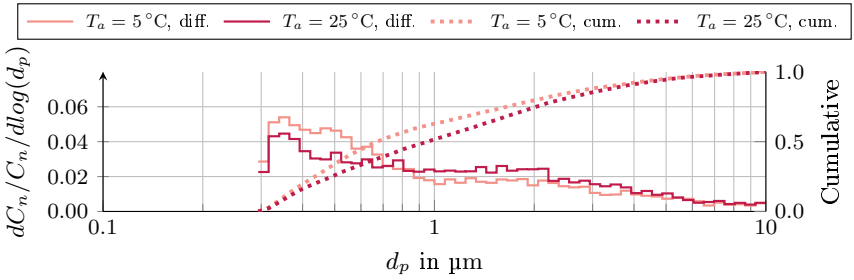

(a) Summer tire with longitudinal force 4 kN

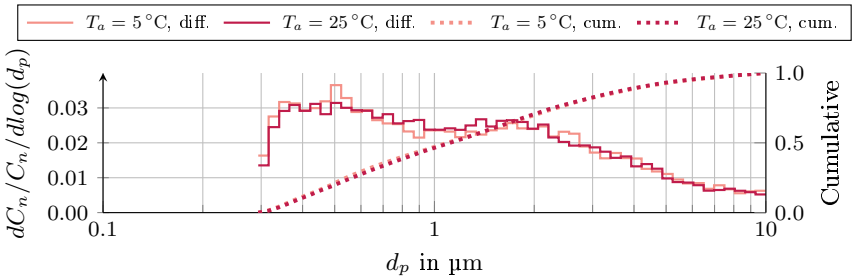

(b) Summer tire with lateral force 4 kN

Figure 5.27: Influence of ambient temperature on the particle size distribution of a summer tire at a wheel load of 6.5 kN, a driving speed of 80 km/h, and an inflation pressure of 2.6 bar in normalized representation.

The lower ambient temperature and the resulting slightly lower surface temperature of the tire for same load conditions could cause the tire material to be more brittle. This in turn could reduce the formation of coarse particles. However, whether this is an actual effect of the tire or just an unidentified measurement influence must be clarified in future tests. The latter is supported by the fact that no comparable trend can be identified for the influence of lateral force (see Figure 5.27b) and for both load conditions with the all-season and the winter tire (see Figure A.8 and A.9).

Precise statements about the quantitative influence of ambient temperature cannot be derived from the results obtained here. For this purpose, tests with other tires

and ambient temperatures are to be carried out, which will allow conclusions to be drawn about the exact relationship and the mechanisms responsible.

5.2.7 Pavement Material

To illustrate the influence of road surface material, the size distributions of the summer tire are shown in Figure 5.28 as representative for all three tire types. The known particle size distributions for longitudinal (see Figure 5.28a) and lateral forces (see Figure 5.28b) on an asphalt surface are compared with those of the same load condition on a concrete surface.

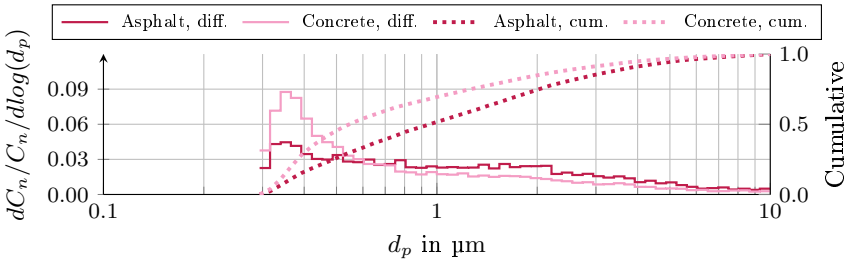

(a) Summer tire with longitudinal force 4 kN

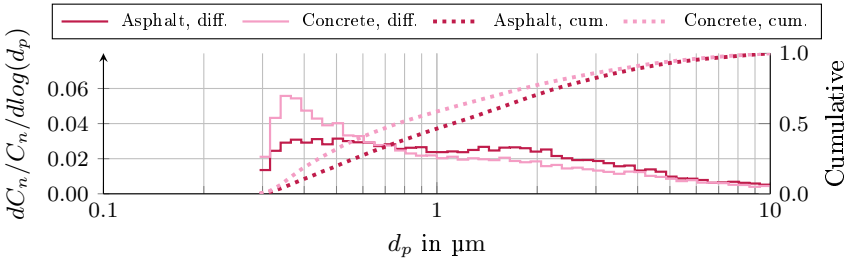

(b) Summer tire with lateral force 4 kN

Figure 5.28: Influence of pavement material on the particle size distribution of a summer tire at a wheel load of 6.5 kN, a driving speed of 80 km/h, an inflation pressure of 2.6 bar, and an ambient temperature of 25 °C in normalized representation.

The concrete surface leads to smaller median particle diameters for both load conditions. While the peak between $0.3\,\mu m$ and $0.4\,\mu m$ is very flat on asphalt, it persists on concrete even at high loads. In contrast, the second peak between $1\,\mu m$ and $2\,\mu m$ is less pronounced. This results in significant differences between the median particle diameters. While they are around $0.93\,\mu m$ and $1.1\,\mu m$ on asphalt under longitudinal and lateral force, respectively, they are around $0.53\,\mu m$ and $0.73\,\mu m$ on concrete.
Whether the fine particles are tire or pavement material, cannot be determined conclusively from the tests conducted in this study. Another question that arises is why the median particle size on concrete is smaller than the one on asphalt. One possible explanation is that the abraded bitumen from the asphalt surface contributes to clogging of particles, thus reducing the number of small particles and increasing the number of large ones. However, as the phenomenon was not investigated in detail, the question cannot be answered conclusively, either.
The particle size distributions for the all-season and the winter tire differ only in the shape of the first peak on concrete. However, the general difference from the asphalt road surface remains, so the corresponding diagrams are not shown here. They can be found in Appendix A.5.

5.2.8 Skid Resistance

Finally, the influence of skid resistance on the particle size distribution was investigated. For this purpose, the particle size distributions of the summer tire loaded with longitudinal force (see Figure 5.29a) and lateral force (see Figure 5.29b) are compared. The size distributions for a high SRT value were obtained by averaging the individual size distributions from the first occurrence of the specific load condition ($4\,kN$ longitudinal force for Figure 5.29a and $4\,kN$ lateral force for Figure 5.29b, both with a wheel load of $6.5\,kN$) in each test passage. As it was the first occurrence of this load condition after regeneration of the road surface, the skid resistance was always high. However, as the order of load conditions varied between the individual programs (see section 4.2), the SRT value at the first occurrence of each load condition differed as well. The particle size distributions

for high skid resistance in Figure 5.29 are therefore based on SRT values between 66 and 61.

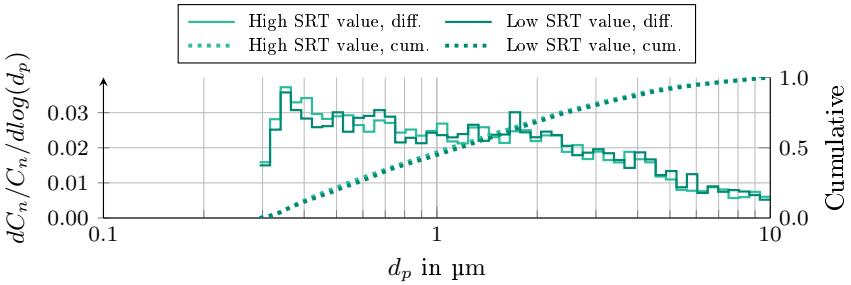

(a) Longitudinal force 4 kN

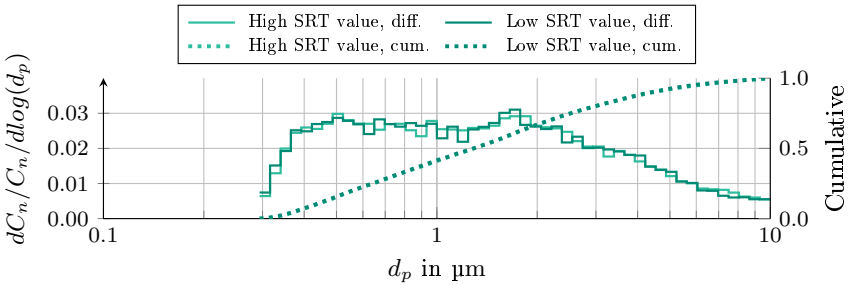

(b) Lateral force 4 kN

Figure 5.29: Influence of skid resistance on the particle size distribution of a summer tire at a wheel load of 6.5 kN, a driving speed of 80 km/h, an inflation pressure of 2.6 bar, and an ambient temperature of 25 °C in normalized representation.

The size distribution for low skid resistance is generated by averaging the individual size distributions of all test runs recorded during the last occurrence of the respective load condition in each test passage. The underlying SRT values also differ here, but to a lesser extent due to the flatter shape of the SRT curve in this range. The SRT values which the size distributions for a low SRT value is based on are therefore between 56 and 54.

This shows that the skid resistance or the associated SRT value have no effect on the particle size distribution, whereas the number of particles is higher for

high SRT values (see section 5.1.8). Under the influence of both longitudinal and lateral force, the size distributions remain practically unaffected. Therefore, it can be concluded that skid resistance has a significant influence on the total emission, but none on the particle size distribution.

6 Modeling

To further illustrate the relationships obtained and to derive realistic emission factors, the results presented in the previous sections are used to calculate average PM emission factors for three realistic driving cycles. This requires two things. First, a model that specifies the PM emission or emission factor as a function of the relevant parameters. The model must be able to assign an individual emission factor to each driving condition occurring during real-world driving. On the other hand, time-resolved driving data are required, which in turn contain the information serving as input variables for the model. The driving data or set of load conditions used (see section 6.1), the exact structure of the model (see section 6.2) as well as its application on the driving data (see section 6.3) are explained in the following sections. Finally, using the model and the tire mass loss data recorded at the internal drum test bench, an estimation of the contribution of particulate matter to total tire mass loss is made (see section 6.4).

6.1 Real Driving Cycles

Driving data was recorded for three different route profiles (see Appendix A.10) to get an impression of the magnitude of emission factors occurring during real-world driving. The data was recorded by the Mercedes-Benz AG using a VBOX in conjunction with an integrated inertial measurement unit (IMU) with a time resolution of $50\,\mathrm{ms}$. The VBOX records all speed and acceleration data determined from GPS data. If the connection to satellites is lost, the system switches to the IMU so that the driving data continues to be recorded.

The first route profile (urban) represents typical city traffic with many turns and start–stops, and a low average speed. The second profile (rural) is a country road with many curves and a higher average speed. Finally, the third profile describes a pure highway trip with the highest average speed. The values of adhesion utilization occurring when driving these three route profiles are shown in Figure 6.1.

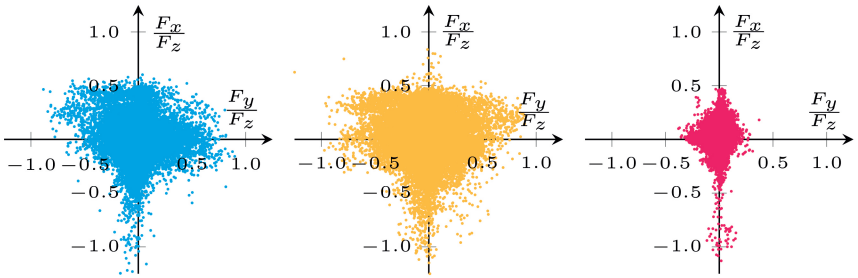

(a) Urban **(b)** Rural **(c)** Highway

Figure 6.1: Ranges of adhesion utilization in longitudinal and lateral direction for three route profiles.

The route profiles differ significantly in terms of adhesion utilization values. This difference is mainly in the lateral direction, which means that different levels of lateral dynamics occur depending on the route profile. The most dynamic profile in this respect is the rural profile, followed by the urban one and lastly the one on the highway. However, there is an enormous difference between the latter two, which underlines that the adhesion utilization in lateral direction plays only a subordinate role on the highway. In longitudinal direction, the differences are much smaller. Both the urban and the rural profile show clear differences between driving and braking directions. In both cases, the range of adhesion utilization in longitudinal direction is greater on the braking side than on the driving side. Accordingly, the highest values of longitudinal adhesion utilization are achieved during braking. The distribution of the highway profile appears to be more balanced overall, but again the absolute highest values of longitudinal adhesion utilization are found on the braking side.

Although the diagrams in Figure 6.1 show the range of adhesion utilization in the

respective route profile, it is not possible to make a statement about the frequency of individual driving conditions due to the large number of overlapping dots. To get an impression of how often individual conditions occur, the frequency distributions are shown in Figure 6.2 based on boxplots. Therein, boxes show the range in which $50\,\%$ of the data points are included (range between the lower and upper quartile); the horizontal line within it shows the median. Upper and lower whiskers indicate the 1.5-fold interquartile range, or the lowest and highest value, respectively, if their deviation from the box is smaller.

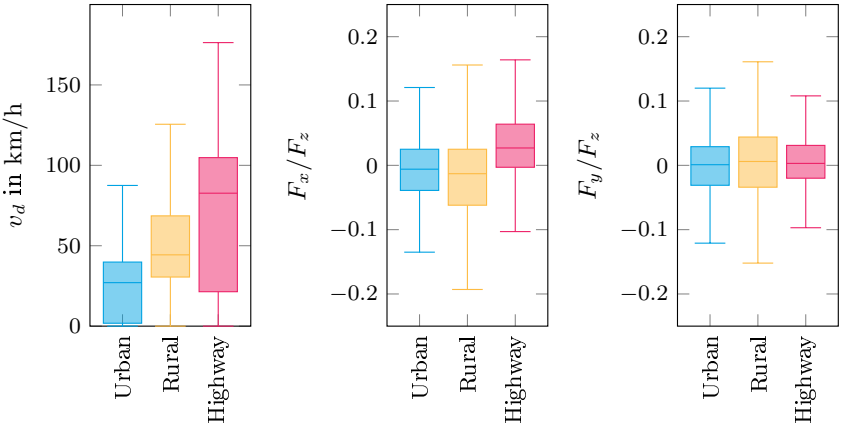

(a) Driving speed **(b)** Long. adh. utilization **(c)** Lat. adh. utilization

Figure 6.2: Frequency distributions of the individual driving parameters during the three route profiles in the form of box plots.

Figure 6.2a shows the difference in driving speed between the route profiles. As expected, driving on the highway includes the highest speeds by far. The fact that the bottom of the box is still lower than for the rural profile is due to slowly-moving traffic in some sections of the highway profile.

Figure 6.2b and 6.2c show the frequency distributions of adhesion utilization in longitudinal and lateral direction, respectively. In longitudinal direction (see Figure 6.2b), two aspects should be emphasized. First, the boxes differ in their position. While braking conditions predominate for the urban and rural profile

(medians slightly below 0), driving conditions are dominant for the highway profile (median above 0). This difference is due to the fact that the vehicle was driven much faster on the highway. In order to maintain its speed, the increased air resistance had to be overcome, i.e., the vehicle had to constantly apply driving force. In the evaluation, this results in an upwards shift. On the other hand, there is also a difference in the range of adhesion utilization. This is expressed in the height of the box and in the length of the whiskers. By far the largest range is found for the rural profile, followed by the urban one and the one of the highway, with the latter two hardly differing from each other. This means that the spread and thus the absolute values of the adhesion utilization in the longitudinal direction are highest for the rural profile.
Differences can also be seen in the lateral direction (see Figure 6.2c), whereby the position of the boxes only provides information as to whether the route contains more left or right-hand bends. Therefore, the range is more important here. The rural profile shows by far the largest range (highest box and longest whiskers), followed by the urban one and finally the one on the highway, which means that the adhesion utilization in lateral direction plays only a subordinate role on the highway, whereas it is pronounced for the rural route profile.
In summary, the individual route profiles can be characterized as follows: The urban profile has the lowest speed and a moderate level of adhesion utilization in both longitudinal and lateral direction. The rural profile consists of a medium speed, but has the highest adhesion utilization in both force directions. The highway profile has the highest speed, longitudinal dynamics are comparable to the urban profile, but lateral dynamics are quite low.

6.2 Four-Dimensional Regression Model

A model is needed to derive the amount of PM emitted during a trip from driving data. For this model, emissions of the summer tire, which was used for all detailed investigations (see section 5.1.1 to 5.1.4), served as the basis. Only for this tire was information on all the investigated influencing parameters available. In addition,

the calculated influence of longitudinal and lateral force for this tire is based on almost twice the number of support points (Nine support points (including 0) for longitudinal and lateral force, respectively, compared to five; see Table 4.1: test series No. 1 compared to test series No. 5), so that the highest accuracy could be assumed. It was necessary to decide which of the investigated parameters should be included in the model. Two conditions had to be met in order to include a parameter: On the one hand, data resulting from the experiments had to prove the influence of the parameter with sufficient certainty. On the other hand, inclusion of a parameter only made sense if the information on this parameter was also contained in the real driving data to be processed (see section 6.1). The only influencing parameters that fulfilled both conditions were the longitudinal and the lateral force as well as the wheel load. Tire inflation pressure was not taken into account for two reasons. First, it is specified by the vehicle manufacturer and can therefore only be influenced by the driver to a limited extent. Second, all drives on public roads were carried out with the specified tire inflation pressure of $2.6\,\mathrm{bar}$, so it was simply not necessary to take the inflation pressure into account in the model in order to demonstrate its function. The driving speed was also not taken into account, as the influence on the emission could not be proven beyond doubt (see section 5.1.4). Information about the ambient temperature, the road surface material, and its skid resistance are not included in the driving data, so they were also not considered. The resulting model is therefore based solely on the forces acting on the wheel. With regard to the parameters not taken into account, the emission functions used are therefore based on the respective values that were chosen for the test series on the influence of tire forces parallel to the road surface: tire inflation pressure $2.6\,\mathrm{bar}$, driving speed $80\,\mathrm{km/h}$, ambient temperature $25\,^{\circ}\mathrm{C}$, and an asphalt surface with an SRT value of 60. A possible further development of the simulation model to include other parameters is discussed in section 7.2.
To create the model, it must first be possible to assign an emission factor to any tire force parallel to the road surface. From the previous considerations, emission factors are only known for pure longitudinal force, pure lateral force, and forces that consist of equal proportions of longitudinal and lateral force (see section 5.1.1.1 to 5.1.1.3). For a better overview, these influences are plotted together in Figure 6.3 over positive resulting force.

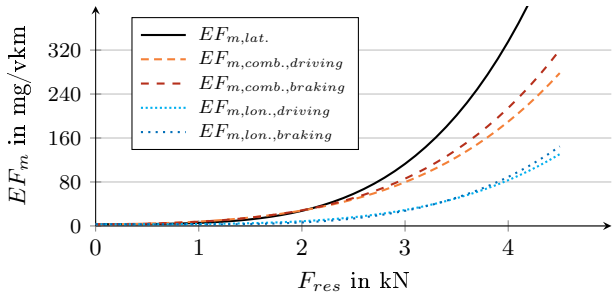

Figure 6.3: Support functions for the 3D emission map [Adapted from 112].

Since the asymmetry in emissions under the influence of lateral force depends on the tire tested, but the model should be as independent as possible from the exact (summer) tire used, only one emission curve is used for lateral force. This corresponds to the mean emissions at positive and negative lateral forces. The comparison clearly shows that longitudinal force causes the lowest emissions and lateral force the highest, the emissions caused by combined forces are in between. However, it should be noted that the support range of the regression functions for combined forces ends at $F_{res} = \sqrt{8}$ kN (according to Equation 5.1 with $F_x = \pm 2\,\text{kN}$ and $F_y = \pm 2\,\text{kN}$). Their emission values are therefore subject to a higher degree of uncertainty in the range of high forces. It should also be noted that the large difference between the emission factors for longitudinal and lateral force is characteristic of summer tires. It is also present for winter and all-season tires, but to a much lesser extent (see section 5.1.5).

Based on these emission curves, it is possible to create a characteristic map that assigns a mass-based emission factor EF_m to each combination of longitudinal and lateral force. Due to different emission factors for driving and braking force (see section 5.1.1.1), the function which the map is based on was determined separately for each quadrant. The target function is a three-dimensional function created by rotation around the vertical axis. Therefore, polar coordinates were used for calculation so that the proportions of longitudinal and lateral force are determined by the angle φ. An angle of $\varphi = 0°$ corresponds to pure driving force. Since the previously determined support functions are fourth-order polynomials

with only even exponents, they can be described using a general formula (see Equation 6.1). Accordingly, $a(\varphi)$ and $b(\varphi)$ are angle-dependent coefficients, which allow for a gradual transition of the support functions into each other.

$$EF_m(F_{res}, \varphi) = a(\varphi) \cdot {F_{res}}^4 + b(\varphi) \cdot {F_{res}}^2 + c \text{ for } F_{res} \geq 0, 0 \leq \varphi < 2\pi \quad (6.1)$$

The coefficients $a(\varphi)$ and $b(\varphi)$ had to be chosen so that all conditions for the emission map could be fulfilled. For each quadrant, these conditions consisted of three boundary conditions specified by the three support functions (see Figure 6.3) contained therein and, in addition, two transition conditions to the respective neighboring quadrants. The latter two conditions ensure a continuously differentiable transition of the emission map between the neighboring quadrants. Therefore, fourth-order polynomials were chosen for $a(\varphi)$ and $b(\varphi)$, so that five coefficients were to be determined for five conditions. For the first quadrant (positive longitudinal force and positive lateral force), the boundary conditions consisted of the specification of the emission curves for purely positive longitudinal force, purely positive lateral force and the curve for combined positive longitudinal and positive lateral force. For the transition conditions, the gradient in the support functions for pure longitudinal and pure lateral force was specified as 0. The conditions for the other quadrants were specified analogously. The coefficient c was given by the emission in the free-rolling condition without lateral force. The coefficients of the polynomials were finally determined analytically (see Appendix A.2). The resulting three-dimensional map is shown in Figure 6.4. The properties described in section 5.1.1 become clear one more time here: On the one hand, the progressive shape of the emission curves, because of which the map only increases slightly in the center (small force), but stronger towards the outer edge (higher force). On the other hand, the difference between the emission factors due to longitudinal and lateral force.
The calculated emission map was validated using the emission factors of those load conditions that had not been used to create the model. Figure 6.5 shows a visual validation of the map. The area covered in Figure 6.4 is shown in plan view. This shows that a circle with the radius of the maximum force acting in

longitudinal and lateral directions results. The values not used to determine the characteristic map (see Figure 5.1) are included as individual points. The color difference between point and map shows that for most load conditions, the map matches the actual measured emission with a high degree of accuracy. Only for the load conditions with a longitudinal force of $\pm 3\,\mathrm{kN}$ does the map underestimate the actual emission. This fact shows that the calculated transition between the support functions is not completely accurate. The influence of lateral force on the level of emissions appears to be higher than assumed by the map. The values which the validation is based on are shown in Table 6.1. Both absolute and relative deviations are included. The highest relative deviations are less than $6\,\%$, which shows that the map predicts emissions with sufficient accuracy for all tire forces parallel to the road surface. The highest occurring emission value was used as reference value for relative deviations.

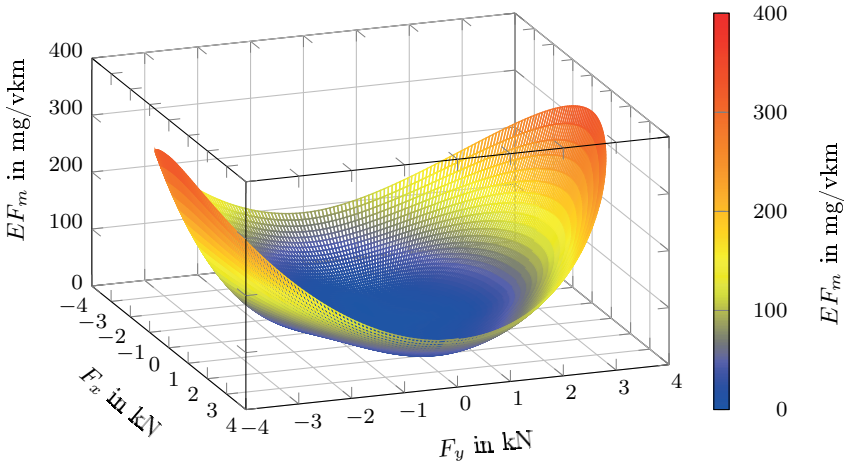

Figure 6.4: Calculated three-dimensional map of the mass-based emission factor in the size range between $0.3\,\mu\mathrm{m}$ and $10\,\mu\mathrm{m}$ for all forces in the tire–road contact parallel to the road surface for a summer tire at a wheel load of $6.5\,\mathrm{kN}$, a driving speed of $80\,\mathrm{km/h}$, an inflation pressure of $2.6\,\mathrm{bar}$, an ambient temperature of $25\,^{\circ}\mathrm{C}$, and at an SRT value of 60 [Adapted from 112].

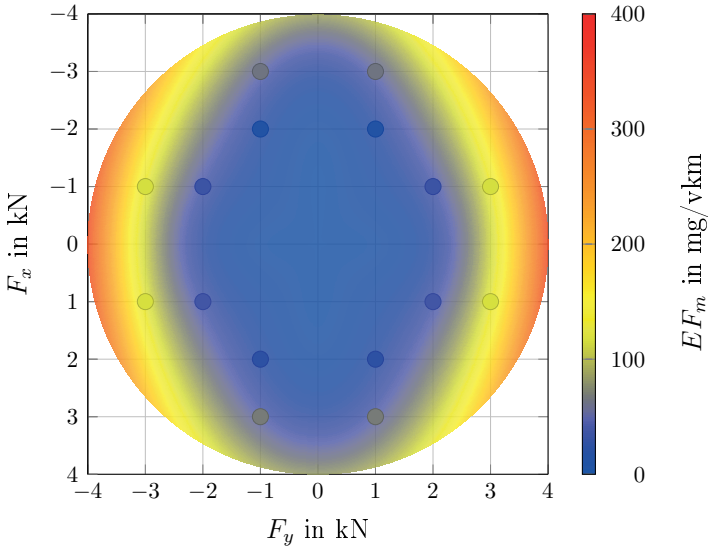

Figure 6.5: Visual validation of the emission map using the emissions at the load conditions which had not been used for determination of the model [Adapted from 112].

Table 6.1: Differences between emission factors calculated by the model and the ones which were only measured but had not been used for its generation [Adapted from 112].

F_x & $\lvert F_y \rvert$ in kN	ΔEF_m in mg/vkm	ΔEF_m in %
3 & 1	−18.98	−5.66
2 & 1	0.22	0.07
1 & 2	3.72	1.11
1 & 3	12.10	3.61
−1 & 3	17.23	5.14
−1 & 2	8.91	2.66
−2 & 1	12.44	3.71
−3 & 1	−11.67	−3.48

In order to account for wheel load in addition to tire forces parallel to the road surface, an additional factor must be incorporated into the model. For this purpose, the gradients for the regression lines shown in Figure 5.8 with different adhesion utilization were calculated and normalized by dividing them by the respective emission factor at a wheel load of $6.5\,\mathrm{kN}$. The normalized gradients thus describe the change in emission factor at constant adhesion utilization and based on a wheel load of $6.5\,\mathrm{kN}$. Based on the emission factors shown in Figure 6.4 (valid for a wheel load of $6.5\,\mathrm{kN}$) and using the normalized gradients, emission factors for any wheel load can be calculated for a given and constant adhesion utilization. However, since the wheel load changes continuously and the normalized gradients show an increasing trend with increasing adhesion utilization, the evolution of the gradient over adhesion utilization was approximated by a linear regression function. As a result, the normalized gradient valid for each adhesion utilization can be assigned, which in turn can be used to calculate the emission factor for a deviating wheel load with a known emission factor at a wheel load of $6.5\,\mathrm{kN}$ (see Figure 6.4).

The visualization of the model is shown in Figure 6.6 for four different wheel loads but unchanged adhesion utilizations. The four wheel loads $F_{z,1}$ to $F_{z,4}$ correspond to the same values examined in section 5.1.2. These are shown only as examples, as the model is able to calculate the emission for any wheel load in the regression range between $3.25\,\mathrm{kN}$ and $8.125\,\mathrm{kN}$.

The function for $F_{z,3} = 6.5\,\mathrm{kN}$ corresponds to that shown in Figure 6.4. Although adhesion utilization values are now plotted on the horizontal axes, the values correspond to the same forces plotted in Figure 6.4 with regard to the underlying driving dynamics ($F_x/F_z = F_y/F_z = 0.62$ corresponds to $F_x = F_y = 4\,\mathrm{kN}$ for $F_z = 6.5\,\mathrm{kN}$).

This allows emission factors to be calculated for each load condition, consisting of a combination of longitudinal and lateral force as well as a wheel load, so that emission factors of vehicles of different weights but same adhesion utilization can be compared. It also allows for the integration of dynamic wheel loads into the model. However, it should be noted that dynamic wheel loads also affect the value of the adhesion utilization.

Based on this model, emissions could be calculated for real driving cycles. For

this purpose, driving speed and acceleration in longitudinal and lateral direction from each time step were used. Driving speed was not taken into account as an independent parameter for calculating the emission factor (see the beginning of this section), but only in the form of an additional driving force required to overcome the resulting aerodynamic resistance. In addition, driving speed was used to calculate the distance traveled by the vehicle within the respective time step.

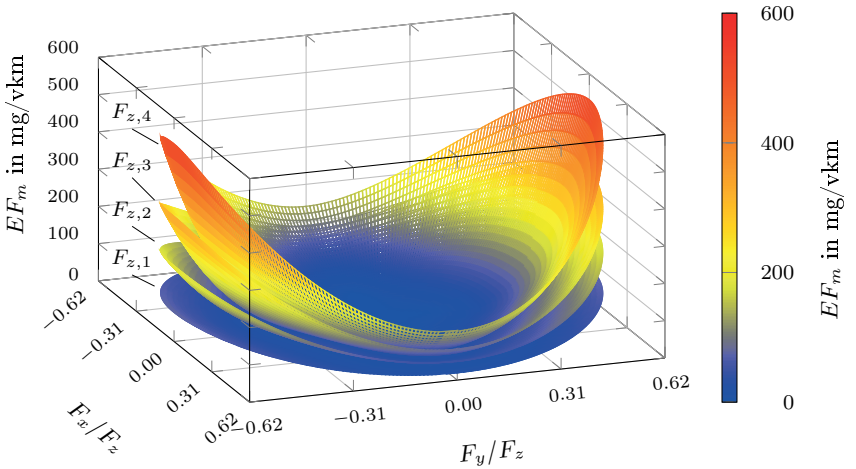

Figure 6.6: Four-dimensional regression model to predict the emission factor as a function of longitudinal and lateral tire forces and wheel load. The included maps correspond to the emission factors at wheel loads of $F_{z,1} = 3.25\,\mathrm{kN}$, $F_{z,2} = 4.875\,\mathrm{kN}$, $F_{z,3} = 6.5\,\mathrm{kN}$ und $F_{z,4} = 8.125\,\mathrm{kN}$. The model is based on the emission of a summer tire at a driving speed of $80\,\mathrm{km/h}$, an inflation pressure of $2.6\,\mathrm{bar}$, and an SRT value of 60.

A filter was first applied to the longitudinal and lateral accelerations of the vehicle, which set positive accelerations above $1.25\,\mathrm{g}$ and negative accelerations below $-1.25\,\mathrm{g}$ to the respective limit value. This prevented individual measurement outliers from distorting the overall emission due to the progressive correlations between emission and tire force. The forces acting on the entire vehicle were then calculated from the vehicle's accelerations and its mass. To allocate the forces

to the individual wheels, a number of assumptions and specifications were made regarding the underlying vehicle:

- A rear-wheel-drive vehicle is modeled in the simulation. Driving forces are therefore only transmitted at the rear axle.
- The braking force distribution between front and rear axle is static. $70\,\%$ of the braking force is transmitted at the front axle and $30\,\%$ at the rear axle.
- Lateral forces are transmitted equally at the front and rear axle as well as at left and right wheels.
- Dynamic wheel loads by pitching (due to accelerating and braking) and by rolling (due to cornering) were calculated according to simple models which are only based on geometric data of the vehicle (see Appendix A.8).
- The vehicle is a luxury-class model, so the required geometric data for this vehicle was adopted (see Appendix A.7).

Using these assumptions, an individual load condition could be calculated for each wheel. Each load condition consists of a value for the adhesion utilization F_{res}/F_z, an angle φ that defines the composition of the resulting force from the longitudinal and lateral force, and a wheel load F_z that includes the static wheel load as well as any dynamic wheel load that may occur. Using these three variables, each load condition could be assigned an emission factor that applies exclusively to that wheel at that point of time. The emission factors determined were multiplied by the distance traveled previously calculated for that time step, resulting in the emission of each individual tire–road contact during that time step. The sum of the four individual emissions over all time steps gave the total emission for the distance traveled. Relating the total emission to the distance traveled gave an average emission factor for the vehicle.
To validate the vehicle model with regard to the effects on PM emission, the vehicle used for the test drives was equipped with wheel force transducers on all four wheels in addition to the VBOX. This allowed the forces acting on the wheels during the test drive to be recorded. For this data, there was no need to

calculate and allocate the wheel forces, so the measurement data from the wheel force transducers could be used directly to calculate the emissions based on the emission correlations determined at the internal drum test bench.
The emission results which have been obtained from the prediction model and the two measurement systems (VBOX and wheel force transducers) were compared for two different calculation approaches to obtain the wheel forces (for the VBOX data) in order to choose the approach with the highest level of agreement.
In the first approach, dynamic wheel loads due to pitching and rolling were calculated to determine the resulting wheel load on each wheel. Longitudinal forces were statically allocated between the front and rear axle. Lateral forces were allocated equally among all four wheels.
In the second approach, dynamic wheel loads due to pitching and rolling were calculated and used in the same manner. In addition, lateral forces were allocated to the four wheels in proportion to the calculated dynamic wheel loads. Longitudinal forces were still statically allocated to the front and rear axle.
Since in reality the allocation of lateral forces is practically proportional to the wheel load, it would be reasonable to assume that the second approach gives better results. However, the agreement of the emission results with the first approach was significantly higher with an average deviation of about only $5\,\%$ with respect to the average emission factor per route profile.
As the first approach gave the better agreement with regard to emission data, the second approach was abandoned and the first one was used for the model. Even though this does not correspond to the real allocation of wheel forces, the main objective of the model was not to represent all influences and processes absolutely accurately. Rather, the main objective was to show that a simple vehicle model and VBOX data from real-world test drives, along with the emission correlations determined at the internal drum test bench, can be used to estimate PM emissions for real-world driving. Given the relatively small differences between the emission results based on measured data from the wheel force transducers and those calculated from driving data, this objective can be considered fulfilled.

6.3 Emissions for Real-World Driving

The emissions for the three route profiles shown in section 6.1 have been calculated using the prediction model. The results for an asphalt surface at three different SRT values are shown in Table 6.2.
This shows that driving on rural roads produces the highest average emissions, followed by driving in urban areas, and finally driving on highways, which produces significantly lower emissions. In conjunction with the driving profile analyses (see Figure 6.1 and 6.2), it becomes apparent one more time that PM emissions are directly linked to the extent of driving dynamics. If the route profile has a particularly high number of bends which are driven dynamically, this results in a large spread in lateral dynamics. This in turn leads to high PM emissions. The same applies to a large spread in longitudinal dynamics, which is mainly caused by starting and stopping as well as strong acceleration and deceleration.

Table 6.2: Comparison of the mean emission factors resulting from the prediction model for the three route profiles and different SRT values. All specifications are given in mg/vkm.

Route profile	SRT 55	SRT 60	SRT 65
Urban	4.84	11.96	36.28
Rural	6.19	16.52	53.02
Highway	3.59	7.21	16.32

The calculated PM emissions for SRT values of 55 and 60 are within the range given in the literature (see Table 1.1). However, it should be noted that the emission factors at an SRT value of 65, especially the one for the rural route profile, are well above this range. There are two reasons why such high emission factors do not tend to apply to passenger cars for real-world driving. First, the microtexture required for high skid resistance is constantly worn away by driving over it. Second, the vehicle which the prediction model is based on is a fairly heavy sedan representing the upper end of the passenger-car range. Thus, for lighter vehicles the EF predicted would also be lower.
In order to provide a visual impression of where the PM is being emitted, in

addition to the purely quantitative evaluation, the emission factor EF_m for the urban route profile is plotted in Figure 6.7 as a function of location. Again, the emission factor is given for an entire vehicle with four wheels.

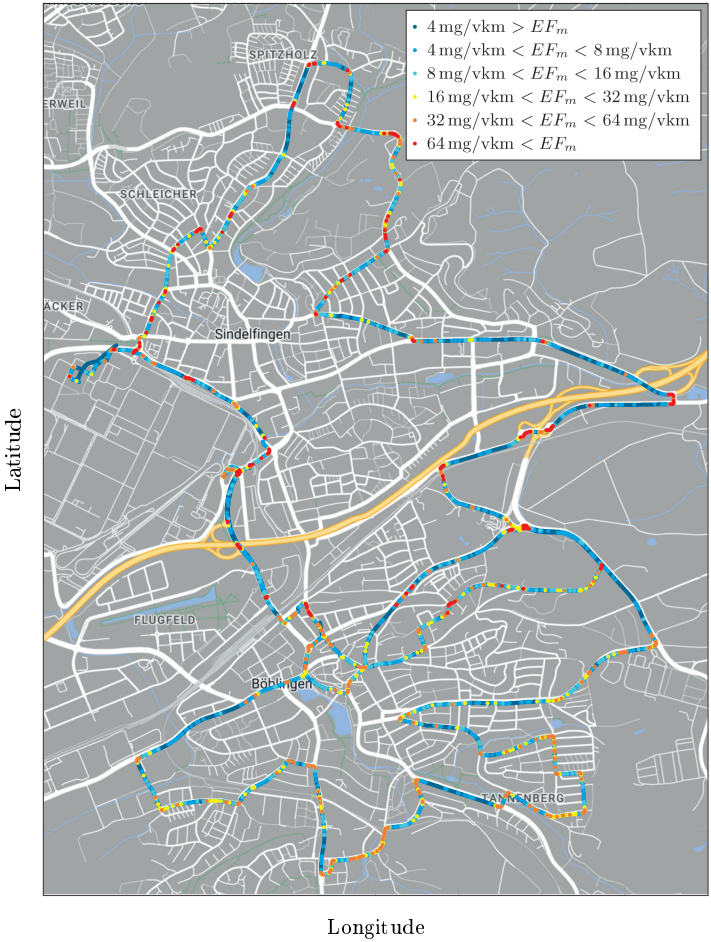

Figure 6.7: Prediction of the emission factor of tire–road PM for a luxury-class vehicle driving with summer tires depending on the location for the urban route profile assuming an SRT value of 60.

This shows which traffic and driving situations have a decisive influence on the level of PM emissions. In urban driving, emission is highest at intersections and junctions. On the other hand, emissions are consistently low during steady driving. This is also true for periods when the car is driven at high speeds (see Figure A.25). All emission factors shown are based on the calculation with an SRT value of 60. For SRT values of 55 or 65 the total emissions would be lower or higher according to Table 6.2.
Analogous to Figure 6.7, maps have been created for the other two route profiles. They can be found in Appendix A.10.

6.4 Contribution of PM to Total Tire Mass Loss

From the tests conducted, it is possible to make a statement about the contribution of particulate matter to the total tire mass loss of a summer tire. For this purpose, the total tire mass loss was determined during the test series on the influence of tire forces parallel to the road surface (see section 5.1.1) by weighing the tire with a precision balance before the start and after the end of the test series. Prior to weighing, the tire was cleaned and after tempered, in order to eliminate as many unwanted influences as possible. The inflation pressure was then adjusted to exactly $2.6\,\mathrm{bar}$ to eliminate any influence of improper inflation pressure on tire mass and thus on the determined tire mass loss.
Finally, based on the emission map shown in Figure 6.4, PM emissions were calculated for the whole test series. For this purpose, all emissions that occurred during the test runs were taken into account. This included the time periods in which a particular load condition was approached, the time periods necessary to build up and reduce the respective load condition (ramp durations), and the time periods in which the tire rolled freely (see Figure 4.4). As with the determination of the relationship between skid resistance and emission (see section 4.4.1), it was further assumed that the SRT value decreased incrementally during the tests. This means that each load condition applied during the test series could be associated with the skid resistance present at that time. Furthermore, the characteristic map

of Figure 6.4 was extended by the SRT value, which made it possible to link the load condition and the emission factor depending on the skid resistance. By multiplying each emission factor with the driving speed and the time that the respective load condition had been applied, the PM emission being generated in this load condition was calculated. Finally, the sum of all individual emissions gave the PM emission for the entire test series.

This value does not only include particulate matter from the tire but also from the road. Therefore, the value had to be multiplied by the fraction of tire material determined previously (18.2 %, see section 4.3.2). The contribution of tire PM to the total tire mass loss was then calculated by dividing the PM emission by the total mass loss. According to this calculation, the PM contribution to total tire mass loss was 3.9 %.

In the literature, numerous data on this contribution are given. Between the upper and lower limit of the range spanned by these values there are two orders of magnitude. In [1], the authors report a PM contribution to total tire mass loss of less than 0.1 % for their test bench experiments. In [45], on the other hand, 0.1 % is given as the lower limit, and the authors suggest that the range could extend to 10 %. The data in [102, as cited in 19] and [13, 22, 50, 63, 126, 133] are also in this range, with most authors reporting values between 2 % and 7 %. However, there are also higher values. 11 % is given in [44], while the authors in [19] even suggest a range up to 20 % from their experiments. It must therefore be assumed that the exact conditions, such as the road surface, the tire used, the test environment, and the test method, have a significant influence on the contribution of particulate matter to total tire mass loss.

7 Summary and Outlook

7.1 Summary

Non-exhaust emissions (NEE) are becoming increasingly important as a result of stricter emission standards and advancing electrification. These include emissions from friction brakes and tire–road contact, as well as those caused by resuspension of previously deposited particles. However, the composition of NEE will shift as the increased use of regenerative braking systems will reduce brake emissions in the long term. Consequently, the tire–road contact will be the major source of particulate matter (PM) in road traffic.

As NEE already account for a large proportion of PM emitted by road traffic, the EU has decided to further accelerate the reduction of emissions through regulation. The Euro 7 emission standards planned for 2026 will limit emissions from brakes and tire–road contact for the first time. For brakes, a limit value is planned that targets PM emissions (particles with a diameter smaller than $10\,\mu\mathrm{m}$). For tires, the regulation will only refer to overall tire wear, i.e., it will not include a more precise specification of particle size. At present, there is a lack of both a reliable database and a test method to perform the necessary tests in a reproducible manner to set such a limit value. Nevertheless, the limit for tires is likely to be just the beginning of more stringent regulations that will, in the long term, also address PM emissions from tire–road contact.

In order to identify the main influencing parameters of tire–road PM emissions, a literature research has been conducted. Although many influencing parameters were identified, only isolated quantitative data were found, some of which were contradictory. Thus, to contribute to a better understanding of emission generation and reduction, experimental investigations were carried out on a tire internal

drum test bench as part of this work. The main objective of the investigations was to quantify the relationships between vehicle-related influences, such as longitudinal and lateral force as well as wheel load, and the emission of tire–road PM. In addition, other influences from the tire, the road surface, and the environment were investigated. For this purpose, the existing internal drum test bench at the Institute of Vehicle System Technology at the Karlsruhe Institute of Technology was modified and extended to measure tire–road PM in real time. Precautions were taken to prevent the ingress of particles from the environment. In addition, a high-performance extraction system was integrated into the test bench, which draws the emitted particles into a control volume and then collects them. Using a specially designed sampling apparatus, a small representative sample is taken from the total extraction flow and analyzed with an optical aerosol spectrometer. This provides real-time information on number and size of the particles in the sample and the particle size distribution.

In order to quantify the individual influencing parameters, a test methodology has been developed in which individual load conditions are repeatedly approached and held stationary for a short period of time. This method makes it possible to precisely assign an emission factor to the associated load condition. However, it was found that the decrease in skid resistance associated with the abrasion of the road surface has a significant influence on the level of PM emissions. To account for this influence, a special test structure was designed to ensure that each load condition was tested at a variety of different skid resistance levels and that the influence of skid resistance could be subsequently eliminated or accounted for by calculation. The collected particles were examined in downstream analyses. This allowed both their density and composition to be determined. Images taken with a scanning electron microscope prove that the particles are realistic tire and road wear particles (TRWP) as found on public roads. Using the particle number concentrations and size information measured at the test bench, as well as the density of the particles, the emission factors describing the emission of an entire vehicle per kilometer driven could be calculated.

One separate test series was performed for each influencing parameter. In the case of longitudinal and lateral force, the force was varied and the curve progression of the emission factor over the force was approximated by regression functions. A

fourth-order dependence was found for both longitudinal and lateral force, with the emission of the summer tire being significantly higher under lateral force than under longitudinal force. To investigate the influence of wheel load, tire inflation pressure, and driving speed, the respective parameters were varied and the effects on emission under tire forces parallel to the road surface were recorded. Both wheel load and tire inflation pressure were found to have a positive linear relationship with PM emissions. Furthermore, their quantitative effect on emissions was found to be similar. A clear correlation between driving speed and PM emissions could not be established. In addition to the vehicle-related influences for which the mathematical correlation with the emission was determined, other parameters of the tire, the road surface, and the environment were investigated by comparing the emissions recorded under different load conditions. For example, it was found that winter tires generate significantly higher emissions than summer tires under all load conditions; that concrete surfaces generate higher emissions than asphalt surfaces; and that ambient temperature has an effect on emissions that depends on the tire type (summer tire, all-season tire, winter tire). In addition to the influence on the level of emissions, the influence on the particle size distribution was analyzed for all parameters. It was shown that the median particle size increases with longitudinal force, lateral force, wheel load, and inflation pressure, while it decreases with driving speed the driving speed. On the other hand, no clear influence on particle size could be determined for the tire type, the road material, and the ambient temperature.

In terms of avoiding or reducing emissions by the driver, a restrained and anticipatory driving style contributes to low PM emissions. Rapid acceleration and deceleration should be avoided, as well as high lateral forces due to high cornering speeds. A direct influence of driving speed, on the other hand, could not be determined. On the vehicle side, lower mass can reduce PM emissions, as can lower tire inflation pressure. However, the latter in particular conflicts with the objective of low overall tire wear, so the advantages and disadvantages must be carefully offset against each other.

There was a particularly large difference between the emissions of summer tires and those of all-season and winter tires. To achieve the lowest possible PM emissions, summer tires should be preferred to all-season and winter tires whenever

possible. With regard to the road surface, two possible ways of reducing PM emissions have been identified. On the one hand, the use of asphalt instead of concrete road surfaces. This statement applies without restriction to summer and all-season tires, but also to winter tires within a normal load range. On the other hand, high skid resistance results in high PM emissions, so there is an opportunity to reduce emissions by producing textures with lower skid resistance. Unfortunately, these two options are in conflict with the requirements for durability or driving safety, so that the best compromise must be found in each situation.

The fear that electrification could not only increase total emissions but also shift the particle size distribution towards smaller particles has not been confirmed. On the contrary, it turned out that the median particle size increases with increasing load. However, this does not mean that fewer small particles are generated at higher loads. Rather, there is an increase across the entire size range, but the increase in large particles is many times higher. In summary, the driver has the largest influence on total emissions as well as on the particle size distribution.

Based on the influences of tire forces parallel to the road surface determined for the summer tire, a three-dimensional emission map was created that assigns an emission factor to each adhesion utilization (longitudinal, lateral, and combined). The map was extended to include the influence of wheel load, resulting in a four-dimensional emissions map. Based on this map, a model was built that uses real driving data as input and calculates tire–road PM emissions over the distance traveled. As an example, this emission calculation was performed for three characteristic route profiles with completely different driving profiles (urban, rural, highway). It turned out that the predicted emissions are in the same range as those reported in the literature for an ordinary driving style.

The identified influences on the emission of tire–road PM contribute to a better understanding of the formation and thus to the avoidance or reduction of this increasingly important source of PM. In conjunction with the prediction model based on the results, a method has been developed for predicting emissions for real-world driving using measurements on an internal drum test bench, i.e., under reproducible boundary conditions. Thus, the method combines high repeatability with realistic driving behavior and can therefore be used to estimate PM emissions for real-world driving.

7.2 Outlook

The methodology developed in this work for determination of tire–road particulate matter can be extended or optimized in several ways. On the one hand, this is about the extraction efficiency of PM emitted. It can be assumed that despite careful design of the extraction performance, not all particles are captured by the extraction system. Specific extraction-efficiency tests or a CFD (computational fluid dynamics) simulation for the internal drum test bench could provide more detailed information and thus allow the extraction efficiency to be taken into account as a function of driving conditions. On the other hand, it is a matter of calculating emission factors using the measured particle concentration and the size of the extraction flow. A flow profile for the sampling plane should be created to provide even more accurate information on the total emission. Knowledge of the dependence of the flow profile on the driving conditions could improve the results at two levels of complexity. The first level requires the creation of a velocity profile in the sampling plane in order to characterize the actual flow. Such measurements have already been made to determine the best sampling position, but not for different driving conditions and therefore potentially different flow conditions. The second stage requires the simultaneous measurement of the particle concentration at several points in the cross section. Thus, profiles for the flow velocity as well as for the particle concentrations could be determined. Knowing this would allow more accurate statements to be made about the total particle content.

Further optimization could be achieved by knowing and subsequently using a TRWP-specific refractive index instead of the preset default value for latex. The determination could not be performed within the scope of this work, but should be aimed at for the benefit of future measurements of tire–road PM using optical measurement technology.

A final improvement relates to the determination of particle density. This was determined based on the material collected from the summer tire and applied to all evaluations. However, it is likely that the particle density depends on the tire and road material used on the one hand, and the skid resistance of the road on

the other. Therefore, based on measurements with real-time cascade impactors, density investigations for specific test series and skid-resistance conditions could be carried out in future tests with significantly lower particle quantities. This is because real-time cascade impactors determine the number and size of particles and also collect the particles separated in size stages. By subsequently weighing the individual stages, a specific density could be calculated for each stage (particle size range) even with minimal particle quantities.

Furthermore, not all observed effects could be explained within the scope of this work. For this purpose, further experiments are required, which allow a more precise observation and analysis of the respective effect. The most striking is the relationship between driving speed and PM emissions. Since the data shown was reproducible in several repetitions, it could be based on a real tire phenomenon. Model investigations on a miniature test bench could help clarifying this. On the other hand, more extensive tests should be carried out to investigate the influence of tire temperature on emission behavior. This is especially true for winter tires, where the influence seems to be significant even at low temperatures.

Further research is also needed where the time and cost constraints in this work did not allow additional investigations. For example, it was not possible to investigate how the influencing parameters affect particles smaller than $0.3\,\mu\mathrm{m}$, especially nanoparticles. The same is true for particles larger than $10\,\mu\mathrm{m}$. An overarching picture about the emission behavior of tires can only evolve if the effects on the entire size range of tire–road wear are known. A second point concerns the relationship between the two most important influencing parameters, longitudinal and lateral force, and sliding slip. In particular, the quantitative relationship remained unaffected within the scope of this work. Last but not least, further tire models have to be investigated with the developed methodology in order to find out to what extent the determined emission factors are representative for the respective tire type.

There is also potential for further development and improvement with regard to the simulation model for predicting PM emissions for real-world driving. The creation of the model was aimed at demonstrating that estimates of PM emissions on real-world driving can be made based on emission data measured on the test bench and driving data recorded with a VBOX and using a simple vehicle model.

However, the model does not claim to make accurate predictions or to take into account all influencing parameters. For greater accuracy, the simulation model could therefore be extended to include additional parameters such as tire inflation pressure, ambient temperature, pavement material, and skid resistance. A more precise vehicle model could be used in order to take into account spring and damper characteristics, for example, in addition to the pure geometry data of the vehicle.

Eventually, it will be explained how the knowledge gained can contribute to the reduction of tire–road PM. First, the correlations between load and PM emissions can be used to derive recommendations for drivers. These include an anticipatory driving style with as few speed changes as possible and low cornering speeds. From a PM perspective, winter and all-season tires should only be used when environmental conditions require it. The automotive industry must be encouraged to develop lighter vehicles. The additional emissions caused by higher masses combined with higher driving forces could be reduced by limiting driving torques, especially when starting off. For road authorities, the skid resistance of the road surface has been primarily a safety issue so far. However, the design and construction of future roads should take into account the conflict of objectives with PM emissions. Accordingly, the range of skid resistance should be set as high as necessary and as low as possible for the respective traffic situation. Second, the mathematical correlations in future autonomous vehicles could be used for trajectory optimization. Minimizing tire forces could thus contribute to the reduction of particulate matter of each individual vehicle .

A Appendix

A.1 Grain Size Distribution of the Added Sand

Table A.1: Grain size distribution of quartz in the added sand [68].

Component Granulation	Quartz 0.1 - 0.5 mm
Particle size in mm	Sum in Ma −%
0.000	0.00
0.100	1.25
0.150	5.40
0.200	18.86
0.250	35.49
0.300	56.86
0.400	86.21
0.500	98.59
0.600	99.99
0.800	100.00

Table A.2: Grain size distribution of corundum in the added sand [67].

Component Granulation	Corundum 0.1 - 0.4 mm
Particle size in mm	Sum in Ma −%
0.000	0.00
0.100	3.00
0.200	11.00
0.315	43.00
0.400	77.00
0.500	98.00
0.630	99.00
0.800	100.00

Table A.3: Grain size distribution of calcium carbonate in the added sand [66].

Component Granulation	Calcium carbonate 0.1 - 0.6 mm
Particle size in mm	Sum in Ma −%
0.063	0.00
0.090	8.00
0.100	8.80
0.150	17.80
0.200	32.00
0.250	38.00
0.315	55.50
0.400	67.90
0.500	78.60
0.600	92.40
0.800	100.00

A.2 Mathematical Relationships between Influencing Parameters and the Emission Factor

The following formulas serve as a supplement to the regression functions shown in section 5.1.1 through 5.1.3. They are to be understood as numerical value equations. If all forces are used in kN, this results in an emission factor in $\mathrm{mg/vkm}$.

Regression functions for the influence of longitudinal force (Figure 5.2):

$$EF_{m,neg}(F_x) = 0.380 \cdot {F_x}^4 - 0.706 \cdot {F_x}^2 + 3.1007$$
$$EF_{m,pos}(F_x) = 0.304 \cdot {F_x}^4 + 0.146 \cdot {F_x}^2 + 3.1007$$

Regression functions for the influence of lateral force (Figure 5.3):

$$EF_{m,neg}(F_y) = 1.063 \cdot {F_y}^4 + 1.988 \cdot {F_y}^2 + 3.1007$$
$$EF_{m,pos}(F_y) = 1.383 \cdot {F_y}^4 + 0.418 \cdot {F_y}^2 + 3.1007$$

Regression functions for the influence of combined forces (Figure 5.4):

$$EF_{m,neg}(F_{res}) = 0.366 \cdot {F_{res}}^4 + 4.435 \cdot {F_{res}}^2 + 3.1007$$
$$EF_{m,pos}(F_{res}) = 0.452 \cdot {F_{res}}^4 + 4.465 \cdot {F_{res}}^2 + 3.1007$$

Regression functions for the influence of wheel load (Figure 5.8):

$$EF_{free\ rolling}(F_z) = 0.187 \cdot F_z + 0.564$$
$$EF_{F_x/F_z=-0.155}(F_z) = 0.793 \cdot F_z + 1.532$$
$$EF_{F_x/F_z=-0.31}(F_z) = 2.237 \cdot F_z - 4.012$$
$$EF_{F_x/F_z=-0.465}(F_z) = 7.170 \cdot F_z - 17.90$$
$$EF_{F_x/F_z=-0.62}(F_z) = 26.95 \cdot F_z - 73.02$$
$$EF_{F_x/F_z=0.155}(F_z) = 0.662 \cdot F_z + 2.269$$
$$EF_{F_x/F_z=0.31}(F_z) = 2.571 \cdot F_z - 6.362$$
$$EF_{F_x/F_z=0.465}(F_z) = 5.284 \cdot F_z - 8.615$$
$$EF_{F_x/F_z=0.62}(F_z) = 20.59 \cdot F_z - 48.432$$

Regression functions for the influence of inflation pressure (Figure 5.9):

$$EF_{free\ rolling}(p_i) = 0.231 \cdot p_i + 0.348$$
$$EF_{F_x=-2\ kN}(p_i) = 0.407 \cdot p_i + 0.213$$
$$EF_{F_x=-4\ kN}(p_i) = 0.905 \cdot p_i - 1.355$$
$$EF_{F_x=2\ kN}(p_i) = 0.501 \cdot p_i - 0.286$$
$$EF_{F_x=4\ kN}(p_i) = 1.187 \cdot p_i - 2.056$$
$$EF_{F_y=-2\ kN}(p_i) = 0.512 \cdot p_i - 0.336$$
$$EF_{F_y=-4\ kN}(p_i) = 0.644 \cdot p_i - 0.654$$
$$EF_{F_y=2\ kN}(p_i) = 0.356 \cdot p_i - 0.110$$
$$EF_{F_y=4\ kN}(p_i) = 0.353 \cdot p_i + 0.076$$

A.3 Explanatory Diagrams

The following figures serve as explanatory supplements to the contents shown in section 5.1.1.1, 5.1.1.2, and 5.1.3.

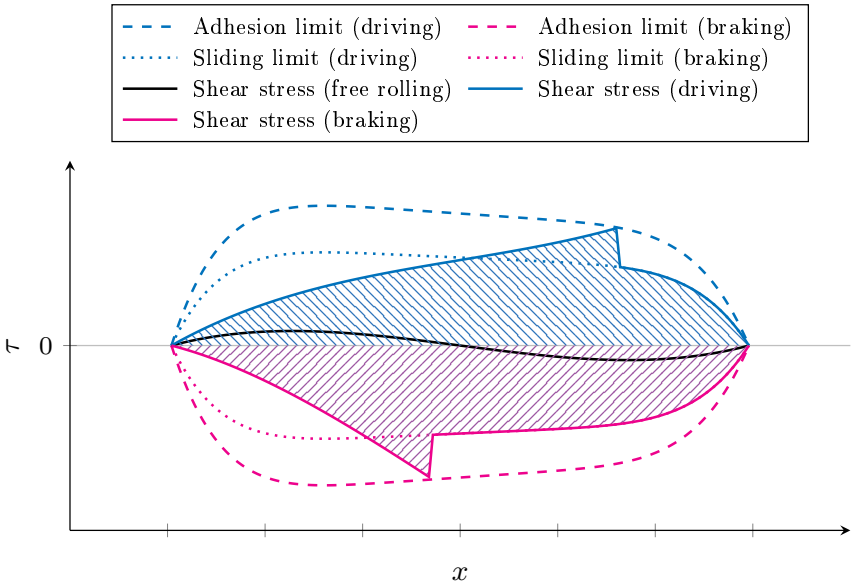

Figure A.1: Shear stress distribution in the tire contact patch for different load conditions. In addition to the basic shear stress distribution (free-rolling condition), a shear stress distribution for both driving and braking is shown. The curves for driving and braking have been selected so that the transmitted forces (area under the respective curve [15]) are equal in magnitude. It is clear that the sliding component is significantly higher for braking, resulting in a longer sliding distance. The adhesion limit as well as the sliding limit have been plotted according to [120].

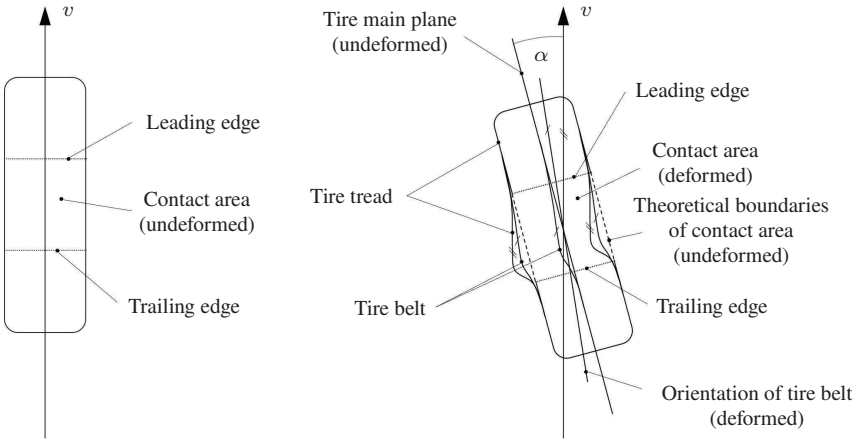

Figure A.2: Schematic representation to explain the higher emission with lateral force in comparison to longitudinal force identified in section 5.1.1.2. The diagram shows a tire running straight ahead (left) and under slip angle (right). The deflection of tread bar elements due to slip angle (between the leading and trailing edge) can be seen (right). In the rear part of the contact patch (between the center of the contact patch and the trailing edge), the surface pressure is decreasing, while the deflection of the tread bar elements continues to increase. Eventually, the shear stress parallel to the road surface becomes too large to be maintained by the surface pressure, so the tread bar elements start sliding and "snap back" into their original position. The high emission is caused by the combination of the existing slip angle α and the snapping back of the tread bar elements.

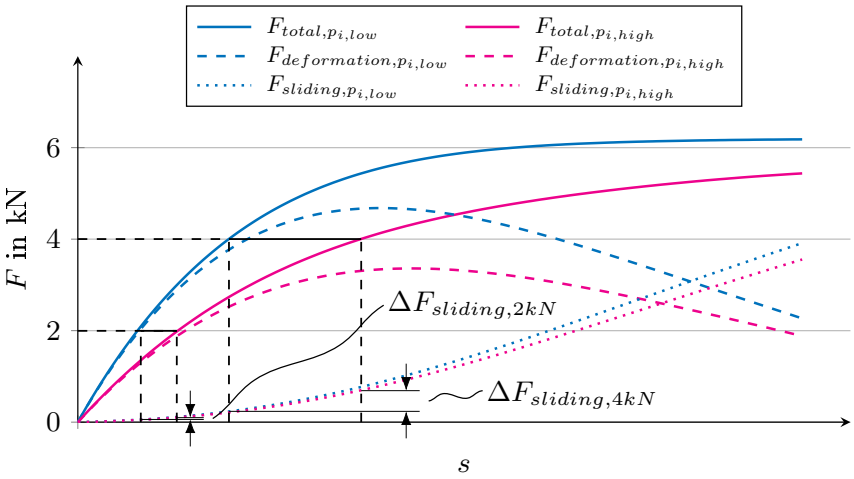

Figure A.3: Relationship between tire force and slip ratio for two different tire inflation pressures. In addition to the absolute tire forces, the respective force components through deformation and sliding are shown [Adapted from 114].

A.4 Tire Tread Profiles

The following illustrations are intended to help clarify the differences between the tire tread patterns described in section 5.1.1.2.

Figure A.4: Tread profile of the summer tire examined.

Figure A.5: Tread profile of the all-season tire examined.

Figure A.6: Tread profile of the winter tire examined.

A.5 Normalized Particle Size Distributions

The following diagrams serve as supplements to the contents shown in section 5.2. They do not contain any new findings compared to those shown before. Nevertheless, they are shown here for the sake of completeness.
Addition to the influence of tire type in section 5.2.5:

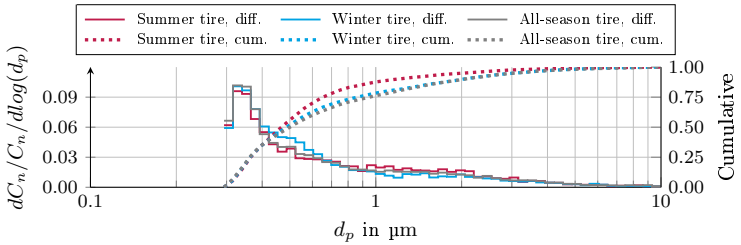

(a) Free rolling

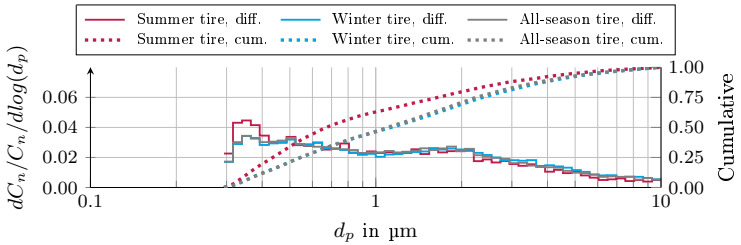

(b) Longitudinal force 4 kN

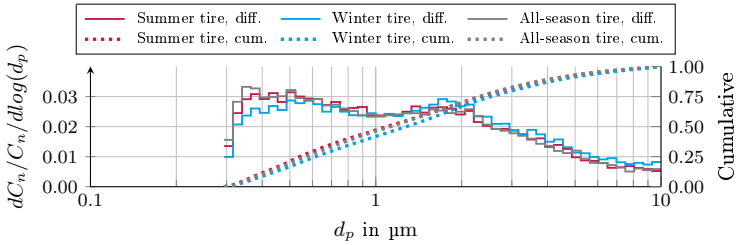

(c) Lateral force 4 kN (identical with Figure 5.26)

Figure A.7: Influence of tire type on the particle size distribution in normalized representation.

Addition to the influence of ambient temperature in section 5.2.6:

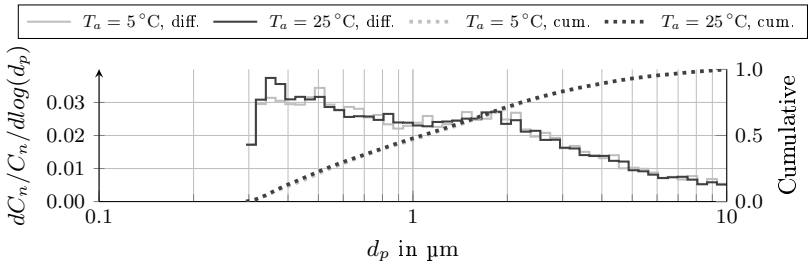

(a) All-season tire with longitudinal force 4 kN

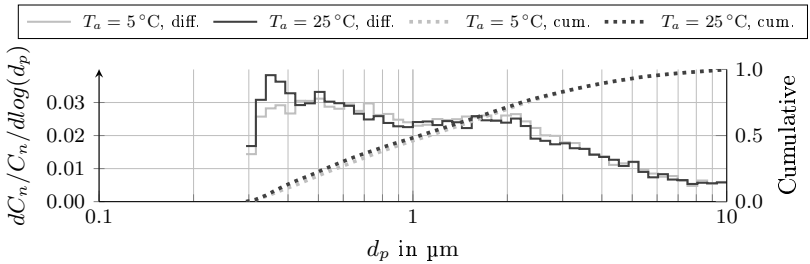

(b) All-season tire with lateral force 4 kN

Figure A.8: Influence of ambient temperature on the particle size distribution of an all-season tire in normalized representation.

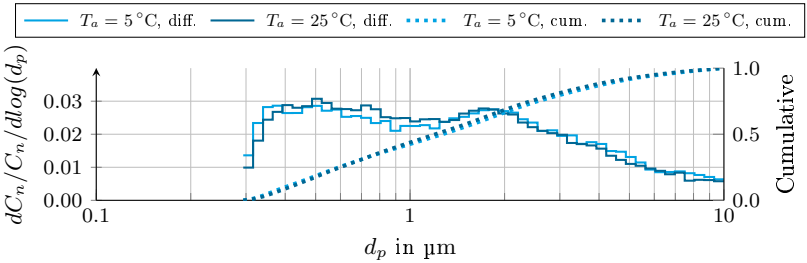

(a) Winter tire with longitudinal force 4 kN

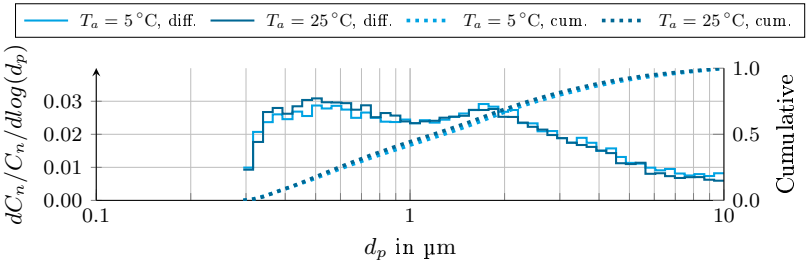

(b) Winter tire with lateral force 4 kN

Figure A.9: Influence of ambient temperature on the particle size distribution of a winter tire in normalized representation.

Addition to the influence of pavement material in section 5.2.7:

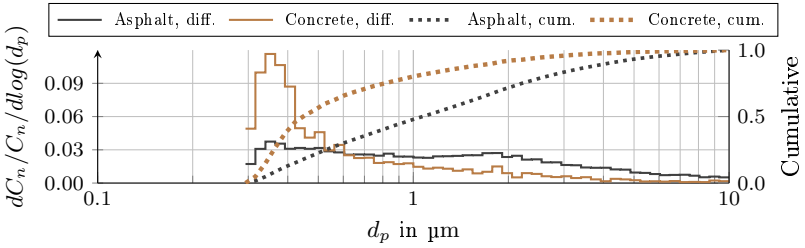

(a) All-season tire with longitudinal force 4 kN

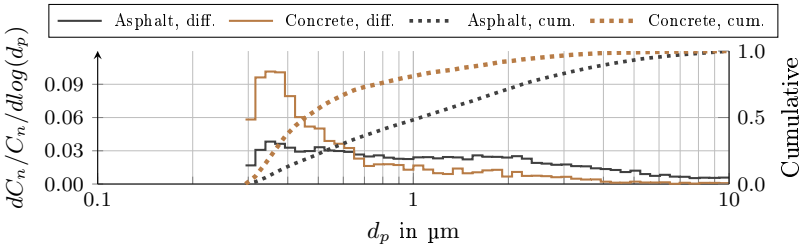

(b) All-season tire with lateral force 4 kN

Figure A.10: Influence of pavement material on the particle size distribution of an all-season tire in normalized representation.

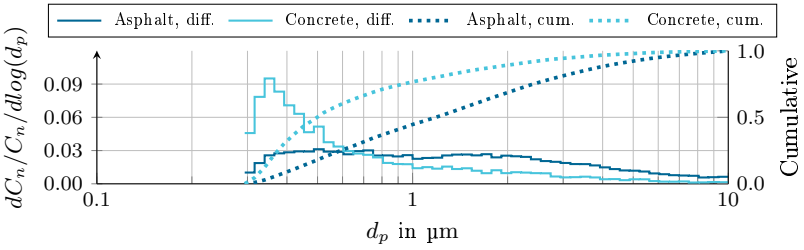

(a) Winter tire with longitudinal force 4 kN

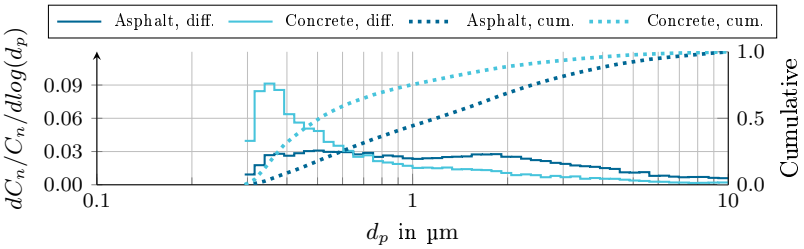

(b) Winter tire with lateral force 4 kN

Figure A.11: Influence of pavement material on the particle size distribution of a winter tire in normalized representation.

A.6 Non-Normalized Particle Size Distributions

The following diagrams serve as a supplement to the normalized particle size distributions shown in section 5.2.
Addition to the influence of tire forces parallel to the road surface in section 5.2.1:

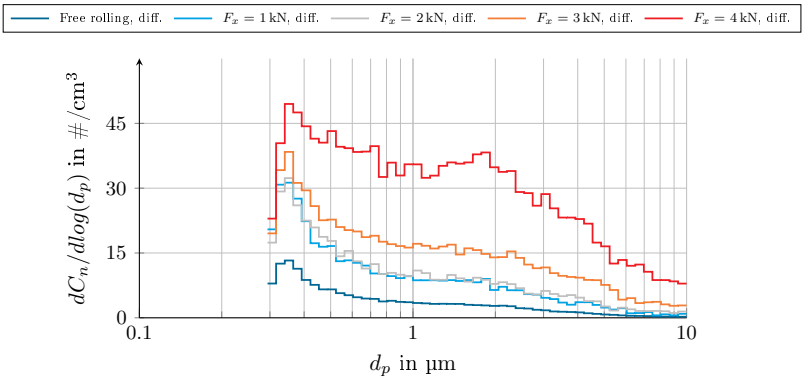

(a) Longitudinal Force [Adapted from 112]

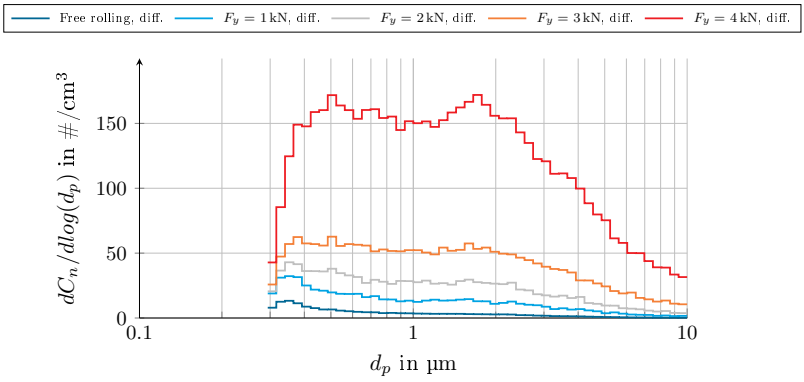

(b) Lateral force

Figure A.12: Influence of tire forces parallel to the road surface on the particle size distribution in non-normalized representation.

Addition to the influence of wheel load in section 5.2.2:

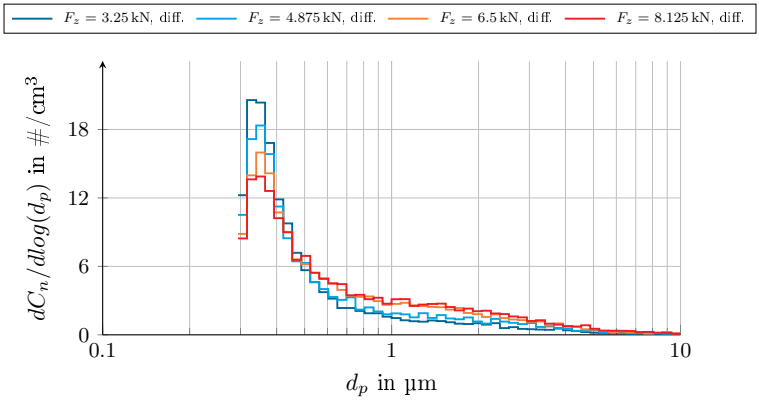

(a) Free rolling

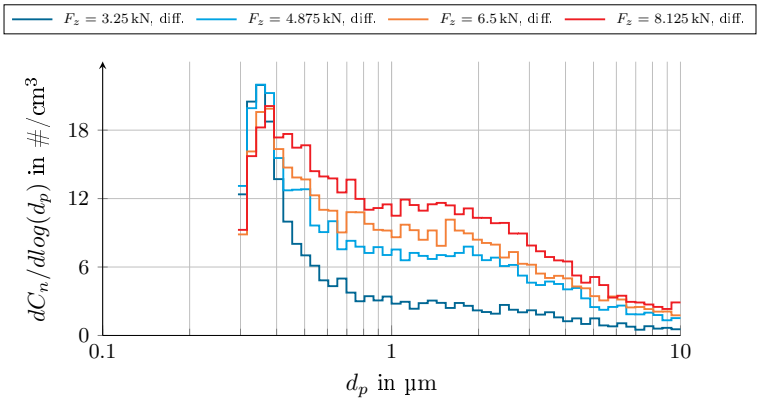

(b) Adhesion utilization 0.62

Figure A.13: Influence of wheel load on the particle size distribution in non-normalized representation [Adapted from 114].

Addition to the influence of tire inflation pressure in section 5.2.3:

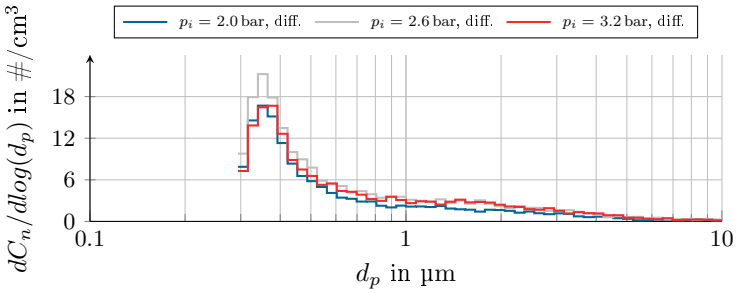

(a) Free rolling

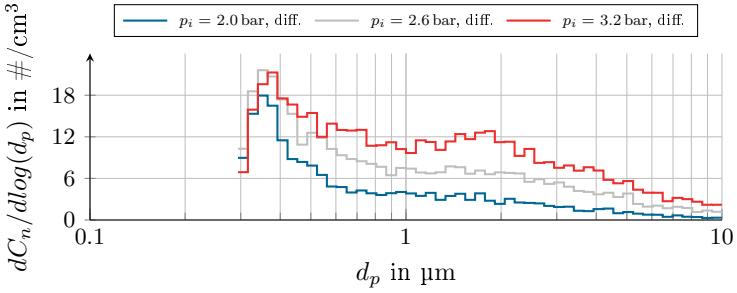

(b) Longitudinal force 4 kN

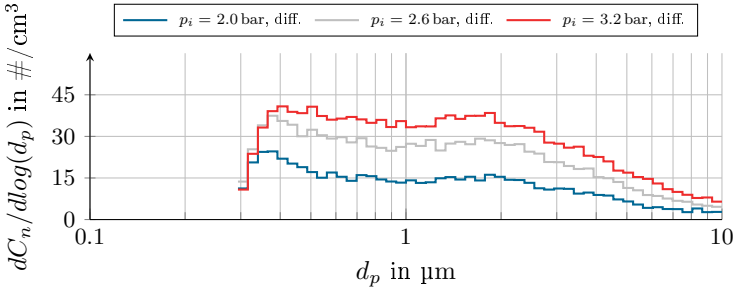

(c) Lateral force 4 kN

Figure A.14: Influence of tire inflation pressure on the particle size distribution in non-normalized representation [Adapted from 114].

Addition to the influence of driving speed in section 5.2.4:

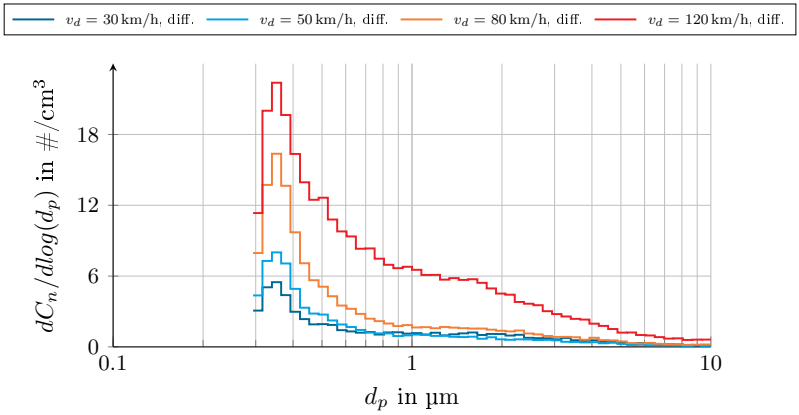

(a) Free rolling

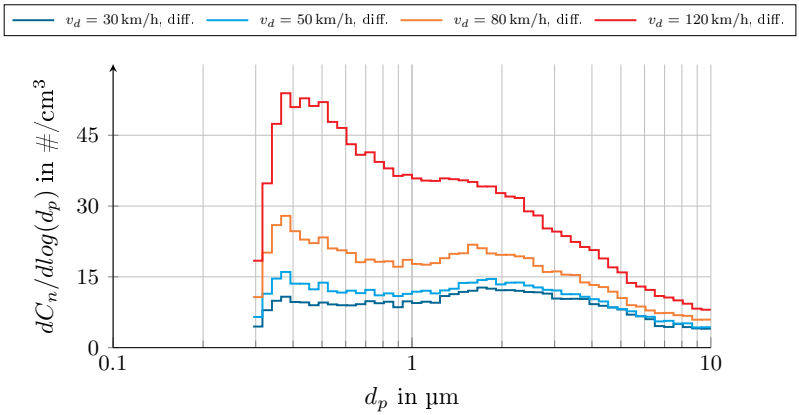

(b) Lateral force 4 kN

Figure A.15: Influence of driving speed on the particle size distribution in non-normalized representation [Adapted from 114].

Addition to the influence of tire type in section 5.2.5:

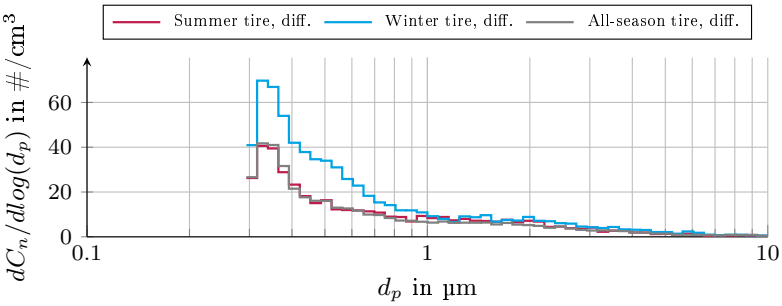

(a) Free rolling

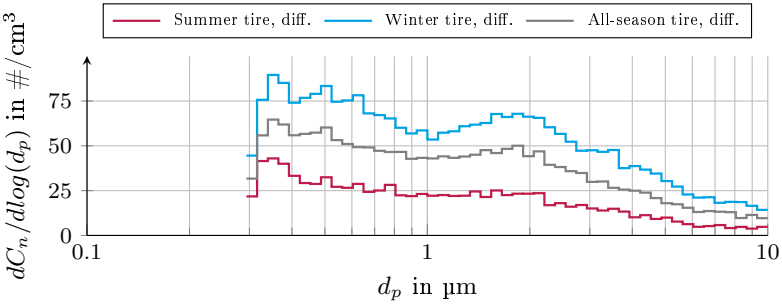

(b) Longitudinal force 4 kN

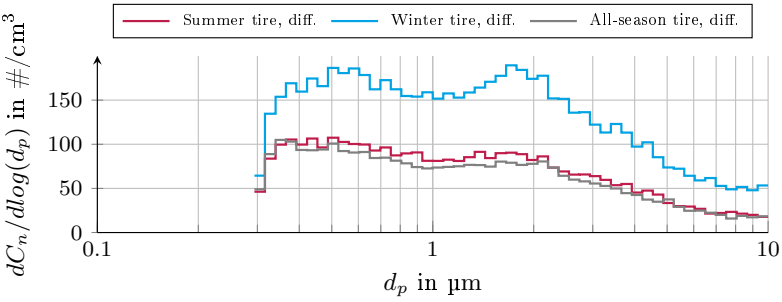

(c) Lateral force 4 kN

Figure A.16: Influence of tire type on the particle size distribution in non-normalized representation.

Addition to the influence of ambient temperature in section 5.2.6:

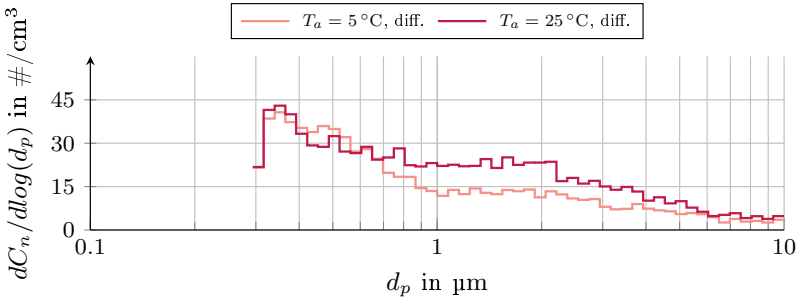

(a) Longitudinal force 4 kN

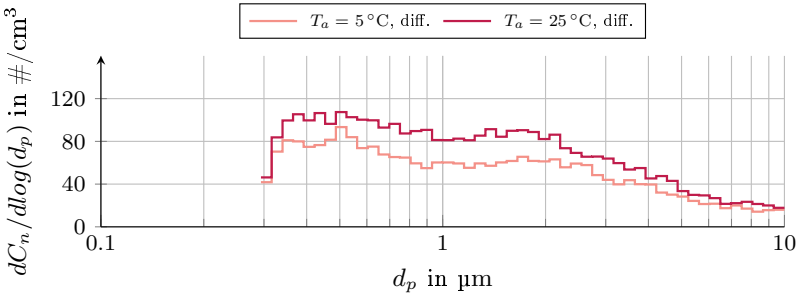

(b) Lateral force 4 kN

Figure A.17: Influence of ambient temperature on the particle size distribution of a summer tire in non-normalized representation.

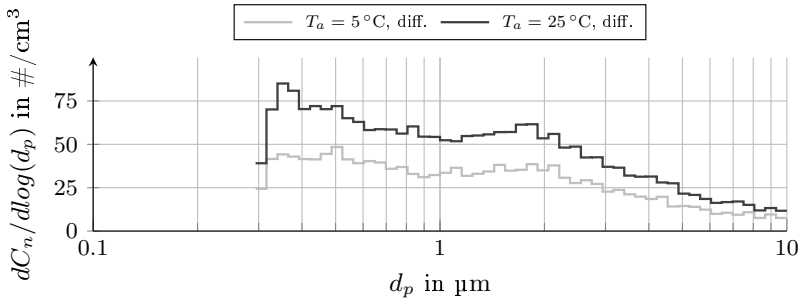

(a) Longitudinal force 4 kN

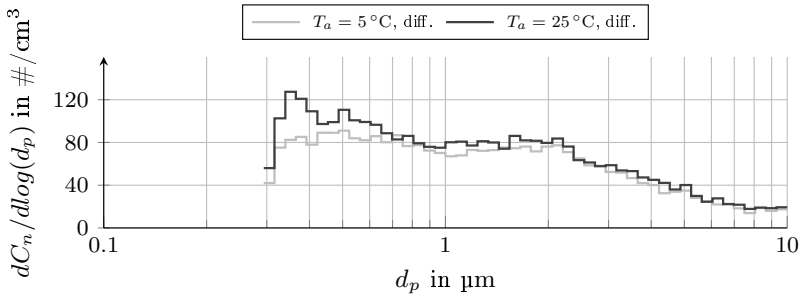

(b) Lateral force 4 kN

Figure A.18: Influence of ambient temperature on the particle size distribution of an all-season tire in non-normalized representation.

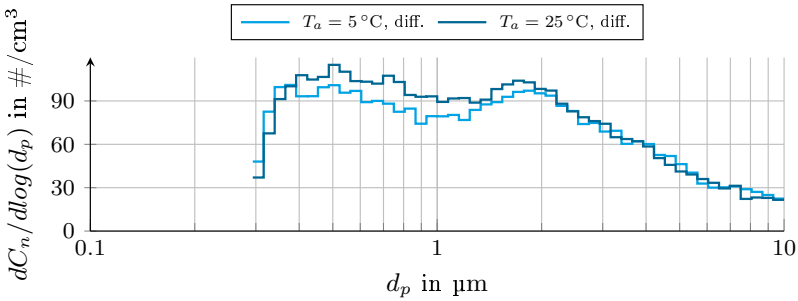

(a) Longitudinal force 4 kN

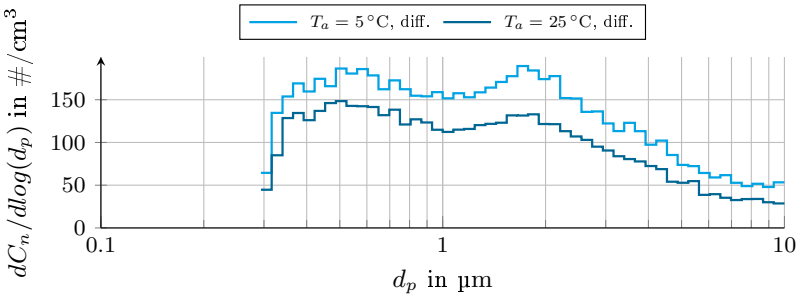

(b) Lateral force 4 kN

Figure A.19: Influence of ambient temperature on the particle size distribution of a winter tire in non-normalized representation.

Addition to the influence of pavement material in section 5.2.7. It should be noted that the SRT values measured during the tests on the asphalt surface were higher than those on the concrete surface. The higher SRT values were accompanied by higher emissions. Therefore, when comparing the non-normalized particle size distributions, it is possible that the total number of particles emitted on asphalt is greater than on concrete, although the total emission diagrams in section 5.1.7 show opposite ratios. The ostensible contradiction is due to the comparison of the total emissions at an SRT value of 60, while the particle size distributions show the emissions at the actually present SRT values:

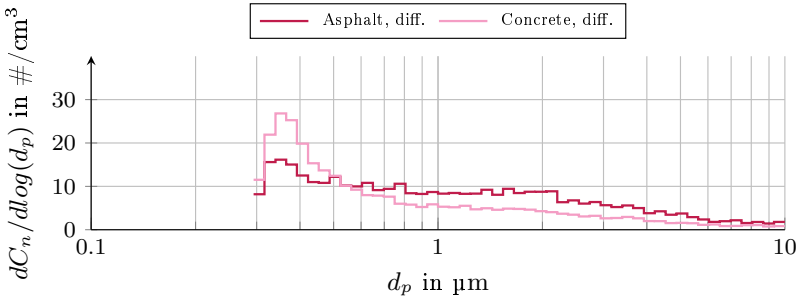

(a) Summer tire with longitudinal force 4 kN

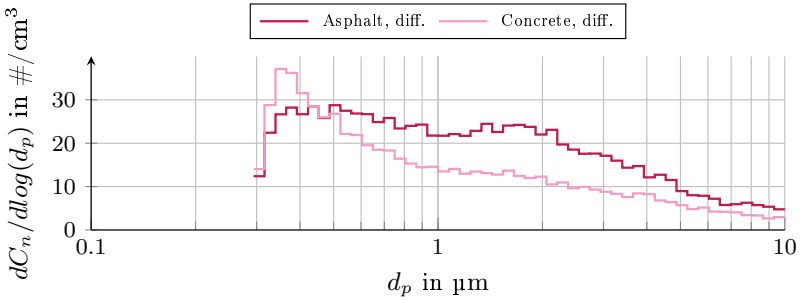

(b) Summer tire with lateral force 4 kN

Figure A.20: Influence of pavement material on the particle size distribution of a summer tire in non-normalized representation.

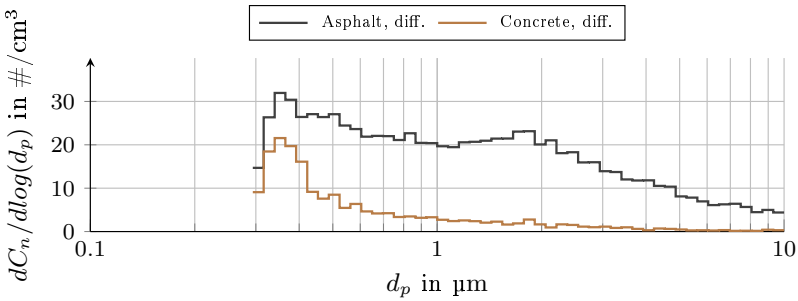

(a) All-season tire with longitudinal force 4 kN

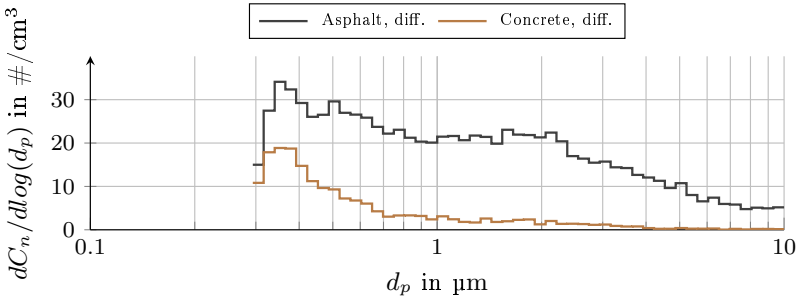

(b) All-season tire with lateral force 4 kN

Figure A.21: Influence of pavement material on the particle size distribution of an all-season tire in non-normalized representation.

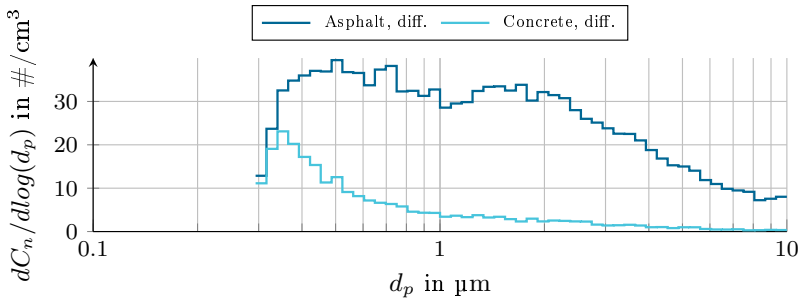

(a) Winter tire with longitudinal force 4 kN

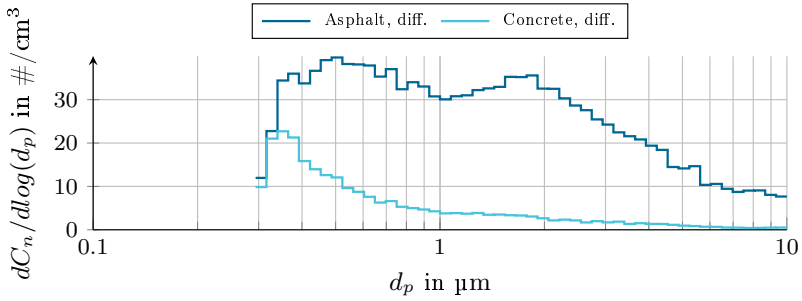

(b) Winter tire with lateral force 4 kN

Figure A.22: Influence of pavement material on the particle size distribution of a winter tire in non-normalized representation.

No non-normalized diagrams are shown for the influence of the SRT value. These would not contain any new findings and the distributions at low SRT values would be hard to recognize, since it is many times smaller than the one at high SRT values.

A.7 Geometric Data of the Vehicle Used

Table A.4: Geometric data of the vehicle used for the model.

Physical parameter	Value	Unit
Axle load distribution front/rear	51.2 %/48.8 %	-
Height of CG	576	mm
Vehicle mass	2297	kg
Wheelbase	3216	mm
Track width front axle	1644	mm
Track width rear axle	1673	mm

A.8 Formulas of the Prediction Model

The following formulas serve as supplement to the emission maps shown in section 6.2. They are to be understood as numerical value equations. If all forces are used in kN and all angles in rad, this results in an emission factor in mg/vkm. Regression functions which the 3D emission map (Figure 6.4) is based on:

$$EF_m(F_{res}, \varphi) = a(\varphi) \cdot {F_{res}}^4 + b(\varphi) \cdot {F_{res}}^2 + c$$
$$\text{for } F_{res} \geq 0, 0 \leq \varphi < 2\pi$$

Driving force with pos. lateral force ($0 \leq \varphi < \frac{\pi}{2}$), wheel load $F_z = 6.5\,\mathrm{kN}$:

$a(\varphi) = -0.8191\varphi^4 + 2.0989\varphi^3 - 0.9034\varphi^2 + 0.3038$

$b(\varphi) = +9.8833\varphi^4 - 31.595\varphi^3 + 25.672\varphi^2 + 0.1454$

$c \quad = + \quad 3.1007$

Braking force with pos. lateral force ($\frac{\pi}{2} \leq \varphi < \pi$), wheel load $F_z = 6.5\,\mathrm{kN}$:

$a(\varphi) = -0.6007\varphi^4 + 6.0966\varphi^3 - 22.343\varphi^2 + 34.378\varphi - 17.620$

$b(\varphi) = +9.9952\varphi^4 - 93.218\varphi^3 + 313.65\varphi^2 - 450.29\varphi + 235.06$

$c \quad = + \quad 3.1007$

Braking force with neg. lateral force ($\pi \leq \varphi < \frac{3\pi}{2}$), wheel load $F_z = 6.5\,\mathrm{kN}$:

$a(\varphi) = -0.6007\varphi^4 + 9.0013\varphi^3 - 49.719\varphi^2 + 120.38\varphi - 107.68$

$b(\varphi) = +9.9952\varphi^4 - 157.99\varphi^3 + 924.11\varphi^2 - 2368.1\varphi + 2243.4$

$c \quad = + \quad 3.1007$

Driving force with neg. lateral force ($\frac{3\pi}{2} \leq \varphi < 2\pi$), wheel load $F_z = 6.5\,\mathrm{kN}$:

$a(\varphi) = -0.8191\varphi^4 + 18.488\varphi^3 - 155.36\varphi^2 + 575.49\varphi - 791.35$

$b(\varphi) = +9.8833\varphi^4 - 216.80\varphi^3 + 1771.2\varphi^2 - 6386.8\varphi + 8580.0$

$c \quad = + \quad 3.1007$

Regression functions which the 4D emission map (Figure 6.6) is based on:

$$EF_m\left(\frac{F_{res}}{F_z},\varphi\right) = \left(a(\varphi)\cdot\left(\frac{F_{res}}{F_z}\right)^4 + b(\varphi)\cdot\left(\frac{F_{res}}{F_z}\right)^2 + c\right)\cdot f_m\left(\frac{F_{res}}{F_z}\right)$$

$$\text{für } \frac{F_{res}}{F_z} \geq 0, 0 \leq \varphi < 2\pi$$

Driving force with pos. lateral force, wheel load $F_z = 6.5\,\mathrm{kN}$:

$a(\varphi) = -1356.8\varphi^4 + 3440.5\varphi^3 - 1411.2\varphi^2 + 526.28$

$b(\varphi) = +418.68\varphi^4 - 1338.0\varphi^3 + 1086.6\varphi^2 + 6.0517$

$c \quad = + \quad 3.1007$

Braking force with pos. lateral force, wheel load $F_z = 6.5\,\mathrm{kN}$:

$a(\varphi) = -961.61\varphi^4 + 9816.4\varphi^3 - 36171\varphi^2 + 55878\varphi - 28599$

$b(\varphi) = +422.71\varphi^4 - 3942.9\varphi^3 + 13269\varphi^2 - 19053\varphi + 9946.6$

$c \quad = + \quad 3.1007$

Braking force with neg. lateral force, wheel load $F_z = 6.5\,\mathrm{kN}$:

$a(\varphi) = -961.61\varphi^4 + 14351\varphi^3 - 78912\varphi^2 + 190155\varphi - 169214$

$b(\varphi) = +422.71\varphi^4 - 6680.9\varphi^3 + 39074\varphi^2 - 100121\varphi + 94841$

$c \quad = + \quad 3.1007$

Driving force with neg. lateral force, wheel load $F_z = 6.5\,\mathrm{kN}$:

$a(\varphi) = -1356.8\varphi^4 + 30658\varphi^3 - 257934\varphi^2 + 956428\varphi + 1316328$

$b(\varphi) = +418.68\varphi^4 - 9184.5\varphi^3 + 75038\varphi^2 - 270597\varphi + 363532$

$c \quad = + \quad 3.1007$

Additional functions $f_m\left(\frac{F_{res}}{F_z}\right)$ required for consideration of wheel loads deviating from $F_z = 6.5\,\mathrm{kN}$:

$$\begin{aligned} f_{m,F_z=3.25\ kN}\left(\frac{F_{res}}{F_z}\right) = &+178.96\cdot\left(\frac{F_{res}}{F_z}\right)^6 - 348.72\cdot\left(\frac{F_{res}}{F_z}\right)^5 \\ &+247.22\cdot\left(\frac{F_{res}}{F_z}\right)^4 - 72.645\cdot\left(\frac{F_{res}}{F_z}\right)^3 \\ &+6.1673\cdot\left(\frac{F_{res}}{F_z}\right)^2 - 0.1166\cdot\left(\frac{F_{res}}{F_z}\right) \\ &+0.5040 \end{aligned}$$

$$\begin{aligned} f_{m,F_z=4.875\ kN}\left(\frac{F_{res}}{F_z}\right) = &+259.45\cdot\left(\frac{F_{res}}{F_z}\right)^6 - 516.87\cdot\left(\frac{F_{res}}{F_z}\right)^5 \\ &+377.77\cdot\left(\frac{F_{res}}{F_z}\right)^4 - 117.07\cdot\left(\frac{F_{res}}{F_z}\right)^3 \\ &+11.802\cdot\left(\frac{F_{res}}{F_z}\right)^2 - 0.3019\cdot\left(\frac{F_{res}}{F_z}\right) \\ &+0.9520 \end{aligned}$$

$$f_{m,F_z=6.5\ kN}\left(\frac{F_{res}}{F_z}\right) = 1$$

$$\begin{aligned} f_{m,F_z=8.125\ kN}\left(\frac{F_{res}}{F_z}\right) = &-561.35\cdot\left(\frac{F_{res}}{F_z}\right)^6 + 1172.1\cdot\left(\frac{F_{res}}{F_z}\right)^5 \\ &-917.07\cdot\left(\frac{F_{res}}{F_z}\right)^4 + 318.23\cdot\left(\frac{F_{res}}{F_z}\right)^3 \\ &-41.221\cdot\left(\frac{F_{res}}{F_z}\right)^2 + 0.9077\cdot\left(\frac{F_{res}}{F_z}\right) \\ &+1.0300 \end{aligned}$$

Formulas used to determine dynamic axle loads due to pitching [15]:

$$F_{z,fa} = \frac{l_{ra}}{l} mg - m \cdot \ddot{x} \cdot \frac{h_{CG}}{l}$$
$$F_{z,ra} = \frac{l_{fa}}{l} mg + m \cdot \ddot{x} \cdot \frac{h_{CG}}{l}$$

where l is the wheelbase, l_{ra} the distance between the Center of Gravity (CG) and the rear axle, l_{fa} is the distance between the CG and the front axle, m the vehicle mass, and h_{CG} is the height of the CG over the road surface. The influence of dynamic axle load distribution due to the design of the wheel suspension and different spring rates front/rear has not been taken into account.

Formulas used to determine dynamic wheel loads due to rolling (for a right bend) [15]:

$$F_{z,fa,l} = \frac{1}{2} \frac{l_{ra}}{l} mg + \frac{h_{CG}}{b} \frac{l_{ra}}{l} m \frac{{v_d}^2}{R}$$
$$F_{z,fa,r} = \frac{1}{2} \frac{l_{ra}}{l} mg - \frac{h_{CG}}{b} \frac{l_{ra}}{l} m \frac{{v_d}^2}{R}$$
$$F_{z,ra,l} = \frac{1}{2} \frac{l_{fa}}{l} mg + \frac{h_{CG}}{b} \frac{l_{ra}}{l} m \frac{{v_d}^2}{R}$$
$$F_{z,ra,r} = \frac{1}{2} \frac{l_{fa}}{l} mg - \frac{h_{CG}}{b} \frac{l_{ra}}{l} m \frac{{v_d}^2}{R}$$

where b is the track width of the vehicle and R the radius of the curve.

A.9 Frequency Analysis of Driving Conditions in the Route Profiles

The following diagrams serve as a supplement to the analyses of the route profiles shown in section 6.1.

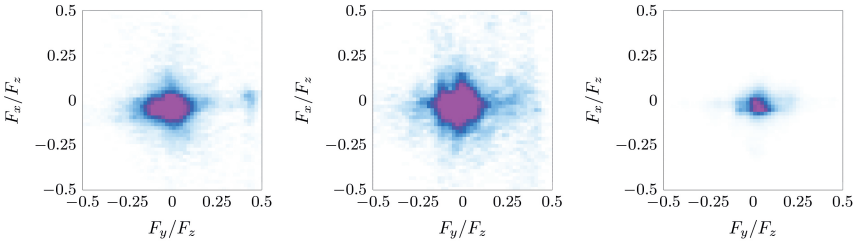

(a) Urban **(b)** Rural **(c)** Highway

Figure A.23: Distribution of driving conditions by frequency of occurrence. The color scale for all three graphs has been chosen so that 25 % of all driving conditions are in the magenta area.

A.10 Emission Maps for Different Route Profiles

The following diagrams serve as a supplement to better visualize the emission depending on the location for the three route profiles shown in section 6.1.

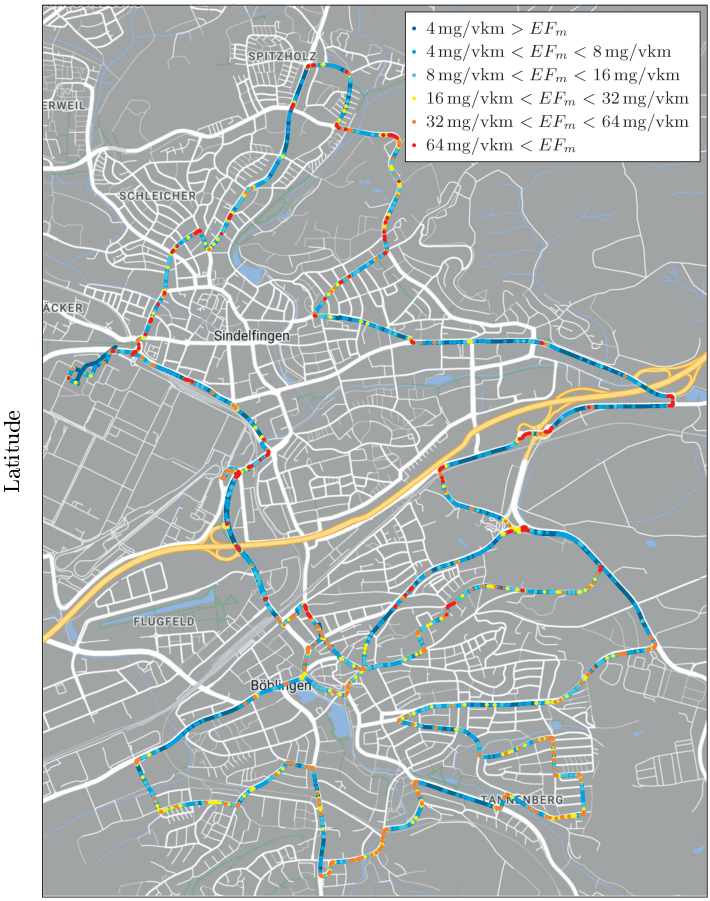

Figure A.24: Prediction of the emission factor of tire–road PM for a luxury-class vehicle driving with summer tires depending on the location for the urban route profile assuming an SRT value of 60 (identical with Figure 6.7).

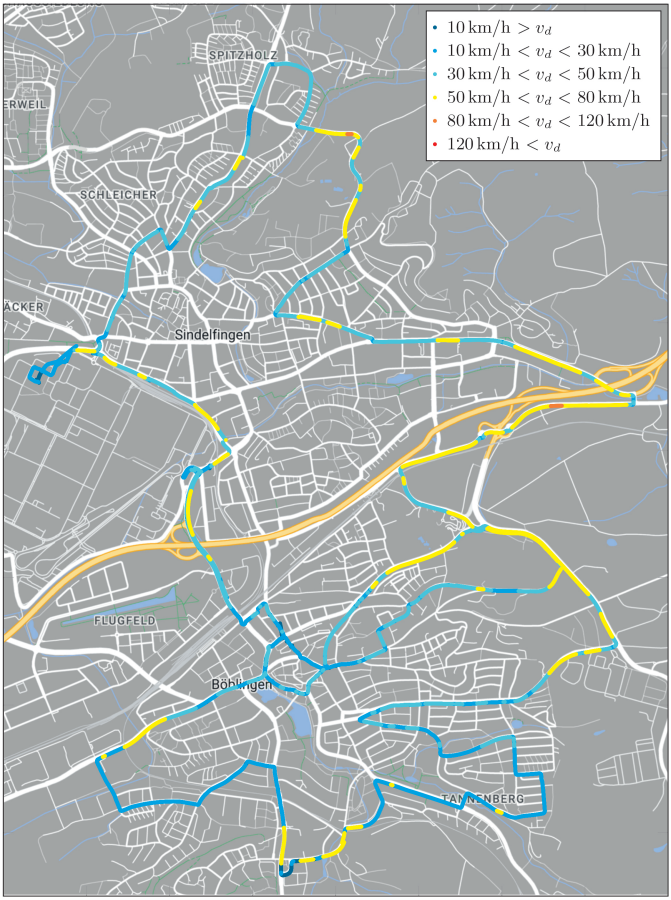

Figure A.25: Location-dependent driving speed for the urban route profile.

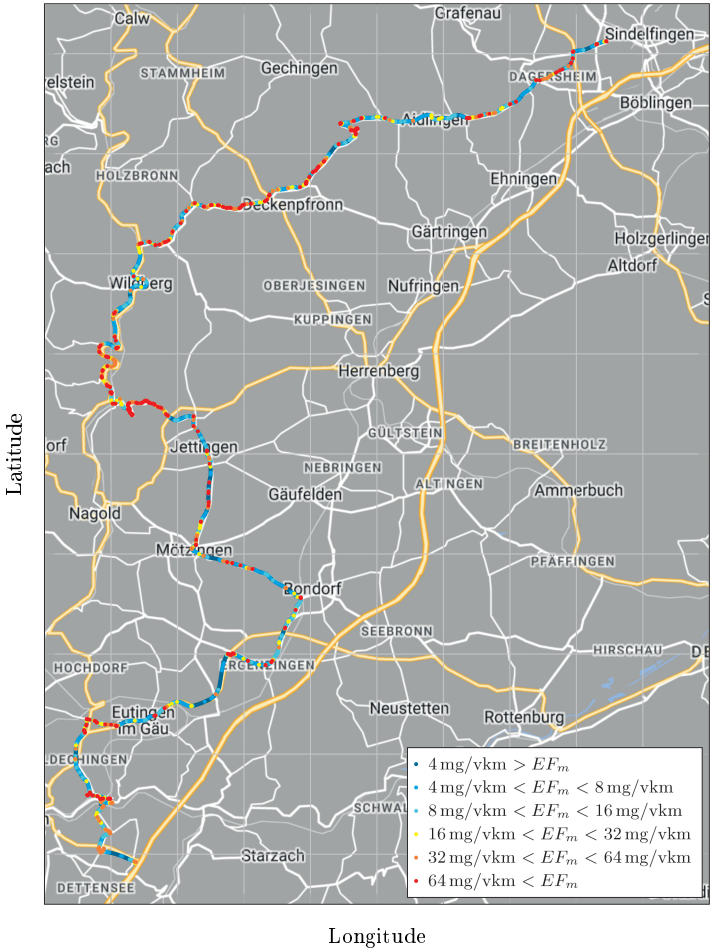

Figure A.26: Prediction of the emission factor of tire–road PM for a luxury-class vehicle driving with summer tires depending on the location for the rural route profile assuming an SRT value of 60.

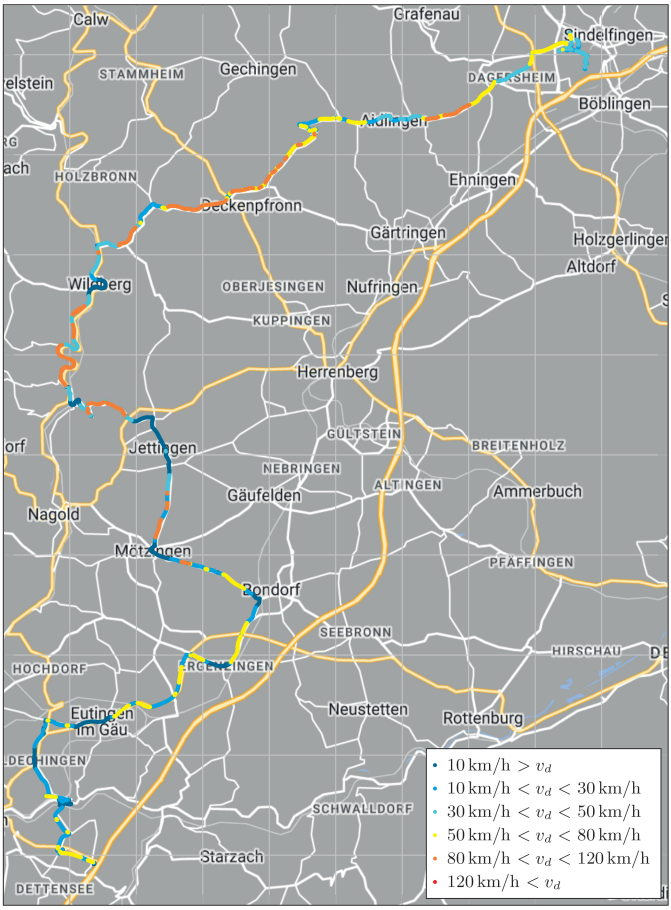

Figure A.27: Location-dependent driving speed for the rural route profile.

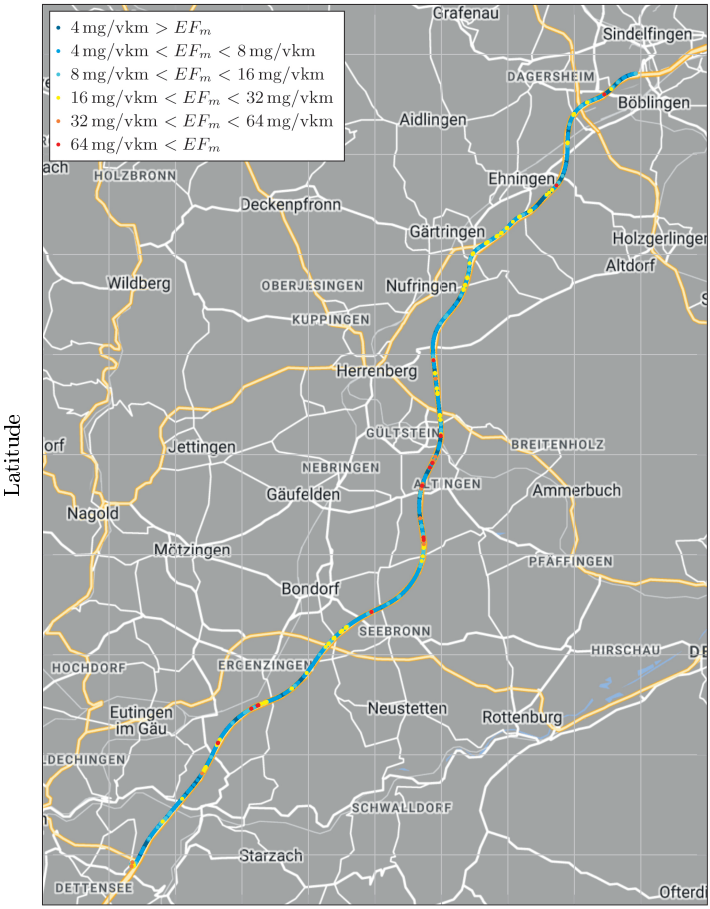

Figure A.28: Prediction of the emission factor of tire–road PM for a luxury-class vehicle driving with summer tires depending on the location for the highway route profile assuming an SRT value of 60.

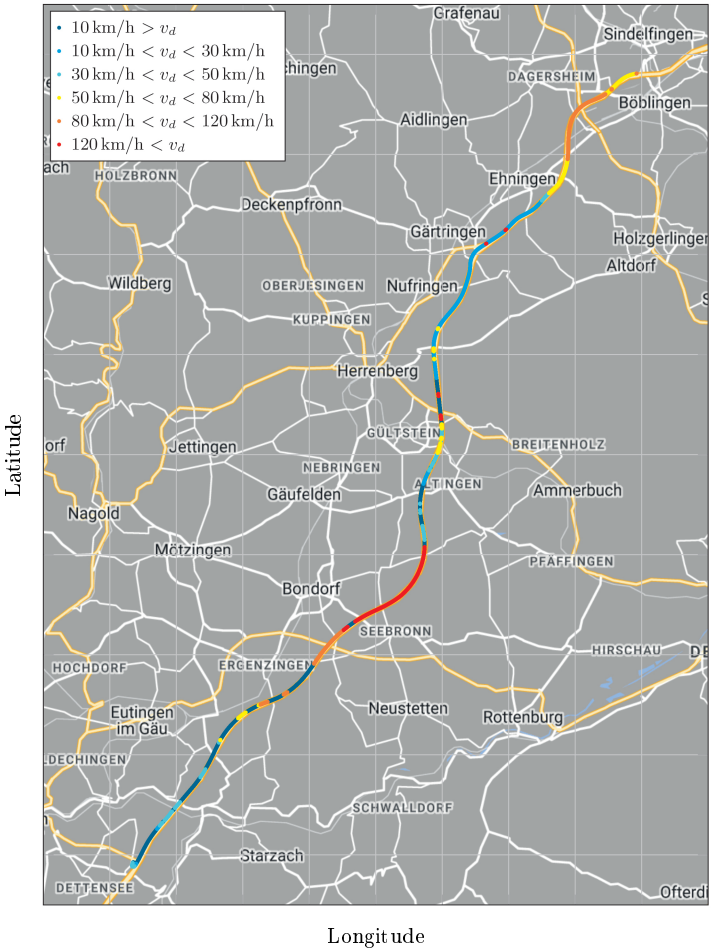

Figure A.29: Location-dependent driving speed for the highway route profile.

List of Figures

List of Tables

Bibliography

[1] Aatmeeyata, D. S. Kaul, and M. Sharma. Traffic generated non-exhaust particulate emissions from concrete pavement: A mass and particle size study for two-wheelers and small cars. *Atmospheric Environment*, 43(35): 5691–5697, 2009. ISSN 13522310. doi: 10.1016/j.atmosenv.2009.07.032.

[2] Air Quality Expert Group. Non-Exhaust Emissions from Road Traffic. Technical Report PB14581, London, UK, 2019. URL `https://uk-air.defra.gov.uk/library/reports.php?report_id=992`.

[3] O. Alexandrova, K. E. Kaloush, and J. O. Allen. Impact of Asphalt Rubber Friction Course Overlays on Tire Wear Emissions and Air Quality Models for Phoenix, Arizona, Airshed. *Transportation Research Record: Journal of the Transportation Research Board*, 2011(1):98–106, 2007. ISSN 0361-1981. doi: 10.3141/2011-11.

[4] J. O. Allen, O. Alexandrova, and K. E. Kaloush. Tire Wear Emissions for Asphalt Rubber and Portland Cement Concrete Pavement Surfaces: Final Report. Technical report, Department of Chemical & Materials Engineering and Department of Civil & Environmental Engineering, Tempe, AZ, USA, April 2006.

[5] Allgemeiner Deutscher Automobil-Club e. V. Auto fit für den Frühling machen: ADAC Nordrhein warnt vor zu frühem Reifenwechsel, 2023. URL `https://presse.adac.de/regionalclubs/nordrhein-westfalen/auto-fit-fuer-den-fruehling-machen-adac-nordrhein-warnt-vor-zu-fruehem-reifenwechsel.html`. Accessed on October 28, 2024.

[6] F. Amato, M. Schaap, H. A. C. Denier van der Gon, M. Pandolfi, A. Alastuey, M. Keuken, and X. Querol. Effect of rain events on the mobility of road dust load in two Dutch and Spanish roads. *Atmospheric Environment*, 62: 352–358, 2012. ISSN 13522310. doi: 10.1016/j.atmosenv.2012.08.042.

[7] C. Asbach, A. M. Todea, M. Zessinger, and H. Kaminski. Entstehung und Möglichkeiten zur Messung von Fein- und Ultrafeinstaub beim Bremsen. In R. Meyer, editor, *XXXVII. Internationales µ-Symposium 2018 Bremsen-Fachtagung*, pages 45–67, Berlin, Germany, 2019. Springer Vieweg. ISBN 978-3-662-58024-0. doi: 10.1007/978-3-662-58024-0_4.

[8] B. Baensch-Baltruschat, B. Kocher, F. Stock, and G. Reifferscheid. Tyre and road wear particles (TRWP) - A review of generation, properties, emissions, human health risk, ecotoxicity, and fate in the environment. *Science of The Total Environment*, 733, 2020. ISSN 00489697. doi: 10.1016/j.scitotenv.2020.137823.

[9] H. J. Beckedahl. Straßenbau. In C. Gertz, editor, *Verkehrsplanung, Bau und Betrieb von Verkehrsanlagen*, pages 109–128. Springer Fachmedien Wiesbaden, Wiesbaden, Germany, 2021. ISBN 978-3-658-29500-4.

[10] D. C. S. Beddows and R. M. Harrison. PM10 and PM2.5 emission factors for non-exhaust particles from road vehicles: Dependence upon vehicle mass and implications for battery electric vehicles. *Atmospheric Environment*, 244: 117886, 2021. ISSN 13522310. doi: 10.1016/j.atmosenv.2020.117886.

[11] A. Beji, K. Deboudt, S. Khardi, B. Muresan, and L. Lumière. Determinants of rear-of-wheel and tire–road wear particle emissions by light-duty vehicles using on-road and test track experiments. *Atmospheric Pollution Research*, 12(3):278–291, 2021. ISSN 13091042. doi: 10.1016/j.apr.2020.12.014.

[12] I. Belkacem, A. Helali, S. Khardi, and K. Slimi. Investigations on vehicle non-exhaust particle emissions: real-time measurements. *International Journal of Environmental Science and Technology*, 19(12):11749–11762, 2022. ISSN 1735-1472. doi: 10.1007/s13762-022-03955-w.

[13] P. G. Boulter. A Review of Emission Factors and Models for Road Vehicle Non-Exhaust Particulate Matter. Technical Report PPR065, TRL Limited, London, UK, 2005. URL https://uk-air.defra.gov.uk/library/reports?report_id=364.

[14] P. G. Boulter, A. J. Thorpe, R. M. Harrison, and A. G. Allen. Road Vehicle Non-Exhaust Particulate Matter: Final Report on Emission Modelling: Published Project Report. Technical Report PPR110, Crowthorne, UK, June 2006.

[15] S. Breuer and A. Rohrbach-Kerl. *Fahrzeugdynamik: Mechanik des bewegten Fahrzeugs*. Springer Fachmedien Wiesbaden, Wiesbaden, Germany, 2015. ISBN 978-3-658-09474-4. doi: 10.1007/978-3-658-09475-1.

[16] N. Bukowiecki, P. Lienemann, M. Hill, M. Furger, A. Richard, F. Amato, A. S. H. Prévôt, U. Baltensperger, B. Buchmann, and R. Gehrig. PM10 emission factors for non-exhaust particles generated by road traffic in an urban street canyon and along a freeway in Switzerland. *Atmospheric Environment*, 44(19):2330–2340, 2010. ISSN 13522310. doi: 10.1016/j.atmosenv.2010.03.039.

[17] Bundesamt für Justiz. Gesetz zum Schutz vor schädlichen Umwelteinwirkungen durch Luftverunreinigungen, Geräusche, Erschütterungen und ähnliche Vorgänge: Bundes-Immissionsschutzgesetz - BImSchG, 15.03.1974. URL https://www.gesetze-im-internet.de/bimschg/BJNR007210974.html. 7. Mai 2013 BGBl. I S. 1274; 2021 I S. 123), das zuletzt durch Artikel 11 Absatz 3 des Gesetzes vom 26. Juli 2023 (BGBl. 2023 I Nr. 202) geändert worden ist.

[18] Bundesministerium für Umwelt, Naturschutz, nukleare Sicherheit und Verbraucherschutz. Feinstaub, 2022. URL https://www.bmuv.de/themen/gesundheit/luftreinhaltung/feinstaub. Accessed on April 5, 2024.

[19] S. H. Cadle and R. L. Williams. Gas and Particle Emissions from Automobile Tires in Laboratory and Field Studies. *Journal of the Air Pollution Control Association*, 28(5):502–507, 1978. ISSN 0002-2470. doi: 10.1080/00022470.1978.10470623.

[20] J. Cao, H. Huang, R. Jiao, J. Pei, Y. Xu, RuiRen, and Y. Wang. The study of wear particle emissions of soft rubber on rolling contact under braking conditions. *Wear*, 506-507:204431, 2022. doi: 10.1016/j.wear.2022.204431.

[21] X. Chang, H. Huang, R. Jiao, and J. Liu. Experimental investigation on the characteristics of tire wear particles under different non-vehicle operating parameters. *Tribology International*, 150:106354, 2020. ISSN 0301679X. doi: 10.1016/j.triboint.2020.106354.

[22] T. Charbouillot, D. C. Janet, P. Schaal, I. Beynier, J.-M. Boulat, A. Grandchamp, and F. Biesse. Methodology for the direct measurement of tire emission factors. *Science of The Total Environment*, 863:160853, 2023. ISSN 00489697. doi: 10.1016/j.scitotenv.2022.160853.

[23] A. J. Cohen, M. Brauer, R. Burnett, H. R. Anderson, J. Frostad, K. Estep, K. Balakrishnan, B. Brunekreef, L. Dandona, R. Dandona, V. Feigin, G. Freedman, B. Hubbell, A. Jobling, H. Kan, L. Knibbs, Y. Liu, R. Martin, L. Morawska, C. A. Pope, H. Shin, K. Straif, G. Shaddick, M. Thomas, R. van Dingenen, A. van Donkelaar, T. Vos, C. J. L. Murray, and M. H. Forouzanfar. Estimates and 25-year trends of the global burden of disease attributable to ambient air pollution: an analysis of data from the Global Burden of Diseases Study 2015. *The Lancet (London, England)*, 389(10082):1907–1918, 2017. doi: 10.1016/S0140-6736(17)30505-6.

[24] I. Cunha-Lopes, C. A. Alves, I. Casotti Rienda, T. Faria, F. Lucarelli, X. Querol, F. Amato, and S. M. Almeida. Characterisation of non-exhaust emissions from road traffic in Lisbon. *Atmospheric Environment*, 286: 119221, 2022. ISSN 13522310. doi: 10.1016/j.atmosenv.2022.119221.

[25] Deutsches Institut für Normung e. V. *DIN ISO 7708:1995, Luftbeschaffenheit — Festlegung von Partikelgrößenverteilungen für die gesundheitsbezogene Schwebstaubprobenahme*. Beuth Verlag GmbH, Berlin, Germany, 1996.

[26] Deutsches Institut für Normung e. V. *DIN EN 13036-3:2002, Oberflächeneigenschaften von Straßen und Flugplätzen, Prüfverfahren Teil 3: Messung der horizontalen Entwässerung von Deckschichten*. Beuth Verlag GmbH, Berlin, Germany, 2003.

[27] Deutsches Institut für Normung e. V. *DIN ISO 13473-2:2002, Charakterisierung der Textur von Fahrbahnbelägen unter Verwendung von Oberflächenprofilen – Teil 2: Begriffe und grundlegende Anforderungen für die Analyse von Fahrbahntexturprofilen*. Beuth Verlag GmbH, Berlin, Germany, 2004.

[28] Deutsches Institut für Normung e. V. *DIN EN 13036-4:2011, Oberflächeneigenschaften von Straßen und Flugplätzen – Prüfverfahren – Teil 4: Verfahren zur Messung der Griffigkeit von Oberflächen: Der Pendeltest: Deutsche Fassung*. Beuth Verlag GmbH, Berlin, Germany, 2011.

[29] Deutsches Institut für Normung e. V. *DIN ISO 8855:2011, Straßenfahrzeuge — Fahrzeugdynamik und Fahrverhalten — Begriffe*. Beuth Verlag GmbH, Berlin, Germany, 2011.

[30] Deutsches Institut für Normung e. V. *DIN EN ISO 16890-1:2016, Luftfilter für die allgemeine Raumlufttechnik - Teil 1: Technische Bestimmungen, Anforderungen und Effizienzklassifizierungssystem, basierend auf dem Feinstaubabscheidegrad*. Beuth Verlag GmbH, Berlin, Germany, 2017.

[31] Deutsches Institut für Normung e. V. DIN EN 1822-1:2019, Schwebstoffilter (EPA, HEPA und ULPA) – Teil 1: Klassifikation, Leistungsprüfung, Kennzeichnung, 2019.

[32] Deutsches Institut für Normung e. V. *DIN EN 12341:2014, Außenluft – Gravimetrisches Standardmessverfahren für die Bestimmung der PM10 oder*

PM2,5-Massenkonzentration des Schwebstaubes; Deutsche Fassung. Beuth Verlag GmbH, Berlin, Germany, 2023.

[33] L. Drüschner, H. Els, U. Habermann, B. Nolle, V. Rauschenbach, S. Sadzulewsky, M. Schellenberger, H. Schgeiner, H. Schmidt, and N. Weiland. Asphaltdeckschichten mit anforderungsgerechter Griffigkeit: Maßnahmenkatalog für Planung und Ausführung. Technical report, Bonn - Berlin, Germany, 2006.

[34] European Commission. Regulation of the European Parliament and of the Council: on type-approval of motor vehicles and engines and of systems, components and separate technical units intended for such vehicles, with respect to their emissions and battery durability (Euro 7) and repealing Regulations (EC) No 715/2007 and (EC) No 595/2009. URL `https://ec.europa.eu/commission/presscorner/detail/en/IP_22_6495`. Accessed on May 10, 2024.

[35] European Environment Agency. How air pollution affects our health, 2023. URL `https://www.eea.europa.eu/en/topics/in-depth/air-pollution/eow-it-affects-our-health`. Accessed on June 4, 2024.

[36] T. Feißel, D. Hesse, V. Ricciardi, M. Schiele, and K. Augsburg. Novel approaches for measuring and predicting particulate emissions from automotive brakes and tires. In P. E. Pfeffer, editor, *12th International Munich Chassis Symposium 2021*, ATZ live, pages 708–728, Berlin, Germany and Heidelberg, 2022. Springer Vieweg. ISBN 978-3-662-64550-5. doi: 10.1007/978-3-662-64550-57.

[37] M.-J. Foitzik, H.-J. Unrau, F. Gauterin, J. Dornhöfer, and T. Koch. Investigation of Ultra Fine Particulate Matter Emission of Rubber Tires. *Wear*, (394-395):87–95, 2018. doi: 10.1016/j.wear.2017.09.023.

[38] Forschungsgesellschaft für Straßen- und Verkehrswesen e. V. *TP Griff-StB (SRT): Technische Prüfvorschriften für Griffigkeitsmessungen im Straßenbau: Teil: Messverfahren SRT*. Cologne, Germany, 2004.

[39] Forschungsgesellschaft für Straßen- und Verkehrswesen e. V. *ZTV Asphalt-StB 07/13, Zusätzliche technische Vertragsbedingungen und Richtlinien für den Bau von Verkehrsflächenbefestigungen aus Asphalt*. FGSV R1 - Regelwerke. FGSV, Cologne, Germany, 2007.

[40] J. C. Fussell, M. Franklin, David C. Green, M. Gustafsson, R. M. Harrison, W. Hicks, F. J. Kelly, F. Kishta, M. R. Miller, I. S. Mudway, F. Oroumiyeh, L. Selley, M. Wang, and Y. Zhu. A Review of Road Traffic-Derived Non-Exhaust Particles: Emissions, Physicochemical Characteristics, Health Risks, and Mitigation Measures. *Environmental Science & Technology*, 56(11): 6813–6835, 2022. ISSN 0013-936X. doi: 10.1021/acs.est.2c01072.

[41] S. D. Gehman, K. C. Ludema, S. Backer, T. Takeyama, and J. Matsui. Material Characteristics. In S. K. Clark, editor, *Mechanics of Pneumatic Tires*, pages 1–305. U.S. Department of Transportation, Washington D.C., USA, 1971.

[42] B. Giechaskiel, T. Grigoratos, M. Mathissen, J. Quik, P. Tromp, M. Gustafsson, V. Franco, and P. Dilara. Contribution of Road Vehicle Tyre Wear to Microplastics and Ambient Air Pollution. *Sustainability*, 16(2):522, 2024. doi: 10.3390/su16020522.

[43] R. Gnadler, H.-J. Unrau, H. Fischlein, and M. Frey. Ermittlung von µ-Schlupf-Kurven an Pkw-Reifen. *FAT Schriftenreihe*, 119, Januar 1995.

[44] A. Grant. Dust to Dust: As new research provides the clearest picture yet of the production and distribution of tire and road wear particles, how might this growing debate affect future tire – and even infrastructure – development? Investigating TRWP. *Tire Technology International*, pages 18–24, 2022.

[45] T. Grigoratos and G. Martini. Non-exhaust traffic related emissions. Brake and tyre wear PM: Literature review. Technical Report EUR 26648 EN, Institute of Energy and Transport, Joint Reserach Centre, European Commission, Luxembourg, Luxembourg, 2014.

[46] M. Gustafsson, G. Blomqvist, A. Gudmundsson, A. Dahl, E. Swietlicki, M. Bohgard, J. Lindbom, and A. Ljungman. Properties and toxicological effects of particles from the interaction between tyres, road pavement and winter traction material. *Science of The Total Environment*, 393(2-3):226–240, 2008. ISSN 00489697. doi: 10.1016/j.scitotenv.2007.12.030.

[47] M. Gustafsson, G. Blomqvist, A. Gudmundsson, A. Dahl, P. Jonsson, and E. Swietlicki. Factors influencing PM10 emissions from road pavement wear. *Atmospheric Environment*, 43(31):4699–4702, 2009. ISSN 13522310. doi: 10.1016/j.atmosenv.2008.04.028.

[48] M. Haugen, P. Bühler, S. Schläfle, D. O'Loughlin, S. Saladin, C. Giorio, and A. Boies. Method development and analysis of nanoparticle size fractions from tire-wear emissions. *Environmental Science: Atmospheres*, 4(9):1079–1090, 2024. doi: 10.1039/D4EA00048J.

[49] J. Heseding and T. Dieckmann. How an Electric Drive in a Semitrailer Improves the Overall Vehicle Performance. In P. E. Pfeffer, editor, *12th International Munich Chassis Symposium 2021*, ATZ live, pages 109–123, Berlin, Germany and Heidelberg, 2022. Springer Vieweg. ISBN 978-3-662-64550-5. doi: 10.1007/978-3-662-64550-57.

[50] D. Hesse, T. Feißel, M. Kunze, E. Bachmann, T. Bachmann, and S. Gramstat. Comparison of Methods for Sampling Particulate Emissions from Tires under Different Test Environments. *Atmosphere*, 13(8):1262, 2022. doi: 10.3390/atmos13081262.

[51] W. C. Hinds. *Aerosol Technology: Properties, Behavior, and Measurement of Airborne Particles*. Wiley-Interscience, New York, USA, second edition, 1999. ISBN 978-0-471-19410-1.

[52] N. Hooftman, L. Oliveira, M. Messagie, T. Coosemans, and J. van Mierlo. Environmental Analysis of Petrol, Diesel and Electric Passenger Cars in a Belgian Urban Setting. *Energies*, 9(2):84, 2016. doi: 10.3390/en9020084.

[53] S. Huschek. Kennzeichnung und Auswirkungen der Textur von Fahrbahnoberflächen. In B. Breuer, editor, *2. Darmstädter Reifenkolloquium*, Fortschritt-Berichte / VDI Reihe 12, Verkehrstechnik/Fahrzeugtechnik, Düsseldorf, Germany, 1998. VDI Verlag. ISBN 3-18-336212-0.

[54] T. Hussein, C. Johansson, H. Karlsson, and H.-C. Hansson. Factors affecting non-tailpipe aerosol particle emissions from paved roads: On-road measurements in Stockholm, Sweden. *Atmospheric Environment*, 42(4):688–702, 2008. ISSN 13522310. doi: 10.1016/j.atmosenv.2007.09.064.

[55] International Organization for Standardization. *ISO 9096:2017, Stationary source emissions — Manual determination of mass concentration of particulate matter*. ISO copyright office, Geneva, Switzerland, 2017.

[56] International Organization for Standardization. *ISO 12103-1:2024, Road vehicles - Test contaminants for filter evaluation - Part 1: Arizona test dust*. ISO copyright office, Geneva, Switzerland, 2024.

[57] D. Jansen and M. Pöppel-Decker. *Griffigkeitsprognose an offenporigen Asphalten - Teil 2: Neue Baumaßnahmen*, volume Heft S 72 of *Berichte der Bundesanstalt für Straßenwesen*. Wirtschaftsverl. NW Verl. für neue Wiss, Bergisch Gladbach, Germany, 2011. ISBN 978-3-86918-149-3. URL https://edocs.tib.eu/files/e01fn14/797391630.pdf.

[58] R. Jansen, L. Geers, R. Kranenburg, P. Coenen, and M. Schaap. Particulate matter formation potential of gas-phase emissions over Germany: Final report. Technical report, TNO Utrecht, Dessau-Roßlau, Germany, 2023. URL https://www.umweltbundesamt.de/sites/default/files/medien/11850/publikationen/107_2023_texte_particulate_matter_formation_potential_of_gas-phase_emissions_over_germany.pdf.

[59] M. Kappel. *Angewandter Straßenbau: Straßenfertiger im Einsatz*. Springer Fachmedien Wiesbaden, Wiesbaden, Germany, third edition, 2020. ISBN 978-3-658-29469-4. doi: 10.1007/978-3-658-29470-0.

[60] M. Kayhanian, E. R. McKenzie, J. E. Leatherbarrow, and T. M. Young. Characteristics of road sediment fractionated particles captured from paved surfaces, surface run-off and detention basins. *Science of The Total Environment*, 439:172–186, 2012. ISSN 00489697. doi: 10.1016/j.scitotenv.2012.08.077.

[61] G. Kim and S. Lee. Characteristics of Tire Wear Particles Generated by a Tire Simulator under Various Driving Conditions. *Environmental Science & Technology*, 52(21):12153–12161, 2018. ISSN 0013-936X. doi: 10.1021/acs.est.8b03459.

[62] F. Küçükay. *Grundlagen der Fahrzeugtechnik*. Springer Fachmedien Wiesbaden, Wiesbaden, Germany, 2022. ISBN 978-3-658-36726-8. doi: 10.1007/978-3-658-36727-5.

[63] Z. Klimont, J. Cofala, I. Bertok, M. Amann, C. Heyes, and F. Gyarfas. Modelling Particulate Emissions in Europe: A Framework to Estimate Reduction Potential and Control Costs: Interim Report IR-02-076. Technical Report IR-02-076, Laxenburg, Austria, 2002. URL `https://pure.iiasa.ac.at/id/eprint/6712/1/IR-02-076.pdf`.

[64] M. Kovochich, M. Liong, J. A. Parker, S. C. Oh, J. P. Lee, L. Xi, M. L. Kreider, and K. M. Unice. Chemical mapping of tire and road wear particles for single particle analysis. *Science of The Total Environment*, 757:144085, 2021. ISSN 00489697. doi: 10.1016/j.scitotenv.2020.144085.

[65] M. L. Kreider, J. M. Panko, B. L. McAtee, L. I. Sweet, and B. L. Finley. Physical and chemical characterization of tire-related particles: comparison of particles generated using different methodologies. *Science of The Total Environment*, 408(3):652–659, 2010. ISSN 00489697. doi: 10.1016/j.scitotenv.2009.10.016.

[66] KSL Staubtechnik GmbH. eskal Körnungen: Produktinformation, 2012. URL `https://www.ksl-staubtechnik.de/wp-content/uploads/2021/10/364-INFO-eskal-Koernungen-de-en.pdf`.

[67] KSL Staubtechnik GmbH. escor Körnungen: Produktinformation, 2022. URL https://www.ksl-staubtechnik.de/wp-content/uploads/2021/10/1134-INFO-escor-Koernungen-de-en.pdf.

[68] KSL Staubtechnik GmbH. esqua Quarz-Sande: Produktinformation, 2022. URL https://www.ksl-staubtechnik.de/wp-content/uploads/2021/10/808-INFO-esqua-Sande-Uebersicht.pdf.

[69] H. W. Kummer. Unified Theory of Rubber and Tire Friction. Technical report, Department of Mechanical Engineering, State College, USA, 1966.

[70] H. W. Kummer and W. E. Meyer. Verbesserter Kraftschluß zwischen Reifen und Fahrbahn – Ergebnisse einer neuen Reibungstheorie. *Automobiltechnische Zeitschrift (ATZ)*, 69(8 and 11):245–251 and 382–249, 1967.

[71] M. Kunze, T. Feißel, V. Ivanov, T. Bachmann, D. Hesse, and S. Gramstat. Analysis of TRWP Particle Distribution in Urban and Suburban Landscapes, Connecting Real Road Measurements with Particle Distribution Simulation. *Atmosphere*, 13(8):1204, 2022. doi: 10.3390/atmos13081204.

[72] K. J. Kupiainen and L. Pirjola. Vehicle non-exhaust emissions from the tyre–road interface – effect of stud properties, traction sanding and resuspension. *Atmospheric Environment*, 45(25):4141–4146, 2011. ISSN 13522310. doi: 10.1016/j.atmosenv.2011.05.027.

[73] K. J. Kupiainen, H. Tervahattu, M. Räisänen, T. Mäkelä, M. Aurela, and R. Hillamo. Size and composition of airborne particles from pavement wear, tires, and traction sanding. *Environmental Science & Technology*, 39(3): 699–706, 2005. ISSN 0013-936X. doi: 10.1021/es035419e.

[74] J. Kwak, S. Lee, and S. Lee. On-road and laboratory investigations on non-exhaust ultrafine particles from the interaction between the tire and road pavement under braking conditions. *Atmospheric Environment*, 97:195–205, 2014. ISSN 13522310. doi: 10.1016/j.atmosenv.2014.08.014.

[75] S. Lawrence, R. Sokhi, and K. Ravindra. Quantification of vehicle fleet PM10 particulate matter emission factors from exhaust and non-exhaust sources

using tunnel measurement techniques. *Environmental pollution (Barking, Essex : 1987)*, 210:419–428, 2016. doi: 10.1016/j.envpol.2016.01.011.

[76] G. Leister. *Fahrzeugräder - Fahrzeugreifen*. Springer Fachmedien Wiesbaden, Wiesbaden, Germany, 2015. ISBN 978-3-658-07463-0. doi: 10.1007/978-3-658-07464-7.

[77] Y. Li, S. Zuo, L. Lei, X. Yang, and X. Wu. Analysis of impact factors of tire wear. *Journal of Vibration and Control*, 18(6):833–840, 2012. ISSN 1077-5463. doi: 10.1177/1077546311411756.

[78] R. W. Lowne. The Effect of Road Surface Texture on Tyre Wear. *Wear*, 15 (1):57–70, 1970. doi: 10.1016/0043-1648(70)90186-9.

[79] L. Luhana, R. Sokhi, L. Warner, H. Mao, P. G. Boulter, I. McCrae, J. Wright, and D. Osborn. Measurement of non-exhaust particulate matter: PARTICULATES - Characterisation of Exhaust Particulate Emissions from Road Vehicles: Deliverable 8. Technical report, Hatfield, UK, October 2004.

[80] B. A. Maher, A. González-Maciel, R. Reynoso-Robles, R. Torres-Jardón, and L. Calderón-Garcidueñas. Iron-rich air pollution nanoparticles: An unrecognised environmental risk factor for myocardial mitochondrial dysfunction and cardiac oxidative stress. *Environmental research*, 188:109816, 2020. doi: 10.1016/j.envres.2020.109816.

[81] M. Mathissen, V. Scheer, R. Vogt, and T. Benter. Investigation on the potential generation of ultrafine particles from the tire–road interface. *Atmospheric Environment*, 45(34):6172–6179, 2011. ISSN 13522310. doi: 10.1016/j.atmosenv.2011.08.032.

[82] M. Mathissen, V. Scheer, U. Kirchner, R. Vogt, and T. Benter. Non-exhaust PM emission measurements of a light duty vehicle with a mobile trailer. *Atmospheric Environment*, 59:232–242, 2012. ISSN 13522310. doi: 10.1016/j.atmosenv.2012.05.020.

[83] K. Mattsson, J. A. de Lima, T. Wilkinson, I. Järlskog, E. Ekstrand, Y. Andersson-Sköld, M. Gustafsson, and M. Hassellöv. Tyre and road wear

particles from source to sea. *Microplastics and Nanoplastics*, 3(1), 2023. doi: 10.1186/s43591-023-00060-8.

[84] H. Mentlein and H. Lorenzl. *Strassenbau, Strassenbautechnik*. WIT. Reguvis, Köln, Germany, 8th updated edition, 2021. URL https://www.reguvis.de/xaver/bautechnik-digital/start.xav.

[85] W. E. Meyer and H. W. Kummer. Die Kraftübertragung zwischen Reifen und Fahrbahn. *Automobiltechnische Zeitschrift (ATZ)*, 66(9):245–249, 1964.

[86] Michelin. *Der Reifen: Haftung - Was Auto und Straße verbindet*. Michelin Reifenwerke KGaA, Karlsruhe, Germany, First edition, 2005.

[87] Michelin. *Der Reifen: Rollwiderstand und Kraftstoffersparnis - Wie Reifen Kraftstoffverbrauch und Emissionen senken können*. Michelin Reifenwerke KGaA, Karlsruhe, Germany, First edition, 2005.

[88] M. R. Miller and D. E. Newby. Air pollution and cardiovascular disease: car sick. *Cardiovascular research*, 116(2):279–294, 2020. doi: 10.1093/cvr/cvz228.

[89] R. Mundl, B. Wies, C. Recker, T. Becherer, M. Ersoy, and B. Schick. Bestandteile Reifen und Räder. In M. Ersoy and S. Gies, editors, *Fahrwerkhandbuch*, ATZ / MTZ-Fachbuch, pages 627–676. Springer Fachmedien Wiesbaden, Wiesbaden, Germany, 2017. ISBN 978-3-658-15467-7. doi: 10.1007/978-3-658-15468-4{\textunderscore}13.

[90] Y. Nakajima. *Advanced Tire Mechanics*. Springer Nature Singapore, Singapore, volume 1 edition, 2019. ISBN 978-981-13-5799-2. doi: 10.1007/978-981-13-5799-2.

[91] Nationale Akademie der Wissenschaften Leopoldina. Saubere Luft - Stickstoffoxide und Feinstaub in der Atemluft: Grundlagen und Empfehlungen : Ad-hoc-Stellungnahme. Technical report, Halle (Saale), Germany. URL https://www.leopoldina.org/uploads/tx_leopublication/Leo_Stellungnahme_SaubereLuft_2019_Web_03.pdf.

[92] OECD. Non-exhaust Particulate Emissions from Road Transport: An Ignored Environmental Policy Challenge. Technical report, Paris, France, 2020. URL https://doi.org/10.1787/4a4dc6ca-en.

[93] F. Oroumiyeh and Y. Zhu. Brake and tire particles measured from on-road vehicles: Effects of vehicle mass and braking intensity. *Atmospheric Environment: X*, 12:100121, 2021. ISSN 25901621. doi: 10.1016/j.aeaoa.2021.100121.

[94] PALAS GmbH. Promo 2000, 2024. URL https://www.palas.de/product/download/promo2000/datasheet/pdf. Accessed on April 15, 2024.

[95] PALAS GmbH. Aerosolsensor welas 2500, 2024. URL https://www.palas.de/en/product/download/aerosolsensor welas2500/datasheet/pdf. Accessed on May 29, 2024.

[96] J. M. Panko, J. Chu, M. L. Kreider, and K. M. Unice. Measurement of airborne concentrations of tire and road wear particles in urban and rural areas of France, Japan, and the United States. *Atmospheric Environment*, 72: 192–199, 2013. ISSN 13522310. doi: 10.1016/j.atmosenv.2013.01.040.

[97] J. M. Panko, M. L. Kreider, and K. M. Unice. Review of tire wear emissions. In F. Amato, editor, *Non-Exhaust Emissions*, pages 147–160. Elsevier, 2018. ISBN 9780128117705. doi: 10.1016/B978-0-12-811770-5.00007-8.

[98] I. Park, H. Kim, and S. Lee. Characteristics of tire wear particles generated in a laboratory simulation of tire/road contact conditions. *Journal of Aerosol Science*, 124:30–40, 2018. ISSN 00218502. doi: 10.1016/j.jaerosci.2018.07.005.

[99] B. N. J. Persson and E. A. Brener. Crack propagation in viscoelastic solids. *Physical review. E, Statistical, nonlinear, and soft matter physics*, 71(3 Pt 2A):036123, 2005. ISSN 1539-3755. doi: 10.1103/PhysRevE.71.036123.

[100] B. N. J. Persson, O. Albohr, G. Heinrich, and H. Ueba. Crack propagation in rubber-like materials. *Journal of Physics: Condensed Matter*, 17(44): R1071–R1142, 2005. ISSN 0953-8984. doi: 10.1088/0953-8984/17/44/R01.

[101] B. N. J. Persson, B. Lorenz, M. Shimizu, and M. Koishi. Multiscale Contact Mechanics with Application to Seals and Rubber Friction on Dry and Lubricated Surfaces. 275(978-3-319-47696-4 (electronic)):103–156, 2017. doi: 10.1007/12{\textunderscore}2016{\textunderscore}4. URL `https://juser.fz-juelich.de/record/860466`.

[102] W. R. Pierson and W. W. Brachaczek. Airborne Particulate Debris from Rubber Tires. *Rubber Chemistry and Technology*, 47:1275–1299, 1974. URL `https://api.semanticscholar.org/CorpusID:137300698`.

[103] R. Pohrt. Tire Wear Particle Hot Spots - Review of Influencing Factors. *Facta Universitatis, Series: Mechanical Engineering*, 17(1):17–27, 2019. ISSN 0354-2025. doi: 10.22190/FUME190104013P.

[104] J. Rausch, D. Jaramillo-Vogel, S. Perseguers, N. Schnidrig, B. Grobéty, and P. Yajan. Automated identification and quantification of tire wear particles (TWP) in airborne dust: SEM/EDX single particle analysis coupled to a machine learning classifier. *Science of The Total Environment*, (803):149832, 2022. ISSN 00489697. doi: 10.1016/j.scitotenv.2021.149832.

[105] A. Rauterberg-Wulff. *Beitrag des Reifen- und Bremsenabriebs zur Rußemission an Straßen*. Fortschritt-Berichte / VDI Reihe 15, Umwelttechnik. VDI-Verlag, Düsseldorf, Germany, 1998. ISBN 3-18-320215-8.

[106] D. Richter and M. Heindel. *Straßen- und Tiefbau: mit lernfeldorientierten Projekten*. B.G. Teubner Verlag, Wiesbaden, Germany, Tenth edition, 2008. ISBN 978-3-8351-0057-2.

[107] P. Riehm, H.-J. Unrau, F. Gauterin, S. Torbrügge, and B. Wies. 3D brush model to predict longitudinal tyre characteristics. *Vehicle System Dynamics*, 57(1):17–43, 2019. doi: 10.1080/00423114.2018.1447135.

[108] N. Rodriguez, P. Mangiagalli, and B. N. J. Persson. Viscoelastic Crack Propagation: Review of Theories and Applications. *Fatigue Crack Growth in Rubber Materials*, 286:377–420, 2020. ISSN 1436-5030. doi: 10.1007/12{\textunderscore}2020{\textunderscore}76. URL `https://link.springer.com/chapter/10.1007/12_2020_76`.

[109] U. Sandberg and J. A. Ejsmont. *Tyre road noise reference book: Reference book*. INFORMEX, Kisa, first edition, 2002. ISBN 9163126109.

[110] S. Schläfle, F. Gauterin, and R. Lallement. Aufbau eines Prüfstands zur Messung von Reifen-Fahrbahn-Feinstaubemissionen auf realen Fahrbahnoberflächen. In VDI Wissensforum GmbH, editor, *Reifen – Fahrwerk – Fahrbahn*, VDI-Berichte, pages 15–33, Düsseldorf, Germany, 2022. VDI Verlag. ISBN 978-3-18-092398-7. doi: 10.51202/9783181023983-15.

[111] S. Schläfle, H.-J. Unrau, and F. Gauterin. Influence of Load Condition, Tire Type, and Ambient Temperature on the Emission of Tire–Road Particulate Matter. *Atmosphere*, 14(7), 2023. doi: 10.3390/atmos14071095.

[112] S. Schläfle, H.-J. Unrau, and F. Gauterin. Influence of Longitudinal and Lateral Forces on the Emission of Tire–Road Particulate Matter and Its Size Distribution. *Atmosphere*, 14(12), 2023. doi: 10.3390/atmos14121780.

[113] S. Schläfle, H.-J. Unrau, F. Gauterin, and A. Killik. Experimentelle Untersuchung der Reifen-Fahrbahn-Feinstaubemission von Premium-Sommerreifen am Innentrommelprüfstand: Experimental Investigation of Tire-Road Particulate Matter Emissions from Premium Summer Tires on an Internal Drum Test Bench. In VDI Wissensforum GmbH, editor, *Reifen - Fahrwerk - Fahrbahn*, VDI-Berichte, pages 181–195, Düsseldorf, Germany, 2023. VDI Verlag. ISBN 978-3-18-092425-0.

[114] S. Schläfle, M. Zhang, H.-J. Unrau, and F. Gauterin. Influence of Vertical Load, Inflation Pressure, and Driving Speed on the Emission of Tire–Road Particulate Matter and its Size Distribution. *Atmosphere*, 15(4):502, 2024. doi: 10.3390/atmos15040502.

[115] F. Schmerwitz, S. Wieting, N. Aschenbrenner, A. Topp, and B. Wies. Characterization of Tire Road Wear Particles in the Field and at Laboratory Scale. In P. E. Pfeffer, editor, *12th International Munich Chassis Symposium 2021*, ATZ live, pages 729–743, Berlin, Germany and Heidelberg, 2022. Springer Vieweg. ISBN 9783662645499.

[116] Å. Sjödin, M. Ferm, A. Björk, M. Rahmberg, A. Gudmundsson, E. Swietlicki, C. Johansson, M. Gustafsson, and G. Blomqvist. Wear Particles from road traffic: a field, laboratory and modelling study: Final report. Technical report, Göteborg, Sweden, 2010.

[117] Statistisches Landesamt Baden-Württemberg. Feinstaub (PM10)-Emissionen des Straßenverkehrs in Baden Württemberg seit 1995, 2023. URL `https://www.statistik-bw.de/Umwelt/Luft/l1a07aub.jsp`. Accessed on June 4, 2024.

[118] M. Stieß. *Mechanische Verfahrenstechnik - Partikeltechnologie 1*. Springer Berlin Heidelberg, Berlin - Heidelberg, Germany, Third edition, 2009. ISBN 978-3-540-32551-2. doi: 10.1007/978/3-540-32552-9.

[119] N. Stojanovic, O. I. Abdullah, I. Grujic, and B. Boskovic. Particles formation due to the wear of tires and measures for the wear reduction: A review. *Proceedings of the Institution of Mechanical Engineers, Part D: Journal of Automobile Engineering*, 236(14):1–15, 2021. ISSN 0954-4070. doi: 10.1177/09544070211067879.

[120] J. Svendenius and B. Wittenmark. Brush tire model with increased flexibility. In *European Control Conference ECC 2003*, pages 1863–1868, Piscataway, New Jersey, 2003. IEEE. ISBN 978-3-9524173-7-9. doi: 10.23919/ECC.2003.7085237.

[121] The Council of the European Union. Council Directive 1999/30/EC of 22 April 1999 relating to limit values for sulphur dioxide, nitrogen dioxide and oxides of nitrogen, particulate matter and lead in ambient air: 99/30/EC, 19/07/1999. URL `https://eur-lex.europa.eu/legal-content/EN/TXT/PDF/?uri=CELEX:31999L0030`. Accessed on May 6, 2024.

[122] The Council of the European Union. Euro 7: Council and Parliament strike provisional deal on emissions limits for road vehicles, 2023. URL https://www.consilium.europa.eu/de/press/press-releases/2023/12/18/euro-7-council-and-parliament-strike-provisional-deal-on-emissions-limits-for-road-vehicles/. Accessed on May 10, 2024.

[123] The European Parliament and the Council of the European Union. Directive 2008/50/EC of the European Parliament and of the Council of May 21 2008 on ambient air quality and cleaner air for Europe: 2008/50/EC, 06/11/2008. URL https://eur-lex.europa.eu/legal-content/EN/TXT/PDF/?uri=CELEX:32008L0050. Accessed on May 6, 2024.

[124] A. Thorpe and R. M. Harrison. Sources and properties of non-exhaust particulate matter from road traffic: a review. *Science of The Total Environment*, 400(1-3):270–282, 2008. ISSN 00489697. doi: 10.1016/j.scitotenv.2008.06.007.

[125] V. R. J. H. Timmers and P. A. J. Achten. Non-exhaust PM emissions from electric vehicles. *Atmospheric Environment*, 134:10–17, 2016. ISSN 13522310. doi: 10.1016/j.atmosenv.2016.03.017.

[126] Y. Tonegawa and S. Sasaki. Development of Tire-Wear Particle Emission Measurements for Passenger Vehicles. *Emission Control Science and Technology*, 7(1):56–62, 2021. ISSN 2199-3629. doi: 10.1007/s40825-020-00181-z.

[127] M. Trzesniowski. *Fahrwerk*. Springer Fachmedien Wiesbaden, Wiesbaden, Germany, second edition, 2019. ISBN 978-3-658-26699-8. doi: 10.1007/978-3-658-26700-1.

[128] Umweltbundesamt. Feinstaubbelastung in Deutschland. Technical report, Dessau-Roßlau, Germany, Mai 2009. URL https://www.umweltbundesamt.de/publikationen/feinstaubbelastung-in-deutschland.

[129] Umweltbundesamt. Was ist Feinstaub?, 2018. URL https://www.umweltbundesamt.de/service/uba-fragen/was-ist-feinstaub. Accessed on April 5, 2024.

[130] Umweltbundesamt. Emission von Feinstaub der Partikelgröße PM10 Umweltbundesamt, 2024. URL https://www.umweltbundesamt.de/daten/luft/luftschadstoff-emissionen-in-deutschland/emission-von-feinstaub-der-partikelgroesse-pm10#emissionsentwicklung. Accessed on June 4, 2024.

[131] Umweltbundesamt. Luftdaten: Jahresbilanzen, 2024. URL https://www.umweltbundesamt.de/daten/luft/luftdaten/jahresbilanzen/eJxrWpScv9BwUWXqEiMDI2MAMLAFtA==. Accessed on May 6, 2024.

[132] K. M. Unice, M. L. Kreider, and J. M. Panko. Comparison of tire and road wear particle concentrations in sediment for watersheds in France, Japan, and the United States by quantitative pyrolysis GC/MS analysis. *Environmental Science & Technology*, 47(15):8138–8147, 2013. doi: 10.1021/es400871j.

[133] K. M. Unice, M. P. Weeber, M. M. Abramson, R. C. D. Reid, J. A. G. van Gils, A. A. Markus, A. D. Vethaak, and J. M. Panko. Characterizing export of land-based microplastics to the estuary - Part I: Application of integrated geospatial microplastic transport models to assess tire and road wear particles in the Seine watershed. *The Science of the total environment*, 646:1639–1649, 2019. doi: 10.1016/j.scitotenv.2018.07.368.

[134] United Stated Environmental Protection Agency. Particulate Matter (PM) Basics, 2023. URL https://www.epa.gov/pm-pollution/particulate-matter-pm-basics. Accessed on May 2, 2024.

[135] United Stated Environmental Protection Agency. Health and Environmental Effects of Particulate Matter (PM), 2023. URL https://www.epa.gov/pm-pollution/health-and-environmental-effects-particulate-matter-pm. Accessed on May 2, 2024.

[136] H. A. C. D. van der Gon, M. Jozwicka, F. R. Cassee, and M. E. Gerlofs-Nijland. The policy relevance of wear emissions from road transport, now and in the future: Workshop report: An International workshop. Technical Report TNO-060-UT-2012-00732, Amsterdam, The Netherlands, 2012.

[137] H. A. C. D. van der Gon, M. E. Gerlofs-Nijland, R. Gehrig, M. Gustafsson, N. Janssen, R. M. Harrison, J. Hulskotte, C. Johansson, M. Jozwicka, M. Keuken, K. Krijgsheld, L. Ntziachristos, M. Riediker, and F. R. Cassee. The policy relevance of wear emissions from road transport, now and in the future–an international workshop report and consensus statement. *Journal of the Air & Waste Management Association (1995)*, 63(2):136–149, 2013. doi: 10.1080/10962247.2012.741055.

[138] B. van Zeebroeck and G. de Ceuster. Elektrische wagens verminderen fijn stof nauwelijks: Analyse op basis van bestaande literatuur Uitgebreide versie. Technical report, Leuven, Belgium, November 2013. URL `https://www.tmleuven.be/uploads/navigationtree/files/belang_niet-uitlaat_fijn_stof_emissies_lang.pdf`.

[139] Verein Deutscher Ingenieure. *VDI 3867-1, Messen von Partikeln in der Außenluft Bestimmung der Partikelanzahlkonzentration und Anzahlgrößenverteilung von Aerosolen Grundlagen*. Beuth Verlag GmbH, Berlin, Germany, 2009.

[140] Verein Deutscher Ingenieure. *VDI 3867-4, Messen von Partikeln in der Außenluft Bestimmung der Partikelanzahlkonzentration und Anzahlgrößenverteilung von Aerosolen Optisches Aerosolspektrometer*. Beuth Verlag GmbH, Berlin, Germany, 2011.

[141] Verein Deutscher Ingenieure. *VDI 3867-6, Messen von Partikeln in der Außenluft Bestimmung der Partikelanzahlkonzentration und Anzahlgrößenverteilung von Aerosolen: Elektrischer Niederdruckimpaktor (ELPI)*. Beuth Verlag GmbH, Berlin, Germany, 2012.

[142] Verein Deutscher Ingenieure. *VDI 3867-5, Messen von Partikeln in der Außenluft Bestimmung der Partikelanzahlkonzentration und Anzahlgrößenverteilung von Aerosolen Flugzeitspektrometer: Flugzeitspektrometer*. Beuth Verlag GmbH, Berlin, Germany, 2013.

[143] Verein Deutscher Ingenieure. *VDI 2066-1, Messen von Partikeln, Staubmessung in strömenden Gasen, Gravimetrische Bestimmung der Staubbeladung*. Beuth Verlag GmbH, Düsseldorf, Germany, 2019.

[144] C. Wang, H. Huang, X. Chen, and J. Liu. The influence of the contact features on the tyre wear in steady-state conditions. *Proceedings of the Institution of Mechanical Engineers, Part D: Journal of Automobile Engineering*, 231 (10):1326–1339, 2017. ISSN 0954-4070. doi: 10.1177/0954407016671462.

[145] T. Wilkinson, I. Järlskog, J. A. de Lima, M. Gustafsson, K. Mattsson, Y. Andersson-Sköld, and M. Hassellöv. Shades of grey—tire characteristics and road surface influence tire and road wear particle (TRWP) abundance and physicochemical properties. *Frontiers in Environmental Science*, 11, 2023. doi: 10.3389/fenvs.2023.1258922.

[146] R. L. Williams and S. H. Cadle. Characterization of Tire Emissions Using an Indoor Test Facility. *Rubber Chemistry and Technology*, 51(1):7–25, 1978. ISSN 0035-9475. doi: 10.5254/1.3535728.

[147] H.-P. Willumeit. *Modelle und Modellierungsverfahren in der Fahrzeugdynamik*. Teubner, Stuttgart and Leipzig, Germany, 1998. ISBN 978-3-663-12248-7. doi: 10.1007/978-3-663-12247-0.

[148] World Health Organization. WHO Air quality guidelines for particulate matter, ozone, nitrogen dioxide and sulfur dioxide: Summary of risk assessment: Global update 2005. Technical Report WHO/SDE/PHE/OEH/06.02, Geneva, Switzerland.

[149] World Health Organization. Globale Luftgüteleitlinien der WHO: Feinstaubpartikel (PM2,5 und PM10), Ozon, Stickstoffdioxid, Schwefeldioxid und Kohlenmonoxid: Zusammenfassung, 2021. URL `https://iris.who.int/handle/10665/346506`. Accessed on June 4, 2024.

[150] G. Wypych, editor. *Handbook of Fillers*. CP ChemTec Publishing, Toronto, Canada, fourth edition, 2016. ISBN 978-1-895198-91-1.

[151] H. Yan, L. Zhang, L. Liu, and S. Wen. Investigation of the external conditions and material compositions affecting the formation mechanism and size distribution of tire wear particles. *Atmospheric Environment*, 244: 118018, 2021. ISSN 13522310. doi: 10.1016/j.atmosenv.2020.118018.

[152] D. Younan, A. J. Petkus, K. F. Widaman, X. Wang, R. Casanova, M. A. Espeland, M. Gatz, V. W. Henderson, J. E. Manson, S. R. Rapp, B. C. Sachs, Marc L. Serre, S. A. Gaussoin, R. Barnard, S. Saldana, W. Vizuete, D. P. Beavers, Joel A. Salinas, H. C. Chui, S. M. Resnick, S. A. Shumaker, and J.-C. Chen. Particulate matter and episodic memory decline mediated by early neuroanatomic biomarkers of Alzheimer's disease. *Brain : a journal of neurology*, 143(1):289–302, 2020. doi: 10.1093/brain/awz348.

[153] M. Zhang, H.-J. Unrau, M. Gießler, and F. Gauterin. A detailed tire tread friction model considering dynamic friction states. *Tribology International*, 193:109342, 2024. ISSN 0301679X. doi: 10.1016/j.triboint.2024.109342. URL `https://www.sciencedirect.com/science/article/pii/S0301679X2400094X`.

List of Publications

Journal Articles

[Journal1] I. Gehrke, S. Schläfle, R. Bertling, M. Öz, and K. Gregory. Review: Mitigation measures to reduce tire and road wear particles. *Science of The Total Environment*, 904:166537, 2023. ISSN 00489697. doi: 10.1016/j.scitotenv.2023.166537.

[Journal2] M. Haugen, P. Bühler, S. Schläfle, D. O'Loughlin, S. Saladin, C. Giorio, and A. Boies. Method development and analysis of nanoparticle size fractions from tire-wear emissions. *Environmental Science: Atmospheres*, 4(9):1079–1090, 2024. doi: 10.1039/D4EA00048J.

[Journal3] S. Schläfle, H.-J. Unrau, and F. Gauterin. Influence of Load Condition, Tire Type, and Ambient Temperature on the Emission of Tire–Road Particulate Matter. *Atmosphere*, 14(7), 2023. doi: 10.3390/atmos14071095.

[Journal4] S. Schläfle, H.-J. Unrau, and F. Gauterin. Influence of Longitudinal and Lateral Forces on the Emission of Tire–Road Particulate Matter and Its Size Distribution. *Atmosphere*, 14(12), 2023. doi: 10.3390/atmos14121780.

[Journal5] S. Schläfle, M. Zhang, H.-J. Unrau, and F. Gauterin. Influence of Vertical Load, Inflation Pressure, and Driving Speed on the Emission of Tire–Road Particulate Matter and its Size Distribution. *Atmosphere*, 15(4):502, 2024. doi: 10.3390/atmos15040502.

Conference Contributions

[Conference1] S. Schläfle, F. Gauterin, and R. Lallement. Aufbau eines Prüfstands zur Messung von Reifen-Fahrbahn-Feinstaubemissionen auf realen Fahrbahnoberflächen. In VDI Wissensforum GmbH, editor, *Reifen – Fahrwerk – Fahrbahn*, VDI-Berichte, pages 15–33, Düsseldorf, Germany, 2022. VDI Verlag. ISBN 978-3-18-092398-7. doi: 10.51202/9783181023983-15.

[Conference2] S. Schläfle, H.-J. Unrau, F. Gauterin, and A. Killik. Experimentelle Untersuchung der Reifen-Fahrbahn-Feinstaubemission von Premium-Sommerreifen am Innentrommelprüfstand: Experimental Investigation of Tire-Road Particulate Matter Emissions from Premium Summer Tires on an Internal Drum Test Bench. In VDI Wissensforum GmbH, editor, *Reifen - Fahrwerk - Fahrbahn*, VDI-Berichte, pages 181–195, Düsseldorf, Germany, 2023. VDI Verlag. ISBN 978-3-18-092425-0.

Published Patent Applications

[Patent1] R. Lallement, F. Gauterin, S. Schläfle, G. Leister, H. Weidlich, and H.-J. Unrau. Feinstaubhemmende Fahrbahndecke: Offenlegungsschrift (DE 10 2021 004 107 A1). *Deutsches Patent- und Markenamt*, 2021.

[Patent2] R. Lallement, F. Gauterin, S. Schläfle, G. Leister, H. Weidlich, and H.-J. Unrau. Fahrzeug-Reifen zur Feinstaubvermeidung: Offenlegungsschrift (DE 10 2021 003 156 A1). *Deutsches Patent- und Markenamt*, 2021.

[Patent3] R. Lallement, F. Gauterin, S. Schläfle, G. Leister, H. Weidlich, and H.-J. Unrau. Reinigungsvorrichtung für eine Waschanlage zum Reinigen von Kraftfahrzeugen sowie Verfahren zum Reinigen von Kraftfahrzeugen:

Offenlegungsschrift (DE 10 2021 003 300 A1). *Deutsches Patent- und Markenamt*, 2021.

[Patent4] R. Lallement, F. Gauterin, S. Schläfle, G. Leister, H. Weidlich, and H.-J. Unrau. Vernebelungseinrichtung für ein Kraftfahrzeug sowie Verfahren zum Betreiben eines Kraftfahrzeugs: Offenlegungsschrift (DE 10 2021 003 436 A1). *Deutsches Patent- und Markenamt*, 2021.

[Patent5] R. Lallement, F. Gauterin, S. Schläfle, G. Leister, H. Weidlich, and H.-J. Unrau. Reifenmaterial für einen Fahrzeugreifen: Offenlegungsschrift (DE 10 2021 003 559 A1). *Deutsches Patent- und Markenamt*, 2021.

[Patent6] R. Lallement, F. Gauterin, S. Schläfle, G. Leister, H. Weidlich, and H.-J. Unrau. Fahrzeugreifen: Offenlegungsschrift (DE 10 2021 002 779 A1). *Deutsches Patent- und Markenamt*, 2022.

Karlsruher Schriftenreihe Fahrzeugsystemtechnik FAST Institut für Fahrzeugsystemtechnik (ISSN 1869-6058)

Eine vollständige Übersicht der Bände finden Sie im Verlagsshop

Band 76 Kai-Lukas Bauer
Echtzeit-Strategieplanung für vorausschauendes automatisiertes Fahren
ISBN 978-3-7315-0949-3

Band 77 Thomas Schirle
Systementwurf eines elektromechanischen Fahrwerks für Megacitymobilität
ISBN 978-3-7315-0995-0

Band 78 Dominik Dörr
Simulation of the thermoforming process of UD fiber-reinforced thermoplastic tape laminates
ISBN 978-3-7315-0998-1

Band 79 Dominik Robert Naake
Simulation of damage mechanisms in weave reinforced materials based on multiscale modeling
ISBN 978-3-7315-1005-5

Band 80 Martin Hohberg
Experimental investigation and process simulation of the compression molding process of Sheet Molding Compound (SMC) with local reinforcements
ISBN 978-3-7315-1007-9

Band 81 Benedikt Fengler
Manufacturing-constrained multi-objective optimization of local patch reinforcements for discontinuous fiber reinforced composite parts
ISBN 978-3-7315-1006-2

Band 82 Johannes Masino
Road Condition Estimation with Data Mining Methods using Vehicle Based Sensors
ISBN 978-3-7315-1004-8

Band 83 **11. Kolloquium Mobilhydraulik**
10. September 2020, Karlsruhe
ISBN 978-3-7315-1036-9

Die Bände sind unter www.ksp.kit.edu als PDF frei verfügbar oder als Druckausgabe bestellbar.

Band 84 Felix Weber
Beitrag zur Entwicklung von Konstantflusspumpen für Frischbeton unter genauerer Betrachtung der Dickstoffventile
ISBN 978-3-7315-1037-6

Band 85 8. Fachtagung
Hybride und energieeffiziente Antriebe für mobile Arbeitsmaschinen. 23. Februar 2021, Karlsruhe
ISBN 978-3-7315-1071-0

Band 86 Sebastian Fünfgeld
Vorausschauende Regelung von Fahrzeugsystemen durch stochastische Vorhersage der Fahrzeugdynamik
ISBN 978-3-7315-1060-4

Band 87 Isabelle Charlotte Ays
Development of a CO2e quantification method and of solutions for reducing the greenhouse gas emissions of construction machines = Entwicklung einer CO2e Quantifizierungsmethode und von Lösungen zur Reduzierung von Treibhausgasemissionen in Baumaschinen
ISBN 978-3-7315-1033-8

Band 88 Alexander Bernath
Numerical prediction of curing and process-induced distortion of composite structures
ISBN 978-3-7315-1063-5

Band 89 Nils Bulthaupt
Objektivierung des Schwingungskomforts schwerer Nutzfahrzeuge
ISBN 978-3-7315-1075-8

Band 90 Lars Brinkschulte
Assistenzsysteme zur Reduktion des Schädigungsverhaltens von Komponenten einer mobilen Arbeitsmaschine
ISBN 978-3-7315-1089-5

Band 91 Dominik Dörr
Adaptive Fahrhinweise für ein längsdynamisches Fahrerassistenzsystem zur Steigerung der Energieeffizienz
ISBN 978-3-7315-1090-1

Band 92 Jürgen Römer
Steuerung und Regelung des Lenkradmoments durch Nutzung radselektiver Frontantriebe
ISBN 978-3-7315-1104-5

Band 93 Christian Riese
Werkzeuge und Konzepte für die Untersuchung und Entwicklung zukünftiger Kfz-Bremssysteme
ISBN 978-3-7315-1125-0

Band 94 Yaoqun Zhou
Dynamisches Bremsverhalten des Reifen-Fahrwerk-Systems
ISBN 978-3-7315-1156-4

Band 95 Stefan Haug
Ganzheitliche Optimierung einer Axialkolbenpumpe durch bedarfsangepasste Entlastung tribologischer Kontakte
ISBN 978-3-7315-1150-2

Band 96 Stefan Scheubner
Stochastic Range Estimation Algorithms for Electric Vehicles using Data-Driven Learning Models
ISBN 978-3-7315-1166-3

Band 97 Yusheng Xiang
AI and IoT Meet Mobile Machines: Towards a Smart Working Site
ISBN 978-3-7315-1165-6

Band 98 Nils Meyer
Mesoscale simulation of the mold filling process of Sheet Molding Compound
ISBN 978-3-7315-1173-1

Band 99 Christian Timo Poppe
Process simulation of wet compression moulding for continuous fibre-reinforced polymers
ISBN 978-3-7315-1190-8

Band 100 Torben Fischer
Modellprädiktive Regelung eines innovativen Thermomanagement-Systems für batterieelektrische Fahrzeuge
ISBN 978-3-7315-1199-1

Band 101 Florian Wittemann
Fiber-dependent injection molding simulation of discontinuous reinforced polymers
ISBN 978-3-7315-1217-2

Band 102 Sebastian Watzl
Experimentelle und numerische Analyse des Körperschallübertragungsverhaltens von Aggregatelagerelementen im akustisch relevanten Frequenzbereich
ISBN 978-3-7315-1226-4

Die Bände sind unter www.ksp.kit.edu als PDF frei verfügbar oder als Druckausgabe bestellbar.

Band 103 Dominik Stretz
Vibroakustische Analyse eines elektrischen Radnabenmotors und Optimierung durch geeignete Steuerungsansätze
ISBN 978-3-7315-1245-5

Band 104 Mohamed Elgharbawy
Measurable Safety of Automated Driving Functions in Commercial Motor Vehicles - Technological and Methodical Approaches
ISBN 978-3-7315-1254-7

Band 105 Bernhard Schmiedel
Indirekte Schätzung des Fahrbahnnässegrads zur Detektion von gefährlichen Fahrzuständen
ISBN 978-3-7315-1258-5

Band 106 9. Fachtagung
Hybride und energieeffiziente Antriebe für mobile Arbeitsmaschinen. 28. Februar 2023, Karlsruhe
ISBN 978-3-7315-1260-8

Band 107 Patrick Riehm
Zur Wechselwirkung zwischen Fahrbahntextur und Laufstreifenmischung von Pkw-Reifen
ISBN 978-3-7315-1268-4

Band 108 Markus Tesar
Deep Reinforcement Learning zur Steigerung von Energieeffizienz und Pünktlichkeit von Straßenbahnen
ISBN 978-3-7315-1277-6

Band 109 Michael Mürken
Methode zur Bewertung der Zuverlässigkeit der elektrischen Energieversorgung in der automobilen Vorentwicklung
ISBN 978-3-7315-1298-1

Band 110 Julien Pinay
Experimental investigation of relevant road surface descriptors for tire-road noise measurements on low-absorbing road surfaces
ISBN 978-3-7315-1328-5

Band 111 Adrian Strigel
Methode zur Ermittlung optimaler Rad- und Reifendimensionen in der frühen Entwicklungsphase von Personenkraftwagen
ISBN 978-3-7315-1321-6

Band 112 Jens Jauch
Trajectory optimization based on recursive B-spline approximation for automated longitudinal control of a battery electric vehicle
ISBN 978-3-7315-1332-2

Band 113 Nicolas Fraikin
Methodik zur effizienten Applikation automatisierter Fahrfunktionen
ISBN 978-3-7315-1339-1

Band 114 Jan Siebert
Effizienzoptimierung mobilhydraulischer Load-Sensing-Systeme durch Reduzierung systembedingter Druckverluste am Beispiel eines Hydraulikbaggers
ISBN 978-3-7315-1343-8

Band 115 Tobias Sebastian Straub
Flottendatenbasierte physikalische Routenenergiebedarfsprognose
ISBN 978-3-7315-1348-3

Band 116 Michael Herrmann
Eine Methodik zur Definition von Zielkriterien am Beispiel des tieffrequenten Geräuschkomforts eines Fahrzeugs
ISBN 978-3-7315-1370-4

Band 117 Adam Thor Thorgeirsson
Probabilistic Prediction of Energy Demand and Driving Range for Electric Vehicles with Federated Learning
ISBN 978-3-7315-1371-1

Band 118 Alexander Jackstadt
Constrained-layer damping in hybrid fibre metal elastomer laminates and its tolerance to damage
ISBN 978-3-7315-1376-6

Band 119 **13. Kolloquium Mobilhydraulik**
8./9. Oktober 2024, Karlsruhe
ISBN 978-3-7315-1381-0

Band 120 Toni Wilhelm
Querdynamik von Velomobilen unter Berücksichtigung der Reifeneigenschaften
ISBN 978-3-7315-1382-7

Band 121 Alexander Brunker
Hochgenaue und robuste odometriebasierte Lokalisierung in einem Parkvorgang
ISBN 978-3-7315-1383-4

Band 122 Daniel Förster
Systemauslegung autarker Hybridantriebe unter Berücksichtigung kundenspezifischer Randbedingungen
ISBN 978-3-7315-1384-1

Band 123 Maurizio Mauro Festa
Objektive Fahrkomfortbewertung des Gesamtfahrzeugs unter Berücksichtigung menschlicher Wahrnehmungsaspekte
ISBN 978-3-7315-1392-6

Band 124 10. Fachtagung
Hybride und energieeffiziente Antriebe für mobile Arbeitsmaschinen. 19. Februar 2025, Karlsruhe
ISBN 978-3-7315-1403-9

Band 125 8. Fachtagung
MOBILE MACHINES – Sicherheit und Fahrerassistenz für Arbeitsmaschinen. 18. Februar 2025, Karlsruhe
ISBN 978-3-7315-1404-6

Band 126 Raphael Mieth
Kundenbedarfsgerechte Auslegung elektrischer Pkw-Antriebssysteme zur Steigerung der Energieeffizienz
ISBN 978-3-7315-1416-9

Band 127 Lukas Michiels
A simulation-based approach to the fluid-structure interaction inside fatigue cracks in hydraulic components
ISBN 978-3-7315-1424-4

Band 128 Felix Deufel
Optimales Energiemanagement mild elektrifizierter Antriebe unter realen Betriebsbedingungen mittels Prädiktionsalgorithmen aus dem Bereich des Maschinellen Lernens
ISBN 978-3-7315-1426-8

Band 129 Andreas M. Billert
Predictive Battery Thermal Management of Electric Vehicles using Deep Learning
ISBN 978-3-7315-1429-9

Band 130 Bastian Benjamin Jascha Schäfer
Macroscopic forming simulation of unidirectional non-crimp fabrics: Hyperelastic material modeling and 3D-solid-shell approach
ISBN 978-3-7315-1430-5

Band 131 Rene Armbruster
Untersuchung des Schwingungsverhaltens der Einheit Reifen, Rad, Radführung im komfortrelevanten Schwingungsbereich
ISBN 978-3-7315-1433-6

Band 132 Constantin Krauß
Direction-Dependent Result Data Transfer in Virtual Process Chains for Fiber-Reinforced Polymers and the Impact on Structural Simulation
ISBN 978-3-7315-1434-3

Band 133 Roland Herberth
Nutzerorientierte Optimierung des Over-the-Air-Updateprozesses vernetzter Kraftfahrzeuge
ISBN 978-3-7315-1438-1

Band 134 Jan Löwer
Untersuchungen zum Bremsverhalten von PKW-Reifen im Grenzbereich zwischen Nassgriff und Aquaplaning
ISBN 978-3-7315-1439-8

Band 135 Timo von Wysocki
Reduction of Selected Road Noise Phenomena by Modifying Suspension Kinematics Using Metamodels in the Digital Vehicle Development Phase
ISBN 978-3-7315-1447-3

Band 136 Stefan Schläfle
The Influence of Vehicle Operating Conditions on Tire–Road Particulate Matter Emissions
ISBN 978-3-7315-1462-6

Karlsruher Schriftenreihe
Fahrzeugsystemtechnik

FAST
Institut für
Fahrzeugsystemtechnik

A significant proportion of the particulate matter (PM) found in ambient air comes from road traffic. As electrification progresses, it is becoming increasingly clear that road traffic will continue to be a substantial source of PM emissions, even once exhaust emissions have been eliminated. Thus, non-exhaust emissions, including particles from friction brakes and tire–road contact, will gain in importance. The upcoming Euro 7 emission standards will include limits for both emitters—on PM emission for friction brakes and on total mass loss for tires. Currently, there is neither a database nor a suitable measurement method to regulate tire or tire–road PM. This work contributes to a better understanding of the generation and measurement of tire–road PM. For this purpose, a tire internal drum test bench was enabled to measure tire–road PM in real time. This allowed for identification and quantification of vehicle, road, and environmental influences on PM emissions from tire–road contact. Based on these findings and using real driving data, a model was developed that predicts PM emissions for real-world driving.

ISSN 1869-6058
ISBN 978-3-7315-1462-6